Characterisation of Laser Cutting For An Adaptive Control Environment

A Thesis
submitted to
the Department of Mechanical Engineering of University of Glasgow
in fulfilment of the requirements
for the
Degree of Doctor of Philosophy

BY

© MING-YAW HUANG

LASER AND OPTICAL SYSTEMS
ENGINEERING GROUP

January 1994

SYNOPSIS

The reactive gas assisted laser cutting process is influenced strongly by characteristics such as: power mode (i.e. CW or pulsed), power density, transverse mode, beam polarisation; set-up of operating system such as: beam delivery optics, nozzle type, assist gas type and gas pressure, beam-focusing, laser beam operating position (offset), and feedrate; and characteristics of target material such as: conductivity, diffusivity, melting temperature, boiling temperature, latent heat of melting and vaporisation, plasma formation, exothermic chemical reaction with reactive gas O_2, and relevant viscosities. So many parameters are involved that inevitably laser cutting is a highly non-linear process and consequently difficult to analyse or predict.

Relationships between the operational parameters and cut quality were investigated empirically. As long as the cut can be initiated, change of focal point offset distance does not greatly influence the size of the heat affected zone (HAZ). The kerf surface roughness is slightly increased when the offset distance is increased. The best focal point position, for cutting mild steel up to 6 mm, is on the surface. Increasing the assist gas pressure reduces the HAZ size slightly, reduces dross attachment and has little effect on the kerf surface roughness. The effects are more pronounced on the mild steel than stainless steel because of the higher viscosity of liquid phase stainless steel. A slower feedrate increases both the HAZ size and the roughness of the kerf surface; therefore, feedrate is chosen as the major control parameter in the cutting system.

Spark cone images from the workpiece lower surface are analysed. An intense uniform cone was observed when a clean cut was performed. Sparser spark cone images were characteristic of poorer quality cuts where dross attachment disturbs the gas-metal mixture flow.

A hierarchically structured environment that integrates a knowledge-based expert system, adaptive process control and pattern recognition techniques for controlling the laser cutting process are developed. Knowledge of the laser cutting process for different materials is organised and encoded into a rule-based system. An adaptive control algorithm based on on-line recursive parameter estimation and on-line control law synthesis was adopted for the highly non-linear cutting process control. Cutting speed was selected as the major control variable. Irradiance emitted from the cut front was used for the feedback signal to this adaptive controller. The irradiance signal feeds the recursive parameter estimator for system identification. Techniques of pattern recognition, which have been well developed in coherent optics, were applied to the cutting quality analysis by characterising the exit spark cone images of the gas assisted laser cutting process. Images from the cutting processes were grabbed, edge enhanced and correlated with a synthetic discriminant function (SDF) filter which was synthesised from reference images known to give good cut quality. The SDF discrimination performance was enhanced by incorporating the Wiener filter into its construction, such that the in-class image and out-of-class image were integrated into a single filter. Results from digital simulations based on these pattern recognition algorithms are also presented.

ACKNOWLEDGEMENT

I wish to express my sincere thanks to Dr. C. R. Chatwin for continuous encouragement and advice throughout this research.

I am also appreciative to the enormous technical assistances from George, Vic, Jimmy and Ian.

I am grateful to Professor B. F. Scott, head of the Department of Mechanical Engineering, for the facilities provided in the Department.

And, finally, my deepest thanks to my wife and my parents for their support and patience.

CONTENTS

PAGE

CHAPTER 4: Experiments, Results and Discussions - 2

CHAPTER 5: Experiments, Results and Discussions - 3

CHAPTER 6: Knowledge-based Adaptive Control For Laser Manufacturing System 134

CHAPTER 7: Spark Cone Image Evaluation Shell 174

LIST OF FIGURES

LIST OF PLATES

LIST OF TABLES

PAGE

CHAPTER 1

INTRODUCTION

1-1 Introduction

CO_2 laser cutting delivers a high processing speed, narrow kerf width, small heat affected zone (HAZ) on the cutting edges, capability of processing traditionally difficult materials, and comparatively low operating costs. It has been developed into an exceptionally effective and powerful materials processing method that is used extensively by industry world-wide [1][2]. World wide investment into laser related processes enjoys continuous growth [3][4].

The effectiveness of laser cutting processes depends on the control of laser characteristics such as: power mode (i.e. pulsed or CW), power density, transverse laser mode, and operating polarisation; set-up of operating system such as: beam delivery optics, nozzle type, assist gas type and pressure, beam focusing, operating distance, and beam feed rate; and characteristics of target material such as: thermal conductivity, thermal diffusivity, melting temperature, boiling temperature, latent heat of melting and vaporisation, plasma formation, heat of chemical reaction with reactive gas O_2, and various viscosities. So many parameters influence the performance of the laser cutting process that inevitably it is highly non-linear and very difficult to analyse. In order to establish an appropriate cutting model, to facilitate process control, numerous investigations into the beam / workpiece interaction process have been conducted. D. Schuocker [5][6], M. Vicanek et al [7], and M. J. Tasi et al [8] have developed a model based on the nearly period striation patterns that are found on the kerf side walls. Their laser cutting model is based on the stability analysis of the melt flow over the transient cut surface. Through the investigation of the dynamic behaviour of this thin film flow, they characterised the thickness of this thin layer and the frequency range for a stable cutting process. The model predicts the necessary feed rate required for the laser cutting process. K. A. Bunting et al [9] used a cylindrical source model to investigate the relationship between the incident power density, the nozzle head and the resulting cutting speed. Bunting established a relationship between the incident power density per unit thickness and the cut speed in terms of the thermal properties of the material. P.G. Klemens [10] proposed a semi-quantitative model to predict the processes. G. Chryssolouris et al [11] and W. M. Steen [12] further simplified the analysis and proposed a simple cutting model to predict the process. Theoretical analysis of laser-material interactions are widely discussed in many books and papers in order to understand and establish models for laser cutting processes, Carslaw et al[13], Bass[14], Ready[15], Bertolotti[16], Duley et al[17], Cohen[18], Duley et al[19].

Experimental investigations provide an alternative approach in understanding laser cutting phenomena and a method with which to establish relationships between the operating parameters and the cut quality. R. Fabbro et al [20], T. T. Saito et al [21] analysed the beam absorption in laser processing of materials. R. Jeanloz et al [22] investigated the temperature distribution in laser heated materials. H.Y. Zheng et al [23] studied the relationship between the kerf and the laser cut quality. Extensive studies into the relationship between operating parameters and cutting quality have been undertaken by many researchers, Nielsen[24], Alwan[25], Hussain[26]. Different techniques utilising experimental results were adapted for laser cutting process control by Zheng et al[23], Nagarajan et al[27], Tivin et al[28], Sellathamby et al[29].

Due to the great difficulty in analysing the complex laser cutting phenomena and the non-linear laser cutting process - a different approach is thus needed.

As mentioned above, the phenomena in laser material processing have been widely studied, the results are scattered in the literature and more or less incomplete. Formula and data discovered by one researcher quite often may not be correct or useful to another. Also, results may deviate from each other significantly when different systems with different set-ups are used. An algorithm that is system independent and set-up unrelated is therefore required.

The recent and rapid development in artificial intelligence and expert systems along with well established control techniques provide a satisfactory solution for this requirement. A hierarchically structured control system that integrates a knowledge-based expert system, adaptive process control and pattern recognition techniques has been developed for a Ferranti MFKP 1.2kW CO_2 laser manufacturing system to assist and control the cutting process.

Laser cutting process knowledge, for different materials, is organised and implemented with a rule-based system. An adaptive control algorithm based on on-line recursive parameter estimation and real-time control synthesis was adopted for the highly non-linear cutting process control. Laser beam feedrate was chosen as the system control input. Irradiance emitted from the cut front was sampled and fed back to this adaptive controller and used as the input to the recursive parameter estimator for system identification. A compensation signal is then evaluated, based on the identified system dynamics, through the synthesised controller and is output to the control actuator for system regulation. A pattern recognition technique that utilises cross correlation with a synthetic discriminant function (SDF) filter was adopted and applied to the cut quality control. Images of the exit spark cone that occurred during the cutting process were grabbed, edge enhanced and cross-correlated with ideal reference images encoded in the SDF filter. Digital techniques based on these pattern recognition algorithms were developed to simulate the performance of the proposed real-time optical implementation. The windows environment was utilised for the graphical user interface. The rapid developments and vast research in the personal computer (PC) industry provides both reliable performance and competitive cost. The PC-based environment was thus chosen for building the control environment for this CO_2 laser cutting manufacturing system.

In chapter 2, fundamental CO_2 laser theories are reviewed and the characteristics of the practical laser manufacturing system are discussed. Theoretical analysis of the laser-material interaction are then discussed and reviewed. Basic laser cutting models are analysed and a reference model that will be used for the adaptive controller is established. Experiments that investigate the relationships between the process operating parameters, such as feedrate, gas pressure, focal height offset distance, and the cut quality are described and discussed in chapter 3. Analysis of the relationships between the characteristics of the kerf surface striation patterns and the operation parameters are presented in chapter 4. Investigations of the spark cone images with respect to cut process quality are discussed in chapter 5. Finally, the whole control system development is described in both chapter 6 and chapter 7. The knowledge-based expert shell and adaptive controller is first described in chapter 6. The spark cone image evaluation system is described in chapter 7. Chapter 8 concludes with a discussion and suggestions for future research.

1-2 References:

[1] 1991 World review and forecast of laser markets, by David Kales, Laser Focus World, Jan. 1991

[2] Review and forecast of laser markets:1992, by David Kales, Laser Focus World, Jan. 1992

[3] EUREKA and BRITE/EURAM LASER OBJECTS, Laser Focus World European Report, Nov. 1992

[4] British technologists focus on industrial lasers, by Bridget Marx, Laser Focus World European Report, Nov. 1992

[5] Reactive gas assisted laser cutting - physical mechanism and technical limitations, by Dieter Schuocker, Industrial Applications of Laser Technology, Apr. 1983

[6] Dynamic Phenomena in Laser Cutting and Cut Quality, by Dieter Schuocker, Appl. Phys. B 40, 1986

[7] Hydrodynamical instability of melt flow in laser cutting, by M.Vicanek, G. Simon, H. M. Urbassek, and I. Decker, J. Phys. D: appl. Phys. 20 1987

[8] Linear stability analysis of molten flow in laser cutting, by Ming-Jye Tsai and Cheng-I Weng, J. Phys. D: Appl. Phys. 26, 1993

[9] Toward a General Theory of Cutting: A Relationship Between the Incident Power Density and the Cut Speed, by K. A. Bunting and G. Cornfield, Transaction of the ASME, Feb. 1975

[10] Heat balance and flow conditions for electron beam and laser welding, by P.G. Klemens, Journal of Applied Physics, Vol. 47, No5, May 1976

[11] Gas jet effect on laser cutting, by G. Chryssolouris and W. C. Choi, SPIE Vol. 1042 CO_2 Lasers and Applications, 1989

[12] Laser Material Processing, by W. M Steen, Springer - Verlag, 1991

[13] Conduction of Heat in Solids, by H. S. Carslaw and J. G. Jaeger, Oxford at the Clarendon Press, 1959

[14] Laser-Materials Processing, by M. Bass, 1983, Oxford

[15] Industrial Applications of Lasers, by J. F. Ready, 1978, New York London Academic Press

[16] Physical Processes in Laser-Materials Interactions, by M. Bertolotti, Plenum Press

[17] Coupling Coefficient for CW CO_2 laser Radiation on Stainless Steel, by W. W. Duley, D. J. Semple, J. P. Morency, and M. Gravel, Optics and Laser Technology, Dec. 1979

[18] Material Processing, by M. I. Cohen, Laser Handbook Vol 2, F4, Edited by F.T. Arecchi and E.O. Schulz-Dubois, North-Halland Publishing Company, 1972

[19] Interaction of CO_2 Laser Radiation with Solids. I. Drilling of Thin Metallic Sheets, by J. N. Gonsalves and W.W. Duley, Canadian Journal of Physics. Vol. 49, 1971

[20] Absorption measurements in continuous high-power CO_2 laser processing of materials, by R. Fabbro, D. Bermejo, J. M. Orza, L. Sabatier, L. Leprince and V. Granier, SPIE Vol. 1276, CO_2 Lasers and Applications II, 1990

[21] Calorimeter to measure the 10.6-μm absorption of metal mirrors, by T.T. Saito, A. B. Callender and L. B. Simmons, Applied Optics Vol. 14(30, Mar. 1975

[22] Measurement of the temperature distribution in CW-laser heated materials, by R. Jeanloz and D. L. Heinz, 1986, Proc. of ICALEO'85, IFS Publications Ltd.

[23] Kerf scanning system for laser cutting quality control, by H. Y. Zheng, D. Brookfield and W. M. Steen, Lasers in Engineering, Vol. 1, 1991

[24] Laser cutting with high pressure cutting gases and mixed cutting gases, by S. E. Nielsen, PhD thesis, Technical University of Denmark, 1985

[25] Surface temperature transients in laser machining of metals, by Adil Abbas Alwan, PhD thesis 1989-A, University of Glasgow

[26] A generalised approach for the prediction of laser cutting parameters, by M. A. Hussain, PhD thesis 1989-H, University of Glasgow

[27] Control of the welding process using infrared sensors, by S. Nagarajan, P. Banerjee, W. H. Chen and B. A. Chin, IEEE Transactions on Robotics and Automation, Vol. 8, No. 1, Feb. 1992

[28] Infrared imaging enhances manufacturing operations, by P. Tivin and T. C. Venable, Laser Focus World, Dec. 1992

[29] Performance characteristics of a high power CO_2 laser with computer vision mode and the power control, by C. V. Sellathamby, H. J. J. Seguin and S. K. Nikumb, Applied Optics, Vol. 29, No. 30, Oct. 1990

CHAPTER 2

Laser Processing Theory

Nomenclature

$a(\omega)$ = Atomic polarizability
A = Einstein 'A' coefficient (sec^{-1})
c = Speed of light
C = Thermal conductivity
D_T = Total dissipation (photons / cm^3 sec)
e = Electron charge
E = Energy (J)
E_{ext} = External electric field on electron
E_{int} = Internal electric field on electron
E_{loc} = Local electric field on electron
F = Coupling efficient
H = Heat flux
IP = Input power (Watt / cm^3)
k = Extinction coefficient
k'_{51} = Transfer rate between level 5 & level 1 (sec^{-1})
k'_{15} = Transfer rate between level 1 & level 5 (sec^{-1})
K = Thermal diffusivity
K_{sp} = A = Spontaneous emission rate (sec^{-1})
K_{132} = Transfer rate between level 1 and level 32 (sec^{-1})
K_{2131}= Transfer rate between level 21 and level 31 (sec^{-1})
K_{2231}= Transfer rate between level 22 and level 31 (sec^{-1})
K_{320} = Transfer rate between level 32 and level 0 (sec^{-1})
m = Mass of electron
n = Complex refractive index
n_x = Molecular population (molecules / cm^3)
N = Number of dipole per unit volume
p = Dipole moment of electron
P = Polarisation
r = Displacement of an electron in an electric field
R = Reflectivity
t_0 = Thermal time constant
t_{sp} = Radiative lifetime (sec)

$v(x,t)$ = Temperature distribution
w_0 = Beam radius in front of focusing lens (mm)
w_k = Focused beam radius (mm)
α = Rate of direct excitation of CO_2 (sec^{-1})
ε_0 = Initial phase
η = Rate of direct de-excitation of CO_2 (sec^{-1})
λ = Wavelength of laser beam
ρ = Specific density
Γ = Damping coefficient of electron
ω = Angular frequency of laser beam (rad / sec)

<u>Subscripts</u>:

conduction = Refers to conduction heat
convection = Refers to convection heat
CO_2 = Carbon Dioxide
e = Electron energy
latent = Refers to latent heat
loss = Refers to energy loss
L = Refers to laser energy
R = Refers to chemical reaction energy
00^01 = Vibrational mode
0,1,2,3,4,5,21,22,31,32 = Refers to energy levels

2-1 Introduction

Since the first observation of the continuous wave (CW) laser action at approximately 10 μm was reported in 1964 by Patel et al [1], the Carbon Dioxide Laser (CO_2 laser) has been intensively investigated and developed, it is now one of the most powerful and efficient laser sources available.

Ranging from milliwatts to multi-kilo watts in CW operation, or to multi-kilo hertz pulse repetition frequencies (PRF) in pulse-mode processing and up to 30% efficiency [2], the CO_2 laser has been widely adopted for various applications which include:

. medical operation: eye and tissue surgery
. materials processing: welding, cutting, and surface engineering
. nuclear research: laser fusion
. military equipment: laser beam weapon

The feasibility and success of these applications relies on the physics of the interaction between the laser and the workpiece. The quality of material processing is determined by how effectively the laser energy is coupled into the processed materials. This laser-material interaction is a function of
(1) laser characteristics: mode, PRF or CW, irradiance (Watt/cm^2), polarisation, beam diameter, pointing stability;
(2) material specifications: reflectivity, absorption, emissivity, thermal conductivity, diffusivity, melting temperature, vaporisation temperature, latent heat of melting, latent heat of vaporisation, specific heat, density;

(3) process factors: laser feedrate, ambient gas - type & pressure, focusing height.

(4) beam delivery system: mirrors, polarizer, focusing lens.

This chapter examines basic laser theory in order to understand the characteristics of the laser. This is followed by analysis of the laser-material interaction and a laser cutting model is established as a reference model for the adaptive control system. Finally, the relationships between the system parameters and cutting quality are discussed.

2-2 Laser Fundamentals

2-2.1 CO_2 Laser Operating Principle

The CO_2 laser is a molecular laser, the energy levels relevant to laser action are those that describe the internuclear vibrations of the molecule. The internuclear vibrations of the molecule are the relative motions of the constituent atoms. The CO_2 molecule executes three basic internal vibrations, the so-called normal modes of vibration. As described in figure 2-2.1.

(i) unexcited molecule: the molecules are at rest.

(ii) symmetric stretch mode: the atoms vibrate along the internuclear axis in a symmetric manner.

(iii) bending mode: the atoms vibrate symmetrically along an axis perpendicular to the internuclear axis which includes two degenerate vibration modes with equal frequency.

(iv) asymmetric stretching mode: the atoms vibrate asymmetrically along the internuclear axis.

These four vibrational energy groupings include all the significantly populated energy levels. The energy groupings are shown in figure 2-2.2. Internal relaxation rates within these groups are considered to be infinitely fast when compared with the rate of energy transfer between groups. In reality the internal relaxation rates are at least an order of magnitude greater than the rates between groups. [3]

The CO_2 laser operates as a 4-level system. The basic operating principles contain three stages which are described respectively as follow, refer to figure 2-2.2:

1. **Population inversion:** the population inversion between the upper laser level and the lower laser level of the CO_2 molecules result from the combination of the following effects:

(1)Direct excitation: the CO_2 molecules are excited by direct electron impact and are pumped from the ground state to the upper laser level ((00^01) level) which contains a single energy quantum of asymmetric stretching mode vibration. The rate of kinetic energy transfer α is given by

$$\alpha = \frac{F_{CO_2} * IP}{E_{00^01} * n_0} (\text{sec}^{-1}) \qquad \textbf{(2-2.1)}$$

(2)Direct de-excitation: The reverse process of the above takes place when molecules loose energy to the electrons and the electrons gain an equal amount of kinetic energy. The rate of de-excitation η is calculated from α by the relationship.

$$\eta = \alpha \exp(\frac{E_{00^01}}{Ee})(\text{sec}^{-1}) \qquad (2\text{-}2.2)$$

(3)Resonant energy transfer: Resonant energy transfer between the CO_2 (00^01) and N_2 (v=1) energy levels proceeds via excited molecules colliding with ground state molecules. A large part of the excitation of the upper laser level takes place via collisions between excited N_2 molecules and ground state CO_2 molecules. The generally accepted value for this rate of energy transfer k'_{51} and k'_{15}, refer to figure 2-2.2, is 1.9×10^4 sec^{-1} torr^{-1} at 300k, hence,

$k'_{51} = 19000\ P_{CO_2}\ (\text{sec}^{-1})$

$k'_{15} = 19000\ P_{N_2}\ (\text{sec}^{-1})$

(4)Radiative relaxation: i.e., the spontaneous radiative decay.

The Einstein 'A' coefficient for the CO_2 laser is:

$$A = \frac{1}{t_{sp}} = 0.213(\text{sec}^{-1}) \qquad (2\text{-}2.3)$$

This is not considered to be a major relaxation process in the CO_2 laser.

2. **Stimulated emission**: To date there are nearly 200 CO_2 laser oscillations resulting from vibration rotation transitions among a number of low-lying ($Ev < 1eV$) vibration levels in the ground electronic 1Σ state of the CO_2 molecule. These oscillations cover the spectral range from 9 to 18 µm. Among them, two of the strongest groups arise from the

(i) 00^01 -> 10^00 band: with band edge at 10.4 µm
(ii) 00^01 -> 02^00 band: with band edge at 9.4 µm

Figure 2-2.3 details the laser transition diagram for the above two bands. Considering a laser oscillator with two plane mirrors, one placed at either end of an active medium, with one mirror partially transmitting, laser action will normally be initiated by spontaneous emission that happens to produce radiation whose direction is normal to the end mirrors and falls within the resonant modes of the cavity. By assuming constant photon flux throughout the cavity length and basing the calculation of stimulated emission on an average unit volume, Moore[4] developed a mathematical model to describe the stimulated emission. A radically improved model was developed by Chatwin[3] which considers the transient development of waves propagating within the volume and takes account of intensity gradients when calculating the stimulated emission. A set of rate equations were obtained as follows:

$$dn_1 = \alpha n_0 - \eta n_1 + K_{51} n_5 - K_{15} n_1 - K_{sp} n_1 - K_{132} \left\{ n_1 - \frac{n_1}{n_{32}} e^{n_{31}} \right\} - D_T \quad (2\text{-}2.4)$$

$$\frac{dn_2}{dt} = K_{sp}n_1 + D_T - K_{2131}\left\{n_{21} - \frac{n_{21}}{n_{31}}e^{n_{31}}\right\} - K_{2231}\left\{n_{22} - \frac{n_{22}}{n_{31}}e^{n_{31}}\right\} \quad (2\text{-}2.5)$$

$$\begin{aligned}\frac{dn_3}{dt} &= 2K_{2131}\left\{n_{21} - \frac{n_{21}}{n_{31}}en_{31}\right\} + K_{2231}\left\{n_{22} - \frac{n_{22}}{n_{31}}e^{n_{31}}\right\} \\ &+K_{132}\left\{n_1 - \frac{n_1}{n_{32}}e^{n_{32}}\right\} - K_{320}\left\{n_{32} - \frac{n_{32}}{n_0}e^{n_0}\right\}\end{aligned} \quad (2\text{-}2.6)$$

$$\frac{dn_5}{dt} = \gamma n_4 - \beta n_5 - K_{51}n_5 + K_{15}n_1 \quad (2\text{-}2.7)$$

3. **Recovery**: the molecules in the low levels return to the ground state by fast radiationless decay.

N_2 and He are usually mixed with CO_2 as the working gas in the laser system in order to raise the laser efficiency. The N_2 molecules excited by the electron impact are pumped up to the (v=1) state. These excited N_2 molecules then collide with the ground state CO_2 molecules and transfer their excitation energy to the CO_2 molecules, which excites them to the (00^01) state. This energy transformation contributes greatly to the population inversion. The He molecules increase the speed at which CO_2 molecules return to their ground state. This process decreases the number of CO_2 molecules retained in the lower level and therefore enhances the population inversion.

2-2.2 Ferranti MFKP CO_2 Laser Manufacturing System Characteristics

The Ferranti MFKP CO_2 Laser manufacturing system includes:

1. Ferranti MFKP CO_2 laser head
2. Pulser unit - power supply
3. Heidenhain TNC 155AR NC controller
4. X-Y working table
5. Auxiliary subsystems:
   (1) water cooling system
   (2) gas control system
   (3) air circulation system
   (4) beam delivery system

A schematic is given in figure 2-2.4.

The Ferranti MFKP CO_2 laser is a slow axial flow type system (with a periodic gas purging function). The characteristics of this system are summarized as follows:

1. **power range**: two ranges - high/1200W, low/500W

2. **operating mode**: (1) continuous wave (CW)
   (2) pulse mode:
      (i) pulse length: 0.0001 ~ 9.9 sec
      (ii) pulse separation: 0.0001 ~ 9.9 sec

3. **laser mode:** A laser cavity is an optical oscillator. When it is oscillating, there will be standing electromagnetic waves set up within the cavity which are defined by the cavity geometry in three dimensions; hence, longitudinal and transverse modes characterise the laser output. The classification of these Transverse Electromagnetic Mode patterns (TEMplq) is :

p = Number of radial zero fields

l = Number of angular zero fields

q = Number of longitudinal zero fields

Figure 2-2.5 illustrates some of the mode patterns.

Most of the slow flow (SF) lasers, such as the Ferranti MFKP laser, operate with a nearly perfect TEM_{00} or TEM_{01}*. The Ferranti MFKP is designed to be operated in the TEM_{00}. This was verified by the beam burn patterns produced in a perspex target. The intensity distribution of this fundamental mode (TEM_{00}) is shown in figure 2-2.6.

4. **beam radius**: [see figure 2-2.7]

The distance between the output collimating mirror and the final beam delivery mirror is about 1 m. From this, it is estimated that the beam radius in front of focusing lens is about 6mm. This estimation was confirmed by the burn pattern generated in a perspex target under the nozzle without the focusing lens.

5. **spot size**: Laser beam exiting the output window is a TEM_{00} (gaussian) mode beam which has been described above. ω is defined as the radial coordinate at which the intensity has fallen to $1/e^2$ times its maximum value.

Fourier Transform Method:

When a TEM wave passes through a lens, the image formed at its focal plane is the Fourier Transform of the input wave function. By using this approach, the focused spot size of a gaussian beam can be evaluated:

The definition of a Fourier Transform is:

$$F(k)=\int_{-\infty}^{+\infty} f(x)\exp(-ikx)dx \tag{2-2.8}$$

for a gaussian distribution function:

$$f(x) = C\exp(-ax^2) \tag{2-2.9}$$

where we define the radius of the beam R as the point where the intensity has fallen to $1/e^2$ of it maximum value. In this case $R = (a)^{-1/2}$.
Taking the Fourier Transform of this gaussian function

$$F(k) = \int_{-\infty}^{+\infty} C\exp(-ax^2)\exp(-ikx)dx$$

$$= \frac{C}{(a)^{1/2}}\exp(-k^2/4a)\int_{-\infty}^{+\infty} \exp(-\beta^2)\, d\beta \tag{2-2.10}$$

where: $\int_{-\infty}^{+\infty} \exp(-\beta^2)d\beta = (\pi)^{1/2}$

therefore :

$$F(k) = C(\pi)^{1/2} / (a)^{1/2} \exp(-k^2/4a) \tag{2-2.11}$$

Figure 2-2.8 illustrates the result.

Defining w_0 as the radius of the beam in front of the focusing lens at which the intensity has fallen to $1/e^2$ of its maximum value

$$w_0 = \frac{1}{e} C = (a)^{-1/2}$$

again w_k the radius of the beam after the focusing lens

$$w_k = \frac{1}{e} (C(\pi)^{1/2} / (a)^{1/2})$$

therefore:

$$w_k = 2(a)^{1/2} = 2/w_0 \tag{2-2.12}$$

e.g. the incoming beam radius of this Ferranti CO_2 laser is approximately 6mm, therefore we can calculate the spot size from the above formula

$$w_k = 2/w_0 = 2/6 \cong 0.3\text{mm}$$

6. **circular polarized output**: by constructing a circular polarizer right after the output window, the two-state randomly linear polarized beam is transferred into a circular polarized beam. This circular polarized beam is favoured for general laser processing of materials as the cut quality remains the same no matter what the direction of the cut.

7. **remote control**: the pulser unit has a built-in interface circuit which enables the laser system to be adjusted remotely through an RS-232 serial interface or parallel interface. That is, the pulsing condition can be controlled through an external controller, like a PC, as is the case for this particular CO_2 laser manufacturing system. Figure 2-2.9 gives a schematic of this particular arrangement.

The original idea of this remote control system is good for batch processing where each batch of components requires different process parameter settings. Because of the built-in shutter interlock, the time needed to change the pulse parameters is quite long, about 200ms. On-line real-time control of the pulsing condition is thus difficult. As most laser processing benefits from operating the laser at a high PRF, real time control is difficult. Due to the limitation on control of the P.R.F., the scan speed of laser beam (feedrate) is , therefore, the major control parameter.

2-3 Laser - Material Interaction

When laser radiation falls onto a target surface during laser processing, part of it is absorbed and part is reflected. The energy that is absorbed begins to heat the surface. Due to different power density, pulse duration, and different material characteristics ,which have been described above, different physical processes will dominate the laser-material interaction. When the power density is low, laser energy is absorbed within the "skin depth", and is transmitted to the main body of the target by thermal conduction. As the power density becomes higher, the surface material quickly rises to its melting temperature; the melting process then dominates the interaction. Melting without vaporization of the target is of particular interest for welding applications. For different materials which have different "thermal diffusivity", there is only a narrow range of laser irradiance, and pulse duration, suitable for each material for welding applications.

As the power density gets higher, the surface temperature of the material reaches its boiling temperature, and part of the material starts to vaporize. When the laser power density becomes even higher, a small amount of target material is vaporized and is heated to a high temperature. It thus becomes slightly thermally ionized and produces an opaque high-temperature plasma plume. During the gas assisted laser cutting process, this plasma plume is blown away as soon as it is generated, therefore, the laser energy can be coupled into the workpiece surface and conducted down to the material main body. The difference between temperatures in the centre part of the interaction zone generates a transverse pressure gradient which exerts a downward pressure on the melted material in the interaction zone and ejects the liquid out from the interaction zone. The transverse pressure gradient causes the liquid to flow in an outward direction. As the amount of energy absorbed increases, a laser supported absorption (LSA) wave occurs and propagates back towards the laser, which effectively cuts off the laser light from the surface. Some experiments have been carried out to demonstrate this effect by Schriempf et al [5].

At very high power density, the physical process is dominated by inverse Bremsstrahlung. In this process, a photon of the laser light is absorbed by a free electron in the plasma. The electron is raised to a higher-lying energy state in the continuum of states available to it. At the same time, an ion recoils in order to take up the residual momentum. At still higher power levels, collective plasma effects become important. In these effects, light is absorbed by interaction with a number of plasma particles collectively, instead of by a single electron. This leads to generation of ion waves in the plasma, collective oscillations of charged particles in the plasma, or other electromagnetic modes (i.e., reradiation of light at frequencies different from the incident laser frequency). These collective plasma effects are of particular interest to the development of laser-assisted thermo-nuclear fusion.

These physical phenomena are schematically summarized in figure 2-3.1(a), figure 2-3.1(b) and the approximate power ranges of laser power density at which different processes dominate are listed in Table 2-3.1.

The maximum output power of this Ferranti MFKP CO_2 is 1200 watts. Therefore the focused power density is approximately 10^6 (watt/cm^2). The dominant phenomenon is thus melting. In the gas assisted cutting process, the tiny portion of the "skin depth" on the surface rapidly rises to the boiling point and forms a plasma layer. Due to the strong gas jet effect, only a very thin plasma layer exists. This thin plasma layer absorbs the laser energy and re-radiates it into the metal workpiece causing it to melt.

In a laser cutting process, the energy absorbed by the material will cause changes of the phase of the material. And, this phase transition also influences the amount of energy the material absorbs. Some people describe this kind of phenomenon as a cyclic effect [6]. Gas is commonly used for cutting processes, especially when cutting thick materials, hence, forced convection will occur. Also oxidization and burning occurs when a reactive gas, like oxygen, is utilized, for example, the cutting process of mild steel. The parameters, such as feedrate (scan_rate) of laser beam, spot size / focusing position, power intensity, will influence the amount of energy absorbed by the material and will thus affect the cut quality.

The physical phenomena that control the laser cutting process are highly non-linear and not directly amenable to analytical techniques. It is difficult to develop a model which is able to incorporate all the above effects.
Starting from energy absorption, and the laser / material coupling effect and temperature distribution, a simplified but adequate model is thereby established in order to develop rules to control the laser parameters for cutting materials with a different specification.

2-3.1 Absorption

Laser energy absorption of material, is not only dependent upon specific characteristics of a certain material, but is also a function of incident power intensity, induced surface temperature and surface roughness.

From the classical viewpoint, the process of optical absorption can be described as an electro-magnetic field, which causes the electrons, within the material, to be moved in the presence of damping or frictional forces.

For metals, the conduction band electrons interact with the optical electric field, the resulting free electron motion is damped by collisions with the vibrating lattice and so some of the light energy is transferred to the lattice. It is in this manner that the material is heated.

H.A. Lorentz [7] and P.K.L. Drude [8] both treat the solid which interacts with the light as a set of harmonic oscillators under the action of an external, periodically changing force field. The description of absorption in a dielectric material is due to the Lorentz-model, and in metal it is described by the Drude-model.

The Lorentz - model:

Consider a bound electron in a solid irradiated by a laser beam of angular frequency $\omega = 2\pi c/\lambda$. The position r of an electron of mass m (neglect the finite mass the nuclei) due to the electrical field is described by:

$$mr + m\Gamma r + m\omega_0 2r = -eE_{loc} \qquad (2\text{-}3.1)$$

where:

$m\Gamma r$: the viscous damping force

$m\omega_0 2r$: the Hooke's law restoring force

E_{loc}: the local electrical field on the electron

one possible solution to (2-3.1) is:

$$r = -(e/m) / [(\omega_0^2 + \omega 2) -i\Gamma\omega] E_{loc} \tag{2-3.2}$$

The dipole moment induced by the motion of an electron is:

$$p = -re / (4\pi\varepsilon_0)^{1/2} \tag{2-3.3}$$

For a small excursion r, p is a linear function of the field, i.e.

$$p = aE_{loc} (4\pi\varepsilon_0)^{1/2} \tag{2-3.4}$$

by (2-3.2), (2-3.3) and (2-3.4) we can define the atomic polarizability

$$a(\omega) = (e^2/4\pi\varepsilon_0.m) / [(\omega_0^2 + \omega^2) -i\Gamma\omega] \tag{2-3.5}$$

This is the microscopic polarizability pertinent to the local electrical field. As for the macroscopic polarization, we can define it as:

$$P = Na\varepsilon_0 <E_{loc}> = \varepsilon_0\varepsilon_0 E_{int} \tag{2-3.6}$$

for a free electron metal, $<E_{loc}> = E_{int}$. The external field E_{ext} is a superposition of the macroscopic field E_{int} plus the induced macroscopic polarization, i.e.

$$E_{ext} = E_{int} + 4\pi P/\varepsilon_0 = E_{int} (1 + 4\pi Na) = \varepsilon E_{int} \tag{2-3.7}$$

This yields the result of ε, the complex dielectric constant as:

$$\varepsilon = 1 + (Ne^2/m\varepsilon_0)/[\,(\omega_0^2 + \omega^2) - i\Gamma\omega] = \varepsilon_1 + i\varepsilon_2 \qquad (2\text{-}3.8)$$

From (2-3.8), the real and imaginary parts of the dielectric constant are:

$$\varepsilon_1 = n^2 - k^2 = 1 + (Ne^2/m\varepsilon_0)\,.\,[(\omega_0^2 + \omega^2)/(\omega_0^2 + \omega^2)^2 + \Gamma^2\omega^2] \qquad (2\text{-}3.9)$$

$$\varepsilon_2 = 2nk = (Ne^2/m\varepsilon_0)\,.\,[\Gamma\omega/\,(\omega_0^2 + \omega^2)^2 + \Gamma^2\omega^2] \qquad (2\text{-}3.10)$$

From (2-3.9), (2-3.10):

$$n^2 = \frac{1}{2}\,[\,(\varepsilon_1^2 + \varepsilon_2^2)^{1/2} + \varepsilon_1] \qquad (2\text{-}3.11)$$

$$k^2 = \frac{1}{2}\,[\,(\varepsilon_1^2 + \varepsilon_2^2)^{1/2} - \varepsilon_2] \qquad (2\text{-}3.12)$$

The Drude - model:

In metals, the optical properties are dominated by free electrons. Therefore, the restoring force term can be set to zero. The real and imaginary dielectric constants become:

$$\varepsilon_1 = n^2 - k^2 = 1 - (Ne^2/m\varepsilon_0)\,.\,[1\,/\,(\omega^2 + \Gamma^2)] \qquad (2\text{-}3.13)$$

$$\varepsilon_2 = 2nk = (Ne^2/m\varepsilon_0)\,.\,[\Gamma\omega\,/\,(\omega^4 + \Gamma^2\omega^2)] \qquad (2\text{-}3.14)$$

2-3.1.1 Surface Temperature

The reflectivity R and the absorption coefficient α are related to n and k of (2-3.11) and (2-3.12) by (Fresnel expression):

$$R = [(n-1)^2 + k^2] / [(n+1)^2 + k^2] \qquad (2\text{-}3.15)$$

$$\alpha = 2\omega k / C = 4\pi k/\lambda \qquad (2\text{-}3.16)$$

The definition of the dc conductivity of a metal is:

$$\sigma = Ne^2 / m\Gamma \qquad (2\text{-}3.17)$$

By using (2-3.17), (2-3.13), (2-3.14) and assuming $\omega/\Gamma << 1$ (for light frequency small compared to the electron - lattice collision frequency Γ), gives:

$$\varepsilon_1 \cong 1 - \sigma_0 / \varepsilon_0\Gamma \qquad (2\text{-}3.18)$$

$$\varepsilon_2 \cong \sigma_0 / \varepsilon_0\omega \qquad (2\text{-}3.19)$$

By using (2-3.18), (2-3.19), (2-3.11), (2-3.12), (2-3.15) and (2-3.16) the reflectivity R is:

$$R = 1 - 2\,(2\varepsilon_0\omega/\sigma)^{1/2} \qquad (2\text{-}3.20)$$

This is also known as the Hagen - Rubens formula [9]. This formula allows the evaluation of the IR reflectivity of a metal from its dc conductivity. The conductivity σ decreases with increasing temperature, and R decreases with increasing temperature.

Figure 2-3.2 describes the effect.

Therefore, more incident power will be absorbed when the surface temperature is raised.

2-3.2: Surface Temperature Distribution .. Beam Location - Cut Front

See figure 2-3.2, due to the high reflectivity of metal, only a very thin layer will be heated during the irradiation. Therefore, the one-dimensional model can be used to analyze the temperature distribution on the metal surface giving some estimate of the relationship between the cut front and focused spot position.

By adopting Fourier heat transfer theory, for constant heat flux H, the temperature distribution is: [10]

$$v(x,t) = \frac{2H}{C}(Kt)^{1/2}\mathrm{ierfc}[x/2(Kt)^{1/2}] \qquad (2\text{-}3.21)$$

the temperature on the surface is given by:

$$v(0,t) = \frac{2H}{C}(Kt/\pi)^{1/2} \qquad (2\text{-}3.22)$$

consider the beam to have a gaussian distribution $H = H_0 \exp(-nr^2)$, by Rykalin [11]:

$$v(r,z,t) = 2P/[\rho C(4\pi K)^{1/2}]\int_0^t (1/[(t_0+t)\sqrt{t}]\exp[-(z^2/4Kt)-(r^2/4k(t_0+t)]dt$$

$$(2\text{-}3.23)$$

where:

$t_0 = 1/4Kn$

$P = H_0\pi a^2$

The temperature distribution on the surface at $r = 0$, $z = 0$ is:

$$v(0,0,t) = P/[\pi\rho C(4\pi Kt_0)^{1/2}]\arctan(t/t_0)^{1/2} \qquad (2\text{-}3.24)$$

now consider a non-constant heat flux that changes with respect to time according to a time function f(t). By Duhamel's theory [10]:

$$v(x,t) = \int_o^t f(\tau)\partial/\partial t[F(x,t-\tau)d\tau \qquad (2\text{-}3.25)$$

where F(x,t) is the solution to the problem with constant heat flux, this yields:

$$v(x,t) = (K^{1/2}/K\pi^{1/2}) \int_{0}^{t} (1/\tau^{1/2})f(t-\tau)\exp(-\lambda^2/4KI)d\tau \qquad (2\text{-}3.26)$$

The gaussian beam ($I = I_0 \exp(-2r^2/a^2)$) scans at speed V (where we can calculate $T = \frac{d}{V}$, d=spot diameter). This maybe simulated as a constant heat flux which changes as a gaussian function with time. Therefore:

$$f(t) = H_0 \exp[-(t-1/2T)^2/2\sigma^2] \quad \text{where } -\infty < t < +\infty \qquad (2\text{-}3.27)$$

but choosing $\sigma = (1/2\ T)/(2\pi)^{1/2}$, the area under the curve is $H_0(1/2\ T)$ then:

$$v(x,t) = (K^{1/2}/K\pi^{1/2}) \int_{0}^{t} (\tau^{1/2})H_0\exp[-(t-\tau-1/2\ T)^2/2\sigma^2]\ \exp[-x^2/4K\tau)d\tau$$

$$(2\text{-}3.28)$$

This was evaluated by Ruth[11] for any material. The result indicates that the gaussian has a shape factor k = 0.758. The result is shown in figure 2-3.3.

2-4 Non-Linearity in Laser Cutting

The cutting quality is controlled by the dynamic behaviour of the target material within the interaction region.

First of all, consider the energy flow condition within the interaction region. Energy supply, E_{supply}, comes from two sources. The energy absorbed from the impinging laser P_{AL}, and the energy generated from the chemical reaction between the reactive gas and the high-temperature target material P_R. The amount of energy absorbed from the impinging laser beam depends on the magnitude of the laser power P_L, the absorption coefficient α, and the interaction area s. That is:

$$P_{AL} = \alpha s P_L \qquad (2\text{-}4.1)$$

The laser power P_L depends on the condition of the optical resonator, the operating gas mixture, the gas temperature, and the gas discharge voltage. Owing to these factors the laser power will fluctuate with time t, $P_L = P_L(t)$. The absorption coefficient α depends on the surface roughness and the characteristics of the target material which is mainly a function of temperature T. Therefore $\alpha=\alpha(T, S_{roughness})$. As for the interaction area s, initially, it will be determined by the optical set-up of the particular laser system. As soon as cutting starts, the area of interaction will change as plasma is generated and the melted material is blown away. So the interaction area s=s(T). Thus, the absorbed laser energy is described by:

$$P_{AL} = \alpha s P_L = \alpha(T, S_{condition}) s(T) P_L(t) \qquad (2\text{-}4.2)$$

The energy generated from the chemical reaction between the reactive gas and the target material P_R depends on both the densities of the reactive gas ρ_{air} and the target material ρ_{metal}, the reaction temperature T, and the reaction area A. That is:

$$P_R = P_R(\rho_{air}, \rho_{metal}, T, A) \qquad (2\text{-}4.3)$$

The density of the reactive gas is related to the gas velocity v_{air} and gas temperature T. The density of the target material is also related to the temperature T. Again the interaction area is a function of temperature T. Therefore, the following relationship prevails:

$$P_R = P_R(\rho_{air}, \rho_{metal}, T, A) = P_R\,[\rho_{air}(v_{air}, T), \rho_{metal}(T), T, A(T)] \qquad (2\text{-}4.4)$$

Now consider the energy losses within the control volume E_{loss}. The energy losses are mainly due to four factors. Heating of the target material - conduction $H_{conduction}$; melting, vaporizing and plasma formation of the target material - latent heat H_{latent}; forced cooling - convection from the surface $H_{convection}$; and the heat loss during the removal process of melted material H_{bulk}. Heating of the material relies on the material's characteristics k, geometrical shape g, and the temperature of the material T. That is, $H_{conduction}=H_{conduction}(k, g, T)$. The latent heat of the material depends on its molecular characteristics. Convection loss relates to the temperature T, surface area a, gas flow condition v_{gas}. Hconvection=Hconvection(T, a, v_{gas}). Energy loss due to the loss of the high temperature material blown away by the gas jet is related to the gas velocity v_{gas}, viscosity between gas and target material η, temperature T. Therefore, $H_{bulk}=H_{bulk}(v_{gas}, \eta, T)$. Hence, the energy loss is described as follows:

$$E_{loss}=E_{loss}[H_{conduction}(k,g,T),\ H_{latent},\ H_{convection}(T,a,v_{gas}),$$
$$H_{bulk}(v_{gas},\eta,T)] \qquad (2\text{-}4.5)$$

The combined effect of the energy gain and energy loss will determine both the transient and steady state situation within the interaction region during a laser cutting process. From the above analysis, the effects of the energy input, like temperature change, affects the amount of energy gained by the control volume. It also affects the amount of energy loss from the control volume, which again affects the resulting temperature. This introduces non-linearity into the system analysis. Further more, the non-steady flow conditions affecting the removal of melted material adds an even greater non-linearity to the process.

Periodic patterns are found on the cutting edge. A model based on the dynamic stability of the molten layer will be described in chapter 5. Simplified models based on a linear system are discussed in the next section.

2-5 Laser Cutting Model

Simple Lumped Heat Model:

Steen[12] proposes that during a gas-assisted laser cutting process, once the penetration hole is made and the cut is started from the edge, then a sufficiently strong gas jet will blow the molten material out of the kerf and avoid the requirement to raise the temperature to the boiling point or above. Therefore, the process can be approximately modelled as in figure 2-5.1.

By assuming that all the energy enters the melt and is removed before significant conduction can occur. Considering the heat balance of figure 2-5.1. The simple lumped heat capacity equation is derived as follow:

$$[P/tV] = wr/h \{ Cp\, \Delta T + l_f + m'L_v \} \qquad (2\text{-}5.1)$$

figure 2-5.2 shows the relationship

Cylindrical Source Model:

By considering the cutting operation as a result of the melting and / or vaporization of the material by a cylindrical beam which transfers its energy to the material through a moving circular spot, Bunting[13] et al have developed a relationship between the power density incident on a material and the resulting cut speed in terms of the thermal properties of the material.

Refer to figure 2-5.3.

Starting from the temperature distribution equation given by Wells[14]

$$T(x,y) - T_0 = (q/2\pi hK)\ \exp(ux/2\alpha)[k_0 u(x^2+y^2)^{1/2}/2\alpha] \qquad (2\text{-}5.2)$$

Bunting derived the equation for the relationship as follows:

$$q'/h = [2k(Tmp - T_0)/R^2\ ][1/I(s)] \qquad (2\text{-}5.3)$$

where:

$$I(s) = \int_0^1 r'dr' \int_0^{2\&} [\exp(-sr'\cos\theta)]\ k_0 s(r'^2 - 2r'\sin\theta + 1)^{1/2}\ d\theta$$

$q' = k_1P$ where k_1 is the fraction of the incident energy transmitted to material

h = thickness

2-6 References

[1] Laser Action on Rotational Transmission of the Σu^+ - Σg^+ Vibrational Band of CO^2, by C. K. N. Patel, W. L. Faust, and R. A. McFarlane, Bull. Am. Phys. Soc., 9, 1964

[2] CO_2 lasers, by P.K. Cheo, LASERS Vol 3, Edited by A.K. Levine and A.J. DeMaria, Marcel Dekker, Inc., 1971

[3] Thermodynamics of Pulsed Carbon Dioxide Laser For Machining Metals, by C. R. Chatwin, PhD Thesis, 1979, Birmingham

[4] Vibrational Energy Transfer in CO_2 Lasers, by C. B. Moore, R. E. Wood, B. L. Hu, and J. T. Yardley, J. Chem. Phys., Vol. 46, No. 11, 1967

[5] Thermal Response of Materials to Pulsed Laser Radiation, by J. T. Schriempf, R. L. Stegman, and G. E. Nash, IEEE J. Quantum Electron. QE-9, 1973

[6] Reactive Gas Assisted Laser Cutting - Physical Mechanism And Technical Limitations, by D. Schuocker, Proc. SPIE, Vol. 398, 1983

[7] Lectures on Theoretical Physics Delivered at the University Leiden, Vol. 2, Thermodynamics, by H. A. Lorentz, 1927, London MacMillan

[8] The Theory of Optics, by P. K. L. Drude, 1902, Longmans, London

[9] The Theory of the Properties of Metals and Alloys, by N. F. Mott, and H. Jones, 1958, Dover

[10] Conduction of Heat In Solids, by H. S. Carslaw, and J. G. Jaeger, 1959, Oxford

[11] Material Processing, by M. I. Cohen, Laser Handbook Vol 2, F4, Edited by F.T. Arecchi and E.O. Schulz-Dubois, North-Holland Publishing Company, 1972

[12] Laser Material Processing, by W. M. Steen, 1991, Springer-Verlag

[13] Toward a General Theory of Cutting: A Relationship Between the Incident Power Density and the Cut Speed, by K. A. Bunting, and G. Cornfield, Transactions of the ASME, Feb., 1975

[14] Heat Flow in Welding, by A. A. Wells, Welding J., Vol. 31, 1952

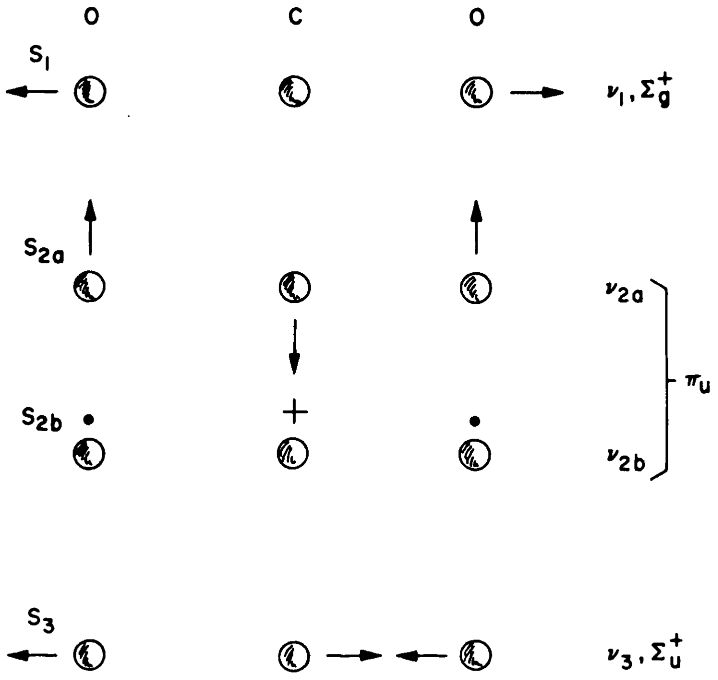

Figure 2-2.1: CO_2 Molecule Vibration Modes

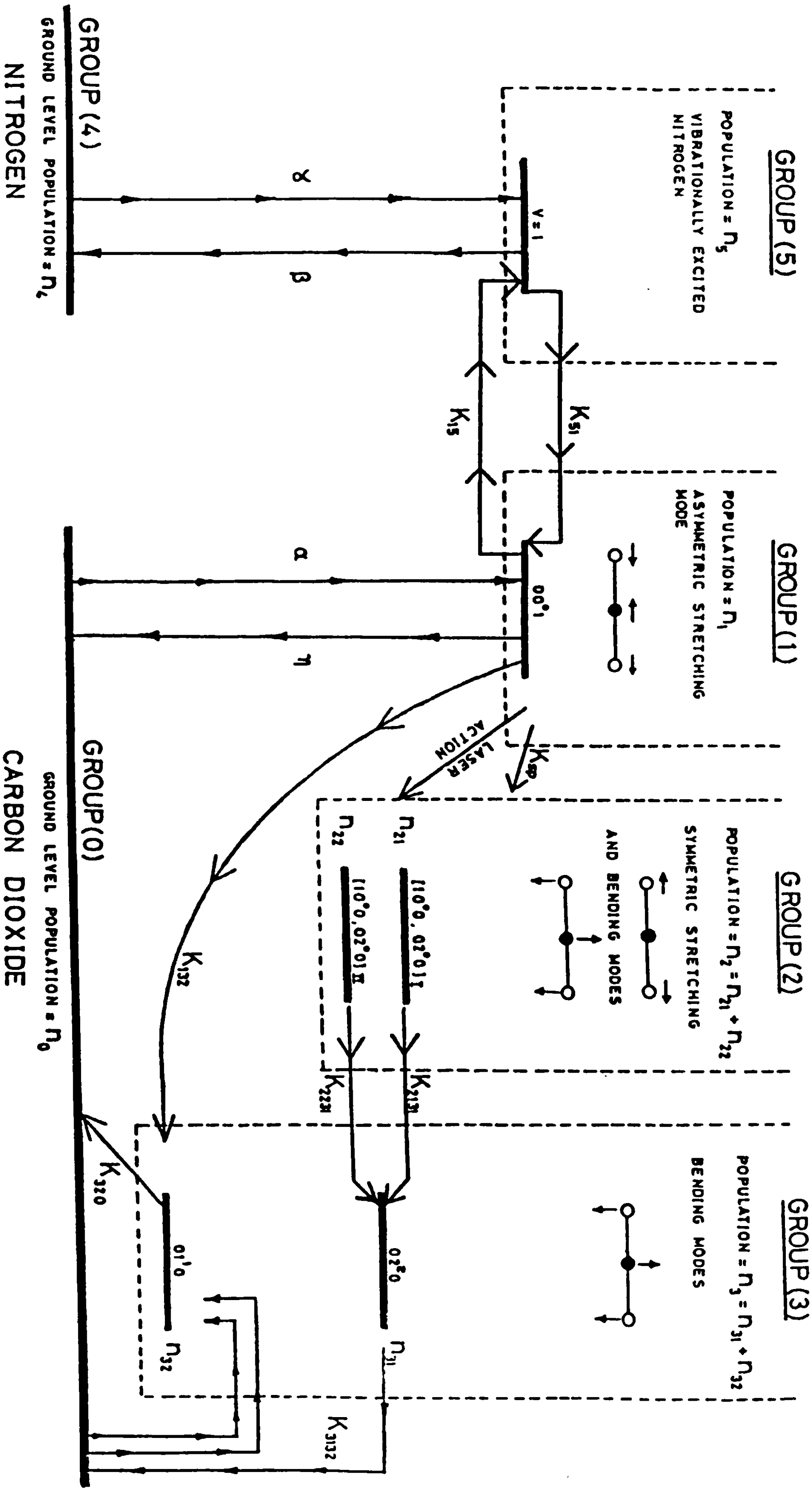

Figure 2-2.2: CO_2 Laser Energy Levels

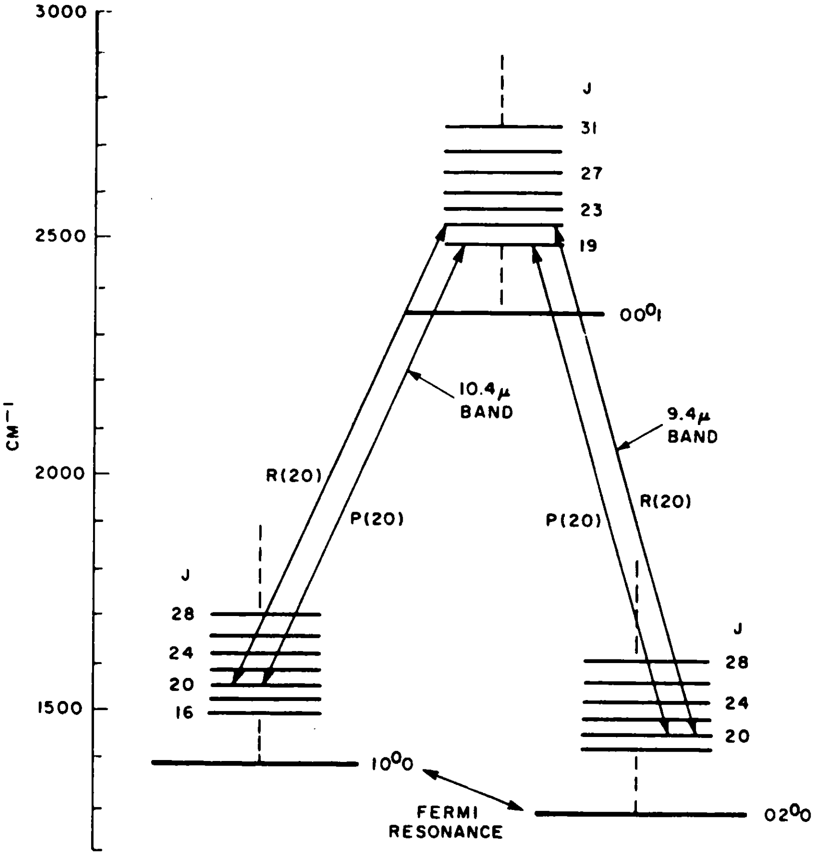

Figure 2-2.3: CO2 Laser Transition Diagram

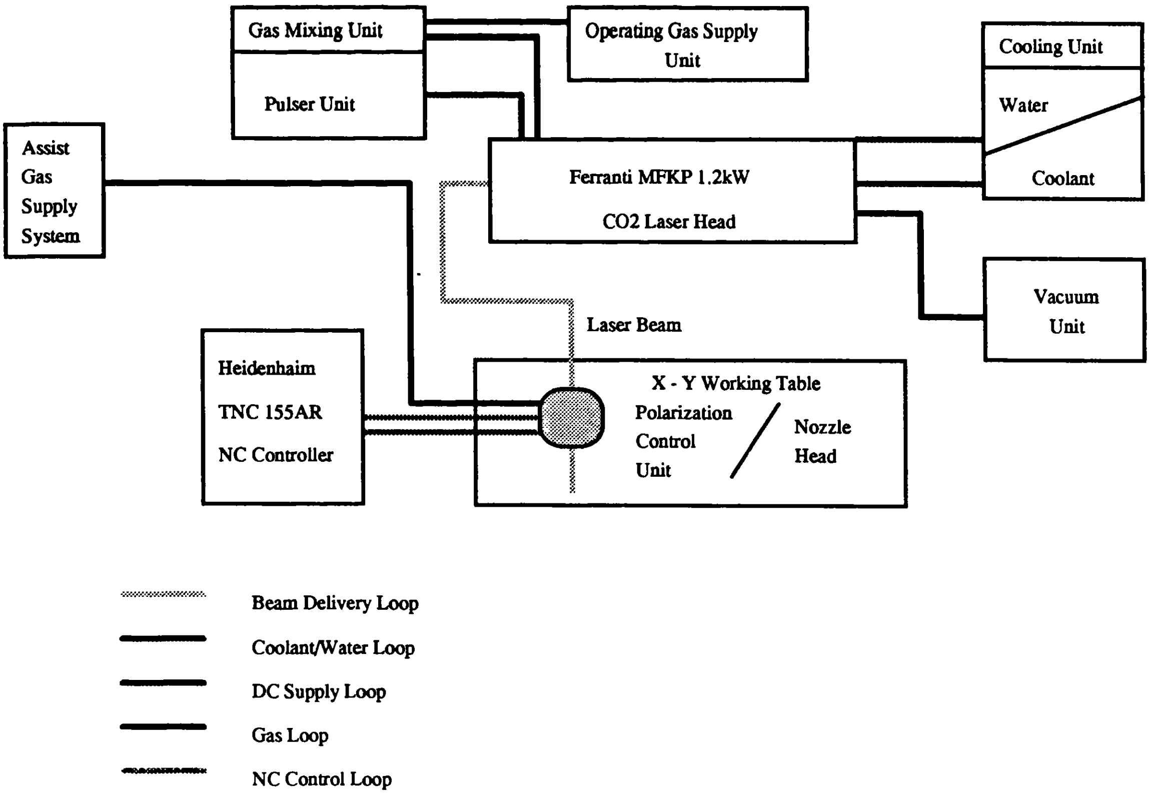

Figure 2-2.4: Ferranti MFKP CO_2 Laser Manufacturing System

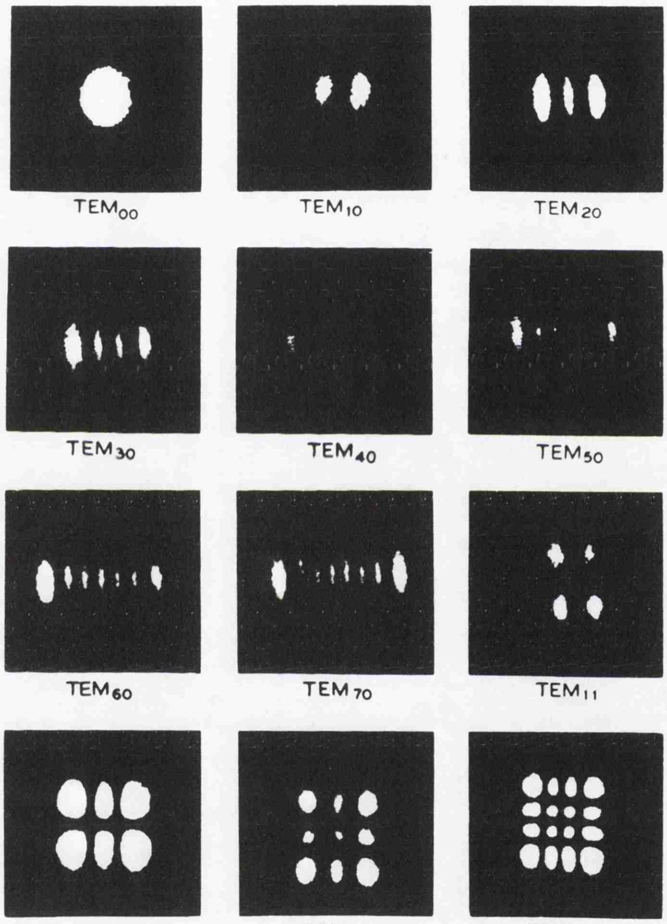

Figure 2-2.5: TEM pattern

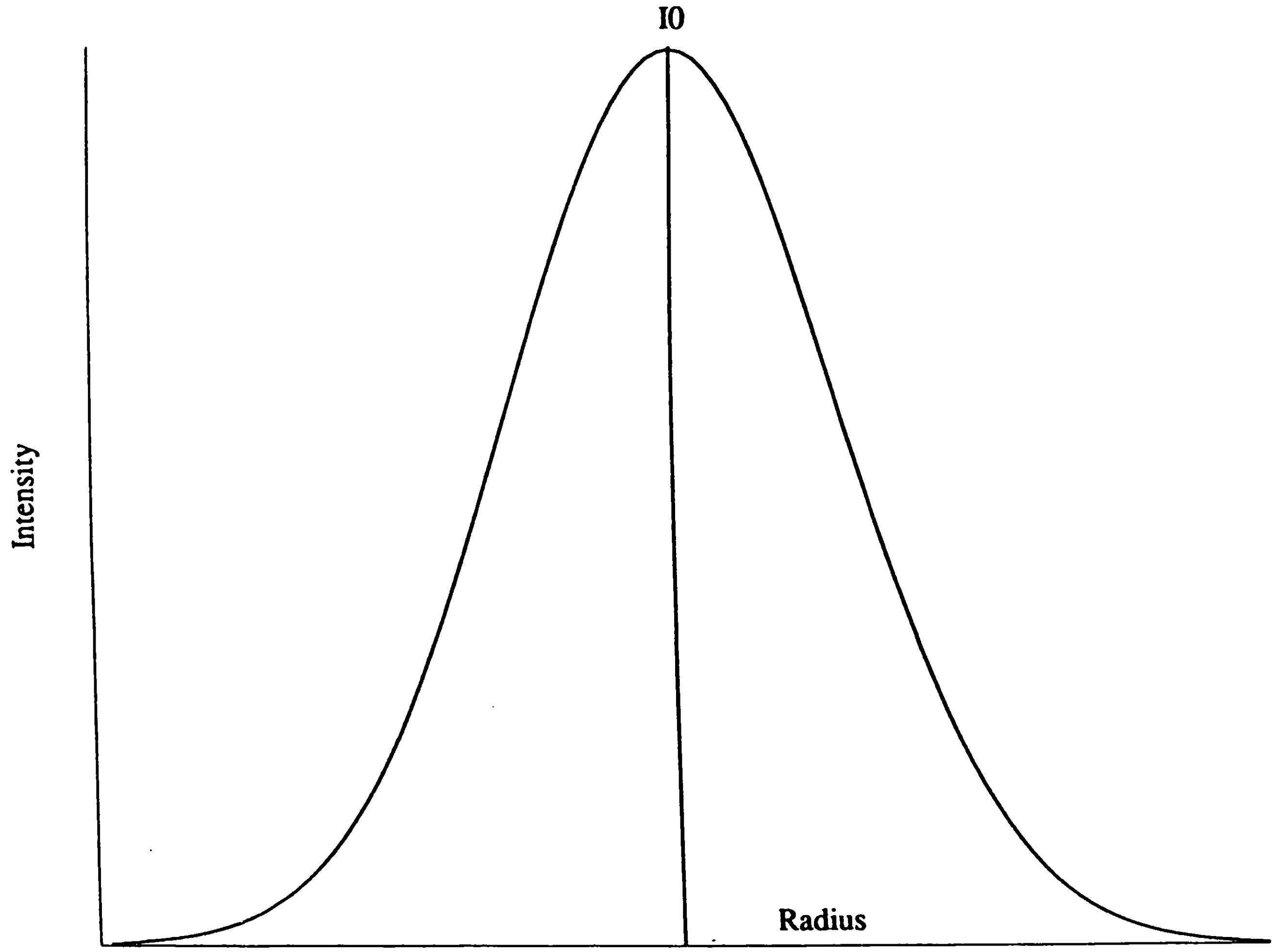

Figure 2-2.6: Intensity Distribution of Fundamental Mode (TEM_{00})

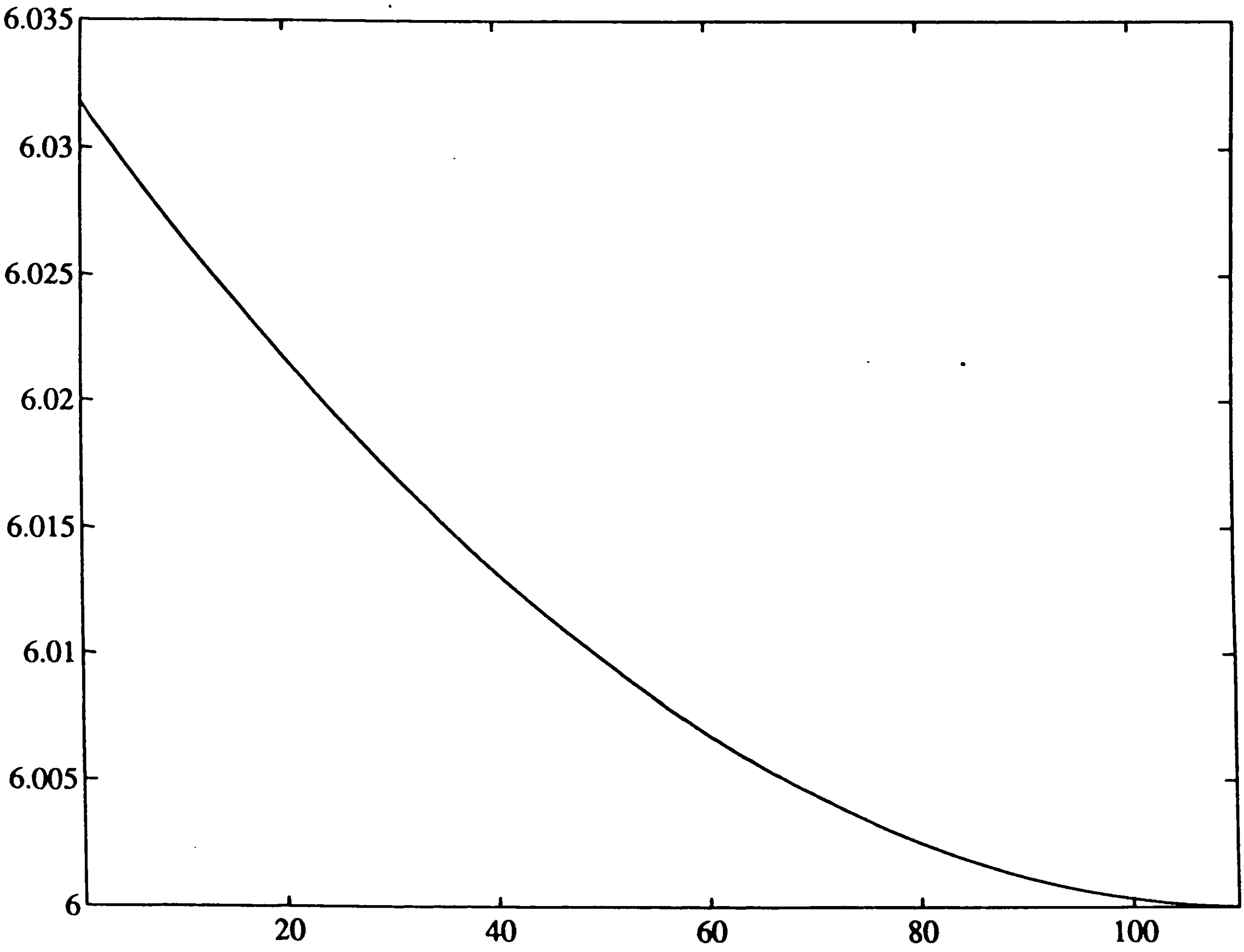

Figure 2-2.7: Beam Radius vs. Distance (for MFKP)

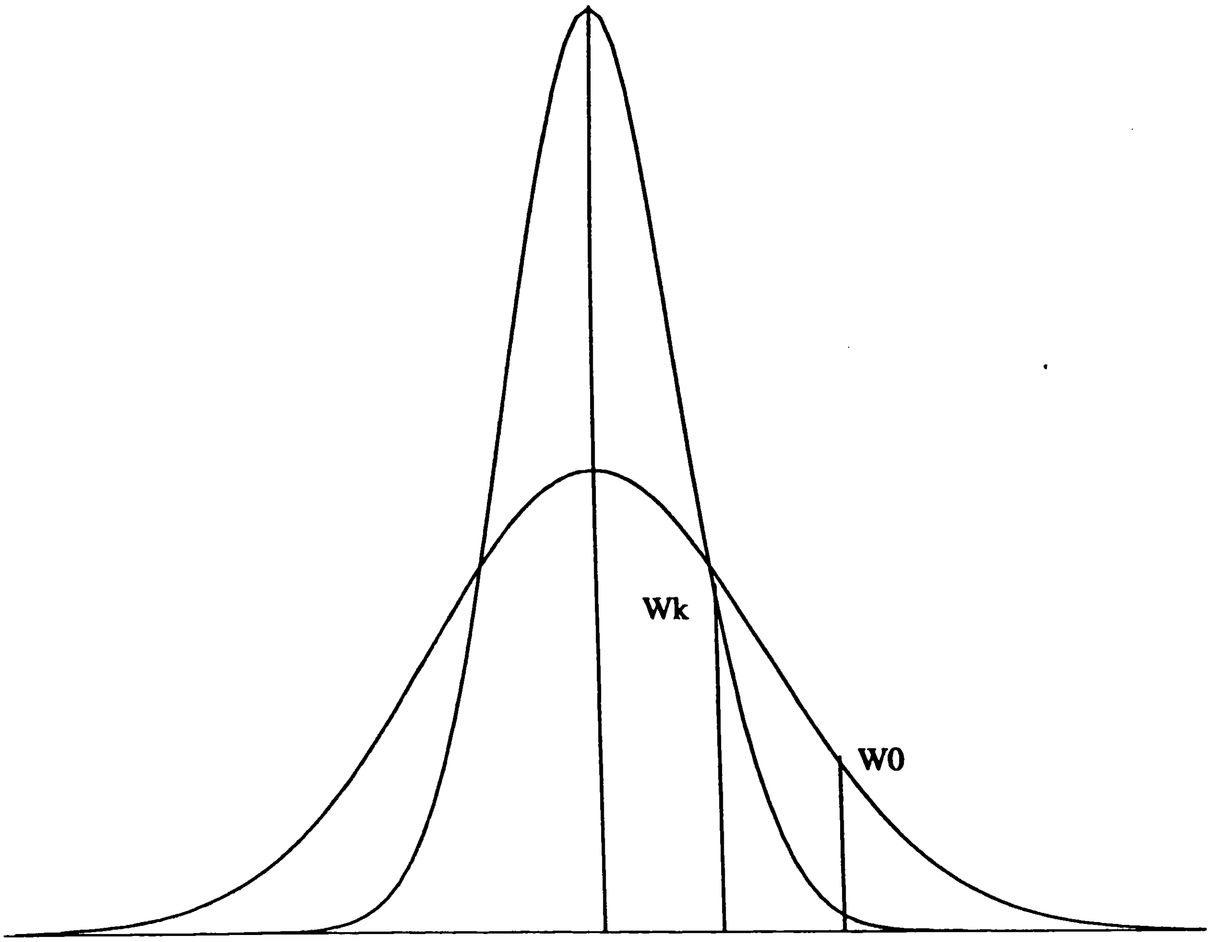

Figure 2-2.8: Gaussian Beam Profile and Its Fourier Transform

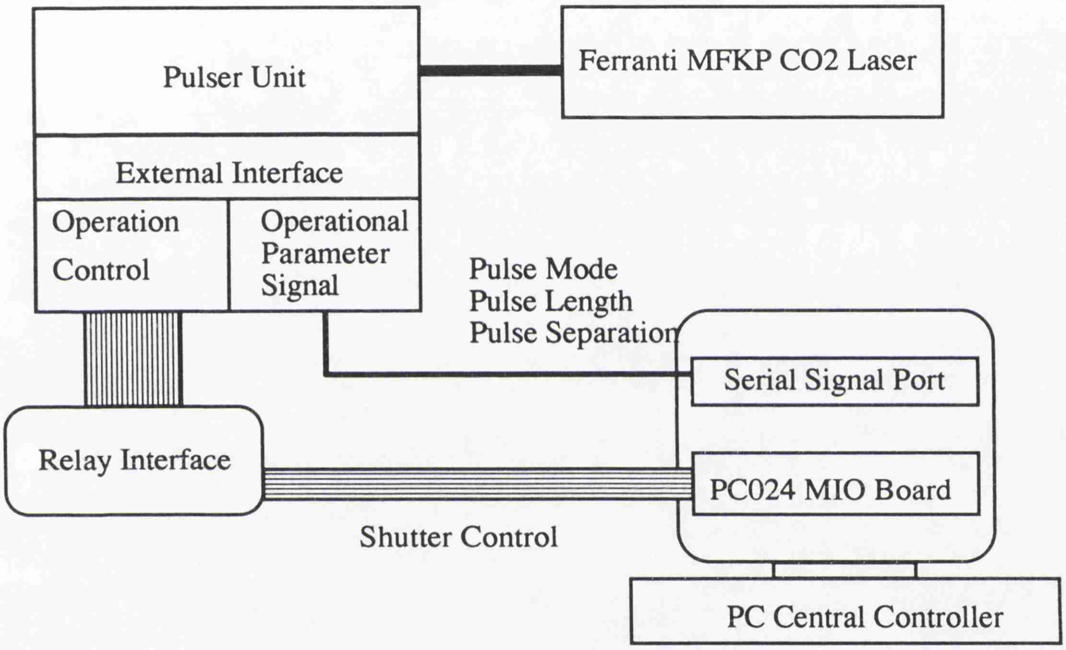

Figure 2-2.9: Pulser Remote Control Diagram

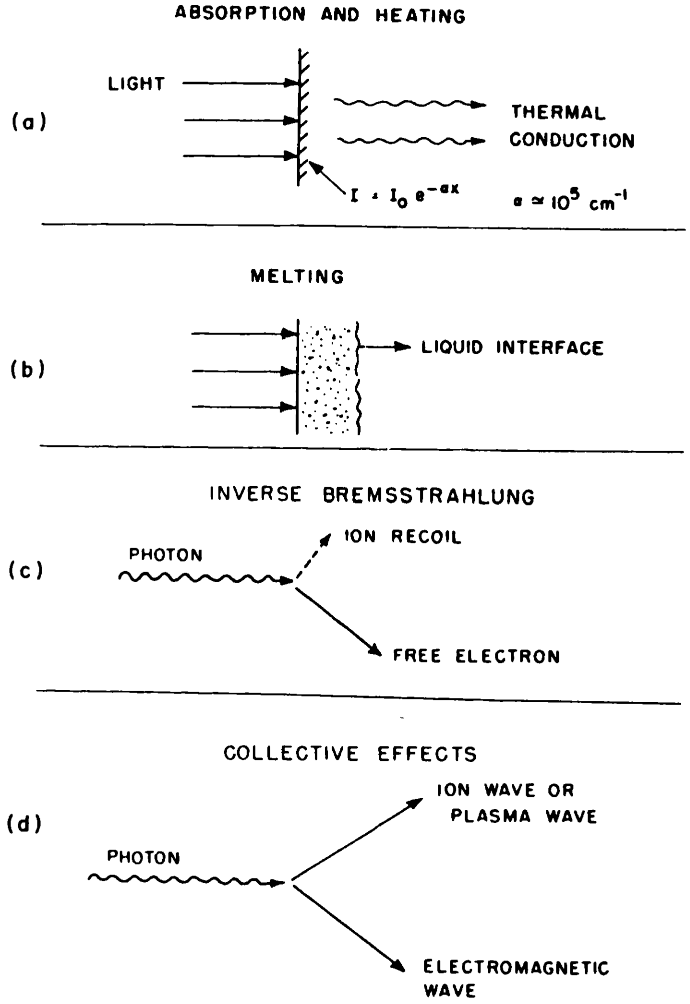

Figure 2-3.1(a): Laser - Material Interaction Phenomena

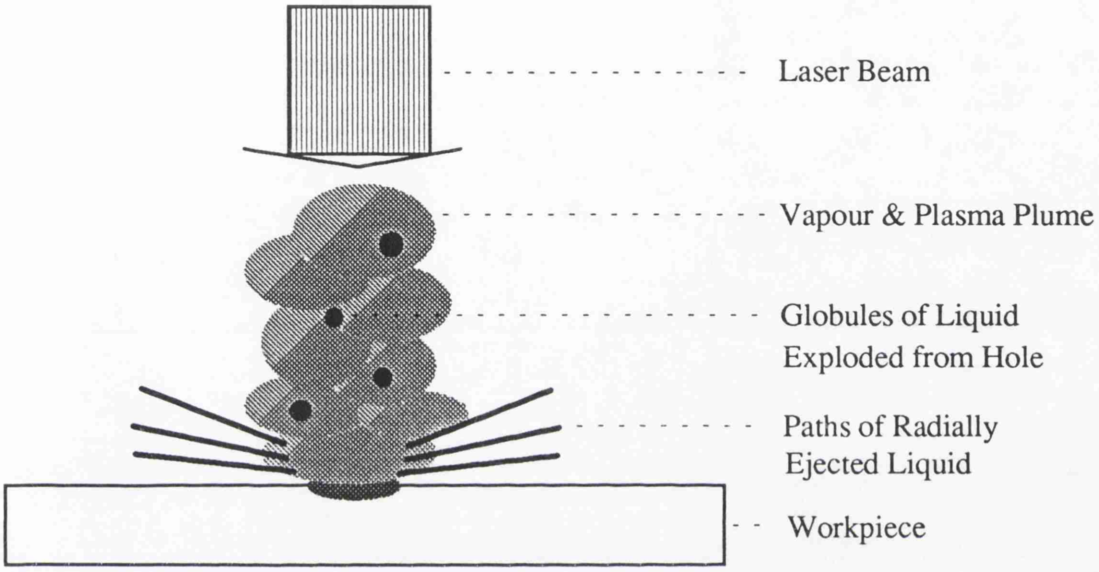

Figure 2-3.1(b): Schematics of Laser Drilling Phenomena

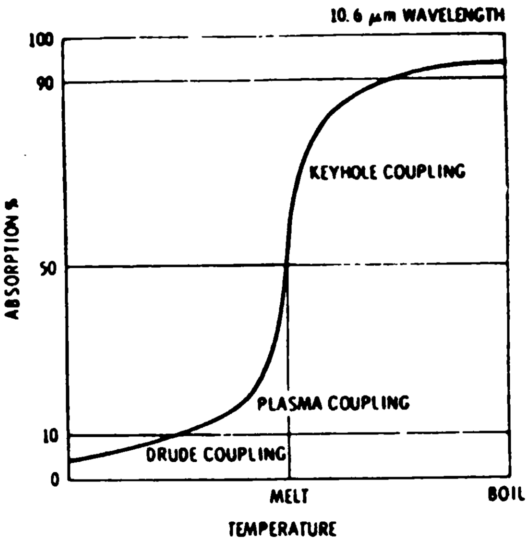

Figure 2-3.2: Reflectivity vs. Temperature

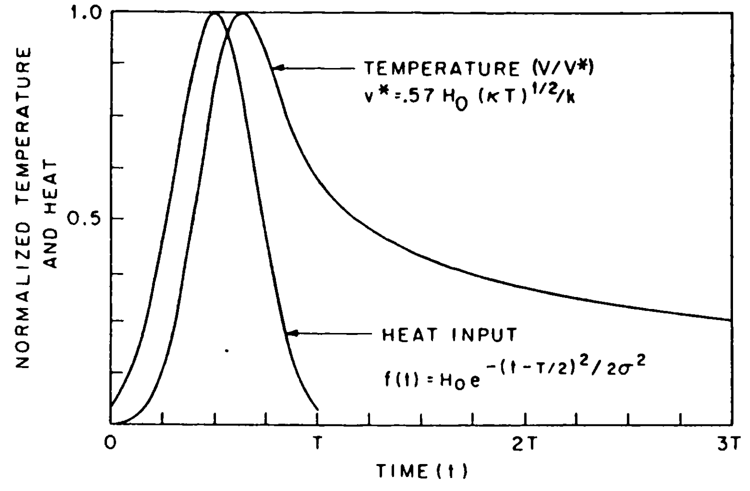

Figure 2-3.3: Time vs. Surface Temperature

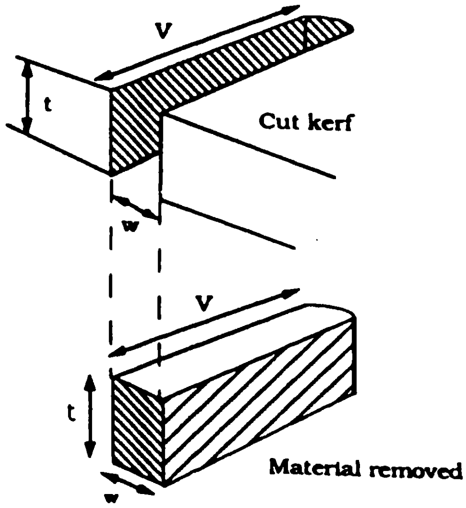

Figure 2-5.1: Simple Lumped Heat Model

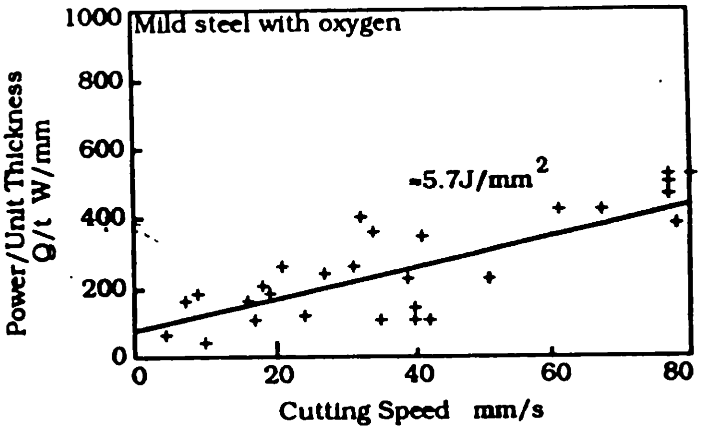

P/t vs V for mild steel

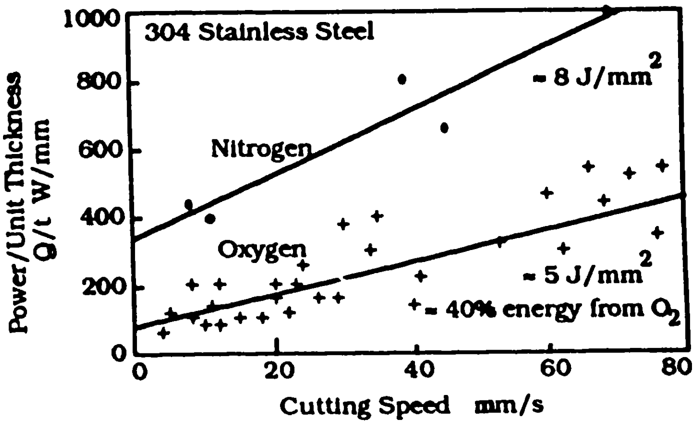

P/t vs V for stainless steel

Figure 2-5.2: P vs tV

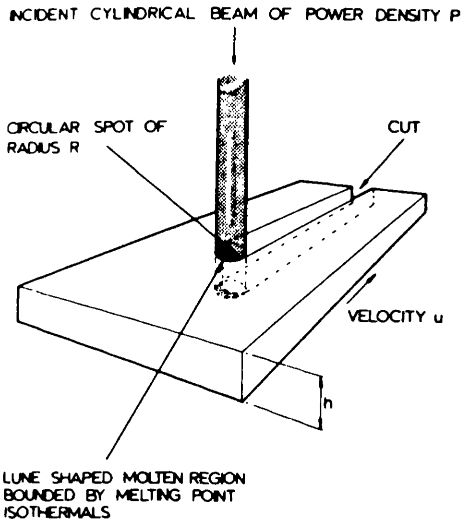

Figure 2-5.3: Cylindrical Source Model

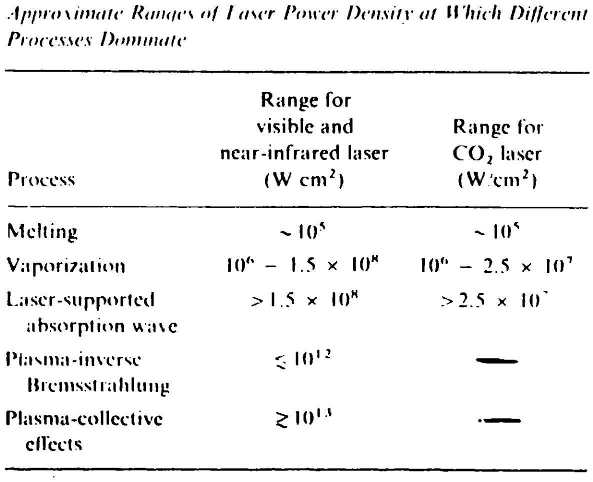

Approximate Ranges of Laser Power Density at Which Different Processes Dominate

Process	Range for visible and near-infrared laser (W cm^2)	Range for CO$_2$ laser (W/cm^2)
Melting	$\sim 10^5$	$\sim 10^5$
Vaporization	$10^6 - 1.5 \times 10^8$	$10^6 - 2.5 \times 10^7$
Laser-supported absorption wave	$> 1.5 \times 10^8$	$> 2.5 \times 10^7$
Plasma-inverse Bremsstrahlung	$\lesssim 10^{12}$	—
Plasma-collective effects	$\gtrsim 10^{13}$	—

Table 2-3.1: Approximate Range of Laser Power Density at Which Different Process Dominate

CHAPTER 3

Experiments, Results and Discussion - 1 Operational Parameter Analysis

PAGE

Nomenclature

a = laser - material interaction distance

b = kerf width

d = distance from the minimum spot waist

D = focused beam diameter calculated by diffraction limited method

E_L = energy absorbed from laser beam

E_R = energy generated from reaction between O2 and metal

f = focal length

$\tilde{m}$ = mass (molar)

P_{atm} = atmosphere pressure

P_c = critical gas pressure

P_L = laser power

P_R = reaction energy

$\tilde{R}$ = gas constant (molar)

t = time

T = temperature

v_g = velocity of assistant gas

v_L = laser beam feedrate

V_c = local sound velocity

Z = beam radius at distance d

α = absorption coefficient

γ = ration of specific heat (c_p/c_v)

λ = wavelength

μ_g = dynamic viscosity of assistant gas

ρ_g = density of assistant gas

ρ_m = density of metal

τ_g = shear stress acting on the molten layer

ω_0 = focused beam radius

ω_1 = beam radius in front of focusing lens

$\omega(d)$ = beam radius as a function of distance

3-1 Kerf Width - Focus Height / Gas Pressure Relationship

The kerf is formed during a laser cutting process, its width is a function of the amount of laser energy absorbed during the process. The kerf width and shape strongly influence the flow conditions of the assist gas when it passes through the kerf. The assist gas flow rate controls the heat of reaction and workpiece cooling rate. Finally, the flow conditions will also influence the melt flow and material removal rate which influences the quality of the cutting process.

The kerf width is determined by a combination of: beam spot size, beam power density, gas flow conditions and material characteristics, which is complex and cannot be resolved analytically. However, kerf width is usually defined in terms of the laser beam spot diameter.

3-1-1 Theoretical Analysis

Consider a Gaussian beam propagating through a thin lens of focal length f. The spot size of the focused beam is calculated as in sec. 2-2.2 and has a radius of 0.3mm. The radius of the laser beam at different distances from the focus is calculated via a simple triangular geometry as shown in figure 3-1.1

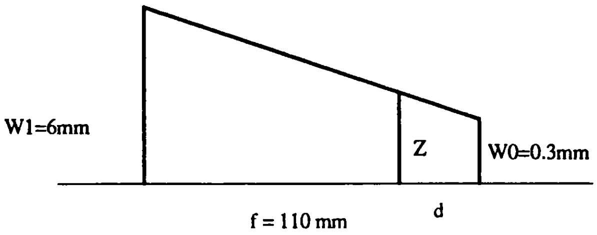

Figure 3-1.1 Beam Diameter Calculation (Simple Geometry Method)

$$Z = \omega_0 + \frac{d}{f}(\omega_1 - \omega_0) \tag{3-1.1}$$

The results are shown in Table 3-1.1 and in figure 3-1.2.

Another method to calculate the radius of the spot size is the diffraction limited method. The diameter of a focused beam is calculated by the following equation from Hecht[1].

$$D = 1.22 \cdot \frac{\lambda\, f}{d} \tag{3-1.2}$$

The diameter of the focused beam is calculated to be 0.475mm.

Equation 3-1.1 can be used to calculate the beam diameter at different heights. The results are shown in Table 3-1.1 and in figure 3-1.2.

A third method (Yariv[2]) utilized to evaluate the spot size of the beam at different heights in a homogeneous media is:

$$\omega^2(d)=\omega_0^2\left[1+\left(\frac{\lambda d}{\pi\omega_0^2 n}\right)^2\right] \tag{3-1.3}$$

where d is the distance from the minimum spot waist.

The results are also shown in Table 3-1.1 and figure 3-1.2.

Offset Distance		0.6 mm	1.1 mm	1.6 mm	2.1 mm	2.6 mm	3.1 mm	3.6 mm	4.1 mm	4.6 mm
2 bar (experiment)	Kerf Width (mm)	0.613	0.637	0.73	0.764	0.806	0.82	0.92	0.958	
3 bar (experiment)		0.587	0.6	0.664	0.741	0.807	0.848	0.94	0.973	1.022
4 bar (experiment)		0.546	0.633	0.639	0.716	0.788	0.845	0.946	1.014	1.046
Fourier-Gaussian		0.6666	0.6668	0.6672	0.6676	0.6686	0.6696	0.6708	0.6724	0.674
Fourier-Straight		0.6666	0.7116	0.763	0.8146	0.8662	0.9178	0.9692	1.0208	1.124
Diffraction-Straight		0.474	0.526	0.579	0.632	0.684	0.736	0.788	0.841	0.894

Table 3-1.1: Kerf Width vs. Focal Height Offset Distance

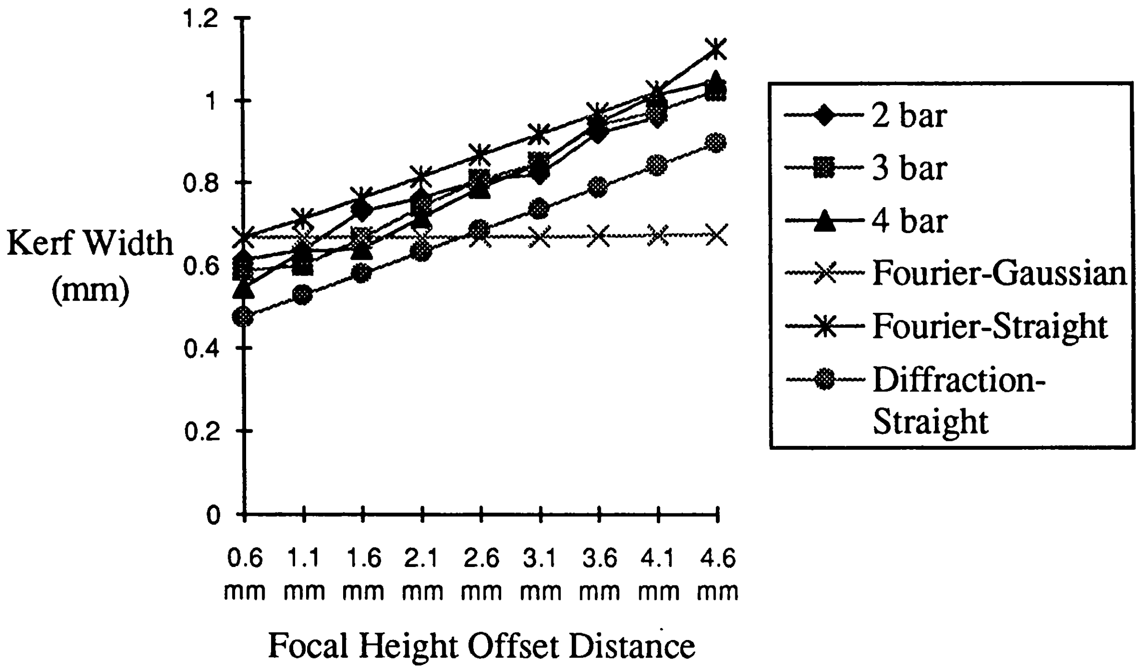

Figure 3-1.2: Kerf Width vs. Focal Height Offset Distance

3-1-2 Experimental Set-up

The laser system set-up is as shown in figure 3-1.3.

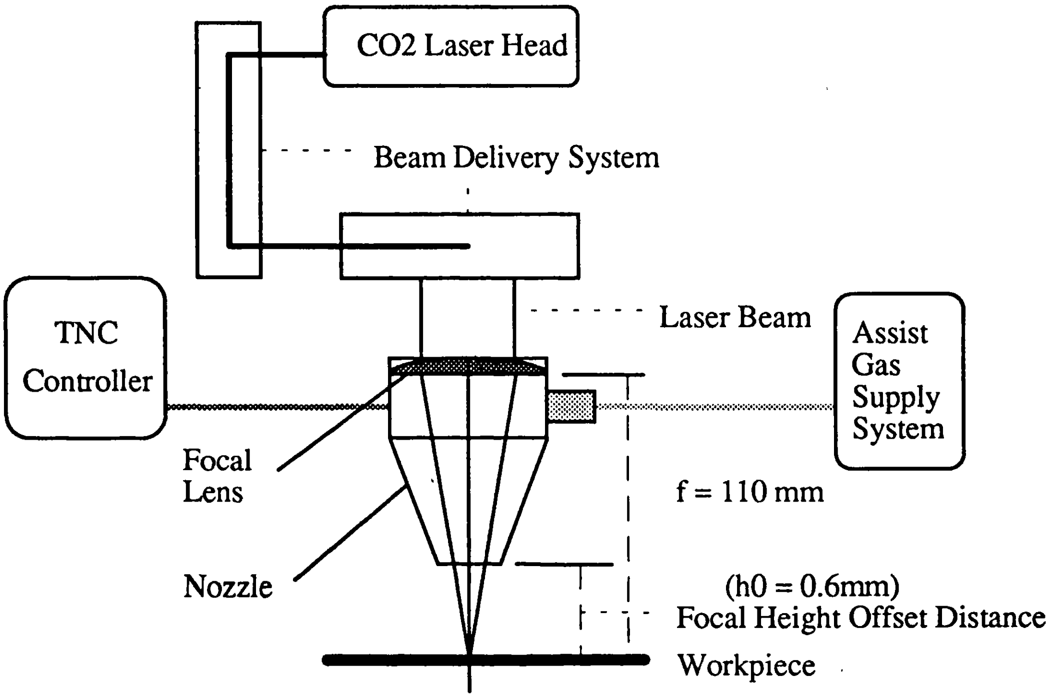

Figure 3-1.3: Laser Cutting Process Set-up

The focal point is adjusted to be 0.6mm, under the tip of the nozzle head outlet. The process parameters are set as follows:

(1) material: 4 mm mild steel

(2) feed rate: 1420 mm/min

(3) assist gas pressure: 2 bar - 4 bar

(4) focal height offset distance: to be adjusted from 0 mm (right on the metal surface) to 4 mm above the metal surface

(5) focusing length: convex-planar lens with focus length f=110 mm

3-1-3 Results

The surface of the kerf wall approximates a periodic wave. The kerf width is calculated as the mean between the narrower gap and wider gap. The result is shown in figure 3-1.2 and summarized in Table 3-1.1.

3-1-4 Discussions

From the experimental results the following conclusions may be drawn. Kerf width is inversely proportional to the assist gas pressure. This means that a narrower kerf width is obtained when a higher gas pressure is used. As the gas pressure is higher, the gas velocity is higher and the removal of the melted material is rapid. Energy loss due to melt removal increases therefore the volume of melt is reduced. As the thickness of the material is fixed, the kerf width must be reduced. Kerf width is proportional to the offset height: this is obvious from the results of the theoretical analysis. However, which method is more accurate to represent the actual cutting process? The Fourier Transform method for calculating the spot size of a focused Gaussian beam is closer to the actual focused spot size when gas pressure reaches the lowest value for cutting to be possible. As the gas pressure is increased, the diffraction limit method gives a more accurate prediction of spot size. The beam diameter at different offset heights was evaluated using the simple triangular geometry method. This gives results closer to the actual phenomenon than the Gaussian beam propagation method.

3-1-5 Conclusion

Although the laser operates in the TEM_{00} mode, delivering a Gaussian laser beam, the simple triangular geometry method gives the best prediction of spot size at different offset heights. When the cutting process is performed using normal and economical settings, that is lowest assist gas pressure, the Fourier transform method gives a more accurate prediction of the effective focused spot size.

3-2 Effect of Focal Height on Cut Quality

Cut quality is based on the combined evaluation of the Heat Affected Zone (HAZ) on the cut edge and roughness of the cut surface. A small HAZ and smooth kerf wall surface is the definition of a high quality cut.

The focal height position influences the diameter of the beam when the laser beam impinges on the target surface. Consequently, this will determine the irradiance (watt/cm^2) of the focused spot, the width and shape of the kerf that is formed during the process and the flow-dynamics within the kerf.

3-2-1 Theoretical Analysis

Recall from the previous chapter, the relationship between the focal height offset distance and the resulting beam diameter, incident power density, and kerf width. The results are illustrated in figure 3-2.1.

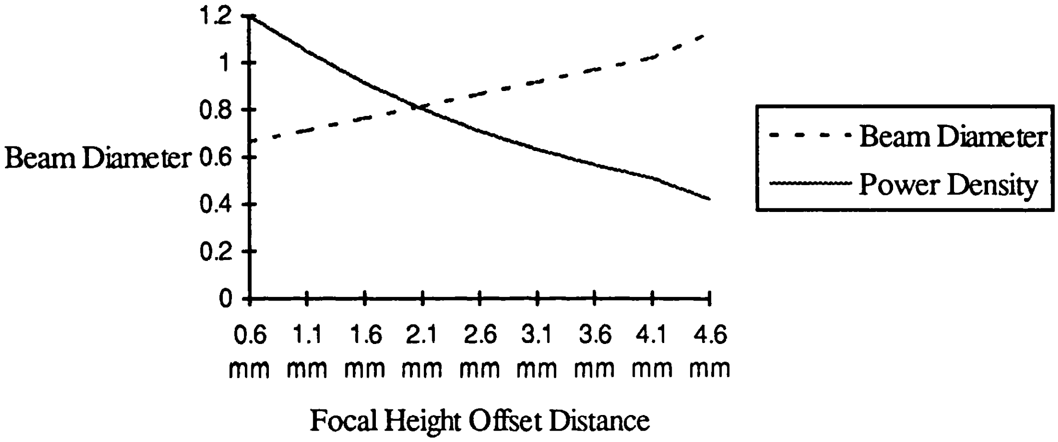

Figure 3-2.1: Beam Diameter/Incident Power Density vs. Focal Height Offset Distance

The most obvious effect of the focal height is the variation of power density. When the power density is lower than a certain level (10^6 watt/cm^2 for mild steel), no cut will be possible. This is clearly shown in the experimental results presented later in this chapter.

As long as the power density is high enough to perform the cutting process, focal height offset distance does not greatly influence the cutting quality. When the spot size is changed, although the kerf is wider or narrower, the overall laser and material interaction condition remains the same but at different scales. Therefore, when the focal height offset distance is changed, the conditions in the cut region are changed, yet the conditions at the edge of the cut region remain the same.

3-2-2 Experimental Set-up

The cutting process is set up as illustrated in figure 3-1.3. The laser beam is delivered from the laser head through the optical beam delivery system to the nozzle head. The focal length of the convex-planar focusing lens f is 110mm. The focusing point is 0.6 mm below the nozzle head. (h_0=0.6mm)
Assist gas = O_2 at a supply pressure of 2 bar
Beam power was held constant at 1150 watts
processed material= (1) mild steel (BS1449-CR4) (0.12%C, 0.6%Mn, 0.05 S, 0.05% P) thickness from 1 mm to 6mm. (2) stainless steel (S304) thickness from 1mm to 4mm

Definition of each focal height offset distance is as follows:

Surface = focus point right on the surface[+]

H_i = i/6 $*$ material thickness + 0.6

where : i = 1, 2, ... 6

Focal height offset distances used in each cutting process for different material thicknesses are tabulated in table 3-2.1. (in mm)

	Material thickness	1 mm	2 mm	3 mm	4 mm	5 mm	6 mm
	Surface	0.6	0.6	0.6	0.6	0.6	0.6
	H1	0.766	0.933	1.1	1.267	1.433	1.6
Nozzle	H2	0.933	1.267	1.6	1.933	2.267	2.6
Height	H3	1.1	1.6	2.1	2.6	3.1	3.6
Offset	H4	1.266	1.933	2.6	3.267	3.933	4.6
	H5	1.433	2.267	3.1	3.933	4.767	5.6
	H6	1.6	2.6	3.6	4.6	5.6	6.6

(Focal height offset = nozzle height offset - 0.6)

Table 3-2.1: Focal Height Offset Distance for Different Material Thicknesses

3-2-3 Results

The heat affected zone data measured is summarized in Table 3-2.2 and the cutting surface roughness is summarized in Table 3-2.3. The results are also shown in figure 3-2.2, figure 3-2.3 and figure 3-2.4.

[+] *When the focal point is on the surface the nozzle offset* h_0 = *0.6mm; hence, the generated focal height offsets should have 0.6mm subtracted from them to get true value.*

			Material Thickness					
			MS 1mm	MS 2mm	MS 3mm	MS 4mm	MS 5mm	MS 6mm
	Surface		0.604	0.183	0.256	0.282	0.258	0.34
Focal	H1		1.362	0.306	0.242	0.2	0.324	0.377
Height	H2	HAZ	1.491	0.227	0.262	0.361	0.408	0.378
Offset	H3	Width	1.356	0.293	0.222	0.34	0.396	0.384
Distance	H4	(mm)	1.063	0.287	0.208	0.339	0.386	0.991
	H5		1.365	0.263	0.224	0.365	X	X
	H6		1.202	0.901	0.752	X	X	X
			Material Thickness					
			SS 1mm	SS 2mm	SS 3mm	SS 4mm		
	Surface		0.118	0.133	0.205	0.329		
Focal	H1		0.124	0.166	0.247	0.382		
Height	H2	HAZ	0.176	0.149	0.256	0.446		
Offset	H3	Width	0.177	0.428	0.267	0.413		
Distance	H4	(mm)	0.172	0.402	0.259	0.472		
	H5		0.163	0.424	0.316	0.5		
	H6		0.155	0.166	0.347	X		

Table 3-2.2: HAZ vs. Focal Height Offset Distance

(Laser Power = 1150 Watts)

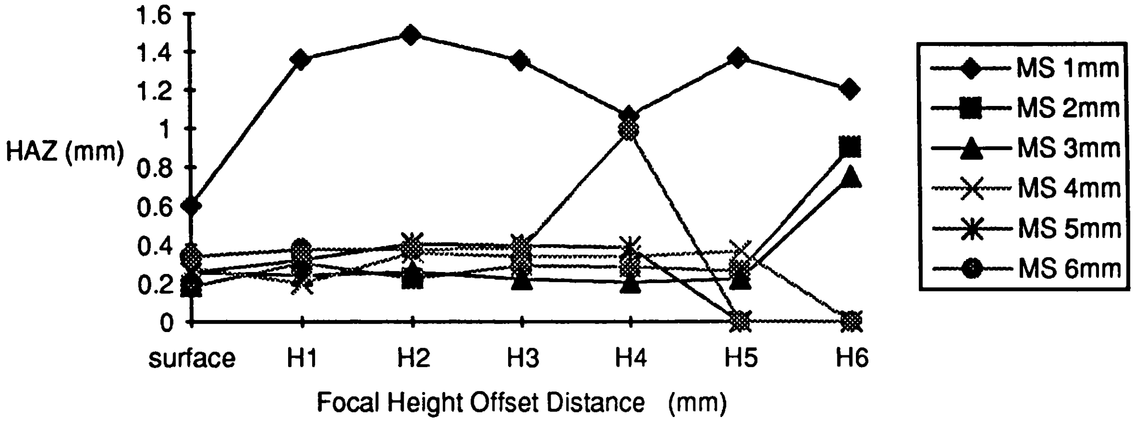

Figure 3-2.2: HAZ vs. Focal Height Offset Distance (mild steel)

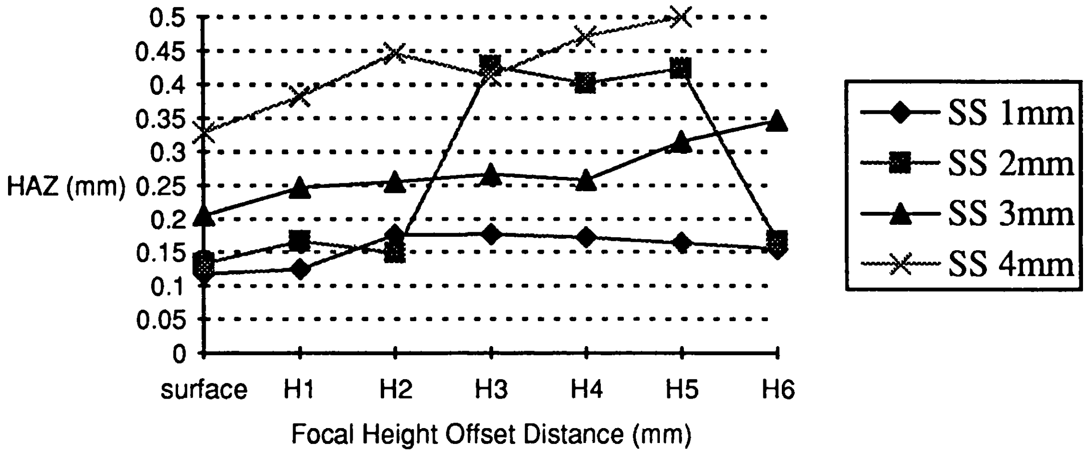

Figure 3-2.3: HAZ vs. Focal Height Offset Distance (stainless steel)

			Material Thickness				
			MS 2mm	MS 3mm	MS 4mm	MS 5mm	MS 6mm
	Surface		1.52	4.8	9.5	19.3	13.7
Focal	H1	Kerf	X	4.3	14.1	38.4	19.3
Height	H2	Wall	2.17	4.7	13.7	36.5	21.6
Offset	H3	Surface	2.62	5.4	13.7	X	X
Distance	H4	Roughness	2.56	5.6	X	X	X
	H5		1.3	8.5	X	X	X
	H6		4.41	8.4	X	X	X

Table 3-2.3: Kerf Wall Surface Roughness vs. Focal Height Offset Distance

(Laser Power = 1150 Watts)

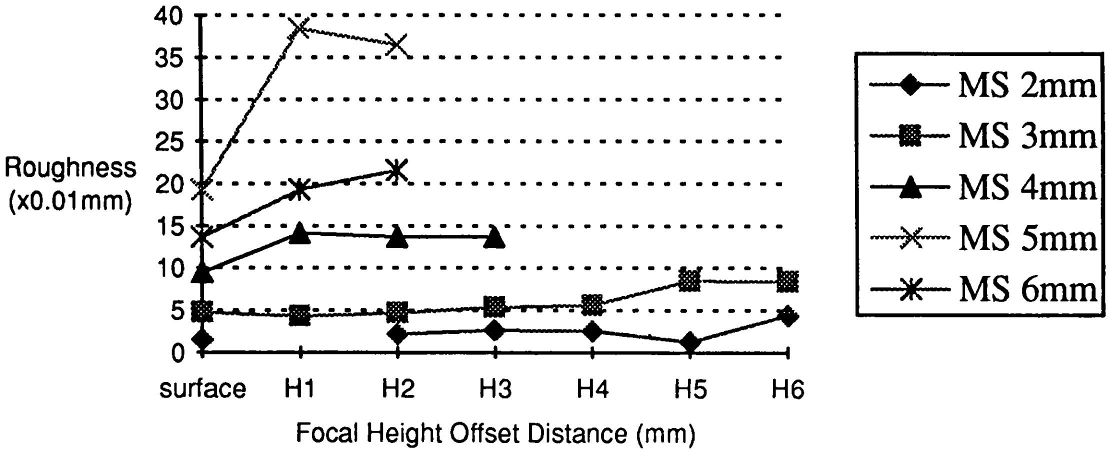

Figure 3-2.4: Kerf Surface Roughness vs. Focal Height Offset Distance

3-2-4 Discussion

As long as the material is cut through, the focal height position does not greatly influence the HAZ, nor does it significantly affect the surface roughness. For mild steel up to 6 mm thickness, and stainless up to 4 mm thickness, the best focus height position for obtaining good cutting quality is right on the surface. The focused spot size generates the narrowest kerf width and the smallest HAZ. When no cut occurs, the HAZ increases in size. This is because the heat generated by the laser energy is absorbed and spreads widely into the nearby region along the kerf. All of the absorbed energy spreads out widely instead of being concentrated in a small spot region.

3-2-5 Conclusion

The best focal height offset distance for cutting thin steel (up to 6mm) is right on the surface. Since this focused beam generates the smallest spot size this gives the highest power density. Material inside the interaction zone is heated up rapidly and easily removed by the assist gas jet without affecting the neighbouring region. The focal height offset distance does not play a major role in influencing the cut quality as long as the material is cut through.

3-3 Effect of Feedrate on Cut Quality

Laser beam feedrate determines the interaction time between laser beam and the material. It therefore determines the energy supply rate to the laser-material interaction zone. This is the major factor that influences the quality of the laser material cutting process.

3-3-1 Theoretical Analysis

In laser material cutting, heating of the material is caused by the energy absorbed by the material. The energy absorbed is as follows:

$$E_L = \alpha \cdot P_L \cdot t \qquad (3\text{-}3.1)$$

where:

(i) α is the absorption coefficient

(ii) P_L is the laser power

(iii) t is the interaction time. $t = \frac{a}{v_L}$

v_L is the laser beam feedrate

a is the interaction distance, defined as the beam diameter

Therefore, $$E_L = \alpha \cdot P_L \cdot \frac{a}{v_L}$$

=> $$E_L \propto \frac{1}{v_L}$$

From the above analysis, the amount of energy absorbed during the interaction is inversely proportional to the laser beam feedrate. Hence, when the laser beam feedrate is reduced, more energy will be absorbed per unit area - thus more heat is generated and consequently, when the amount of energy exceeds the permitted stable range, severe fluctuations in the absorption of power will occur inside the cutting region. As a result of this fluctuation, a rougher kerf wall surface is formed. For lower feedrates more energy is absorbed by the parent material, this results in a larger HAZ.

3-3-2 Experimental Set-up

Figure 3-1.3 illustrates the cutting system set-up. The feedrate was adjusted through the TNC 155AR NC controller. Process parameter settings were as follows:

(1) material : as 3-2-2
(2) focal height offset distance: right on the surface (0.6 mm below nozzle)
(3) assist gas pressure: 2 bar (O_2)
(4) laser Power: 1150 Watts
(5) feed rate: the feedrate used is defined below:
    (i) goodcut: the fastest feedrate obtained for each thickness
    (ii) V1 -V6: Vi = Vgoodcut [1 - i * (10%)] where i =1 to 6

They are also listed in table 3-3.1.

	Material hickness	1mm	2mm	3mm	4mm	5mm	6mm
	Vgoodcut	5200	2700	2000	1420	1200	950
	V1	4680	2430	1800	1280	1080	860
	V2	4160	2160	1600	1140	960	760
Feedrate	V3	3640	1890	1400	1000	840	670
(mm/min)	V4	3120	1620	1200	860	720	570
	V5	2600	1350	1000	720	600	480
	V6	2080	1080	800	580	480	380

Table 3-3.1: Feedrate used for Different Cutting Conditions and Material Thicknesses

3-3-3 Results

The heat affected zone (HAZ) thickness is defined in figure 3-3.1.

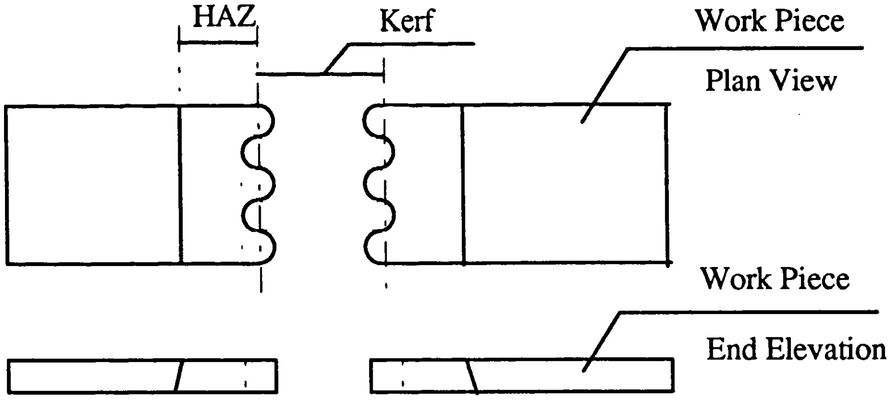

Figure 3-3.1: Definition of HAZ Thickness

The HAZ data measured from each specimen is summarized in Table 3-3.2. Surface roughness data is summarized in Table 3-3.3. The results are plotted in figure 3-3.2, figure 3-3.3 and figure 3-3.4.

			Material Thickness					
			MS 1mm	MS 2mm	MS 3mm	MS 4mm	MS 5mm	MS 6mm
	Vgoodcut		0.604	0.183	0.256	0.282	0.258	0.34
	V1		0.669	0.192	0.244	0.351	0.329	0.352
Feedrate	V2	HAZ	0.756	0.244	0.284	0.34	0.348	0.363
Setting	V3	(mm)	0.972	0.302	0.339	0.422	0.388	0.349
	V4		1.413	0.296	0.692	0.544	0.391	0.393
	V5		1.669	0.305	0.993	0.917	0.471	0.422
	V6		2.006	0.846	1.598	0.935	0.632	0.351
			Material Thickness					
			SS 1mm	SS 2mm	SS 3mm	SS 4mm		
	Vgoodcut		0.118	0.133	0.205	0.329		
	V1		0.147	0.16	0.223	0.365		
Feedrate	V2	HAZ	0.153	0.22	0.305	0.386		
Setting	V3	(mm)	0.169	0.227	0.317	0.437		
	V4		0.224	0.223	0.328	0.53		
	V5		0.254	0.289	0.454	0.58		
	V6		0.387	0.32	0.53	0.769		

Table 3-3.2: HAZ vs. Feedrate

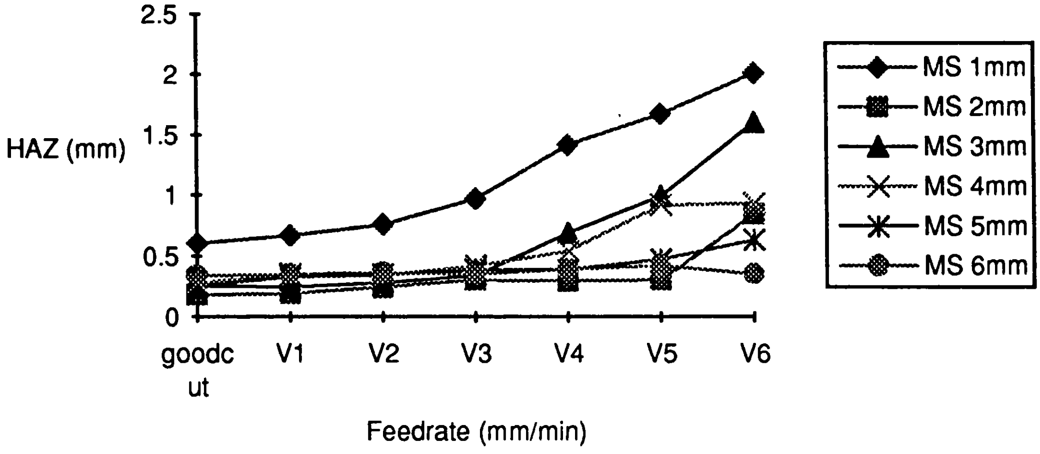

Figure 3-3.2: HAZ vs. Feedrate (mild steel)
(Laser Power = 1150 Watts)

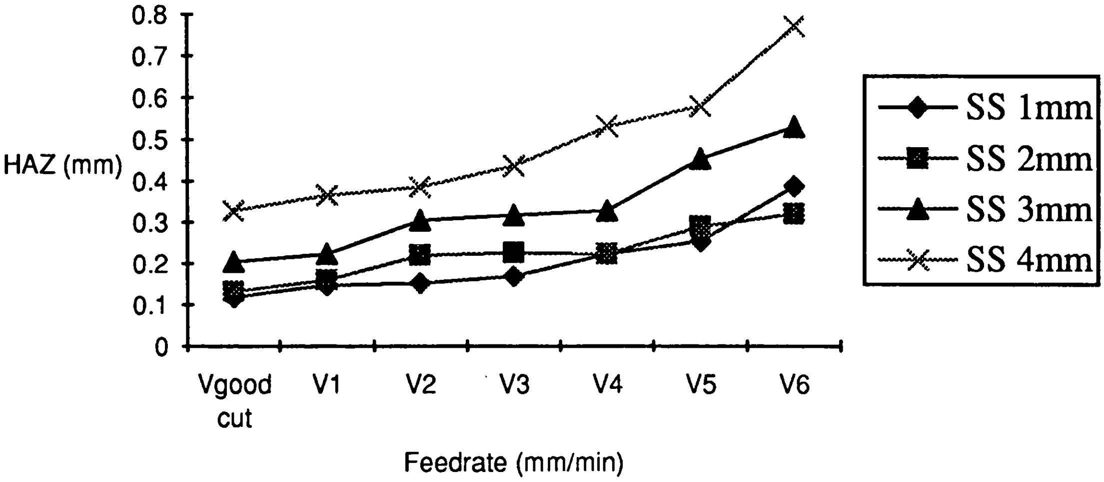

Figure 3-3.3: HAZ vs. Feedrate (stainless steel)
(Laser Power = 1150 Watts)

			Material Thickness				
			MS 2mm	MS 3mm	MS 4mm	MS 5mm	MS 6mm
	Vgoodcut		1.52	4.8	9.5	19.3	13.7
	V1		2.4	5.6	12.4	25.5	13.6
Feedrate	V2	Kerf	2.02	6.1	19.2	25.4	10.5
Setting	V3	Surface	3.02	8.9	24.7	31.9	10.6
	V4	Roughness	3.98	12.4	21.3	31.9	11.8
	V5		11.02	17.7	22.1	31.2	18.5
	V6		11.95	18.7	24.8	37.5	24.7

Table 3-3.3: Kerf Surface Roughness vs. Feedrate

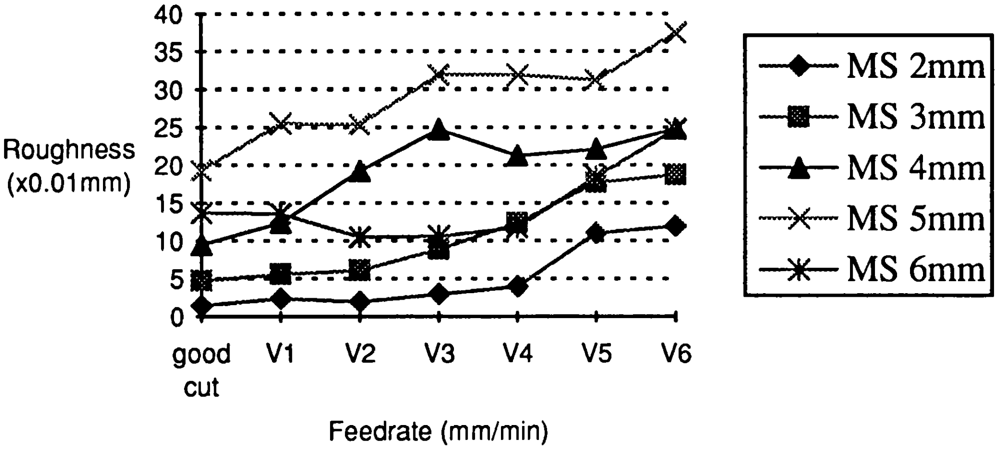

Figure 3-3.4: Kerf Surface Roughness vs. Feedrate
(Laser Power = 1150 Watts)

3-3-4 Discussion

Both in mild steel and stainless steel laser cutting, the size of the HAZ increases as the feedrate is reduced. This is because more energy is absorbed per unit mass, therefore the temperature in the cutting region is higher. As more energy enters the material adjacent to the kerf the HAZ becomes larger. Surface roughness increases as the feedrate is reduced and energy absorption exceeds the system stable range. Fluctuations inside the kerf are more severe and the roughness of the kerf wall surface increases.

3-3-5 Conclusion

As the feedrate is decreased, more and more energy is absorbed in the interaction zone. This causes both the magnitude of the HAZ and surface roughness to increase. For any particular assist gas pressure, focal height offset distance and laser power there is an ideal laser beam feedrate which delivers a good quality cut.

3-4 Effect of Assist Gas Pressure on Cut Quality

A high speed, reactive gas jet blows down through the nozzle head and kerf and has the following effects:

(1) energy supply: chemical reaction between the O2 gas and the melted metal particles.
(2) forced cooling : forced convection occurs as the high speed gas stream passes the surface of the hot melt.
(3) melt removal: the friction between the gas and the melted metal causes the gas stream to carry away the melted metal and eject it at the lower surface.

3-4-1 Theoretical Analysis

1. Energy supply:

The chemical reaction between the reactive gas and the melt generates another source of heat in the interaction region. The amount of energy generated is :

$$E_R = p_R \cdot b \cdot d \cdot \rho_m \cdot v_L \tag{3-4.1}$$

where: (i) b is the kerf width

(ii) d is the material thickness

(iii) ρ_m is the material density

(iv) P_R is the reaction energy

(v) v_L is the laser beam feedrate

In the laser cutting process, the liquid material inside the cutting region remains contiguous until it is carried out through the lower surface of the kerf. At this stage it mixes with the gas rapidly. Therefore, the assist gas pressure will not greatly affect the reaction energy within the cutting region. As long as the kerf width and material thickness remain the same, the energy released in the kerf due to exothermic chemical reaction is quite small.

2. Cooling effect:

The forced convection that occurs when the gas flows over the hot metal surface is small when compared to the heat loss through conduction and melt removal in the cutting region.

3. Melt removal:

Melt in the cutting region is removed due to the net frictional force acting on the molten layer. From Vicanek[3], Tsai[4], the shear stress generated by the gas flow and acting on the molten layer is:

$$\tau_g = \left(\rho_g \mu_g v_g^3 / d\right)^{1/2} \qquad (3\text{-}4.2)$$

where: (i) d is material thickness

(ii) ρ_g is gas density

(iii) μ_g is the gas dynamic viscosity

(iv) v_g is gas velocity

The shear force generated by the gas flow increases as the gas velocity is increased, that is a higher gas supply pressure. Hence, the melt will be removed from the cutting region more rapidly and less melt will remain. Therefore, less heat remains in the cutting region. Consequently, there is a smaller heat affected zone. Thus the higher the nozzle gas supply pressure the smaller the HAZ.

3-4-2 Experimental Set-up

The cutting system set-up is the same as sec. 3-2-2. The process parameter settings are as follows:

(1) material: the same as sec. 3-2-2

(2) focal height offset distance: right on the surface

(3) feed rate: best cut for each thickness

(4) laser power: 1150 Watts

(5) assist gas pressure: The gas pressure is adjusted via the gas system external valve. The settings were 1.5 bar, 2.0 bar(good cut), 2.5 bar, 3.0 bar, 3.5 bar. 4.0 bar and 4.5 bar.

3-4-3 Results

The measured HAZ data is summarized in Table 3-4.1. The kerf surface roughness of each specimen is summarized in Table 3-4.2. The results are also shown graphically in figure 3-4.1. figure 3-4.2 and figure 3-4.3.

		Material Thickness					
Supply Pressure		MS 1mm	MS 2mm	MS 3mm	MS 4mm	MS 5mm	MS 6mm
1.5bar		0.783	0.2	0.305	0.281	0.443	0.311
2.0bar		0.604	0.183	0.256	0.282	0.258	0.34
2.5bar	HAZ	0.5	0.2	0.259	0.272	0.296	0.308
3.0bar	(mm)	0.531	0.187	0.236	0.346	0.318	0.31
3.5bar		0.493	0.191	0.233	0.1	0.284	0.317
4.0bar		0.358	0.154	0.226	0.1	0.353	0.295
4.5bar		0.442	0.157	0.201	0.25	0.303	0.317
		Material Thickness					
Supply Pressure		SS 1mm	SS 2mm	SS 3mm	SS 4mm		
1.5bar		0.123	0.158	0.271	X		
2.0bar		0.118	0.133	0.205	0.329		
2.5bar	HAZ	0.121	0.156	0.227	0.329		
3.0bar	(mm)	0.152	0.16	0.236	0.389		
3.5bar		0.137	0.142	0.222	0.36		
4.0bar		0.119	0.154	0.238	0.329		
4.5bar		0.147	0.146	0.239	0.365		

Table 3-4.1: HAZ Thickness vs. Assist Gas Pressure

(Laser Power = 1150 Watts)

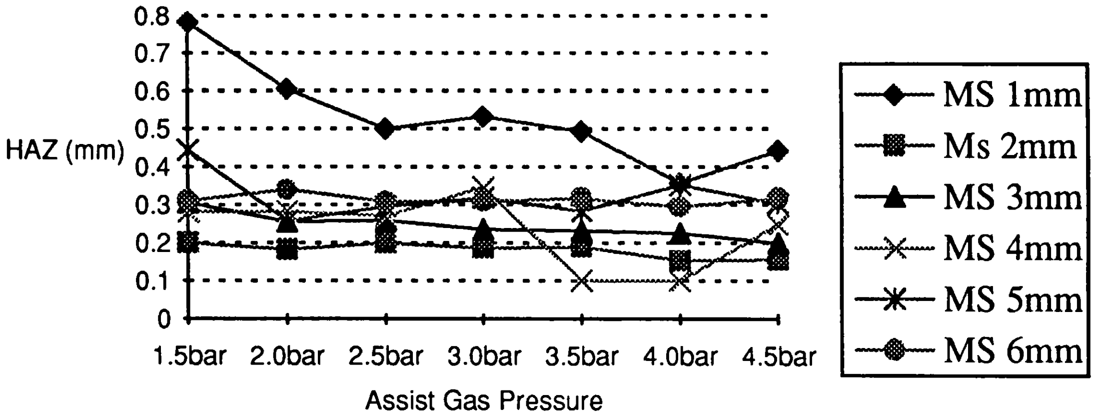

Figure 3-4.1: HAZ vs. Assist Gas Pressure (mild steel)

(Laser Power = 1150 Watts)

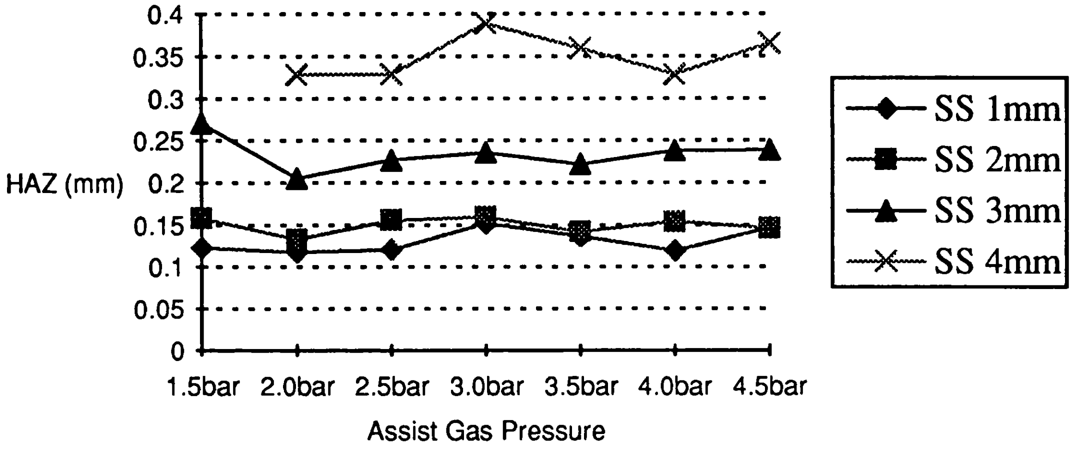

Figure 3-4.2: HAZ vs. Assist Gas Pressure (stainless steel)

(Laser Power = 1150 Watts)

Supply		Material Thickness				
Pressure		MS 2mm	MS 3mm	MS 4mm	MS 5mm	MS 6mm
1.5bar		X	6.7	X	X	11.7
2.0bar		1.52	4.8	9.5	19.3	13.7
2.5bar	Kerf	1.3	4.9	22.7	22.1	12.8
3.0bar	Surface	1.45	4.8	16.2	22.2	9
3.5bar	Roughness	1.47	3.7	21.8	26.2	10.2
4.0bar		2.13	5.7	22.4	24	9.9
4.5bar		1.52	6.4	20.1	18	11.5

Table 3-4.2: Kerf Surface Roughness vs. Assist Gas Pressure

(Laser Power = 1150 Watts)

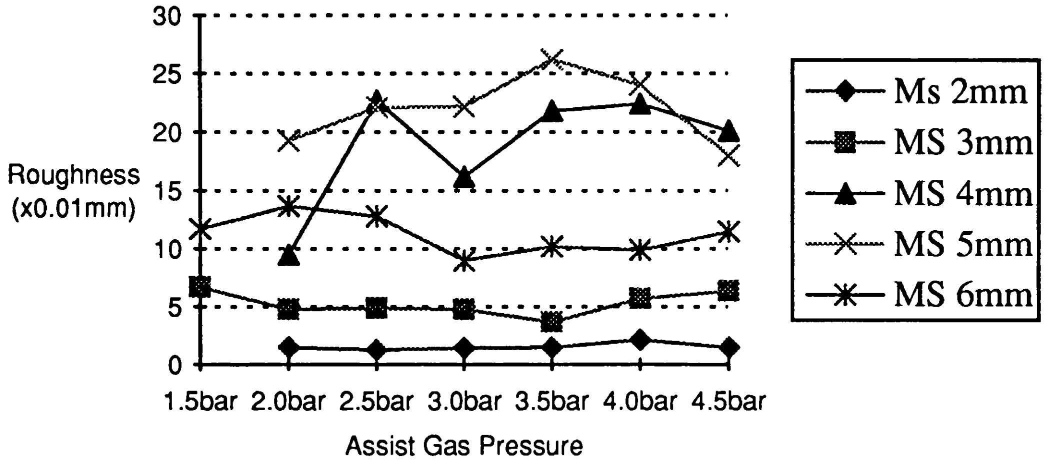

Figure 3-4.3: Kerf Surface Roughness vs. Assist Gas Pressure
(Laser Power = 1150 Watts)

3-4-4 Discussion

For mild steel, the HAZ is slightly reduced by increasing the gas pressure. This is because melt is removed more rapidly. Less melt is allowed to stay in the cutting region. Also less dross is attached to the lower surface, the cut is clean and the HAZ is small.

For stainless steel, the extent of the HAZ remains the same as the gas pressure is increased. Because the viscosity within stainless steel is much higher. The high gas pressure (up to 4.5 bar) does not have such a significant effect on the removal of the melt. Dross still remains on the lower surface even under high gas pressure. Therefore, the HAZ is the same for most of the settings.

Surface roughness remains the same, as the gas pressure is increased. Since the gas pressure difference does not play an important role in the energy balance of the cutting region. Although the melt removal rate is increased this does not affect kerf surface roughness in any significant way. Therefore, the melt removal pattern remains the same. That is, almost the same surface roughness results even when the gas pressure is increased.

An examination of nozzle gas flow conditions

Normally, gas flow velocity is increased as it flows through a convergent nozzle with sub-sonic speed. As the flow velocity reaches the local speed of sound, V_C, the flow is choked and there will be no more increase in the flow velocity no matter how much the gas supply pressure is increased. In this particular nozzle head design, it is important to check whether or not the gas flow becomes choked as the gas supply pressure is increased. When the gas flow is choked, increasing the gas supply pressure will have no effect downstream of the nozzle throat. The critical gas supply pressure P_C is calculated as follows:

The local sound speed is:

$$V_c = \sqrt{\frac{\gamma \tilde{R} T}{\tilde{m}}} \qquad (3\text{-}4.1)$$

And the critical gas supply pressure is obtained from:

$$V_c = \sqrt{\frac{P_c - P_{atm}}{\rho}} \qquad (3\text{-}4.2)$$

For oxygen at room temperature (298.15K) exiting to 1 atm environment, the critical gas supply pressure is about 3.8 bar. Experiments are also conducted by using a hot wire anemometer. The results are plot in figure 3-4.4 where it is found that the flow rate remain the same when gas supply pressure is higher than 4 bar. This confirms the theoretical calculation and shows that the gas flow is not choked until the gas supply pressure reaches 4 bar.

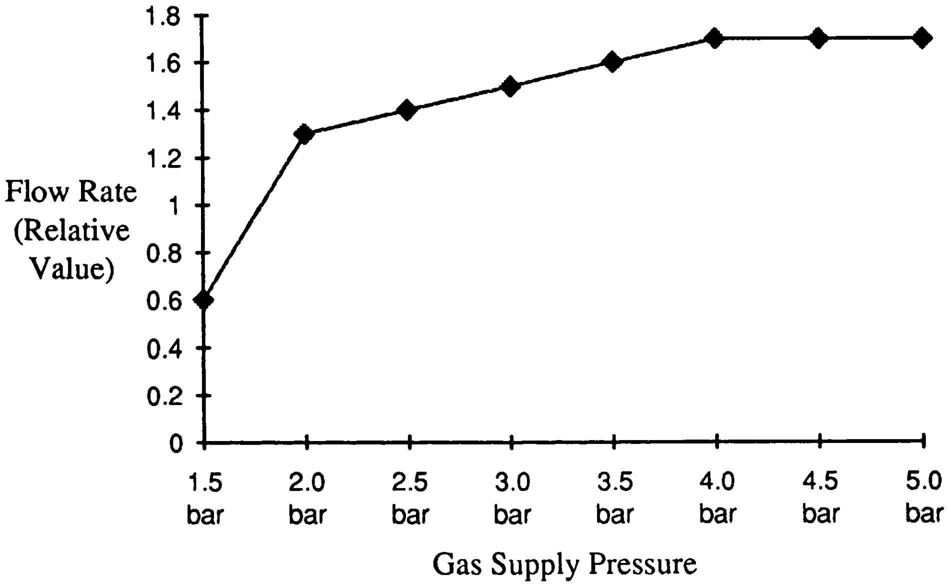

Figure 3-4.4: Flow Rate vs. Assisted Gas Supply Pressure

3-4-5 Conclusion

Assist gas pressure influences the allowable cutting feedrate. For acceptable cutting quality, a higher gas supply pressure enables a faster cutting rate. As long as cutting is possible, differences in gas pressure exerts little influence on the cutting quality, especially on the kerf surface roughness.

For the same process settings, (laser power, laser beam travelling speed, focus height offset position), a higher gas pressure gives a cleaner cut. However, the HAZ and cutting surface roughness will not be greatly improved.

3-5 References:

[1] Optics, 2nd Edition, by E. Hecht, Addison-Wesley Publishing Co., 1987

[2]Optical Electronics, 4th Edition, by A. Yariv, Saunders College Publishing, 1991

[3] Hydrodynamical instability of melt flow in laser cutting, by M. Vicanek, G. Simon, H. M. Urbassek and I. Decker, J. Phys. D: Appl. Phys. 20, 1987

[4] Linear stability analysis of molten flow in laser cutting, by M. J. Tsai and C. I. Weng, J. Phys. D: Appl. Phys. 26, 1993

CHAPTER 4

Experiments, Results and Discussions - 2 Kerf Surface Striation Analysis

Nomenclature

c = specific heat

E_L = absorbed laser energy

E_R = reaction energy

h = melton layer thickness

h_{fv} = latent heat of the melt liquid

k = thermal conductivity

μ = dynamic viscosity

n = interface area

p = pressure in the molten region

P_g = pressure within the gas stream

ρ = density of the melt

R_f = radius of curvature of the interface

s = surface tension coefficient of the molten layer

t = time

T = temperature

τ = shear stress tensor acting interface by the molten layer

u = molten flow velocity in the x direction

v = molten flow velocity in the y direction

V = surface velocity

4-1 Introduction

In most laser cutting, an almost periodic structure is observed on the kerf side wall surfaces. Plate 4.1 illustrates a typical kerf surface pattern. Two distinct layers with different striation frequencies (the **bi-level** layer) exist on the surface. Generally, the upper layer of the bi-level exhibits a high striation frequency and a lower striation frequency was found on the lower layer. These two layers are separated by a nearly straight line during the whole cut. The striations, on the kerf surfaces, are believed to be due to unsteady motion of the melt whilst being removed from the kerf.

Arata et al [1] first described striation phenomena by investigating laser cutting of acrylic glass. Based on Arata's experimental result, Schuocker [2][3] proposed a thin film flow model to explain and predict the striation occurring in reactive gas assisted laser cutting. He pointed out that the erosion takes place on a nearly vertical plane at the cut front. The cut front is covered by a thin molten layer, that is heated by absorbing laser radiation and by the exothermic reaction (oxidation/burning). The removal of material from this layer is partially by evaporation but mainly by ejection of molten material due to the shear stresses set up between the melt and the reactive gas jet flow. The liquid layer formed at the cut front of the kerf can exhibit periodic oscillations of its width and temperature, either by resonance with fluctuations of the laser power[+] or reactive gas flow or the unstable nature of the molten layer.

[+] *Radiation reflected from the workpiece can couple back into the optical resonator and cause fluctuations in the laser power*

Following Schuocker's proposal, Vicanek et al [4] refined the former model and concentrated on investigating the dynamic behaviour of the molten layer based on film flow stability. By considering the stability of the molten layer flow, he was able to predict the thickness of the molten layer and the striation frequency with respect to the cutting speed and material characteristics.

Further improvements in the model by considering the balance of momentum and energy and the effect of phase change at the interfacial boundary are presented by Tsai et al [5]. He includes further non-linear kinematic equations for the molten film thickness for a more complete analysis of the molten layer.

Striations in the laser cut surface are undesirable as they reduce surface quality. However, as they are almost implicit to laser cutting, understanding their origin and development is important so that they can be controlled.

In addition to purely theoretical research, experimental data can be collected and analysed; empirical relationships between the laser operational parameters (such as feedrate, assist gas pressure, and focal point offset position) and the striation characteristics are established and provide another level of understanding.

4-2 Theoretical Analysis

4-2.1 Film flow stability analysis

From the model proposed by Schuocker [2][3], Vicanek [4] and Tsai [5], the non-linear dynamic phenomena in reactive gas assisted laser cutting are analysed numerically, with flow stability analysis techniques applied to the thin molten layer generated on the cut front surface.

Figure 4-2.1 illustrates a simplified geometry of the transient cut surface.

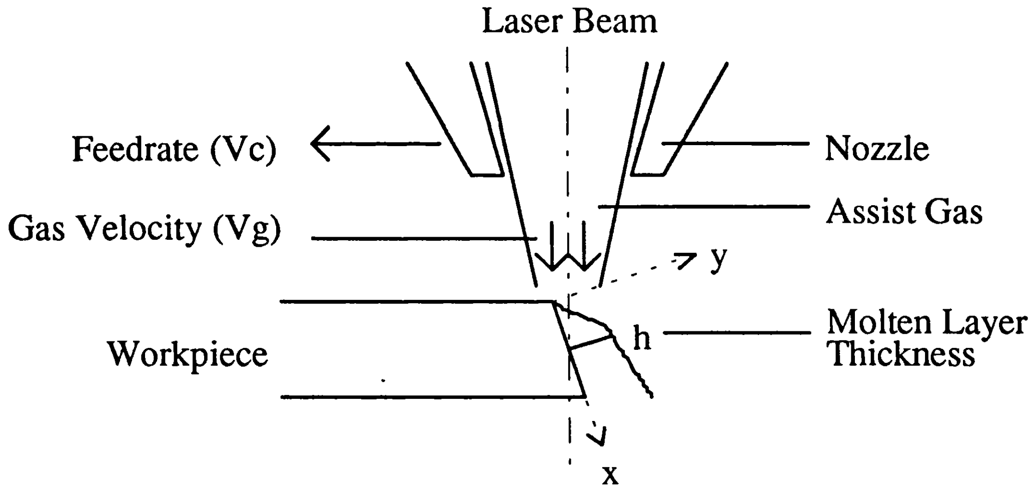

Figure 4-2.1: Simplified Geometry of The Transient Cut Surface

Following the analysis by Tsai [5], the equations that govern the thin film flow system are:

(i) boundary layer equations:

$$\frac{\partial u}{\partial x}+\frac{\partial v}{\partial y}=0 \tag{4-2.1}$$

$$\rho\left(\frac{\partial u}{\partial t}+u\frac{\partial u}{\partial x}+v\frac{\partial u}{\partial y}\right)=-\frac{\partial p}{\partial x}+\mu\left(\frac{\partial^2 u}{\partial x^2}+\frac{\partial^2 u}{\partial y^2}\right)+\rho\ g(1-\gamma) \tag{4-2.2}$$

$$\rho\left(\frac{\partial v}{\partial t}+u\frac{\partial v}{\partial x}+v\frac{\partial v}{\partial y}\right)=-\frac{\partial p}{\partial y}+\mu\left(\frac{\partial^2 v}{\partial x^2}+\frac{\partial^2 v}{\partial y^2}\right) \tag{4-2.3}$$

$$\rho\ c\left(\frac{\partial T}{\partial t}+u\frac{\partial T}{\partial x}+v\frac{\partial T}{\partial y}\right)=k\left(\frac{\partial^2 T}{\partial x^2}+\frac{\partial^2 T}{\partial y^2}\right) \tag{4-2.4}$$

where:

c = the specific heat

k = the thermal conductivity

μ = the dynamic viscosity

p = the pressure in the molten region

ρ = the density of the melt

t = the time

T = the temperature

u and v = the molten flow velocities in the x and y directions.

(ii) kinematic condition at the interface:

$$\frac{\partial h}{\partial t}+U\frac{\partial h}{\partial x}=V \tag{4-2.5}$$

where:

h is the molten layer thickness to be determined

V represents the surface velocity

(iii) mass conservation:

$$\dot{m}v + \dot{m}_v v_v + \left(p - p_g\right)n - \left(\overset{\leftrightarrow}{\tau}n - \tau_g v\right) + \frac{s}{R_f}n = 0 \qquad (4\text{-}2.6)$$

where:

R_f = the radius of curvature of the interface

p_g = the pressure within the gas stream

s = the surface tension coefficient of the molten layer

τ = the shear stress tensor acting interface by the molten liquid

(iv) energy conservation:

$$E_L + E_R = -k\left(\frac{\partial T}{\partial x} + \frac{\partial T}{\partial y}\right) \cdot n + \dot{m}h_{fv} \qquad (4\text{-}2.7)$$

where:

E_L = the absorbed laser energy

E_R = the reaction energy

h_{fv} = the latent heat of the melt liquid

n = the interface area

Through the stability analysis detailed in [5], the thickness of the molten layer as a function of cutting speed v_C, gas stream velocity v_g, workpiece thickness d and material characteristics can be obtained from the followed two equations:

$$S_1(\bar{h}) + S_2(\bar{h})\bar{h}_x = 0 \tag{4-2.8}$$

$$\dot{m} h_{fv} = \varepsilon_v \frac{133.3}{(2\pi k_b T_s m_s)^{1/2}} 10^B T_s^C 10^{A/T_s} \tag{4-2.9}$$

where:

$$S_1(\bar{h}) = \frac{k}{\rho c} Ku\left(\frac{Ku}{3} - 1\right) / \bar{h} + \left(1 - \frac{Ku}{3}\right) \times \frac{(E_L + E_R)}{\rho h_{fv}} - v_c\left(1 + \frac{Ku}{6}\right)$$

$$\begin{aligned} S_2(\bar{h}) = {} & \frac{5\rho g(1-\gamma)c(E_L + E_R)}{6\mu \Pr k h_{fv}} \bar{h}^3 - \frac{4\rho^2 g(1-\gamma)v_c}{3\mu^2} \bar{h}^3 + \frac{\rho g(1-\gamma)}{\mu} \\ & \times \left(1 - \frac{7Ku}{120} - \frac{5Ku}{8\Pr}\right)\bar{h}^2 - \left(\frac{\rho v_c \tau_g}{\mu^2} + \frac{p_{gx}}{\mu}\right)\bar{h}^2 \\ & + \frac{\tau_g}{\mu}\left(1 - \frac{Ku}{12}\right)\bar{h} \end{aligned}$$

Theoretical predictions of striation frequency as a function of feedrate are illustrated in figure 4-2.2.

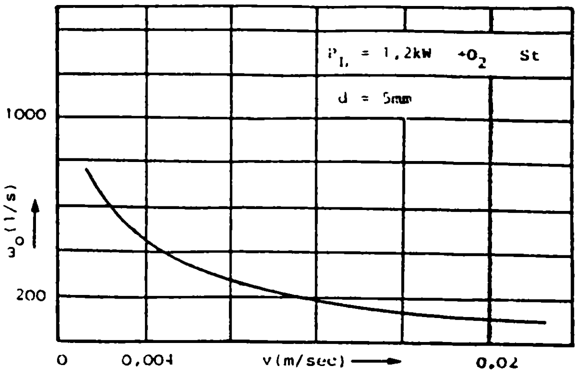

Figure 4-2.2: Striation Frequency as a Function of Feedrate (Theoretical Prediction)

4-3 Experiment Set-Up

A coaxial type nozzle head was adopted for the cutting process. Figure 4-3.1 illustrates the experimental system set-up. The laser beam is focused onto the workpiece through a convex-planar lens with diameter D and focal length f. The focal point of the lens is positioned 0.6mm beneath the nozzle outlet. Focal height offset position was adjusted by moving the nozzle head up and down. Oxygen assist gas was supplied through the gas inlet on the top-side of the nozzle head. The gas pressure was adjusted by means of a supply valve. Laser beam feedrate was controlled by moving the nozzle head relative to the workpiece via a CNC controller. Specimens are then measured by using a contouring machine with a 10x lens.

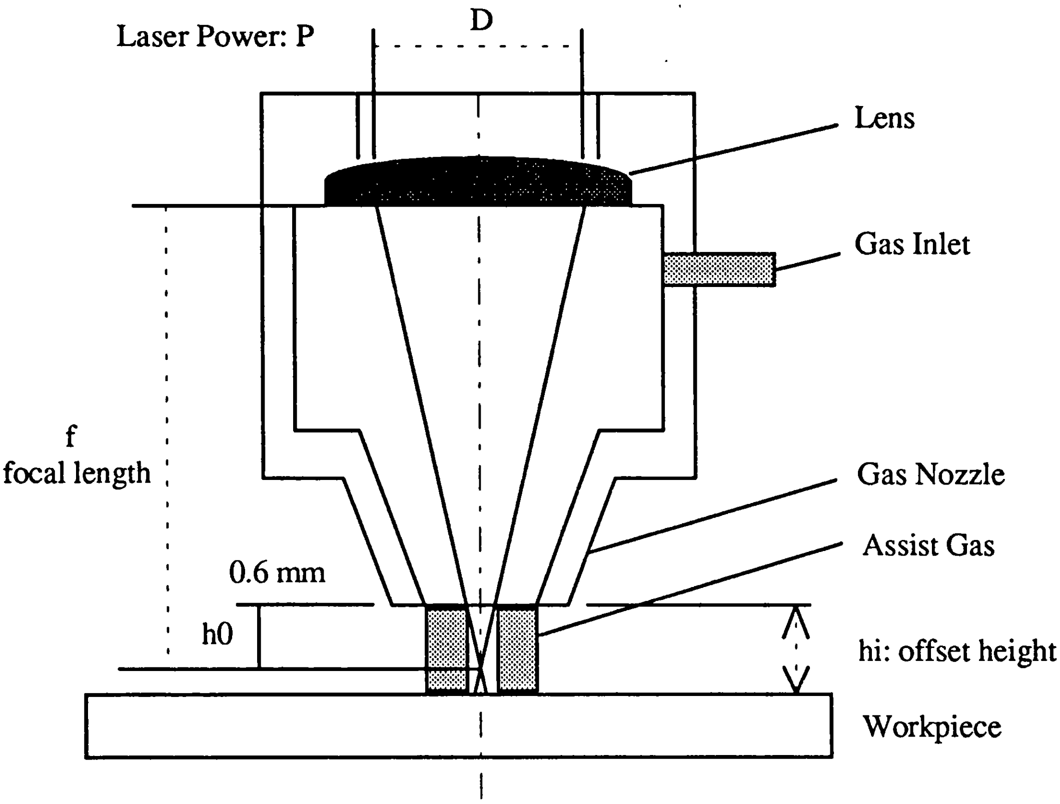

Figure 4-3.1: Coaxial Type Nozzle Set-up

4-4 Results and Discussion

Frequency for the surface striation is presented in **cycles/cm**. Feedrates used for different thicknesses of mild steel were set according to the following equation:

$$Vi = Vgoodcut\,[1 - i*(10\%)] \quad \text{Where } i = 1 \text{ to } 6 \qquad (4\text{-}4.1)$$

The feedrates used are listed in table 4-4.1:

Material Thickness		Vgoodcut	V1	V2	V3	V4	V5	V6
MS 5 mm	Feedrate	1200	1080	960	840	720	600	480
MS 6 mm	(mm/min)	950	860	760	670	570	480	380

Table 4-4.1: Feedrates For Different Cutting Conditions And Material Thicknesses

4-4.1 Striation Frequency vs. Feedrate

Results of cut surface striation frequency with respect to different feedrate are summarized in Table 4-4.2.

		Feedrate Setting						
		Vgoodcut	V1	V2	V3	V4	V5	V6
5mm exper.	Striation	29.11	28.64	34.29	29.88	28.86	27.22	28.02
5mm theory	Frequency	105	125	137	165	190	232	280
6mm exper.		30.5	37.74	38.51	41.72	42.25	36.28	37.02

Table 4-4.2: Striation Frequency vs. Feedrate (mild steel)

(Laser Power = 1150 Watts)

Graphical representation is shown in Figure 4-4.1.

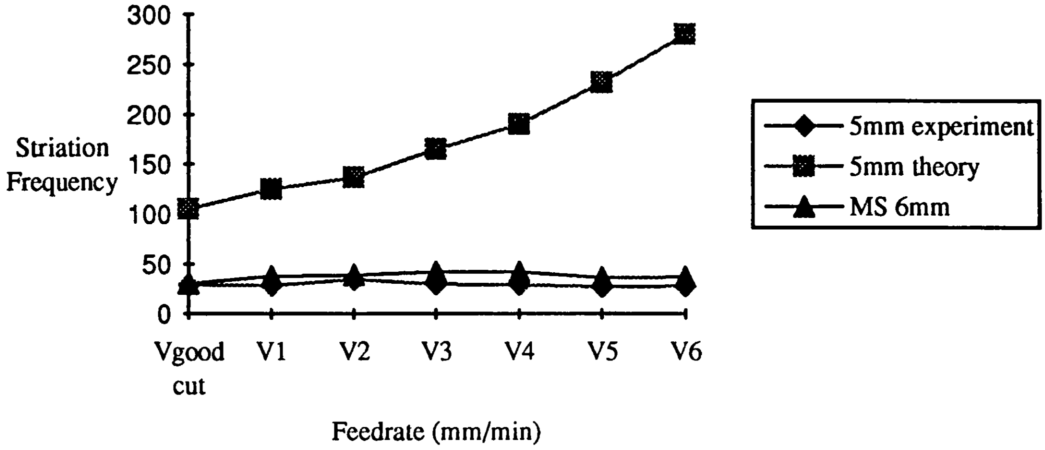

Figure 4-4.1: Striation Frequency vs. Feedrate

(Laser Power = 1150 Watts)

Plate 4.2 and plate 4.3 show the resulting kerf surface.

4-4.2 Striation Frequency vs. Assist Gas Pressure

Results of cut surface striation frequency with respect to different assist gas pressure are summarized in Table 4-4.3.

Material Thickness		Assist Gas Supply Pressure 1.5 bar	2.0 bar	2.5 bar	3.0 bar	3.5 bar	4.0 bar	4.5 bar
5mm	Striation	24.72	29.11	26.43	27.01	30.03	29.71	31.34
6mm	Frequency	38.04	30.5	39.73	43.86	42.63	53.3	34.26

Table 4-4.3: Striation Frequency vs. Assist Gas Pressure (mild steel)

(Laser Power = 1150 Watts)

The graphical representation is shown in Figure 4-4.2.

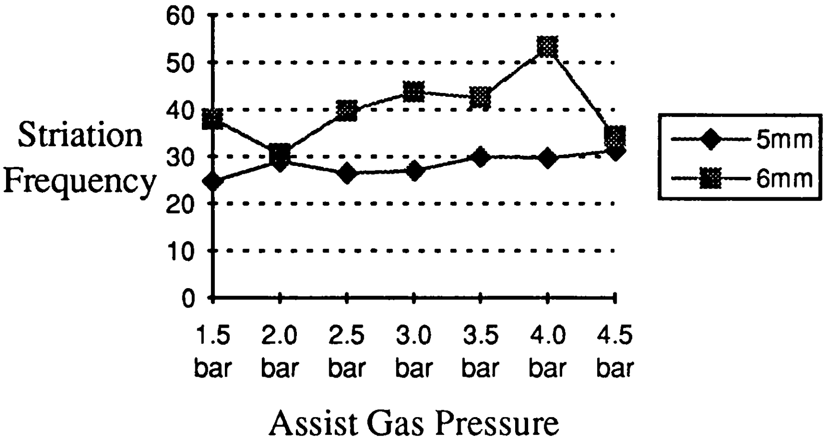

Figure 4-4.2: Striation Frequency vs. Assist Gas Pressure (mild steel)

(Laser Power = 1150 Watts)

From the results it can be seen that the cutting surface striation frequency increases as the assist gas pressure increases. Plate 4.4 and plate 4.5 show the resulting kerf surface.

4-4.3 Striation Frequency vs. Focal Height Offset Distance

Results of cut surface striation frequency with respect to different focal height offset distances are summarized in Table 4-4.4.

Material		Focal Point Off-set					
Thickness		Surface	H1	H2	H3	H4	H5
5mm	Striation	29.11	22.52	18.1	10.06	10.58	12
6mm	Frequency	30.5	31.9	25.8	24.72	X	X

Table 4-4.4: Striation Frequency vs. Focal Point Offset (mild steel)

(Laser Power = 1150 Watts)

The Graphical representation is shown in Figure 4-4.3.

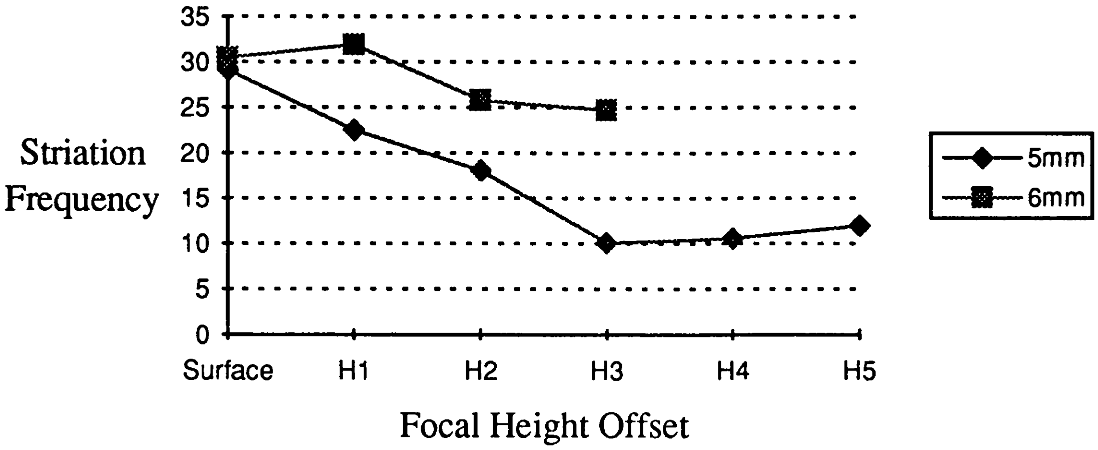

Figure 4-4.3: Striation Frequency vs. Focal Point Offset (mild steel) (Laser Power = 1150 Watts)

Plate 4.6 shows the resulting kerf surface. It is clear that the striation frequency decreases as the focus point is adjusted to a higher position. That means lower power density per area (watt/cm^2) and larger beam spot size.

The results of an investigation into the combined effect of focal height offset position and gas pressure on 4mm mild steel are summarized in table 4-4.5.

Supply Pressure		Focal Height Offset Distance								
		0.6 mm	1.1 mm	1.6 mm	2.1 mm	2.6 mm	3.1 mm	3.6 mm	4.1 mm	4.6 mm
2 bar	Striation Frequency	27.06	22.31	19.74	18.85	16.05	14.02	14.66	14.39	X
3 bar		27.72	23.35	20.08	20.06	16.74	13.64	12.76	13.35	14.11
4 bar		29.73	25.42	20.03	20.12	15.31	15.43	14.55	13.67	13.4

Table 4-4.5: Striation Frequency vs. Focal Height Offset/Gas Pressure (Laser Power = 1150 Watts)

The graphical representation in shown in Figure 4-4.4.

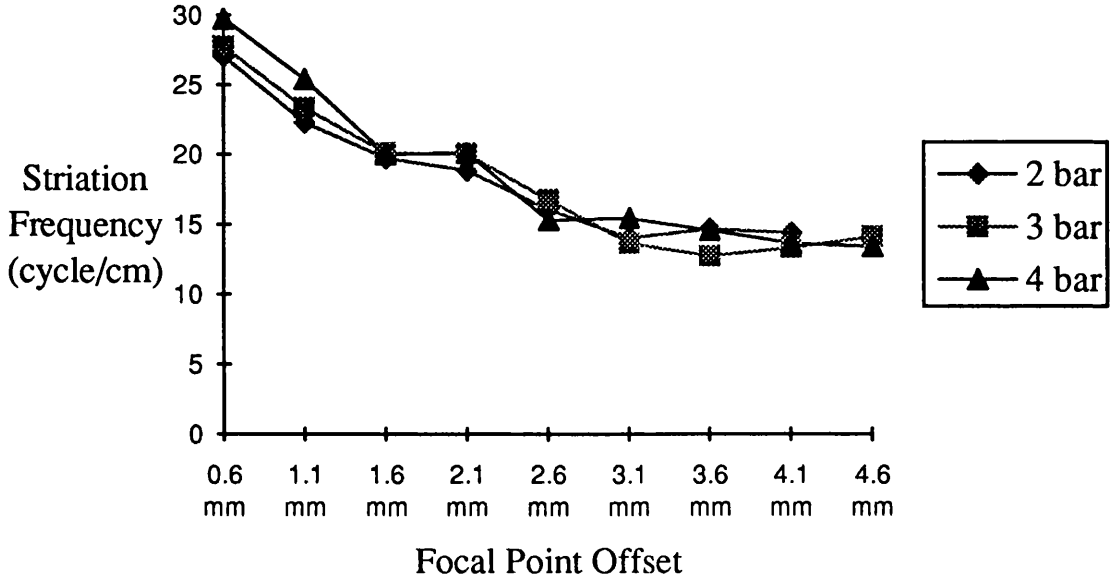

Figure 4-4.4: Striation Frequency vs. Focal Point Offset/Gas Pressure

(Laser Power = 1150 Watts)

From figure 4-4.4 it can be observed that although an increase in assist gas pressure increases the kerf surface striation frequency. The focal height offset position plays a major role in influencing the kerf surface striation frequency. There appears to be a fixed relationship between the focal height offset position and the striation frequency even when the assist gas pressure is changed.

This can be explained, as when the focus height offset position is increased, the laser beam spot size becomes larger. The volume of material to be melted and removed increases as the kerf width becomes larger. Furthermore, the power density decreases as the beam diameter increases. Also the gas flow velocity reduces as the kerf width increases. These combined effects result in a coarser kerf surface and lower striation frequency. The increase of gas flow velocity inside the kerf through increased assist gas pressure does not compensate the effect induced by the increased beam spot size.

4-4.4 Striation Frequency vs. Material Thickness

Kerf surface striation frequency with respect to different material thicknesses are summarized in Table 4-4.6.

	Material Thickness				
	3 mm	4 mm	5 mm	6 mm	8 mm
Striation Frequency	18.55	19.64	20.1	28.79	34.11

Table 4-4.6: Striation Frequency for Different Thicknesses of Mild Steel (Laser Power = 1150 Watts)

The graphical representation is shown in Figure 4-4.5.

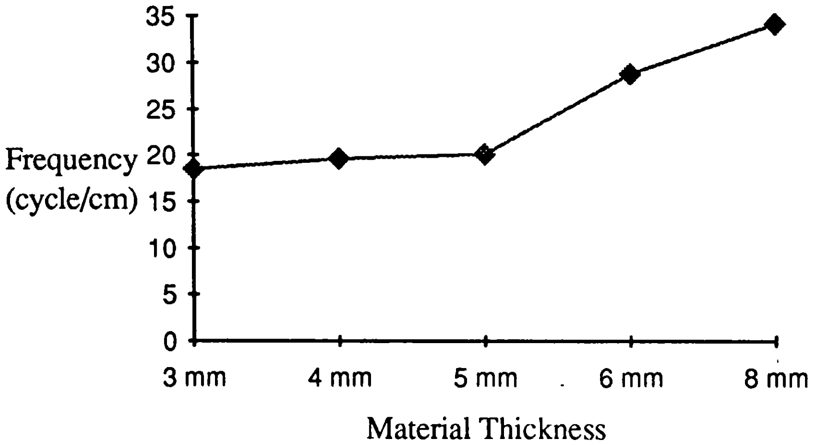

Figure 4-4.5: Striation Frequency vs. Mild Steel Thickness (Laser Power = 1150 Watts)

The experimental result show that in general, the striation frequency increases as the material thickness becomes larger.

4-4.5 Striation Bi-Level Pattern Depth vs. Material Thickness

Results of the kerf surface striation depth distribution with respect to different material thicknesses are summarized in Table 4-4.7.

	Material Thickness					
	2 mm	3 mm	4 mm	5 mm	6 mm	8 mm
Depth(mm)	0.465	0.735	0.922	0.879	1.006	0.911
Depth(%)	23.25	24.5	23.05	17.58	16.77	11.39

Table 4-4.7: Striation Bi-Level Pattern Depth vs. Mild Steel Thickness (Laser Power = 1150 Watts)

These results are plotted in figure 4-4.6(a) and figure 4-4.6(b).

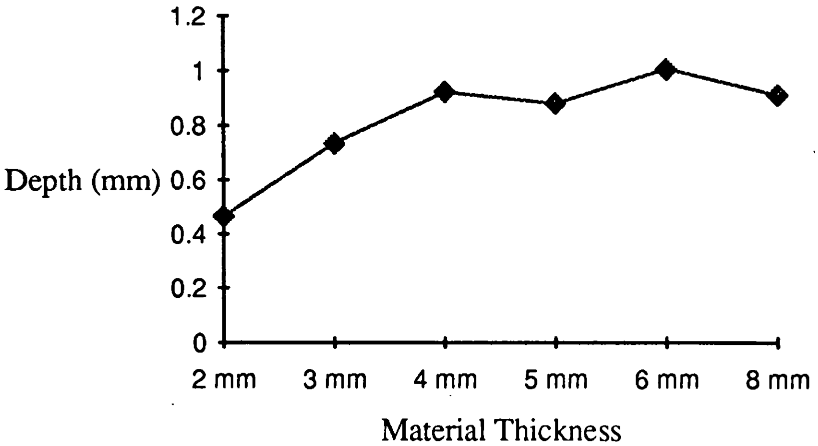

Figure 4-4.6(a): Striation Bi-Level Pattern Depth vs. Mild Steel Thickness (In mm)(Laser Power = 1150 Watts)

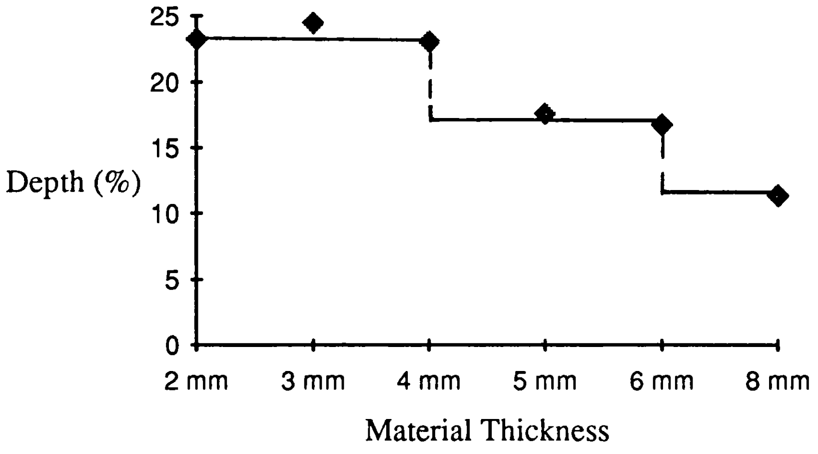

Figure 4-4.6(b): Striation Bi-Level Pattern Depth vs. Thickness
(As a % of the Material Thickness)
(Laser Power = 1150 Watts)

From the above data, especially from figure 4-4.6(b), the resulting bi-level depth changes in a non-linear step-wise manner. As the material thickness increases, for a number of material thicknesses the bi-level depth remains at nearly the same level; when the thickness reaches a certain value, the bi-level depth jumps to another level and then stays approximately constant until the material thickness reaches another critical value. Plate 4.7 shows the resulting kerf surface.

4-5 Conclusion

Two distinct striation layers were found in most of the kerf surfaces for material above certain thickness (about 2mm for mild steel). A higher frequency and rougher-surface striation is found in the upper part of the bi-level striation pattern where the effects of the laser beam dominate those of fluid dynamics. A lower frequency and smoother-surface striation is found in the lower part of the bi-level striation pattern where the melt is blown and ejected by the assist gas. A very smooth surface is observed on the kerf of thin material where the kerf striation patterns almost disappear.

Higher frequency striations occurred when the assist gas jet pressure was increased and the focal height offset was reduced. The depth of the bi-level striation pattern implies that the system jumps from one stable state to another for different thicknesses of mild steel, this non-linear behaviour cannot be described by a continuous function.

4-6 References

[1] Dynamic behaviour in laser gas cutting of mild steel, by Arata Y, Maruo H, Miyamoto I and Takeuchi S, 1979, Trans. JWRI 8 14-26

[2] Reactive gas assisted laser cutting - physical mechanism and technical limitations, by Schuocker D., 1983, Proc. of SPIE, Vol 398

[3] Dynamic phenomena in laser cutting and cut quality, by Schuocker D., 1986, Applied physics B 40, pp9-14

[4] Hydrodynamical instability of melt flow in laser cutting, by Vicanek M, Simon G, Urbassek M H, and Decker I 1987, J. Phys. D: Applied Phyics 20

[5] Linear stability analysis on molten flow in laser cutting, by Tsai M J and Weng C I, 1993, J. Phys. D: Applied physics 26

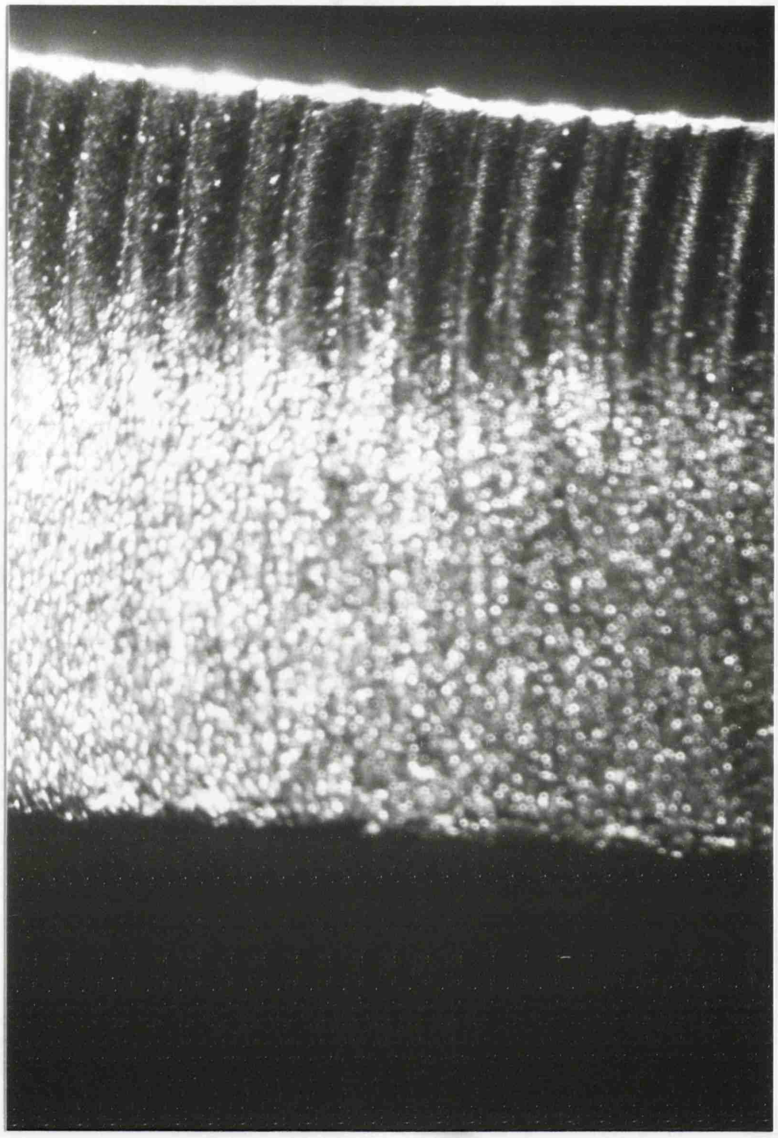

Plate 4.1: Typical Kerf Surface Pattern

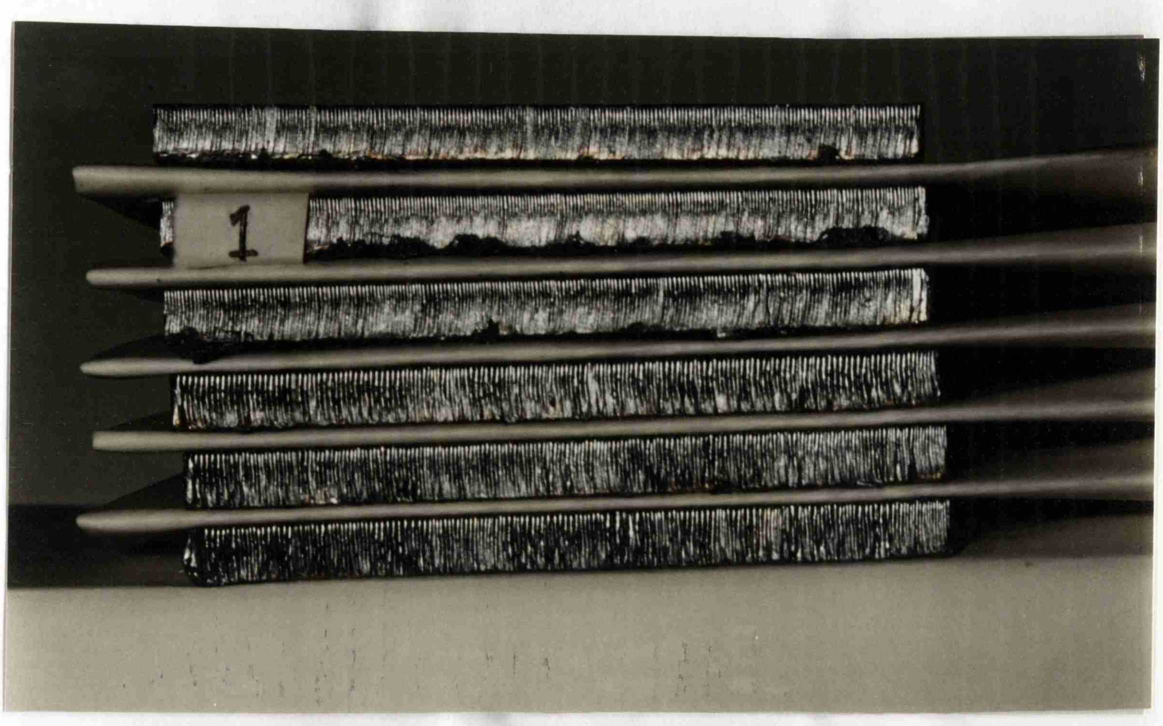

Plate 4.2: Striation Pattern vs. Feedrate (5mm mild steel)

(From Top: 1080, 960, 840, 720, 600, 480 mm/min)

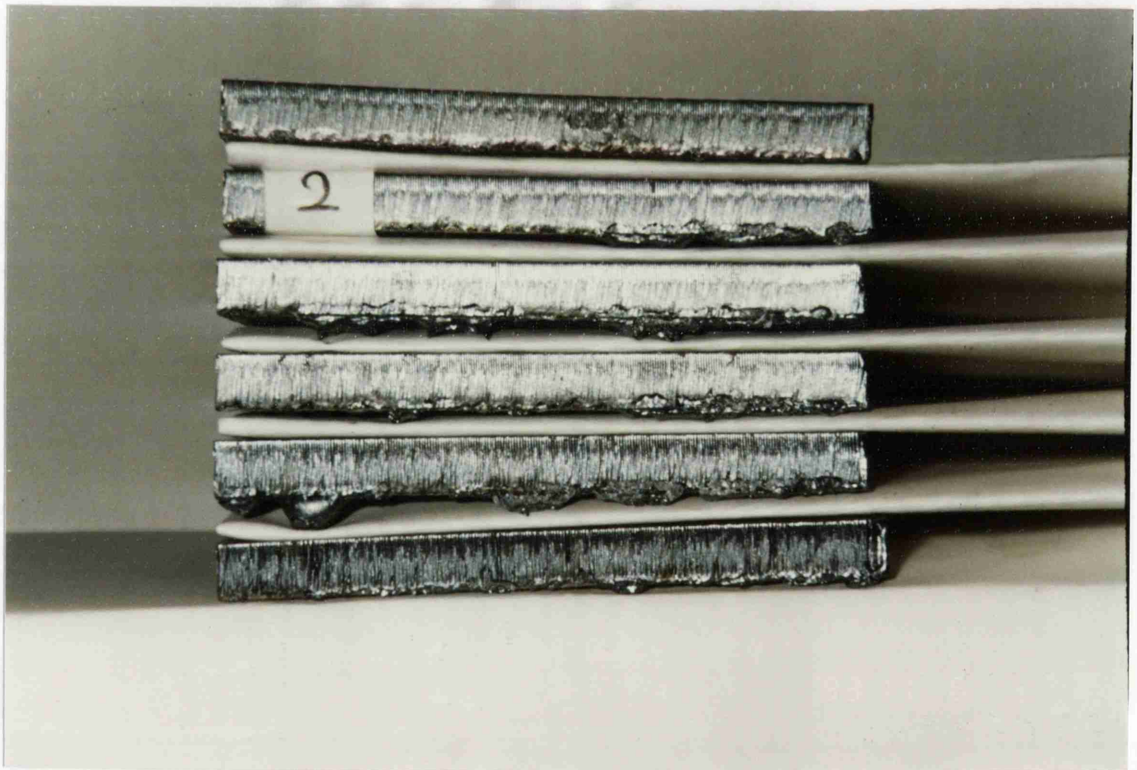

Plate 4.3: Striation Pattern vs. Feedrate (6mm mild steel)

(From Top: 860, 760, 670, 570, 480, 380 mm/min)

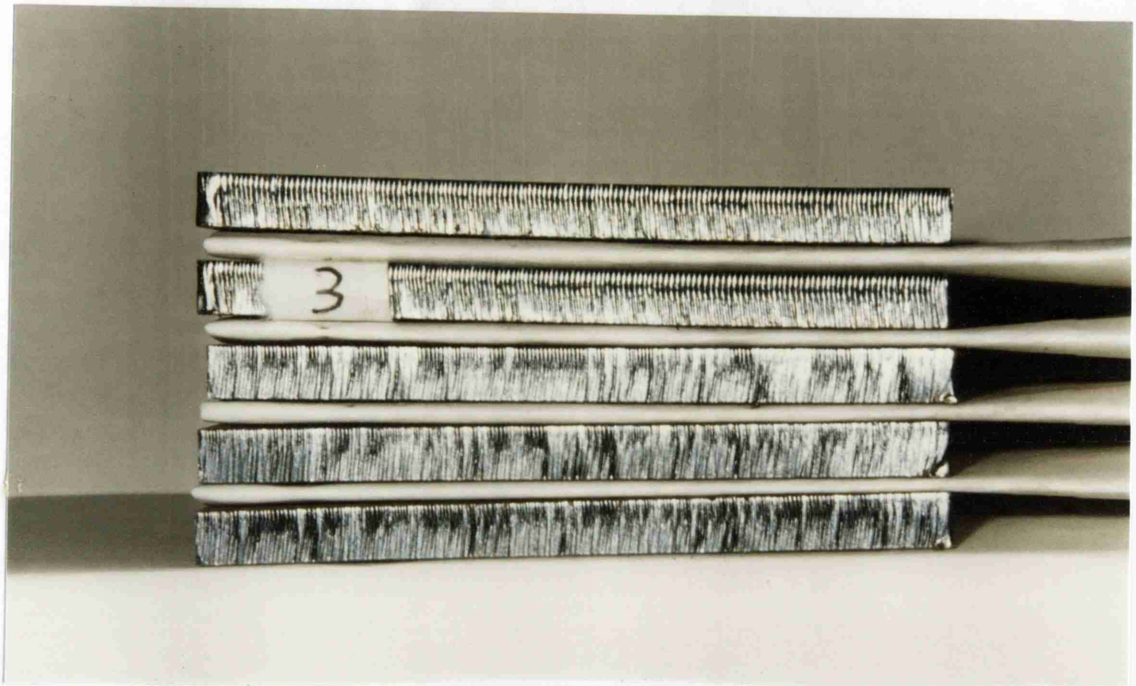

Plate 4.4: Striation Pattern vs. Assist Gas Pressure (5mm mild steel)

(From Top: 2 bar, 2.5 bar, 3.0 bar, 3.5 bar, 4.0 bar)

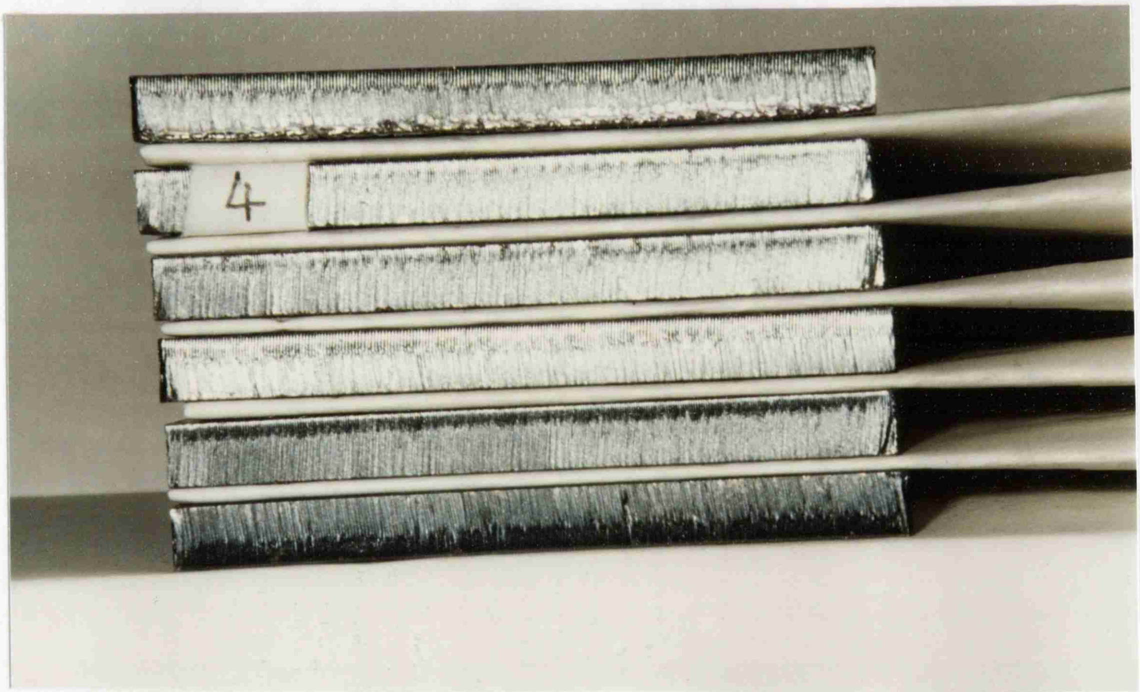

Plate 4.5: Striation Pattern vs. Assist Gas Pressure (6mm mild steel)

(From Top: 2 bar, 2.5 bar, 3.0 bar, 3.5 bar, 4.0 bar)

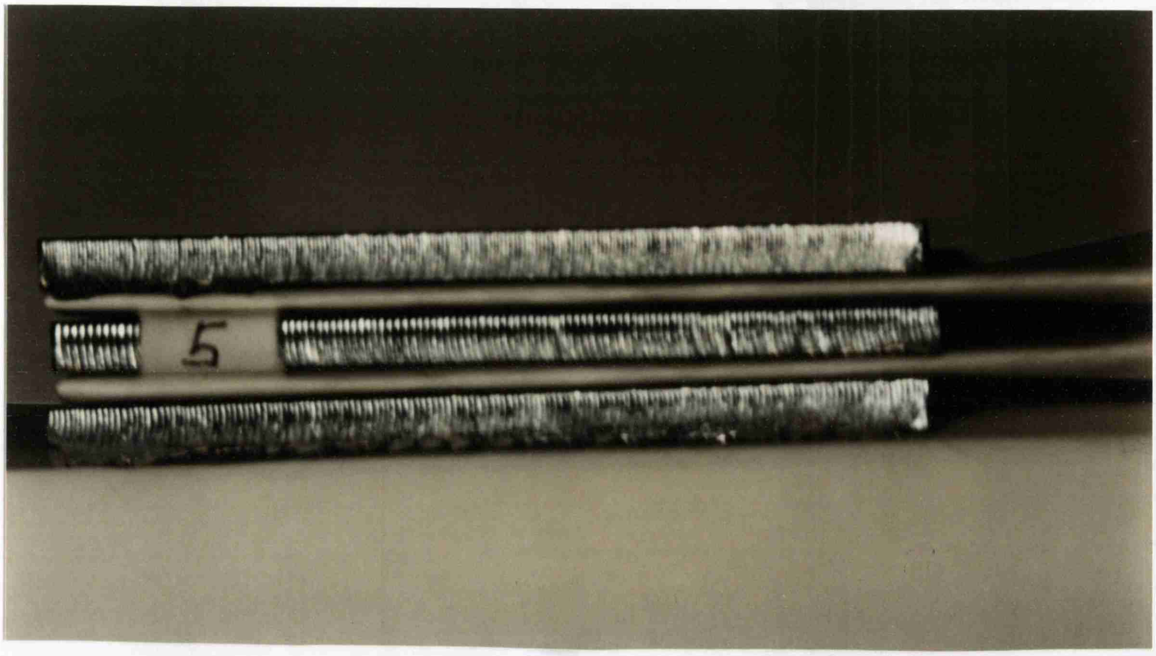

Plate 4.6: Striation Pattern vs. Focal Height Offset Distance (4mm mild steel)
(From Top: 0, 0.667, 1.333 mm above surface)

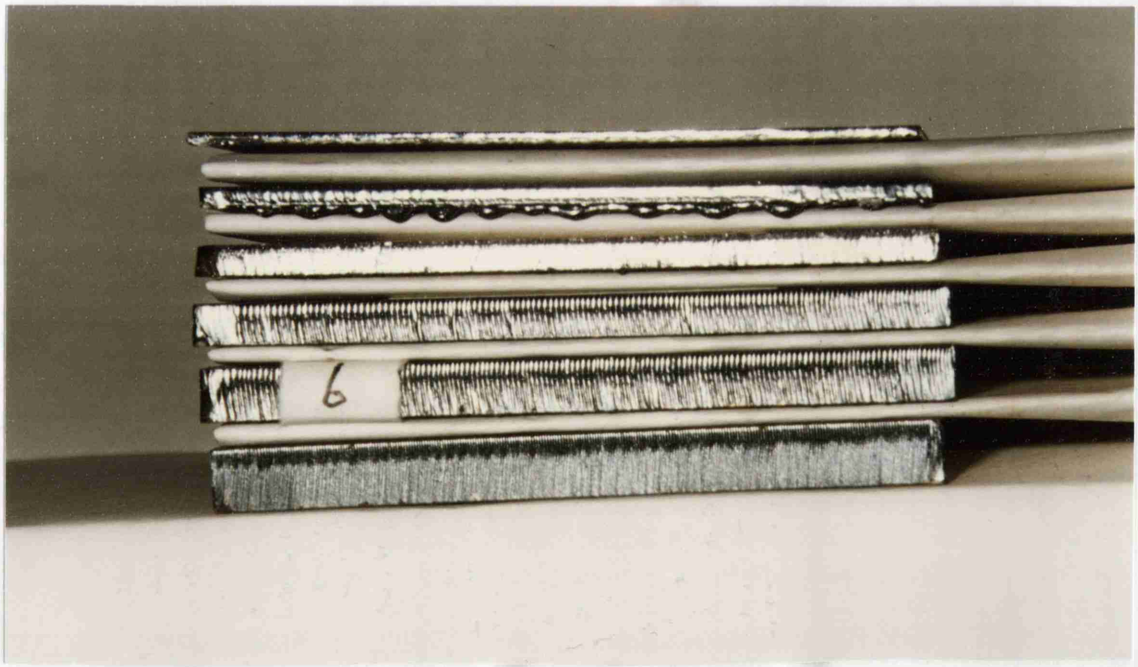

Plate 4.7: Bi-Level Depth Pattern vs. Material Thickness
(From Top: 1, 2, 3, 4, 5, 6 mm mild steel)

CHAPTER 5

Experiments, Results and Discussions - 3 Spark Cone Analysis

5-1 Spark Cone - Cutting Quality Analysis

The reactive gas oxygen (O_2) is normally used in mild steel cutting to assist the cutting process and increase the cutting speed. Figure 5-1.1 illustrates a coaxial type nozzle which is normally adopted in industrial applications.

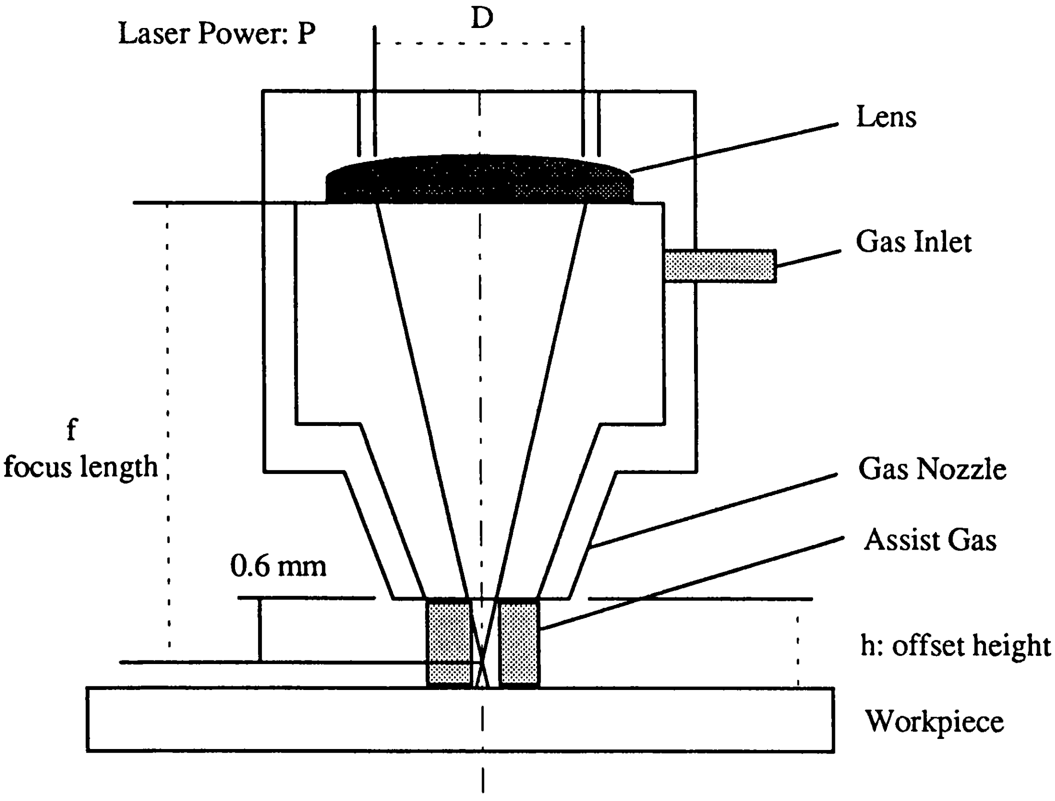

Figure 5-1.1: Coaxial Type Nozzle

The strong, reactive gas jet flows through the narrow kerf, liquid and vaporized metal phases are ejected from the kerf outlet on the lower surface due to the net frictional force between the gas stream and the melt and between the melt and the solid metal as well as the pressure gradient generated in the region.

When liquid and vapour of the processed metal are carried out through the lower kerf outlet, the reactive assist gas and the metal liquid/vapour mix expand rapidly as if they have passed through a convergent nozzle. A characteristic spark cone is thus formed which is a function of the specific kerf geometry and flow dynamics.

Upon ejection of the melt and vapour, where effective mixing with the oxygen takes place, a strong reaction between the metal and the oxygen is initiated. The high temperature results in burning of the metal particles. The burning pattern, or more commonly named - spark cone, provides an easy and effective method for a skilled technician to judge the quality of the cutting process. Image processing devices that operate in the visible part of the EM spectrum, connected to highly developed computers, facilitate effective digital spark cone analysis.

5-2 Experiment Set-Up

The schematic diagram of the system set-up is shown in figure 5-2.1.

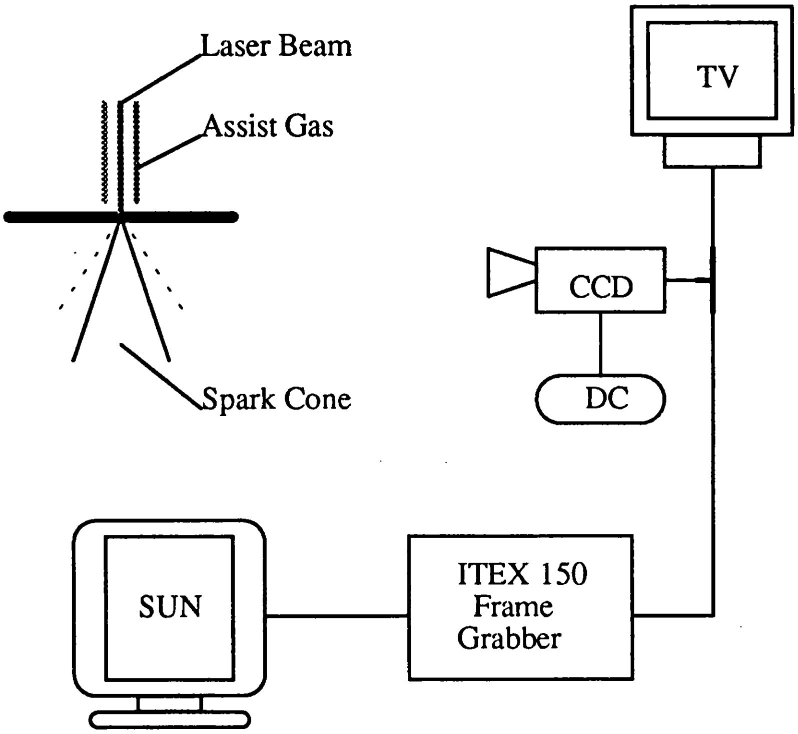

Figure 5-2.1: Spark Cone Analysis System Schematics

A CCD camera is placed 50 cm away from the cutting point along the Y-direction. The camera is positioned so that the cutting point is in the upper centre part of the image, therefore most of the spark cone image is visible in the 512x512 frame. Image signals from the CCD camera were transferred to - both the monitoring TV beside the operator, for supervising the cutting process - and the ITEX-150 frame grabber where images of the cutting spark cone were grabbed for further analysis. When the operator initiates the cutting process from the control console, sub-commands for trigging the spark cone analysis sub-system were sent to the SUN workstation through the local networking system. When the spark cone analysis sub-system activate signal is acknowledged, the cutting process is started, commands are then sent to the

ITEX-150 frame grabber to grab the spark cone images. These digital spark cone images were then transferred through the internal bus link to the frame store unit in the ITEX-150 frame grabber for temporary storage and through the external bus link to the SUN workstation for immediate image analysis and permanent storage.

Spark cone images from mild steel and stainless steel cutting, of different thicknesses, were grabbed as a 512x512 pixel array. Image analysis was performed digitally. Results were presented through SUNview/Openwin and MATLAB, where a digital print-out function is available.

5-3 Results

5-3.1 Spark Cone Pattern:

Analysis of the spark cone histogram revealed that two or three different intensity layers were distinguishable within the cutting spark cone. Plate 5-3.1 is a typical spark cone image from cutting mild steel. Figure 5-3.1 shows the histogram of this spark cone image. For convenience, the spark cones are considered to consist of two separate sub-cones, an intense concentrated inner cone, and a lighter sparse outer cone. The relative size of the inner and outer cones were found to alter as a function of the dross attachment conditions on the workpiece lower surface.

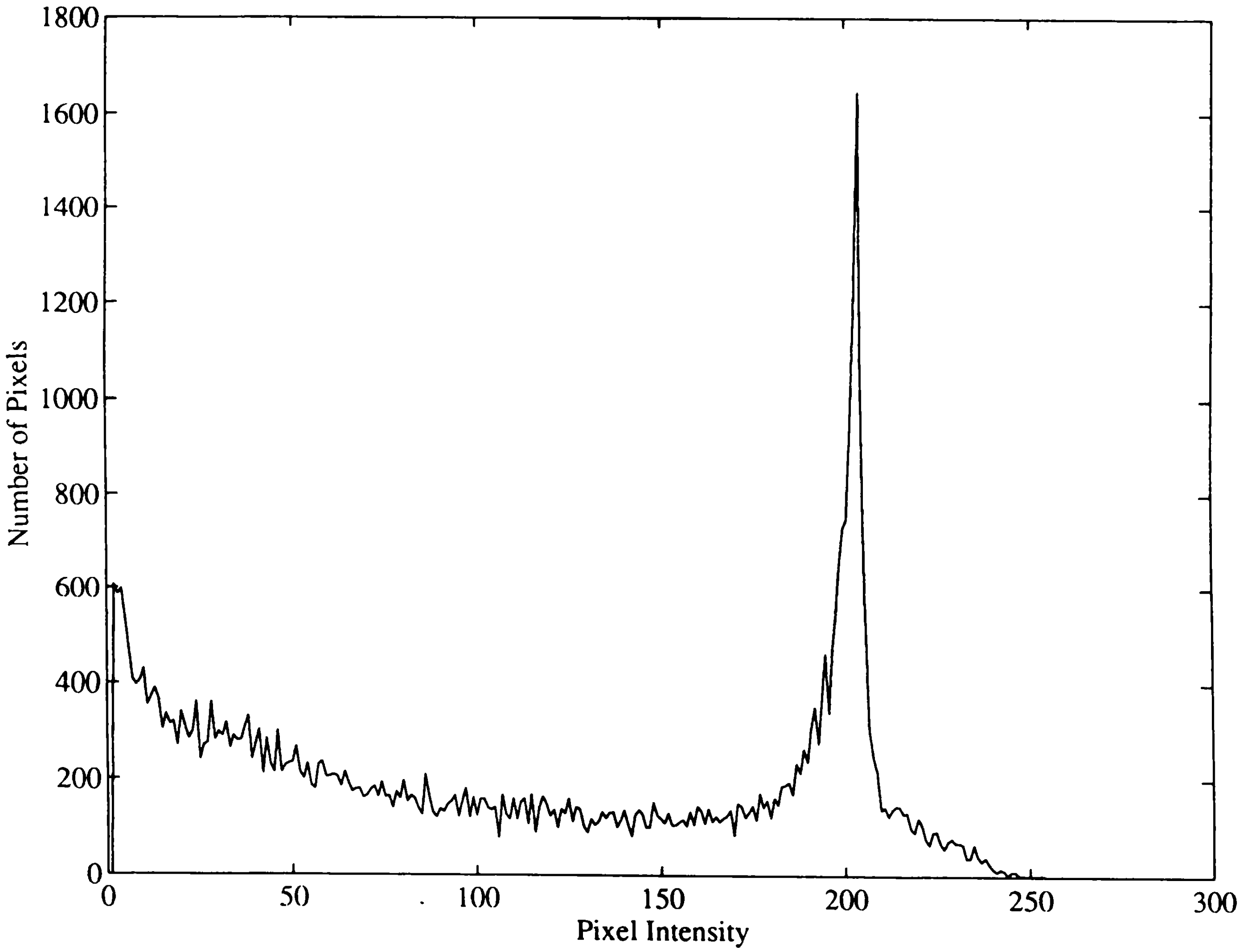

Figure 5-3.1: Histogram of The Spark Cone Image From A Typical Mild Steel Cutting Process

Plate 5-3.2 to Plate 5-3.6 are spark cone images from mild steel of different thicknesses (2mm to 6mm). These images were taken from a cutting process with good kerf quality. That means, little or no dross attachment to the lower surface (nearly dross free). The spark cones are very intense with virtually no sparse sparks in the outer layer of the cone. Figure 5-3.2 is the histogram of the 4mm result (where the value of the zero intensity has been removed). One peak is clearly observed in the diagram. Plate 5-3.7 is a spark cone image of a 4mm mild steel cutting process with some dross attachment to the lower surface. It is clear that there are some sparse sparks formed in the outer layer of the cone. Figure 5-3.3 is the histogram of this spark cone image. It can seen that there are three peaks present in the diagram.

Plate 5-3.8 to Plate 5-3.11 are spark cone images for different dross attachment conditions for a 4mm mild steel cutting process. The plate runs from plate 5-3.8, dross free, to plate 5-3.11 which exhibits severe dross attachment. The smaller the sparse spark region the cleaner the cut.

For the stainless steel cutting process, since the melted liquid is more viscous, dross is not easy to eliminate from the lower surface for most of the cutting processes. Plate 5-3.12 to Plate 5-3.15 are spark cone images of stainless steel cutting, with material thickness from 1mm to 4mm, these results gave good cutting quality. Dross was present on the lower surface for every process. Predictably, no intensive spark cone image is present, most of the results exhibited a sparse spark cone pattern. Plate 5-3.16 to plate 5-3.19 are spark cone images for different dross attachment conditions for stainless steel cutting process. The plate runs from plate 5-3.16, almost dross free, to plate

5-3.19 which exhibits sever dross attachment. The amount of intense inner spark cone increases as the cut becomes better.

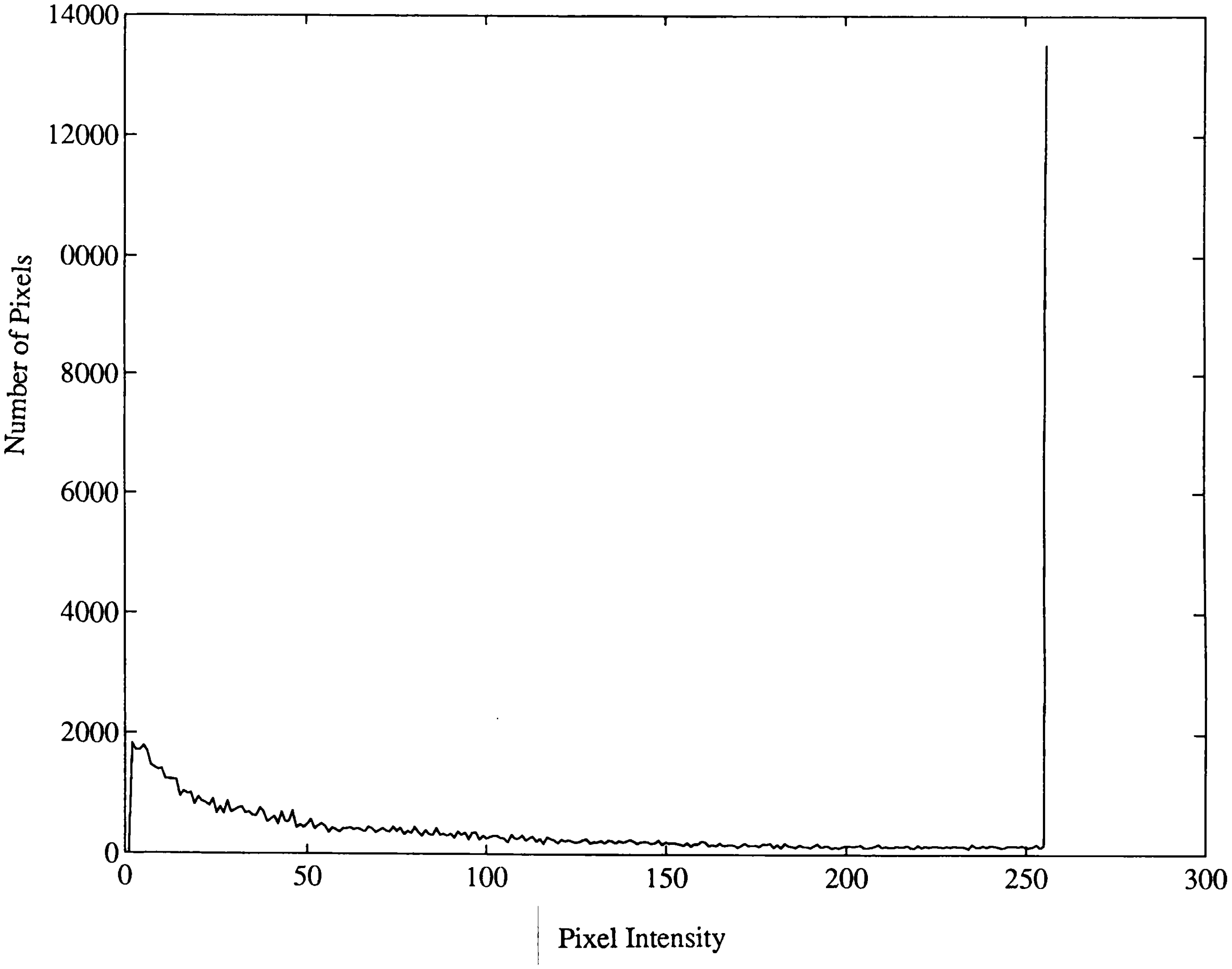

Figure 5-3.2: Histogram of The Spark Cone Image of 4 mm Mild Steel - Good Cut Process

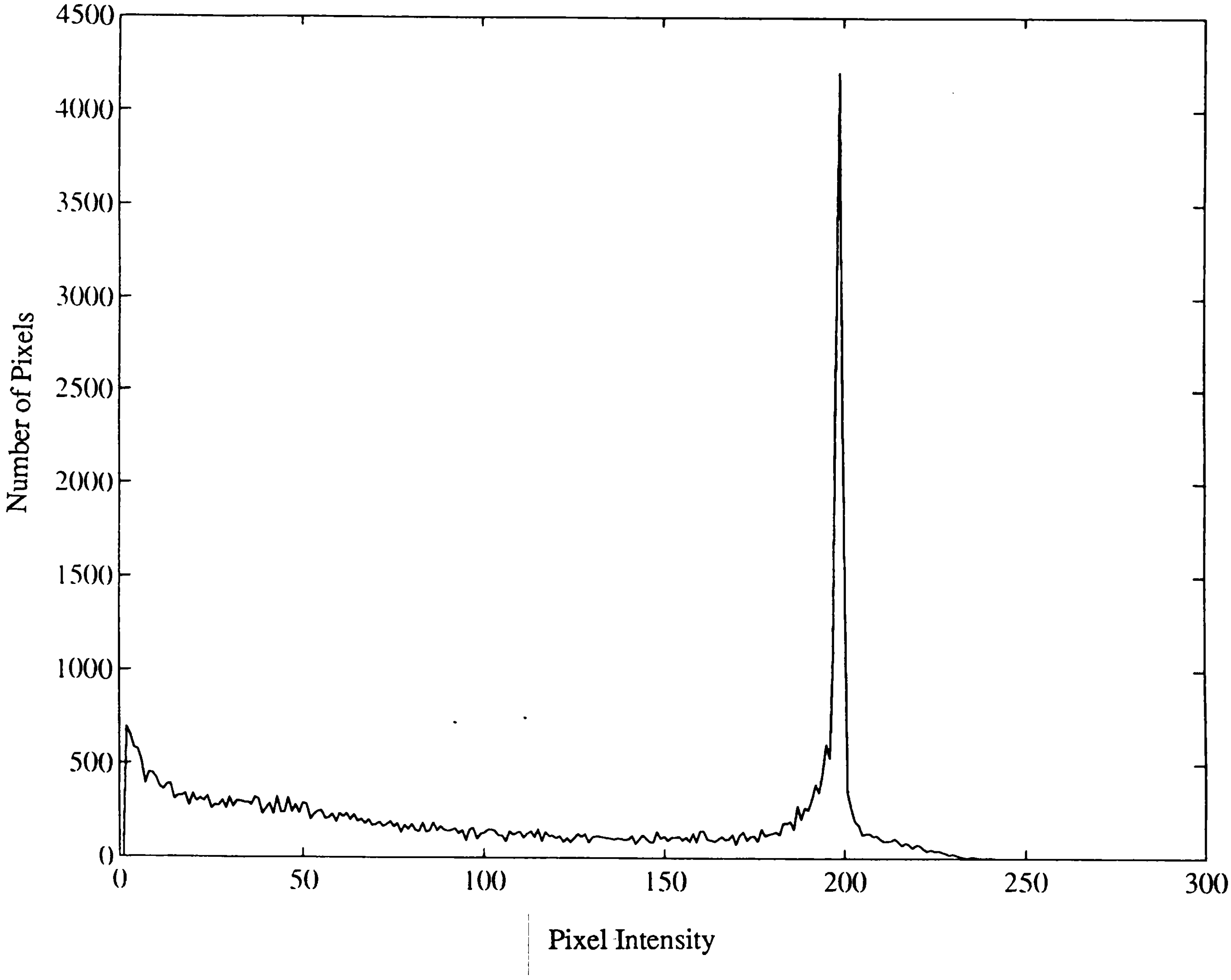

Figure 5-3.3: Histogram of The Spark Cone Image of a 4 mm Mild Steel - Poor Cut Process

5-3.2 Spark Cone Angle

In mild steel cutting, the spark cone angle is defined as the angle of the inner intensive cone, which is found in most mild steel cutting, especially good quality cutting processes. Good quality cutting of mild steel is characterised by a high irradiance intensive spark cone. The width of the kerf, roughness condition on the cut surface and the assist gas pressure affect the blow-out spark cone angle. The measured results of the spark cone angle under different process conditions are summarized in Table 5-3.1(a), 5-3.1(b), 5-3.1(c).

Supply Pressure		Material Thickness					
		1mm	2mm	3mm	4mm	5mm	6mm
1.5 bar	Spark Cone Angle (deg)	123	x	x	21	x	x
2.0bar		133	27	28	23	18	10
2.5 bar		117	28	x	24	x	14
3.0 bar		116	31	30	23	x	12
3.5 bar		104	31	29	21	20	13
4.0 bar		139	34	31	22	20	12
4.5 bar		129	31	29	23	18	11

Table 5-3.1(a) Spark Cone Angle for Mild Steel Cutting
With Different Gas Pressure (Laser Power = 1150 Watts)

Focal Point Offset		Material Thickness		
		3mm	4mm	6mm
H1	Spark Cone Angle (deg)	28	32	20
H2		18	32	30
H3		23	40	x
H4		20	114	x
H5		108	x	x
H6		116	x	x

Table 5-3.1(b) Spark Cone Angle for Mild Steel Cutting
With Different Focal Point Offset (Laser Power = 1150 Watts)

Feedrate Setting		Material Thickness		
		2mm	4mm	5mm
V1		120	50	39
V2	Spark	126	54	40
V3	Cone	130	48	40
V4	Angle	130	60	42
V5	(deg)	110	58	42
V6		90	65	x

Table 5-3.1(c) Spark Cone Angle for Mild Steel Cutting
With Different Feedrate (Laser Power = 1150 Watts)

Figure 5-3.4(a), 5-3.4(b), 5-3.4(c) are the graphic representations of the above results.

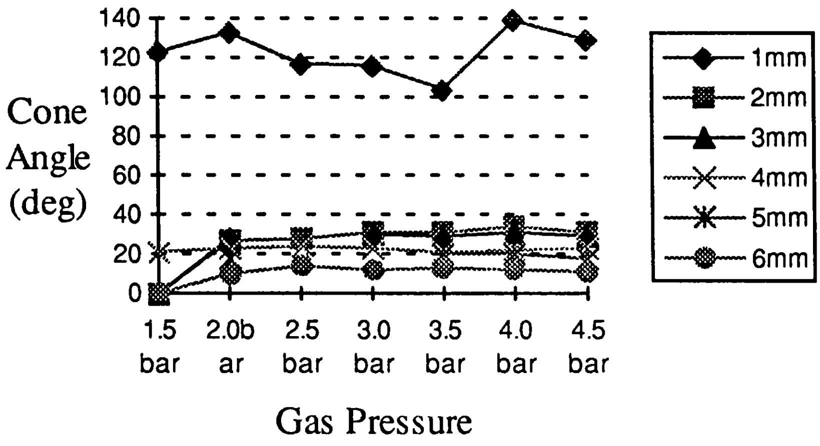

Figure 5-3.4(a): Spark Cone Angle for Mild Steel Cutting
With Different Gas Pressure (Laser Power = 1150 Watts)

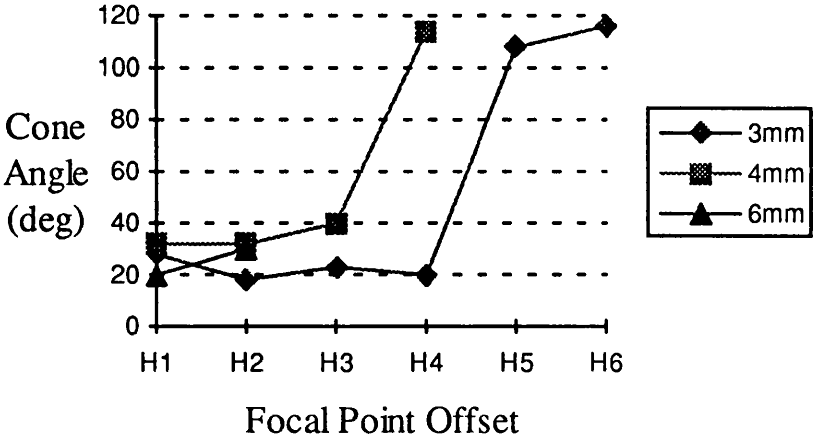

Figure 5-3.4(b): Spark Cone Angle for Mild Steel Cutting With Different Focal Point Offset (Laser Power = 1150 Watts)

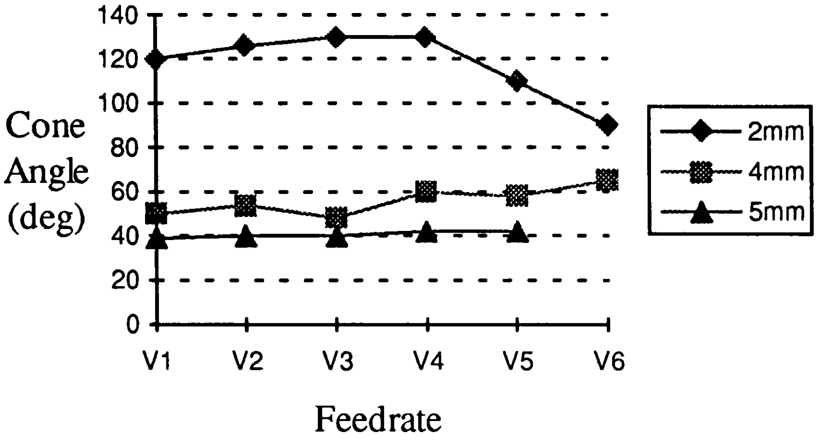

Figure 5-3.4(c): Spark Cone Angle for Mild Steel Cutting With Different Feedrate (Laser Power = 1150 Watts)

Spark cone angles for different material thickness mild steel cutting processes with good cutting quality are summarized in Table 5-3.2.

	Material Thickness					
	1mm	2mm	3mm	4mm	5mm	6mm
Cone Angle(deg)	133	27	28	23	18	10
Operational Parameters:						
Supply Gas Pressure: 2 bar for all thicknesses						
Focal Point Offset: 0 mm for all thicknesses (right on the surface)						
Feedrate(mm/min	5200	2700	2000	1420	1200	950

Table 5-3.2: Spark Cone Angle vs. Mild Steel Thickness

Figure 5-3.5 is the graphic representation of the data.

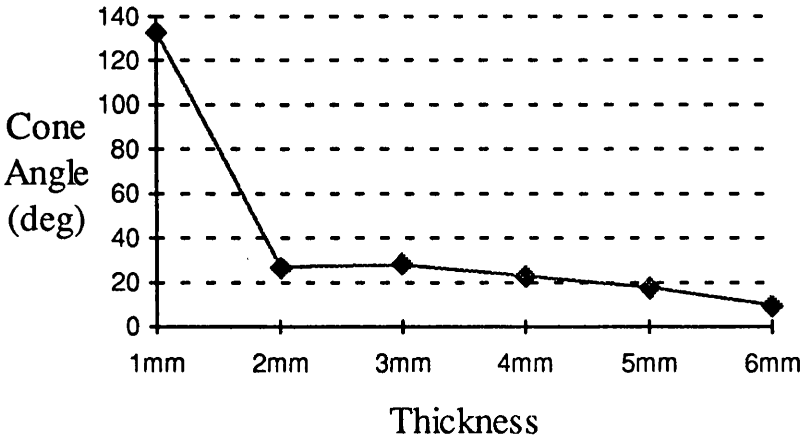

Figure 5-3.5: Spark Cone Angle vs. Mild Steel Thickness

5-4 Discussion and Conclusion

The spark cone pattern reflects the flow conditions of the liquid-gas mixture blown out from the kerf. Hence the presence of dross on the lower surface disturbs the exiting flow and thus the spark cone pattern. From the results shown in the previous section the following conclusions are made:

1) Very intensive cones were observed when the kerf walls were clean and dross free. Since there is no dross attachment on the lower surface, the blown-out liquid-gas mixture flows out smoothly and establishes an intense cone shape.

2) More and more sparse spark lines were formed as greater amounts of dross were attached to the lower surface of the workpiece. The dross attachment retarded and disturbed the flow. As a result, the spark cones became sparser.

3) The spark cone angle increases when gas pressure is increased until the cut surface is clean. This can be seen from data of 1.5 bar to data of 2.0 bar. Where at 1.5 bar most cuts have some dross attachment on the lower surface, and become dross free at a pressure of 2.0 bar and above. When the cuts are clean, the spark cone angle becomes stable.

4) Spark cone angles do not change as the feedrates are reduced. The spark cone patterns are dominated by the gas dynamics within the cut region. Flow conditions did not alter greatly when the feedrate was changed. Therefore, the spark cone angle remain unchanged.

5) Spark cone angle increases as the focal point offset is increased. Kerf width increases as the focal point offset is increased. The amount of flow per unit time is increased and results in a wider blow-out spread from the lower surface.

6) Spark cone angle decreases as the thickness of the material increases. As the thickness of the material increases, the kerf effectively acts as a duct and the flow inside the kerf tends to be fully developed. As a result, the angle of the spark cone decreases.

7) In the stainless steel cutting process, due to the higher viscosity, dross attachment remains on most of the workpiece lower surfaces, which disturbs the exiting gas-metal mixture flow and causes a sparse spark cone. Nevertheless, the relative size of the intense inner cone increases as the cut quality improves. Due to the form of these sparse spark cones - the spark cone evaluation system developed for assessing the cut quality - is more effective when used for the mild steel cutting process than for stainless steel cutting.

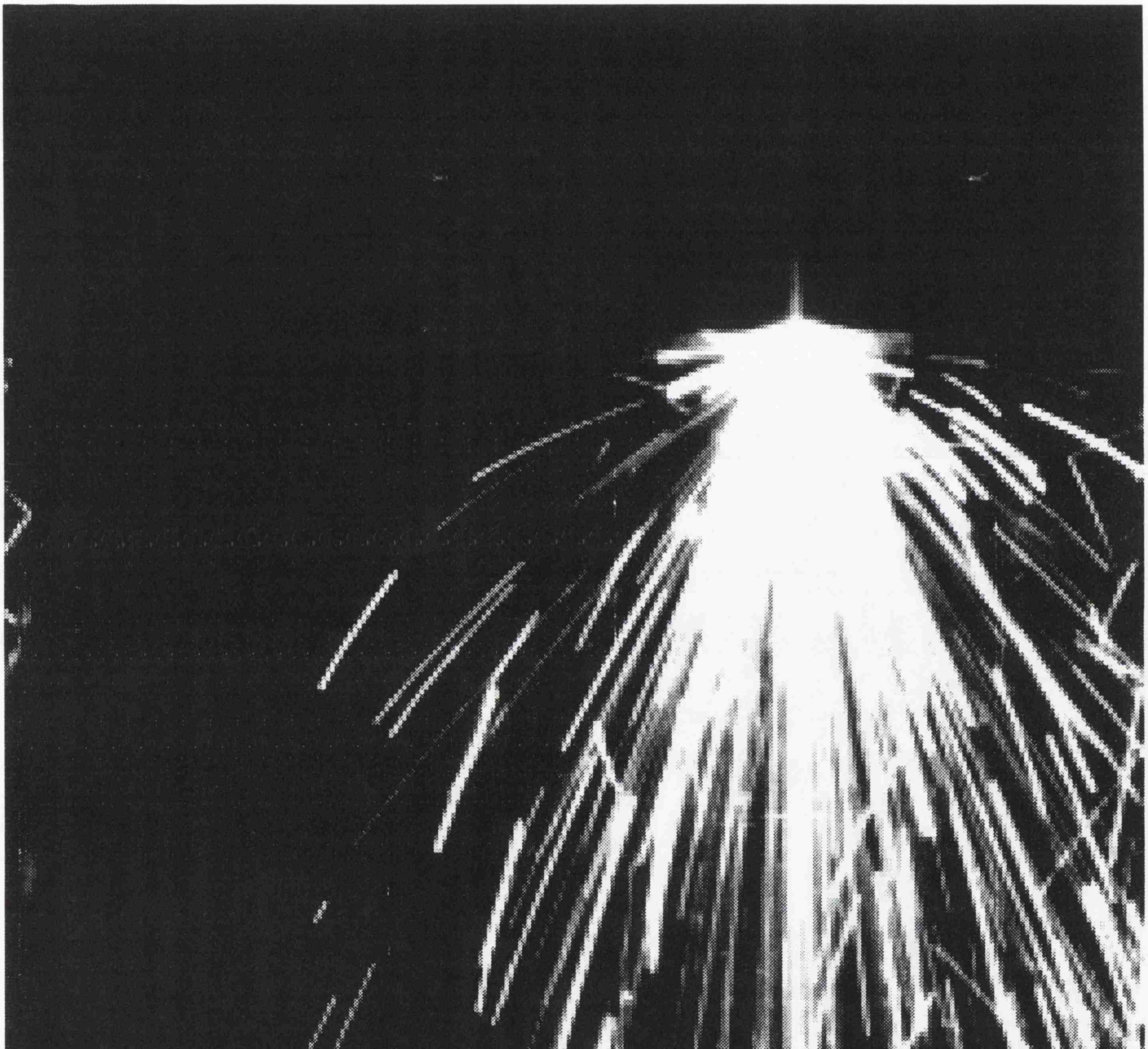

Plate 5-3.1: Spark Cone Image of A Typical Mild Steel Cutting Process

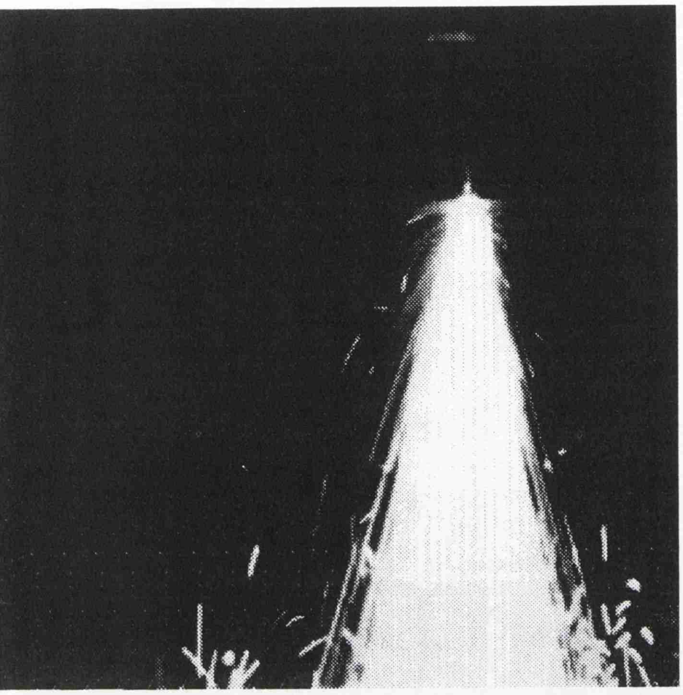

Plate 5-3.2: Spark Cone Image of 2 mm
Mild Steel Cutting Process - Good

(Feedrate = 2700 mm/min)

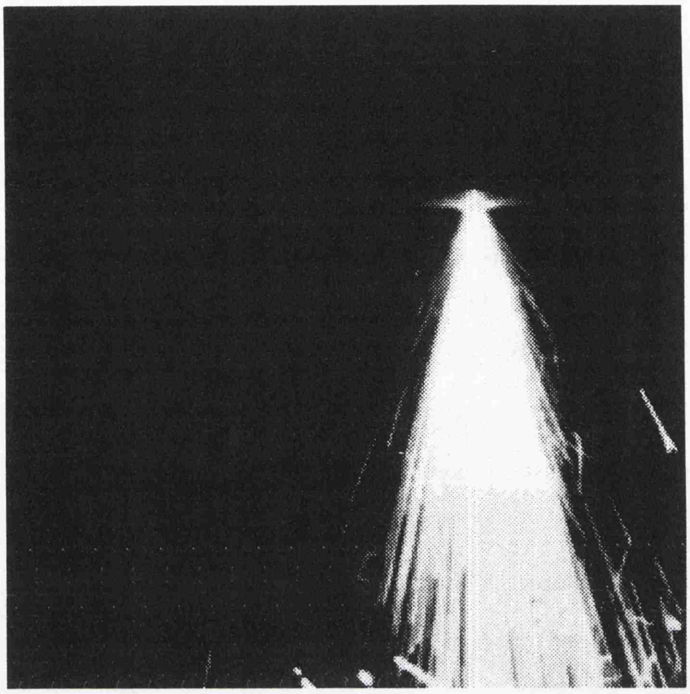

Plate 5-3.3: Spark Cone Image of 3 mm
Mild Steel Cutting Process - Good

(Feedrate = 2000 mm/min)

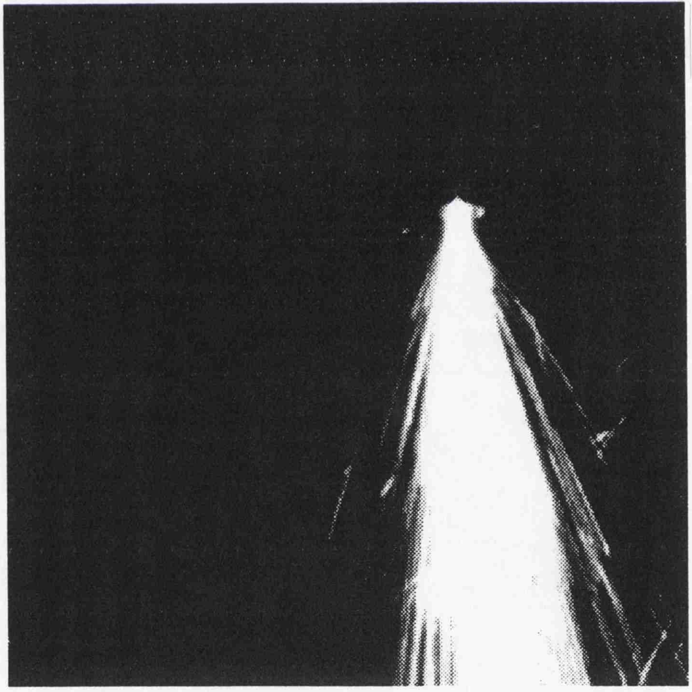

Plate 5-3.4: Spark Cone Image of 4 mm
Mild Steel Cutting Process - Good

(Feedrate = 1420 mm/min)

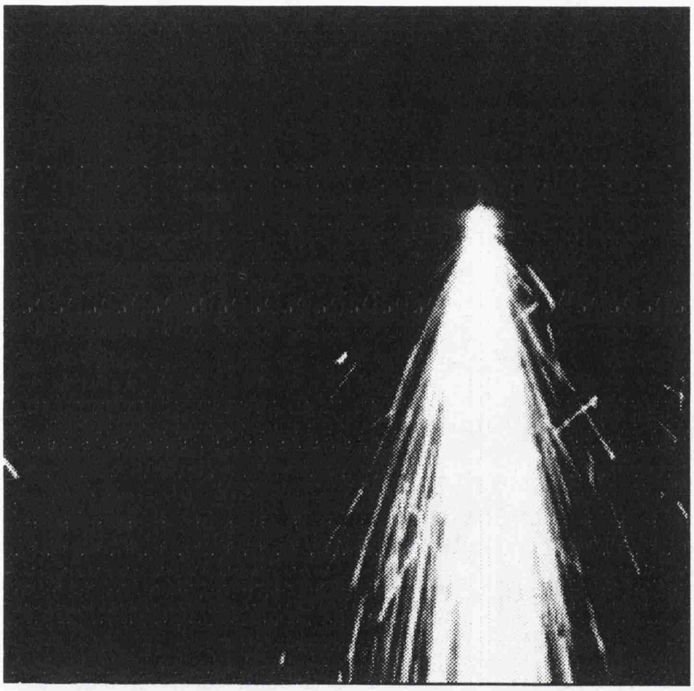

Plate 5-3.5: Spark Cone Image of 5 mm Mild Steel Cutting Process - Good

(Feedrate = 1200 mm/min)

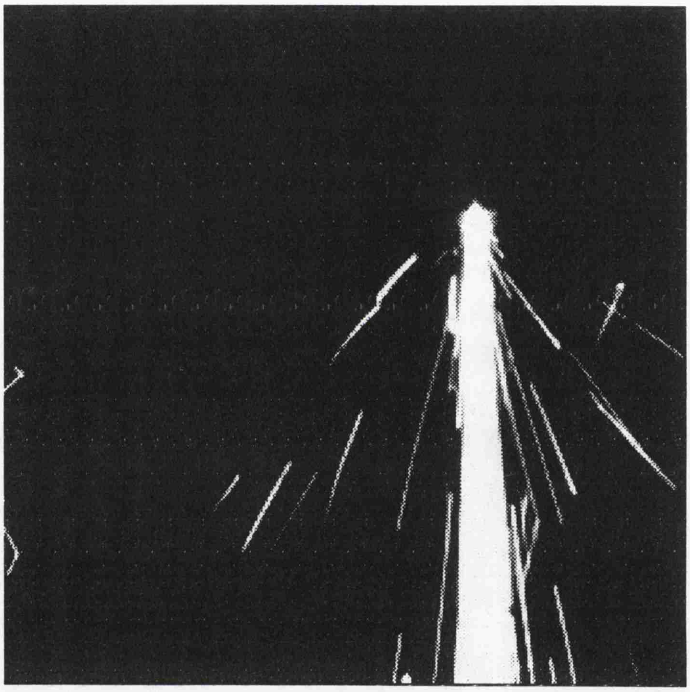

Plate 5-3.6: Spark Cone Image of 6 mm Mild Steel Cutting Process - Good

(Feedrate = 950 mm/min)

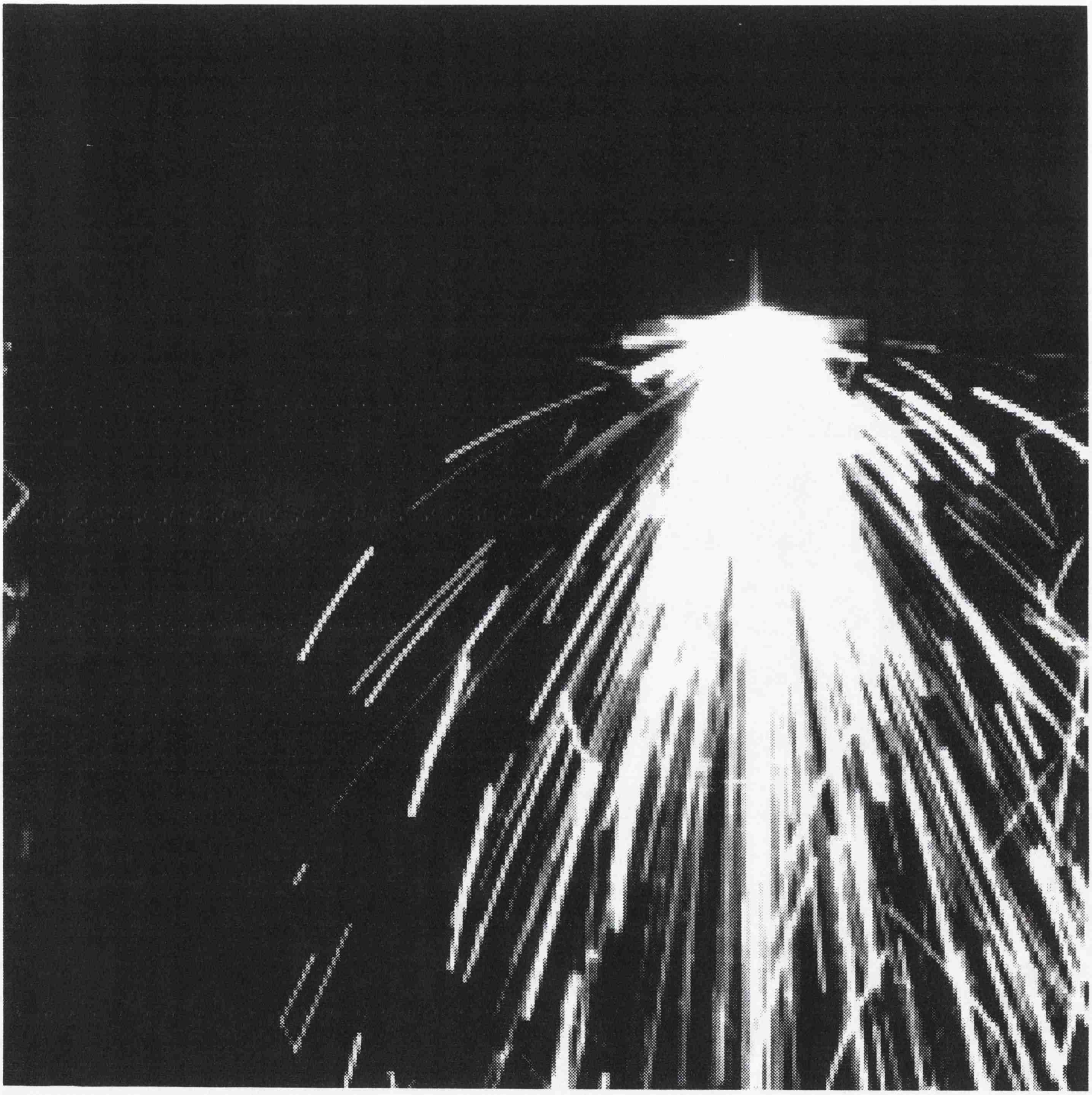

Plate 5-3.7: Spark Cone Image of 4 mm Mild Steel Cutting Process With Some Dross Attachment

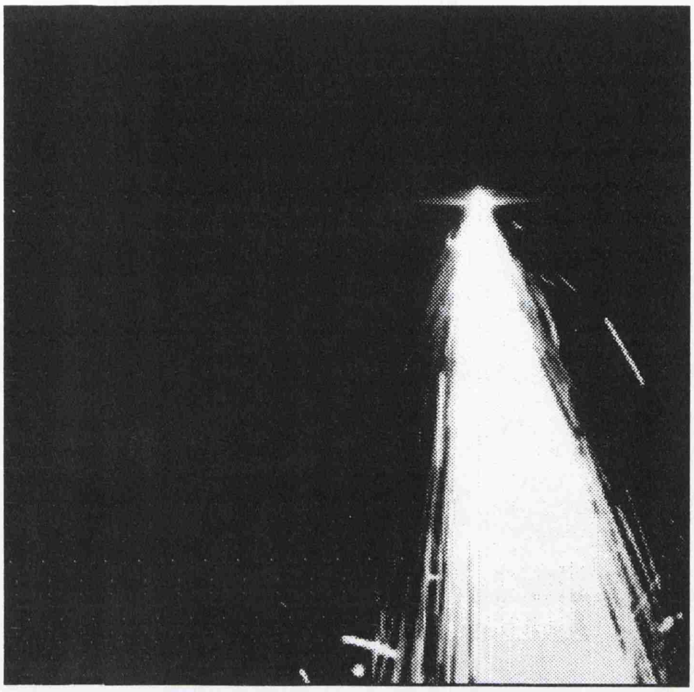

Plate 5-3.8: Spark Cone Image of Clean Cutting Process - Mild Steel

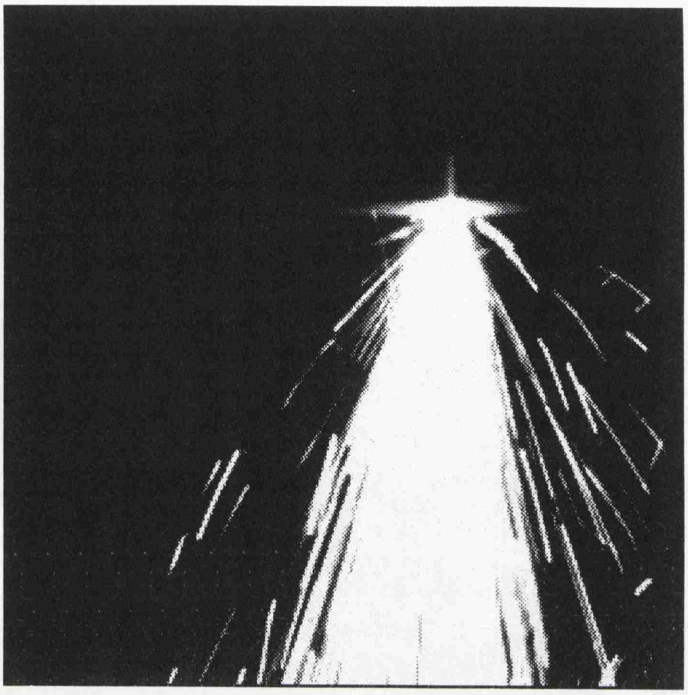

Plate 5-3.9: Spark Cone Image of Less Dross Cutting Process

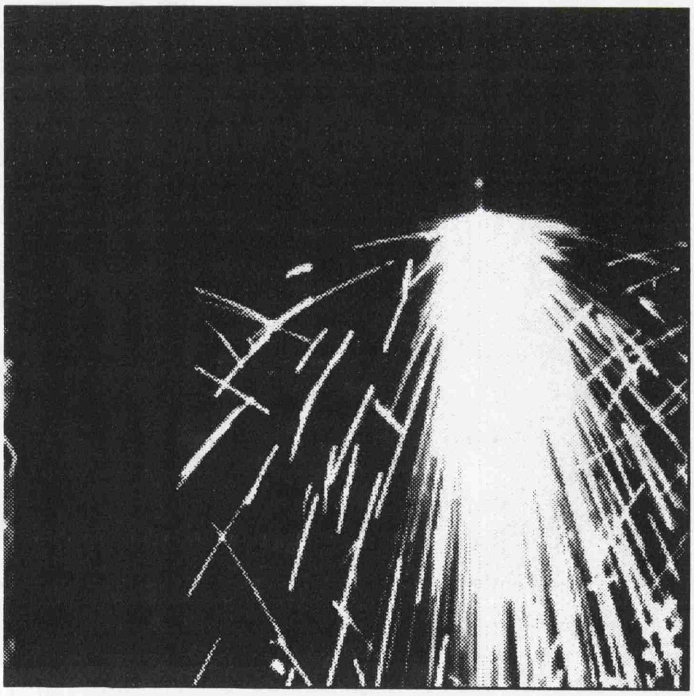

Plate 5-3.10: Spark Cone Image of Median Dross Cutting Process

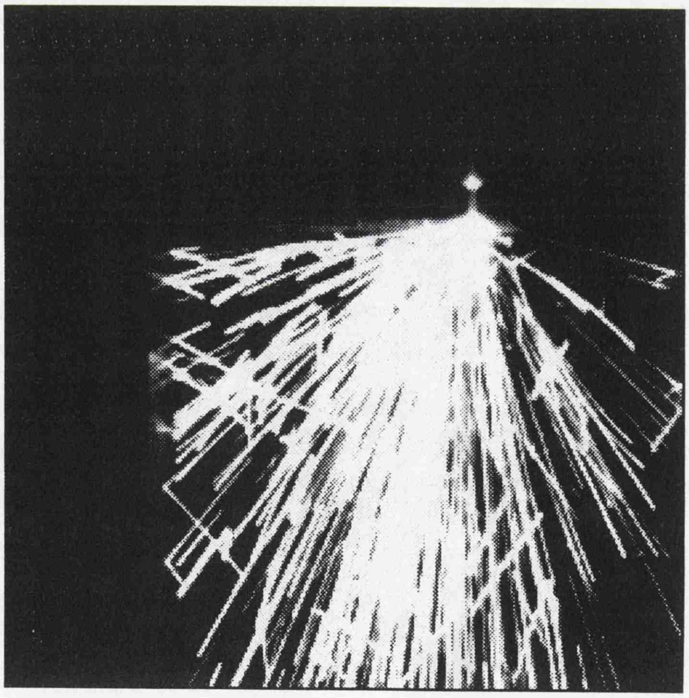

Plate 5-3.11: Spark Cone Image of Heavy Dross Cutting Process

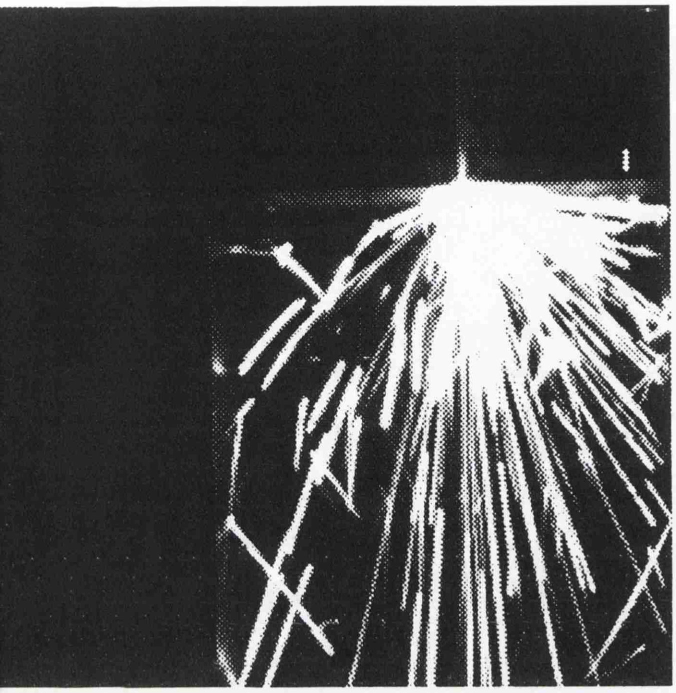

Plate 5-3.12: Spark Cone Image of 1 mm Stainless Steel Cutting Process - Good

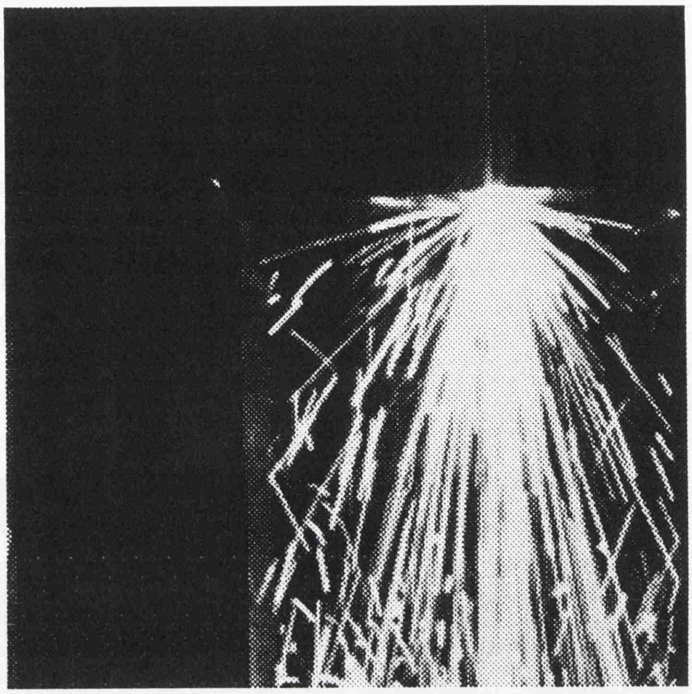

Plate 5-3.13: Spark Cone Image of 2 mm Stainless Steel Cutting Process - Good

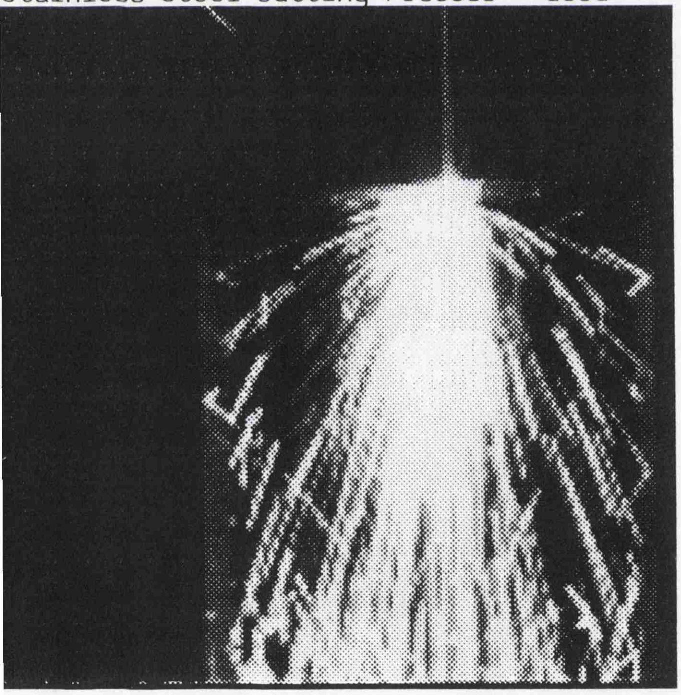

Plate 5-3.14: Spark Cone Image of 3 mm Stainless Steel Cutting Process - Good

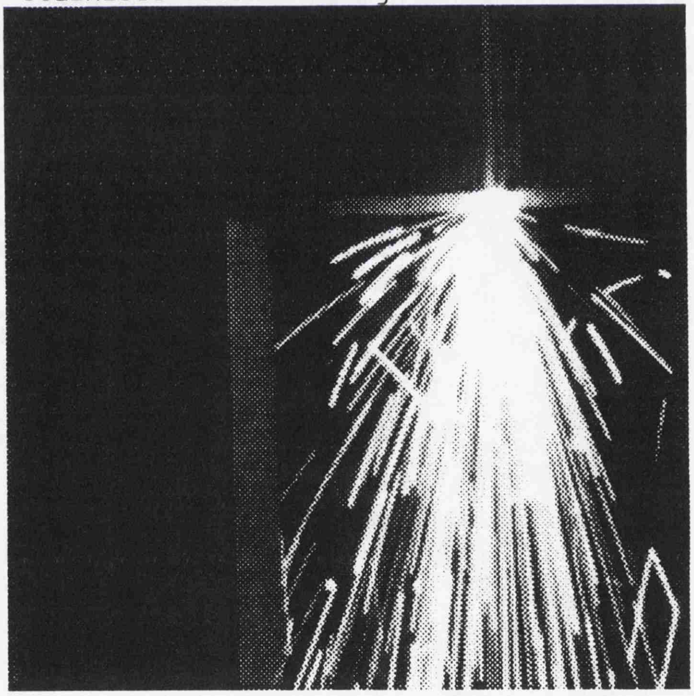

Plate 5-3.15: Spark Cone Image of 4 mm Stainless Steel Cutting Process - Good

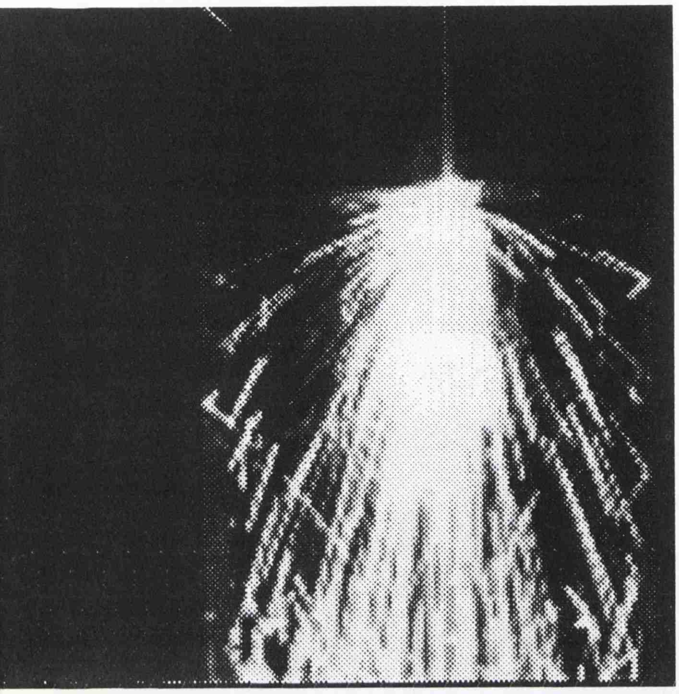

Plate 5-3.16: Spark Cone Image of Clean Cutting Process - Stainless Steel

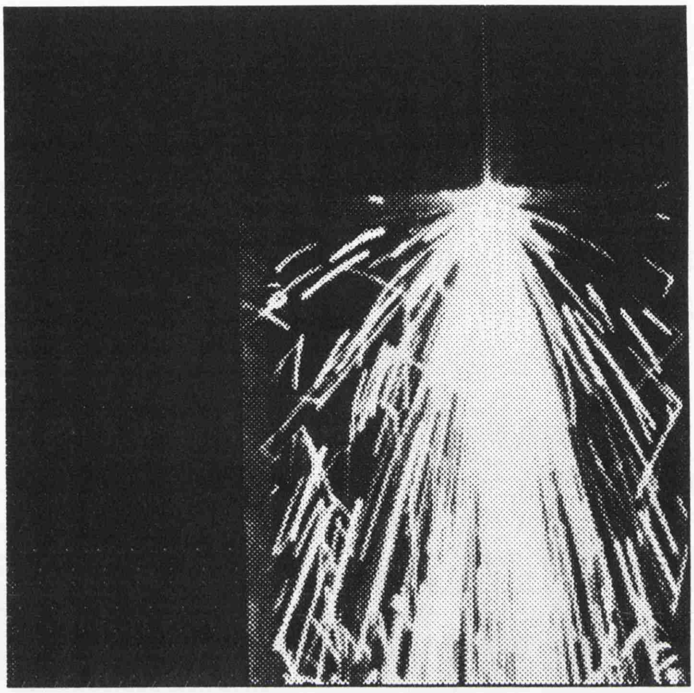

Plate 5-3.17: Spark Cone Image of Less Dross Cutting Process - Stainless Steel

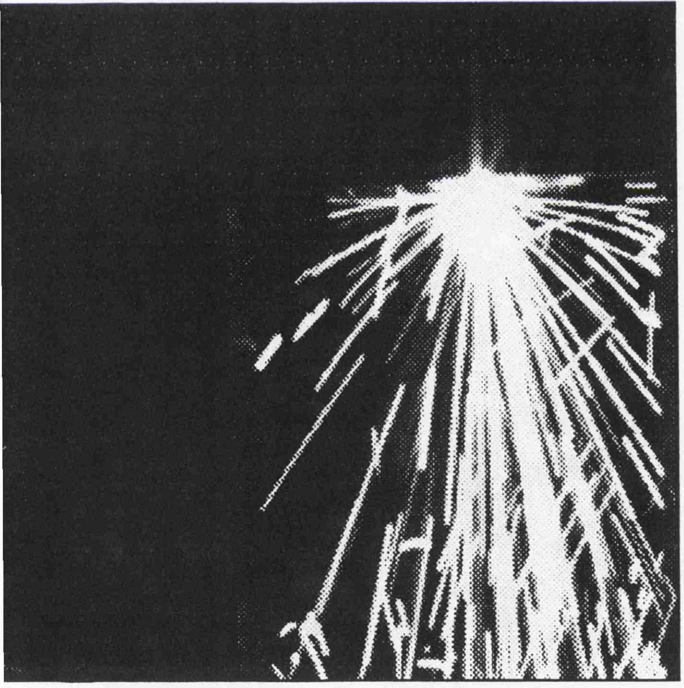

Plate 5-3.18: Spark Cone Image of Median Dross Cutting Process - Stainless Steel

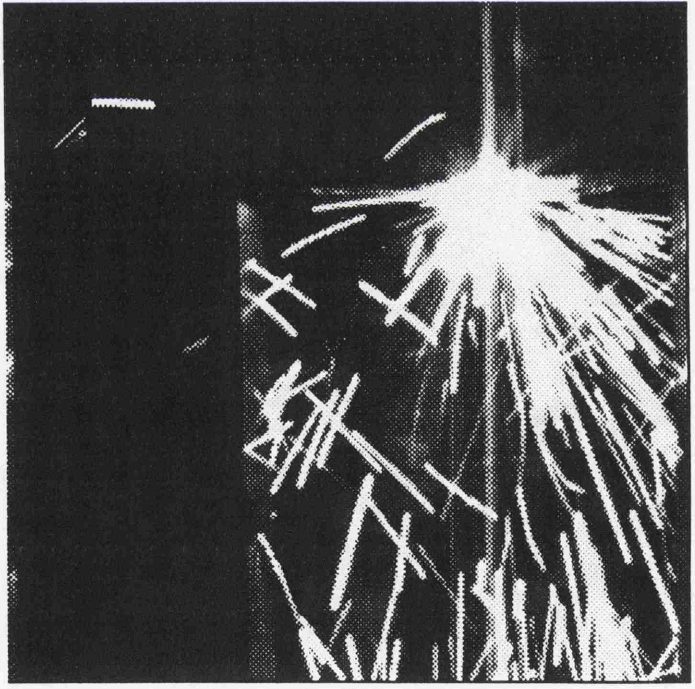

Plate 5-3.19: Spark Cone Image of Heavy Dross Cutting Process - Stainless Steel

Chapter 6

Knowledge-based Adaptive Control Laser Manufacturing System

Nomenclature

C_p = thermal conductivity

E = total radiated energy

η = coupling coefficient

L_f = latent heat of fusion

L_v = latent heat of vaporisation

λ = wavelength

m' = fraction of melt vaporised

P = incident laser power

ρ = density

t = thickness

T = temperature

V = cutting speed (feedrate)

w = average kerf width

6-1 Introduction

The laser cutting process is influenced strongly by characteristics such as: power mode (i.e. CW or pulsed), power density, transverse mode, beam polarisation; set-up of operating system such as: beam delivery optics, nozzle type, assist gas type and gas pressure, beam focusing, laser beam operating position (offset), and feedrate; and characteristics of target material such as: conductivity, diffusivity, melting temperature, boiling temperature, latent heat of melting and vaporisation, plasma formation, exothermic chemical reaction with reactive gas O_2, and relevant viscosities. So many parameters are involved that inevitably laser cutting is a highly non-linear process and consequently very difficult to analyse or predict analytically. Numerous researchers have investigated these complex laser cutting phenomena in order to establish an appropriate cutting model to describe and control laser cutting processes. D. Schuocker [1][2], M. Vicanek et al [3], and M. J. Tasi et al [4] proposed a laser cutting model based on stability analysis of the melt flow over the transient cut surface. Almost periodic striation patterns were predicted and found on the kerf walls. Through the investigation of the dynamical behaviour of these thin film flow patterns they characterized, based on operating parameters and target material characteristics, the thickness of the thin layer and predicted the striation frequency range for stable cutting processes. This gives a prediction of the laser beam feedrate. K. A. Bunting et al [5] simplified the analysis assumptions and used a cylindrical source model to investigate the relationship between the incident power density, the nozzle head and the resulting cutting speed. Relationships between the incident power density per unit thickness and the cut speed (feedrate) in terms of the thermal properties of the target material were established for predicting and controlling the cutting processes. G. Chryssolouris et al [6] and W. M. Steen [7] further simplified the analysis assumptions and proposed a simple cutting model to predict the process. Theoretical analyses of the laser-material interaction aimed at establishing models that facilitate control of the laser cutting process are presented in [8][9][10][11].

Many models and discoveries related to laser cutting processes have been developed. Yet, the results are scattered in the literature and more or less incomplete or inconclusive. Formulae and data generated by one researcher quite often may not be correct or be useful to another because they are system and set-up dependant. A control algorithm that is system independent and set-up unrelated is thus needed.

The recent and rapid development in artificial intelligence and expert systems along with well-established control techniques provide a satisfactory solution to the problem. A hierarchically-structured control system that integrates a knowledge-based expert system, adaptive process control and pattern recognition techniques has been developed for a Ferranti MFKP 1.2kW CO_2 Laser Manufacturing System. This is illustrated by figure 6-1.1.

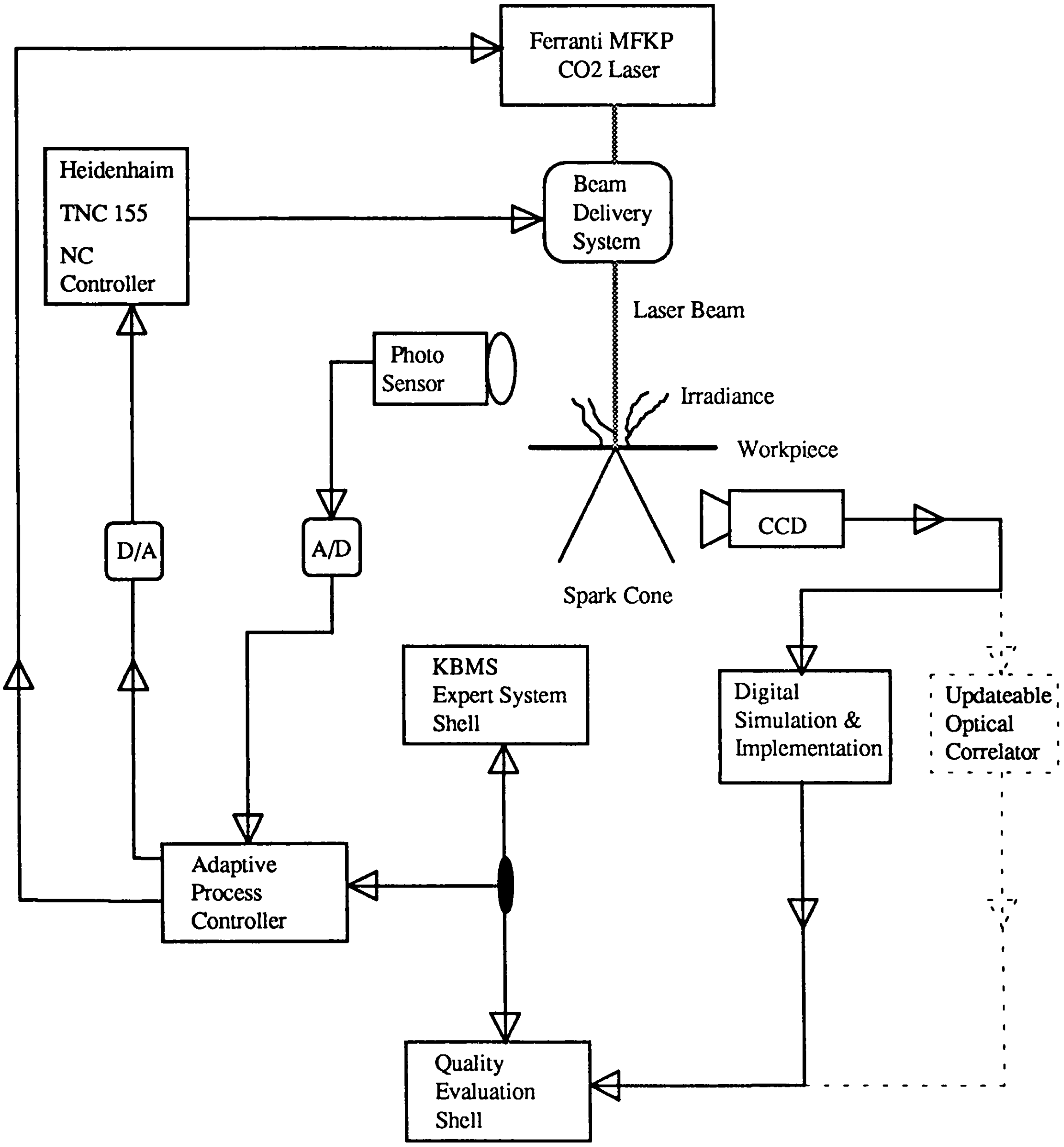

Figure 6-1.1: Knowledge-Based Adaptive Control Environment

Laser cutting process knowledge, for different materials, is organised and implemented with a rule-based system. An adaptive control algorithm based on on-line recursive parameter estimation and real-time control synthesis was adopted for the highly non-linear cutting process control. The laser beam feedrate was chosen as the system control input. The magnitude of the irradiance emitted from the cut front was detected and fedback to this adaptive controller and used as the input to the recursive parameter estimator for system identification. Pattern recognition that utilises cross correlation with a synthetic discriminant function (SDF) filter was applied to the cutting quality control. Images of the exit spark cone that occurred during the cutting process were grabbed, edge enhanced and cross-correlated with ideal reference images encoded into a SDF filter. Digital techniques based on these pattern recognition algorithms were developed to simulate the performance of a control system that has been designed for a real-time optical implementation.

6-2 System Description

The adaptive control and tasking environment of the CO_2 laser manufacturing system consists of three sub-systems:

1. a pre-process KBMS expert shell
2. an adaptive process controller
3. a post-process quality analysis shell

6-2.1 General Implementation Description

The system is illustrated by figure 6-2.1.

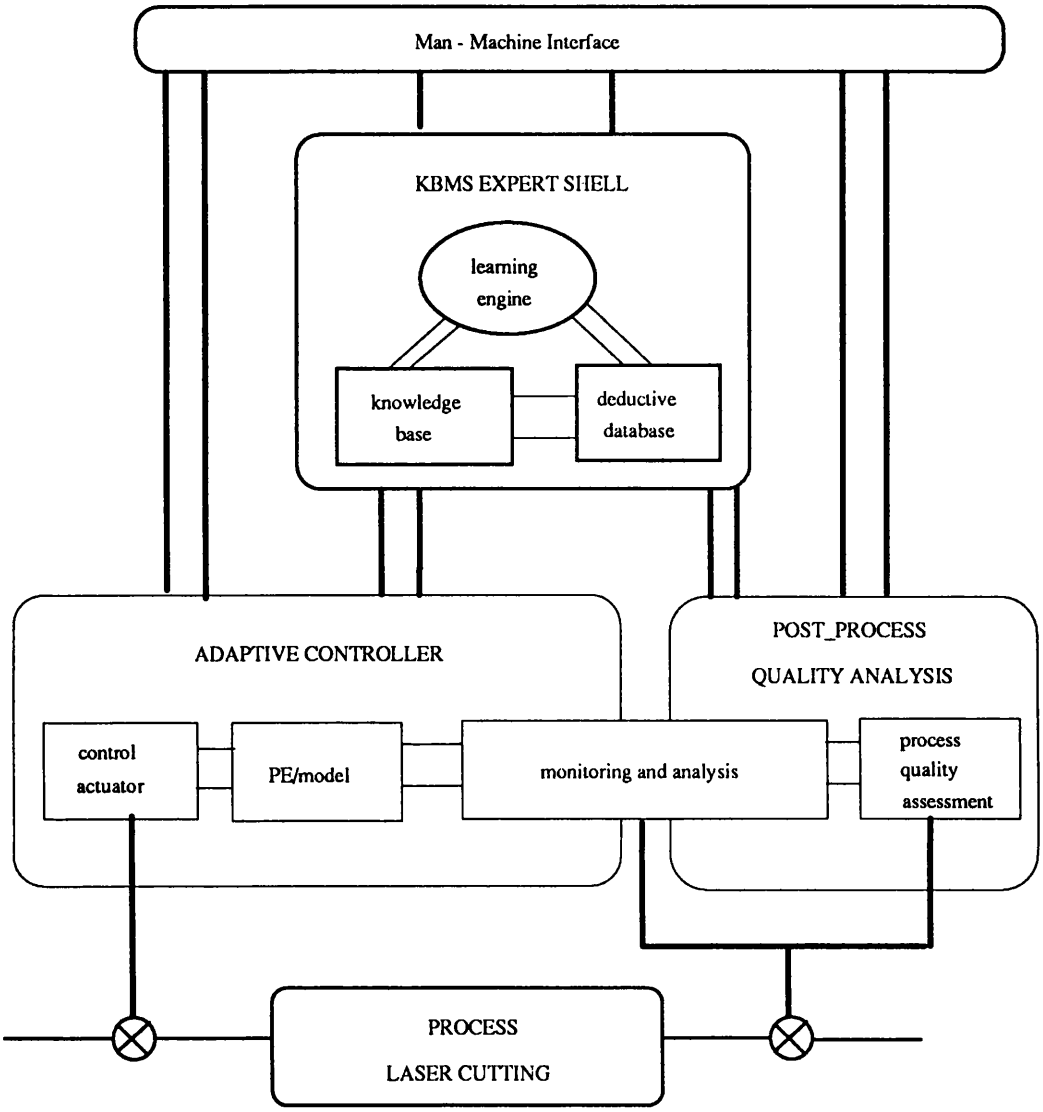

Figure 6-2.1: System Diagram of a Knowledge-Based Adaptive Control Environment For a CO_2 Laser Manufacturing System (PC-Based Windows Environment)

Knowledge of the initial best-process parameter settings for different laser processes and materials are stored in the knowledge base. The spark cone images are also stored in the knowledge base for post-process quality analysis and subsequent exploitation in constructing the SDF's. A rule-based chaining inference engine and least square parameter estimation are used to relate material selection to process parameter evaluation.

The laser operator communicates and operates the system through the graphically based user interface (GUI). When the technician makes a query for a specific laser process, for a particular material, the knowledge-based expert shell searches through the data base using the embedded rules and chaining methods and then displays the process parameter data via the GUI. When the technician initiates the cutting process, the associated spark cone SDF filter is called up from the data base and then loaded to the spark cone image evaluation system built into the SUN workstation, the SUN is linked to the controller via the network. The evaluation system stands by for post process quality analysis. Meanwhile, initial best-estimate process parameter settings are inferred from the knowledge base and sent to the controller. Setting of laser power mode (i.e. pulsed or CW) and power range are downloaded to the laser pulser unit. Feedrate settings are downloaded to the TNC controller. The process is then initiated through the TNC controller. During the laser cutting process, irradiance emitted from the cut front and spark cone image are sampled and fedback to the adaptive controller and spark cone image evaluator respectively. The irradiance emitted from the cut front is used to regulate the cutting process in real-time; the spark cone data is used to evaluate post process quality.

6-2.2 Hardware Schematics

The adaptive control and tasking environment (ACTE) for this specific laser manufacturing system, which is illustrated in figure 6-2.2, includes five sub-systems:

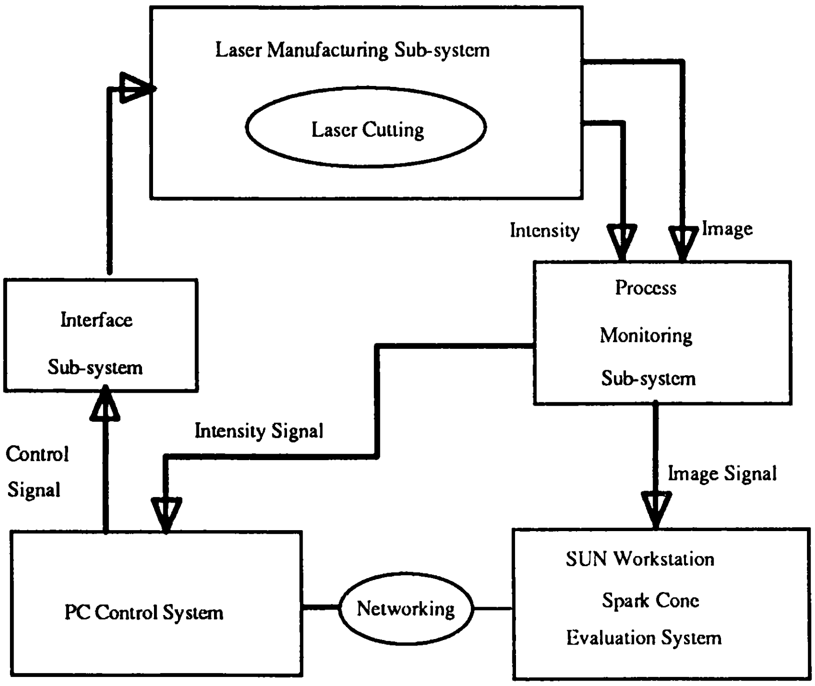

Figure 6-2.2: ACTE Laser Manufacturing System

1. laser manufacturing sub-system
2. PC control sub-system
3. SUN workstation spark cone image evaluation sub-system
4. process monitoring sub-system
5. interface sub-system

1. laser manufacturing subsystem:

The main function of this sub-system is to generate, maintain, and regulate the laser needed for the material processing operation. The diagram of this subsystem is shown in figure 6-2.3.

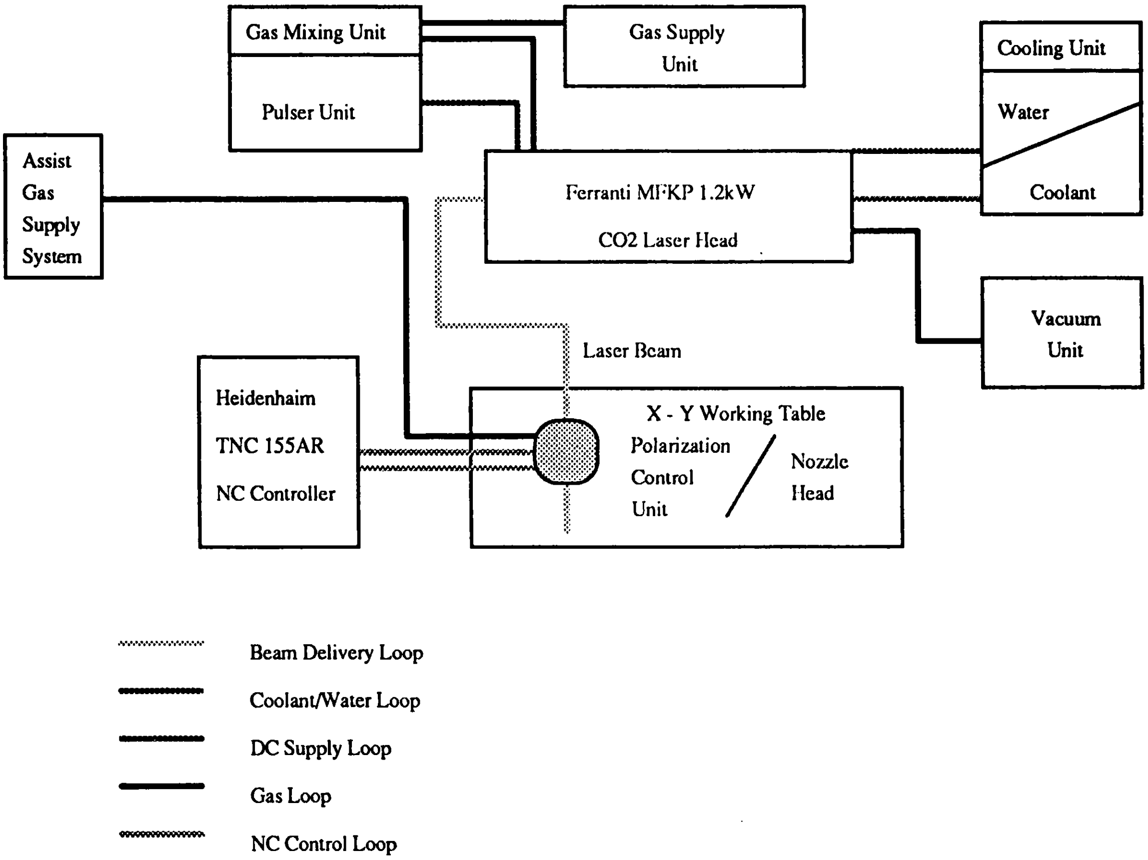

Figure 6-2.3: Laser Manufacturing System

It includes the following components:

(1) Ferranti MFKP CO$_2$ laser system:

(i) laser head

(ii) pulser unit
(iii) gas supply unit
(iv) assist gas supply unit
(v) cooling unit (water/coolant)
(vi) vacuum unit (pump)
(vii) laser beam delivery system

(2) Heidenhain TNC 155AR NC working table:
(i) TNC 155AR NC controller
(ii) X Y working table

(3) Polarization control unit:
(i) Coherent 4 MIRROR ECQ module - depolarizer
(ii) A4890TS rotation stage

2. PC control subsystem:

The PC control subsystem is the central control unit, the core of the entire system. This is where the knowledge base, adaptive controller and monitoring system are hosted. The diagram of this subsystem is shown in figure 6-2.5. It includes the following components:

(1) Viglen Vig IV 33 486 PC
(2) National Instrument AT-MIO-16F-5 . Multi-channel data acquisition card
(3) Licom serial communication card
(4) R S PC 24 digital I/0 card
(5) multi-protocol communication card

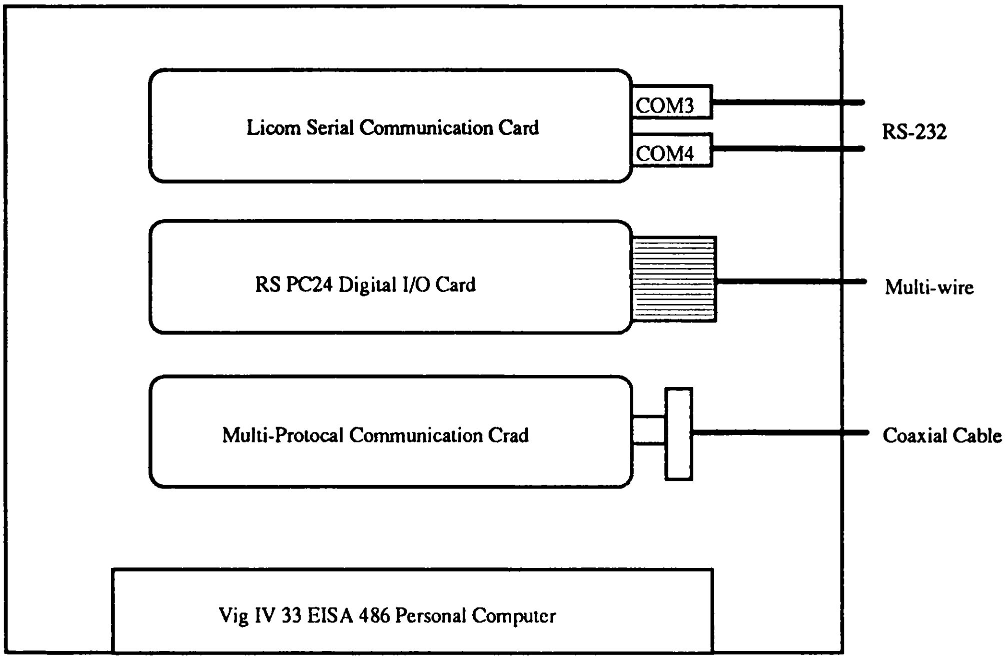

Figure 6-2.4: PC Control System

3. SUN spark cone image evaluation subsystem:

Digital image analysis is executed on the SUN workstation, this simulates the coherent optical techniques to analyze the spark cone image in order to analyze the process quality. The diagram of this subsystem is shown in figure 6-2.5. It includes the following components:

(1) Sun IV sparc workstation
(2) ITEX 150 frame grabber
(3) TV monitor

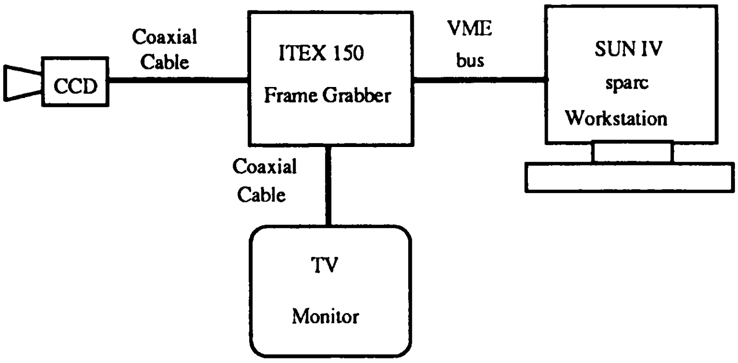

Figure 6-2.5: Spark Cone Evaluation System

4. Process monitor subsystem:

The monitoring sub-system acquires information during the process. The central controller uses this information to effectively and correctly supervise and control the processing in order to achieve best processing quality. The diagram of this subsystem is shown in figure 6-2.6. It includes the following components:

(1) cut front irradiance measuring unit
    (i) fibre optic + optics head
    (ii) photo sensor unit
    (iii) signal conditioning unit

(2) spark cone image grabbing unit
    (i) CCD camera + lens
    (ii) TV monitor
    (iii) transmission cables
    (iv) power supply

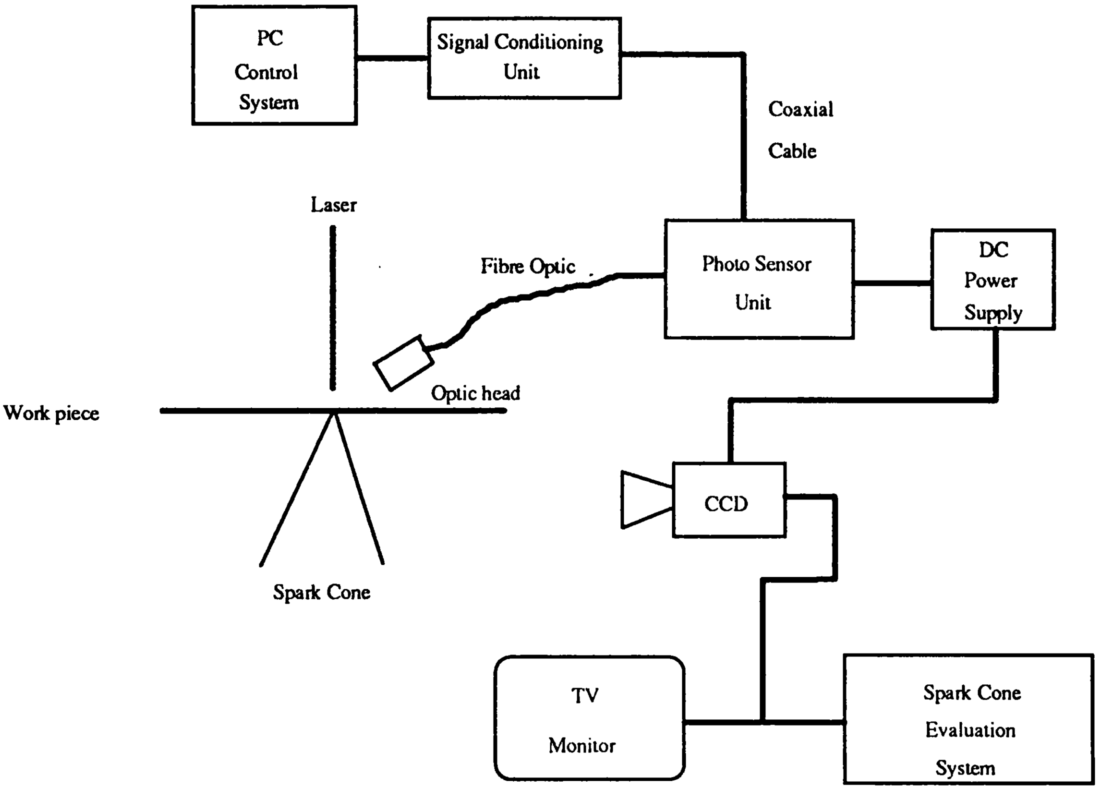

Figure 6-2.6: Process Monitoring Sub-system

5. interface subsystem:

Several kinds of interfaces are built into this system. Communication messages and control commands can then route through these interfaces. The diagram of this subsystem is shown in figure 6-2.7. It includes the following components:

(i) PC controller - laser pulser unit interface
(ii) PC controller - NC controller interface

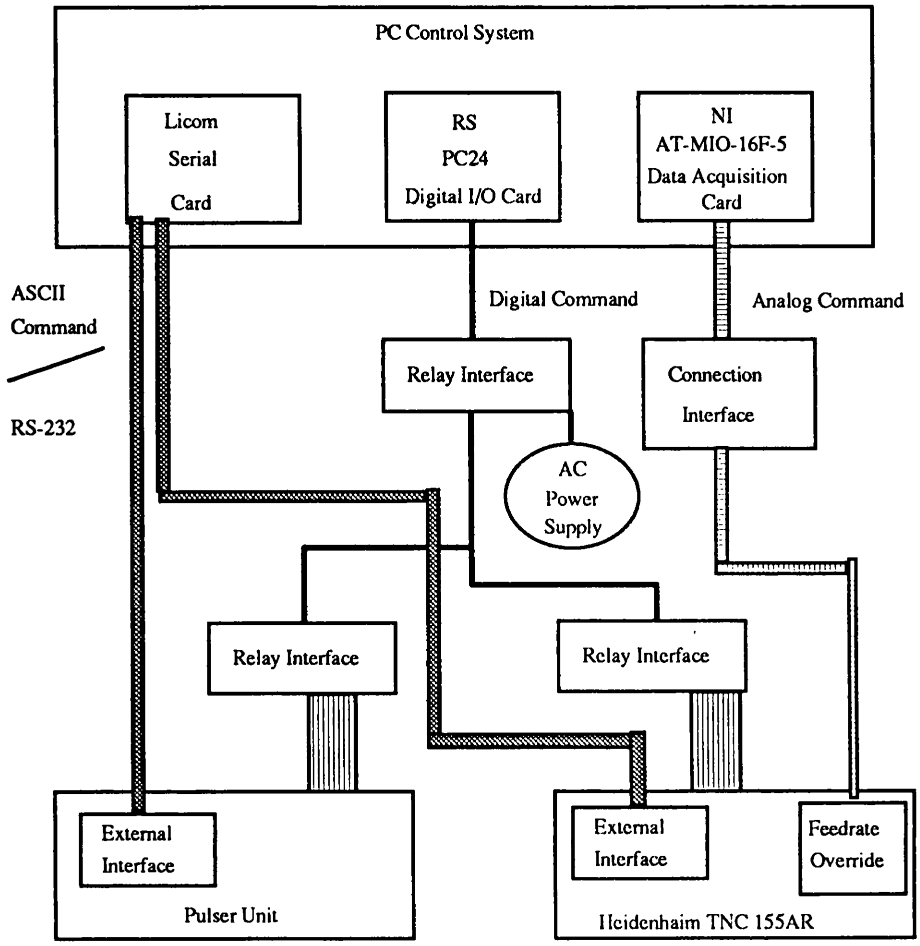

Figure 6-2.7: Interface Sub-system

6-2.3 Software Schematics

The software structure of the system is detailed as follows:

1. Pre-process KBMS expert subsystem:

Expertise regarding material recommendation, process parameter settings and process quality judgement are provided through this KBMS expert sub-system. The diagram of this subsystem is shown in figure 6-2.8.

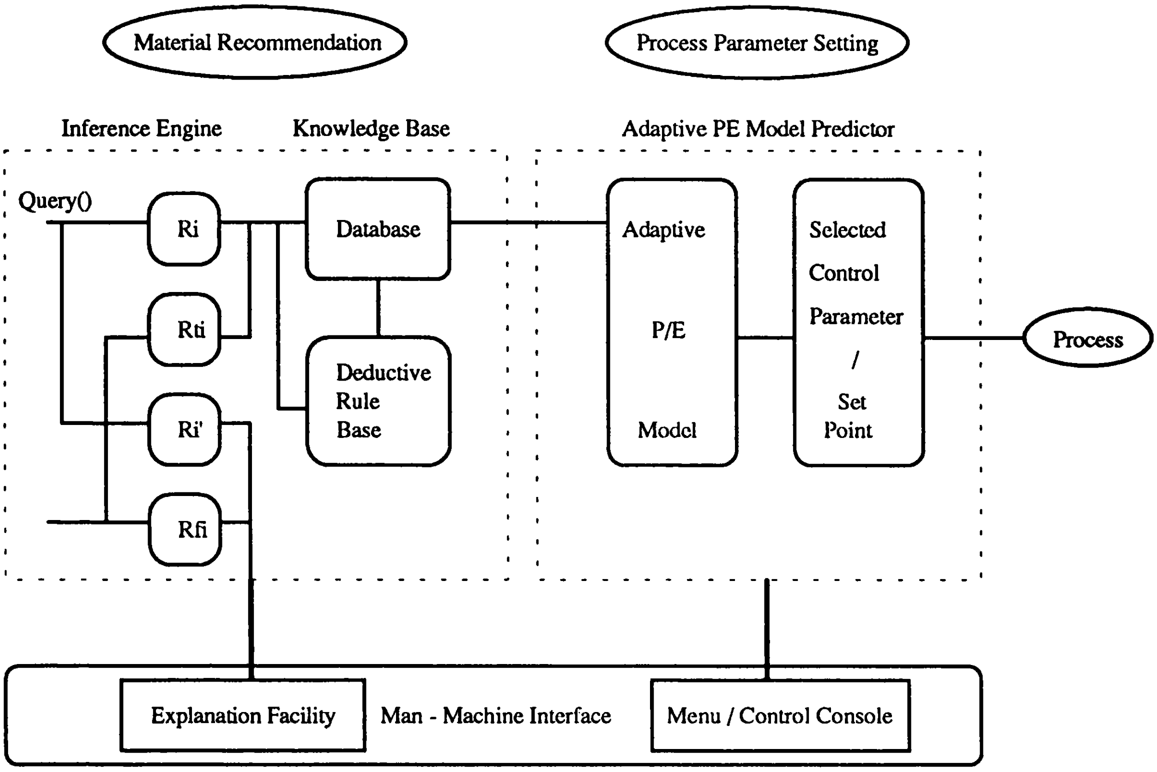

Figure 6-2.8: KBMS Expert Sub-system

It includes the following components:

(i) relational data base

(ii) deductive rule base

(iii) inference engine

(iv) adaptive parameter estimator

(v) man-machine interface

  (a) explanation facility

  (b) operation window/ control system

(vi) Inter-subsystem interface

2. Adaptive Process Controller:

Information about the process is sampled and fed into the parametric estimator for model construction. The resulting model is then used to construct the controller and the appropriate control set-up is actuated through the DNC interface upon the laser manufacturing system. The main function of this sub-system is to maintain the laser processing stability within the required specification. The diagram of this subsystem is shown in figure 6-2.9.

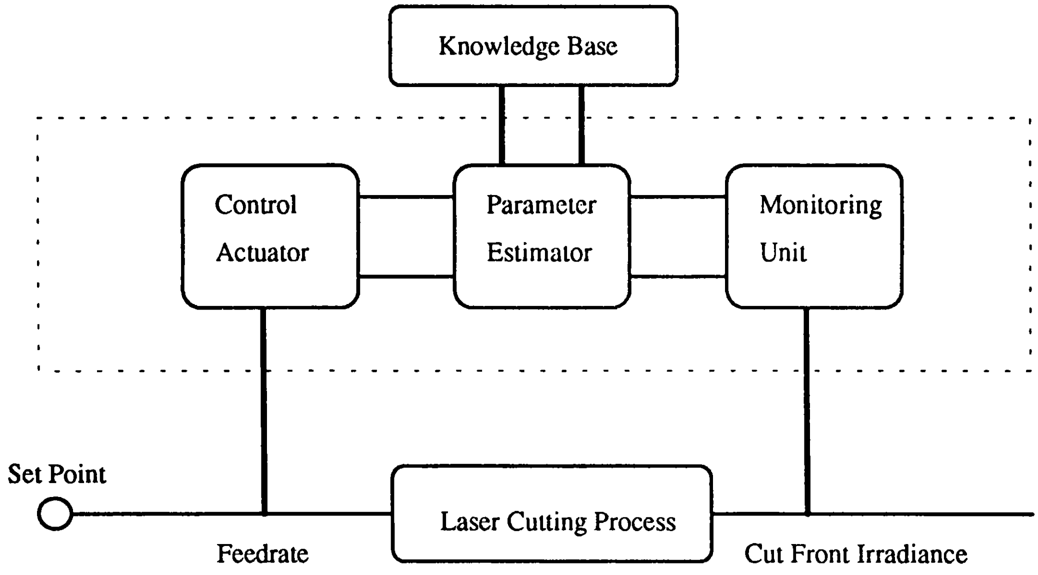

Figure 6-2.9: Adaptive Process Controller

It includes the following components:

(i) monitoring unit:

- (a) data acquisition - intensity
- (b) signal A/D conversion and analysis
- (c) man-machine interface

(ii) Parameter estimator

(iii) Control actuator

  (a) controller
  (b) D/A converter
  (c) DNC interface
  (d) man-machine interface

(iv) Inter- subsystem interface

3. Post-process quality analysis and consultation sub-system:

Images of the cutting process are analyzed by this spark cone image evaluation sub-system. Digital processing of these images enable the knowledge expert sub-system to assess the quality of the process. The diagram of this subsystem is shown in figure 6-2.10. It includes the following components:

(i) Image acquisition - spark cone image

(ii) Image pre-processing

(iii) Image comparison:

  (a) matched filtering
  (b) half cone angle comparison

(iv) man-machine interface

  (a) control screen
  (b) consultation screen

(v) inter sub-system interface

The whole software structure is illustrated in figure 6-2.11.

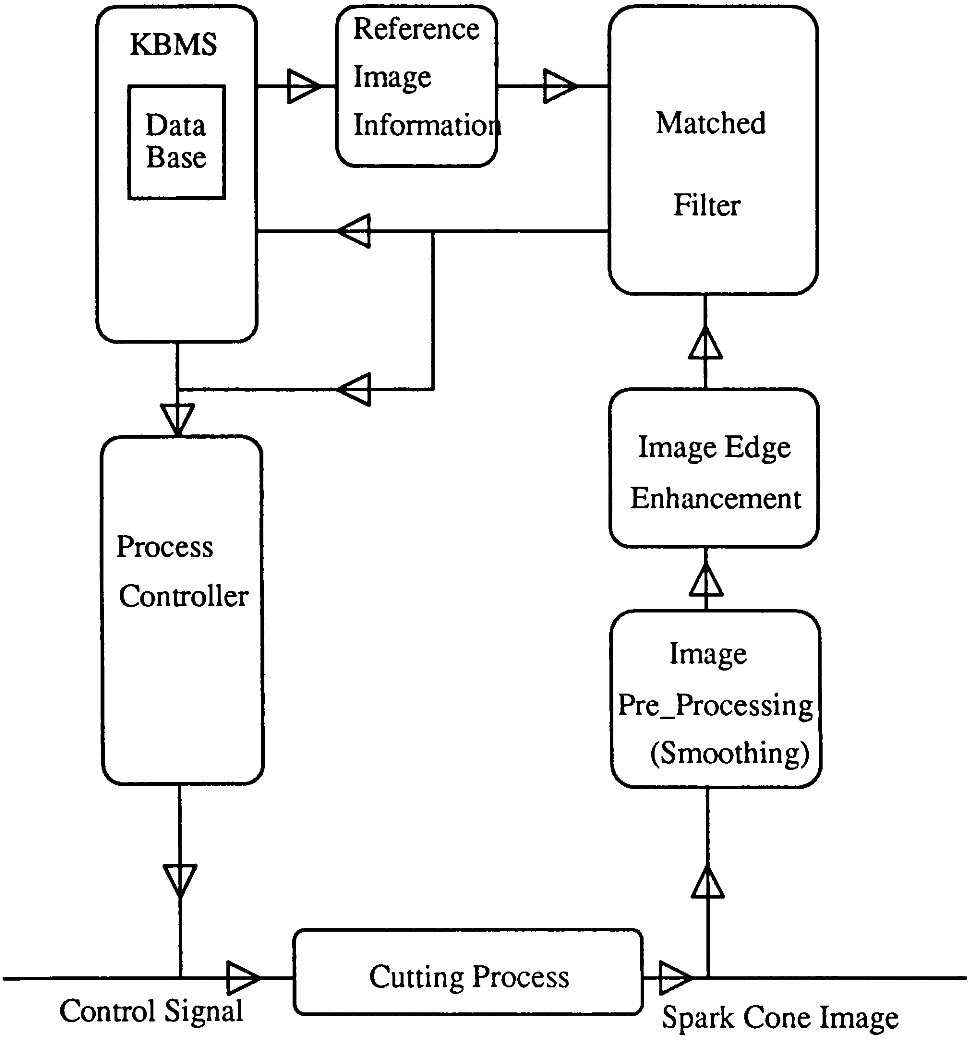

Figure 6-2.10: Quality Analysis Sub-system

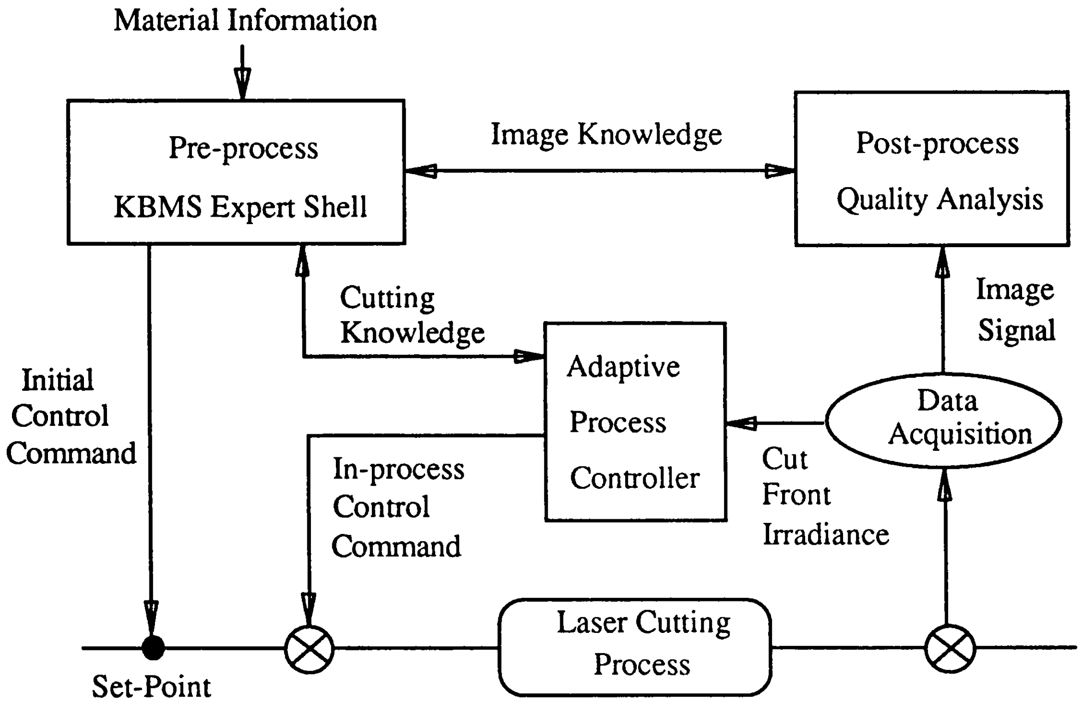

Figure 6-2.11: System Software Structure Diagram

6-3 KBMS Expert Shell

what is an expert system:

Expert systems form a branch of Artificial Intelligence. One of the most outstanding examples of expert systems is that of medical diagnosis. The most representative and famous system is MYCIN [12][13][14]. An expert system developed at Stanford University to aid physicians in the diagnosis and treatment of meningitis and bacteremia infections. Since then, numerous systems were developed for different areas. PROSPECTOR [15] was designed to provide consultation for geologists. HEARSAY II [16] was developed for speech understanding. MOLGEN was used for analysis and synthesis of DNA. And R.1. was developed to configure PDP and VAX computer systems [17]. Many other expert systems have been developed for mathematics, chemistry and engineering.

An expert system, which is a set of software modules, mimics the behaviour of an expert in a particular pre-defined field of interest. Expert-system does not necessarily mean that the piece of computer software will become an expert itself, but emphasizes that the software contains knowledge of domain experts.

components of an expert system:

Expert systems mainly include the following components:

i. The knowledge acquisition sub-system.

ii. The knowledge base.

iii. The deductive data base - temporary working memory.

iv. The inference engine.

v. The explanation sub-system - interface.

vi. The learning sub-system.

tools for building expert system:

Basically, three kinds of tools are available for building an expert system:

i. conventional programming languages: like C, Pascal, FORTRAN

ii. artificial intelligence tools: like Lisp, Prolog

iii. expert system shells: like KAE

C was selected as the language to develop this system as it gave the following advantages:

(i) comparatively high processing speed when compared with LISP and Prolog

(ii) it supports complex data structures and is able to process numerically intensive problems quickly

(iii) compatibility and portability with different hardware

(iv) easier integration with different software packages

(v) no special hardware needed - cost effective

(vi) excellent low level hardware manipulation power

6-3.1 The Knowledge Base

Knowledge Base Structure: Laser-Material Interaction Analysis

Knowledge relating to laser cutting processes can be classified into two categories: structured knowledge and heuristic knowledge. Structured knowledge represents the conceptual understanding of laser cutting phenomena such as laser cutting models. Heuristic knowledge which contains factual data, which can be represented in an IF-THEN form, such as relationships between the cutting process quality and laser operating parameters, and relationships between material characteristics and laser processing suitability.

6-3.1.1 The structured knowledge:

This type of knowledge relates to the fundamental research into laser cutting behaviour. Such as why the cut is formed and how it is formed. Through the analysis of the cutting phenomena based on physical laws, mathematical equations are formulated that describe and explain the interaction phenomena. The mathematical equations that describe the behaviour of the system are termed the laser cutting models. These models originate from two main sources: theoretical analysis and experimental deduction (statistics) leading to empirical models.

knowledge from theoretical analysis:

As mentioned in the previous section, many models have been developed to explain the laser cutting phenomenon. Models that are suitable for on-line process control must give a reasonably accurate process prediction and also be sufficiently simple that they can be computed in real-time. Only then is real-time control possible.

The **Simple Cutting Model** proposed by G. Chryssolouris et al [6] and W. M. Steen [7] was adopted as one of the reference models. They assumed that all the energy enters the melt and is removed before significant conduction can occur. Hence using a heat balance in the cutting region gives a simple mathematical equation that describes the cutting process:

$$[P/tV] = w\frac{\rho}{\eta}\{C_p \Delta T + L_f + m' L_v\} \tag{6-3.1}$$

where: C_p = thermal conductivity
η = coupling coefficient
L_f = latent heat of fusion
L_v = latent heat of vaporisation
m' = fraction of melt vaporised
P = incident laser power
ρ = density
t = thickness
V = cutting speed (feedrate)
w = average kerf width

knowledge from experimental deduction (statistics):

Using regression analysis, data collected from experiments can be used to establish useful experimentally based empirical models for the cutting processes. Table 6-3.1 represents a set of feedrate data for mild steel (BS1449-CR4) and stainless steel (S304) of different thicknesses. A graphical representation is given in figure 6-3.1.

		Material Thickness					
Material Type		1mm	2mm	3mm	4mm	5mm	6mm
MILD STEEL(hp)		5200	2700	2000	1420	1200	950
STAINLESS STEEL(hp)	Feedrate	3500	3100	1300	900	X	X
MILD STEEL(lp)	(mm/min)	2320	1460	840	600	480	427
	hp: 1150 Watts lp: 500 Watts						

Table 6-3.1: Best Cut Feedrate vs. Material Thickness

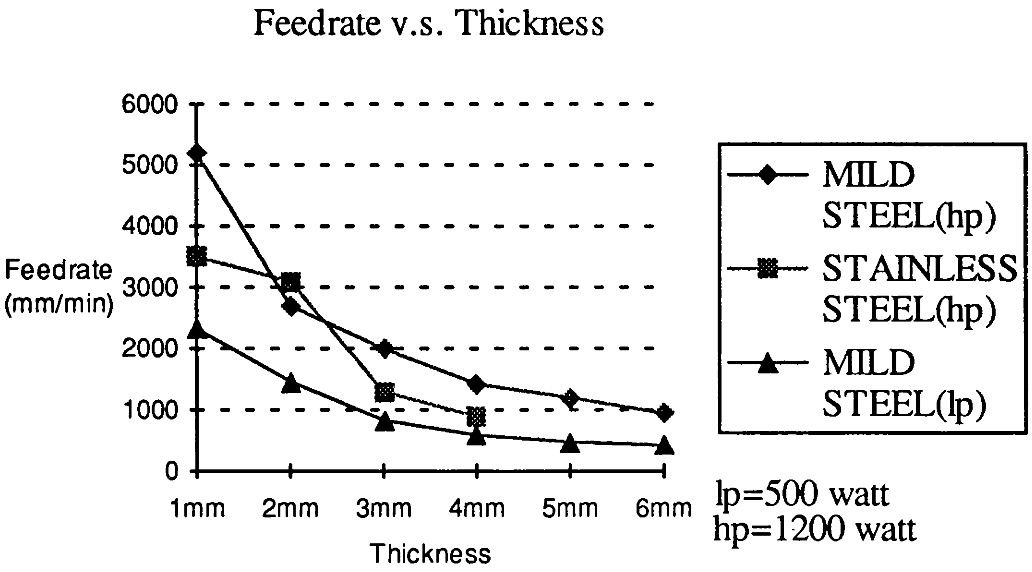

Figure 6-3.1: Feedrate vs. Material Thickness

Using least square regression on the feed rate data experimental models for the laser cutting process of these materials were obtained. For example, take the feedrate - thickness relationship data of mild steel (high power) from table 6-3.1, by using least square regression based on a cubic model, the following equation is obtained:

$$Y = 9040.0 - 4872.9X + 1054.8X^2 - 78.056X^3 \qquad (6\text{-}3.2)$$

6-3.1.2 The heuristic knowledge:

This type of knowledge relates mainly to the relationships between the operating parameters and the cut quality. They also come from definitions /or theoretical analysis and experience /or experimental deduction.

knowledge from definitions /or theoretical analysis:

The quality of laser cutting processes is mainly defined by: the size of heat affected zone (HAZ), the amount of dross attachment, the kerf width, the surface roughness of kerf side walls and the kerf wall angle. Although the quantitative definition of a good cut is relative, for different applications, the following form of rules have general applicability; tolerances vary from one process to another, these are handled through the data base. For example:

R11: IF HAZ > a **THEN** the cut quality is bad

R12: IF surface roughness < b **THEN** the cut quality is good

Knowledge relating to the operating conditions can be deduced and extracted from the theoretical study of the cutting model. Take the simple cutting model for example.

$$A = [P / tV] = w\frac{\rho}{\eta}\{C_p \Delta T + L_f + m' L_v\} = B \qquad (6\text{-}3.1)$$

For the material to be cut, A must be equal to or greater than B. By assuming that the laser didn't cut through the target material (i.e. A < B), either the laser power P has to be increased or the beam feedrate V must be decreased. Thus, rules are implemented as:

R21: IF no cut & low power **THEN** increase laser power

R22: IF no cut & high power **THEN** reduce feedrate

knowledge from experience /or experimental deduction:

The laser operator's experience plays an important part in determining the cutting quality and time needed for such processes. Experienced technicians can correctly adjust the operating parameters according to the phenomena observed and they achieve this quite quickly. But an inexperienced operator will take a lot of time using a trial and error approach. These skilled technicians are the domain experts, their knowledge is implemented in the following form:

R31: IF scale of spark cone sparsity > c
THEN the amount of dross attached is high
R32: IF the amount of dross attached is high &
laser power is okay
THEN increase the assist gas pressure

Relationships deduced from experimental data forms another source of knowledge. For example, figure 6-3.2 shows the relationships between the size of the HAZ and the feedrate and figure 6-3.3 illustrates the relationships between the cut edge surface roughness and feedrate. Feedrates used in figure 6-3.2 and figure 6-3.3 for different thicknesses of mild steel were set according to the following equation:

$$V_i = V_{goodcut}\,[1 - i*(10\%)] \qquad \text{Where } i = 1 \text{ to } 6 \qquad (6\text{-}3.3)$$

The feedrates used are listed in table 6-3.2:

		Material Thickness					
Feedrate Setting		1mm	2mm	3mm	4mm	5mm	6mm
Vgoodcut		5200	2700	2000	1420	1200	950
V1		4680	2430	1800	1280	1080	860
V2		4160	2160	1600	1140	960	760
V3	Feedrate (mm/min)	3640	1890	1400	1000	840	670
V4		3120	1620	1200	860	720	570
V5		2600	1350	1000	720	600	480
V6		2080	1080	800	580	480	380

Table 6-3.2: Feedrates for Different Cutting Conditions and Material Thicknesses (Laser Power = 1150 Watts)

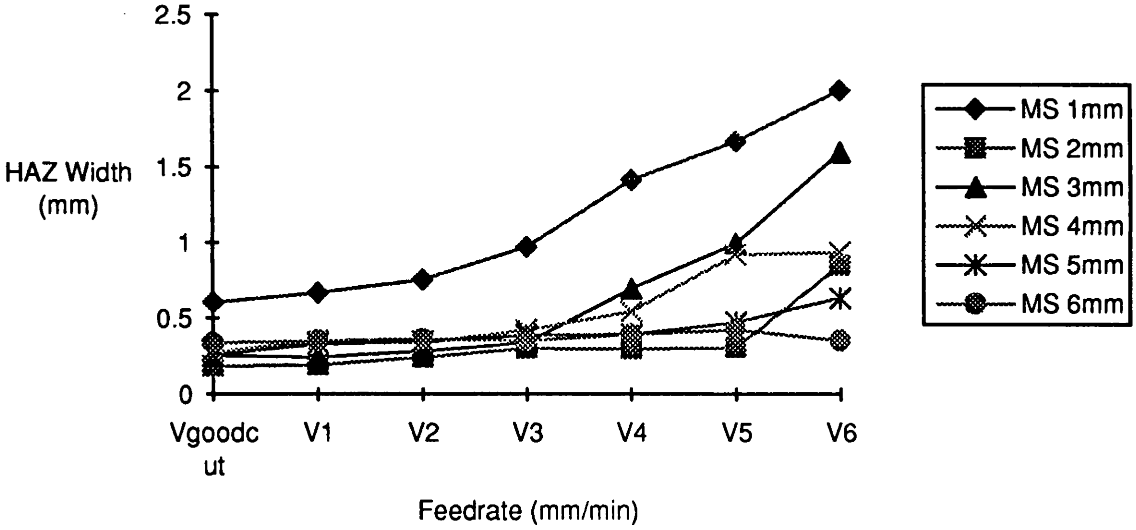

Figure 6-3.2: HAZ vs. Feedrate (Laser Power = 1150 Watts)

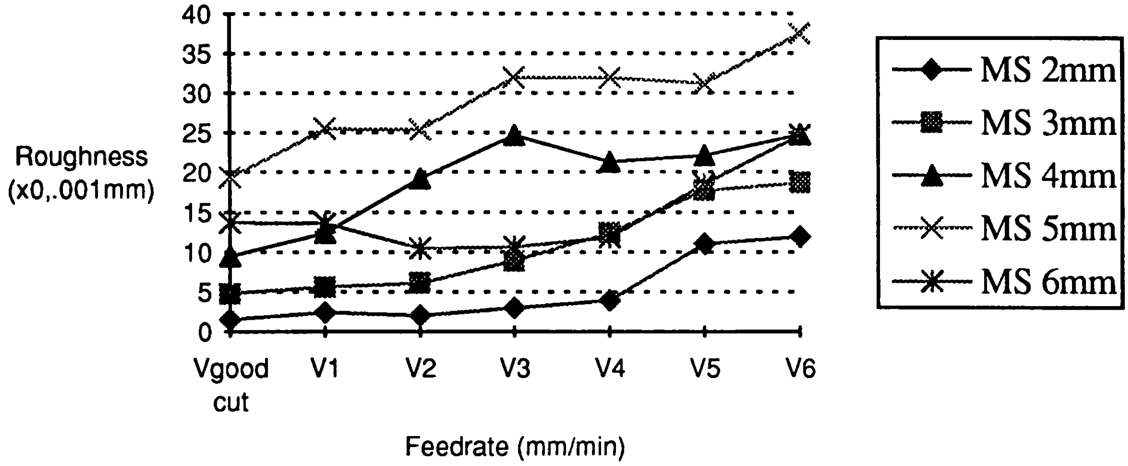

Figure 6-3.3: Kerf Surface Roughness vs. Feedrate

(Laser Power = 1150 Watts)

Rules can be deduced from analysis of this data, hence:

R41: IF feedrate decrease **THEN** HAZ increase

R42: IF feedrate decrease **THEN** surface roughness increase

Expertise relating material types and thicknesses to initial process parameter settings and process quality assessment are then provided through the KBMS expert sub-system. The diagram of this subsystem is shown in figure 6-2.8. It includes the following components:

(i) relational data base
(ii) deductive rule base
(iii) inference engine
(iv) adaptive parameter estimator
(v) man-machine interface
  . explanation facility
  . operation window / control system

6-4 Adaptive Controller

Phenomena within the laser cutting process are extremely complex and highly non-linear. This complexity and non-linearity presents great difficulties in analysizing the process in detail. Because of so many known and unknown parameters involved in the phenomena, the system dynamics are barely analytically predictable. Therefore, conventional control algorithms based on analytical mathematical models are not adequate for controlling the laser cutting processes.

From the analysis on the relationships between the cutting quality and the cutting process parameters, steady state phenomena were observed during the laser cutting process. For a good quality stable cutting process periodic striations were found on the cutting edge surface, a uniform heat affected zone, and characteristic spark cones were generated for good cutting processes. All these phenomena are related to, and result from the temperature dynamics of the target material within the laser-material interaction zone during the laser cutting process. The combined effect of the process parameters results in a steady state temperature fluctuation within the cutting region which is confirmed from both the observation of the laser cutting process results and the theoretical analysis of the striations. Therefore, cut front temperature was used for the feedback parameter in the control process. Due to the non-linear nature of the laser cutting process, adaptive control was applied to control the cutting process.

In 1899, Lummer and Pringsheim examined the distribution of the radiation from a black body, i.e. the relative intensity at different wavelengths, by using an infra-red spectrometer and a bolometer consisting of a single platinum strip. The results of the experiment form a set of curves that give the relative intensities of the different wavelengths at different temperatures. These curves show that as the temperature rises, the intensity of every wavelength increases, and the intensities of the shorter wavelengths increase more rapidly. This is known as the black body radiation law. Each temperature exhibits a characteristic distribution of radiation.

From **Stefan's Law**,

$$E = \sigma \ T^4 \qquad (6\text{-}4.1)$$

where: $\sigma = 5.7 \times 10^{-8}\ \mathrm{Wm^{-2}K^{-4}}$, is called Stefan's constant

the total energy radiated from the black body at temperature T is proportional to T^4. This means that no matter how the process proceeds, the radiation emitted from the workpiece is a function of the temperature only.

$$E = f(T) \qquad (6\text{-}4.2)$$

And from the Wien's Displacement Law,

$$\lambda_m T = \text{constant} \qquad (6\text{-}4.3)$$

where: (i) the constant is 2.9×10^{-3} mK

(ii) λ_m is the wavelength of the peak of the curve

Also from the relationship between the height of the peak of the curve and the temperature T, the following equation is obtained [18]:

$$E_{\lambda m} \propto T^4 \qquad (6\text{-}4.4)$$

Once these quantities are measured for a good quality cut the pattern of the radiation is then fixed. As the "pattern" of the intensity-wavelength relationship is fixed, the energy radiated from a black body for a certain wavelength λ, in band δλ, at temperature T is fixed also. Which is expressed as follows:

$$E_{\lambda T} = E_{\lambda}\delta\lambda \qquad (6\text{-}4.5)$$

where: (i) $E_{\lambda T}$ is the energy radiated in band λ to λ+δλ $(m^{-2}s^{-1})$

(ii) E_{λ} is the emissive power of a black body for the wavelength λ at temperature T

From the above analysis, the amount of energy absorbed by a photodetector is proportional to its wavelength sensitivity range, distance from the radiation source and the detector area. Therefore, by proper design of the optical head (the absorbing area), fixing the distance between the absorbing head to the laser cutting point and selection of the proper photo-sensor (the effective response range, λ to λ+δλ), the response of the photo-sensor is therefore proportional to the temperature of the laser cutting point only. That is:

$$P_{response} = f(T^4) \qquad (6\text{-}4.6)$$

Since the temperature within the laser cutting region consists a wide range of temperatures, according Stefan's Law, the highest temperature contributes most of the energy to the total response from the photo-sensor. That is:

$$P_{response} = f(T_{\max}^4) \qquad (6\text{-}4.7)$$

It may be concluded from the above analysis, that the intensity measurement from the laser cutting region is a function of the temperature of the cutting region and thus is an extremely useful parameter to feedback to the adaptive controller and certainly produced successful results.

6-5 System Evaluation

simulation:

A simulation of a laser cutting process is first developed to validate the KBMS adaptive control system. The adaptive controller was first tested against the simple lumped heat model:

$$\eta P = wtV\rho[C_p \Delta T + L_f + m' L_v] \qquad (6\text{-}5.1)$$

The control measurands are the laser power, P, and the workpiece temperature, T. The simulation results are plotted in figure 6-5.1.

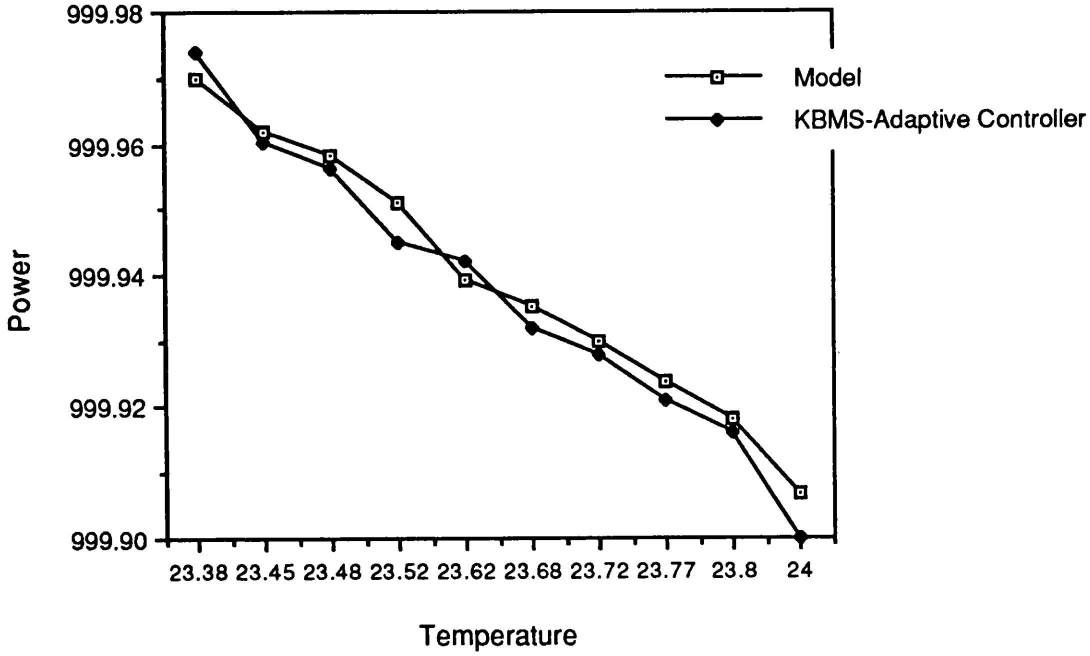

Figure 6-5.1: Adaptive Controller Simulation Result

From the above figure, it can seen that the deviation between the temperature set-point and the measured in-process temperature regulates the adaptive controller to activate a correcting action and adjust the laser power to minimise the difference.

experiment:

Mild steel of different thicknesses were first cut without activating the KBMS adaptive control system. Laser power was set to high power (1150 watts), assist gas pressure was 2 bar. The feedrate used in each cutting process was set to a constant speed, which was 900 mm/min. The resulting kerf surfaces are illustrated in plate 6-5.1.

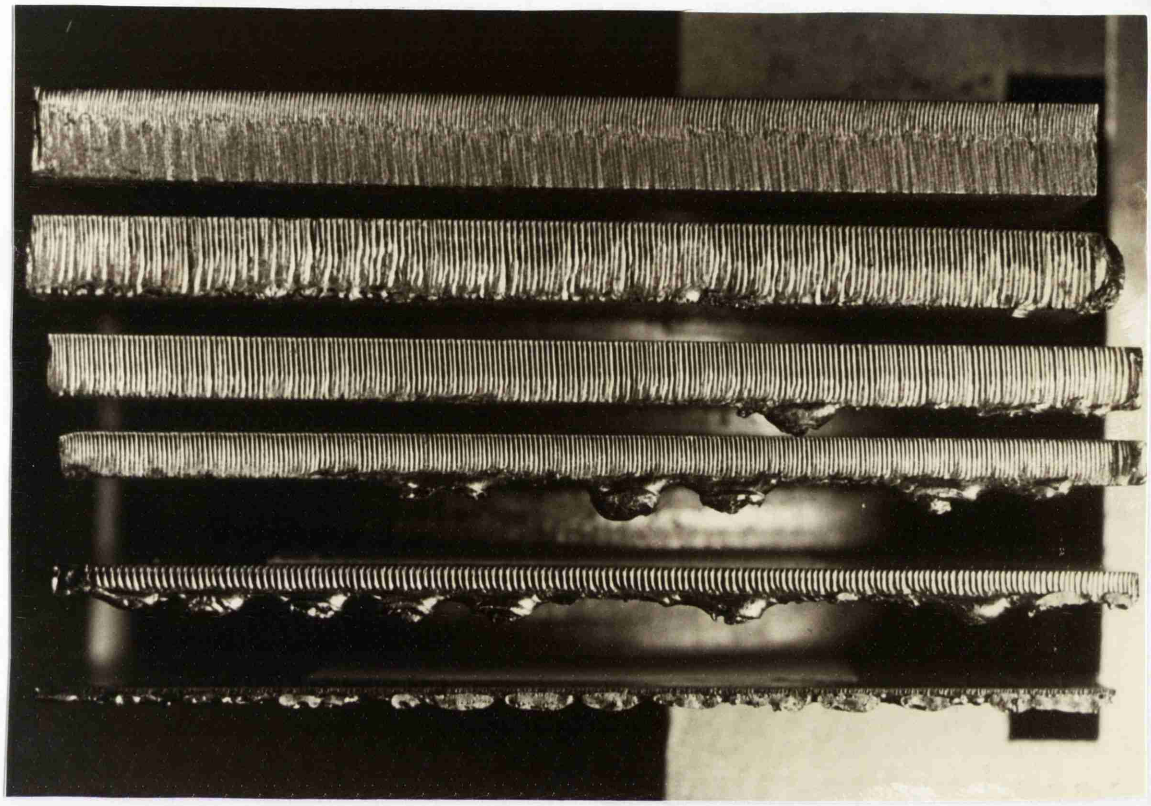

Plate 6-5.1: Kerf Surfaces of Different Thicknesses Mild Steel With Constant Feedrate (Without Activation of KBMS Adaptive Controller)

It is obvious from the plate that the quality of the kerf surface varies with the material thickness.

4 mm mild steel was then cut with the KBMS adaptive controller activated. The laser power was set to high power (1150 watts), the assist gas pressure was 2 bar. The feedrate was first set to 900 mm/min. Figure 6-5.2 illustrates the Irradiance-Time strip chart during the cutting process.

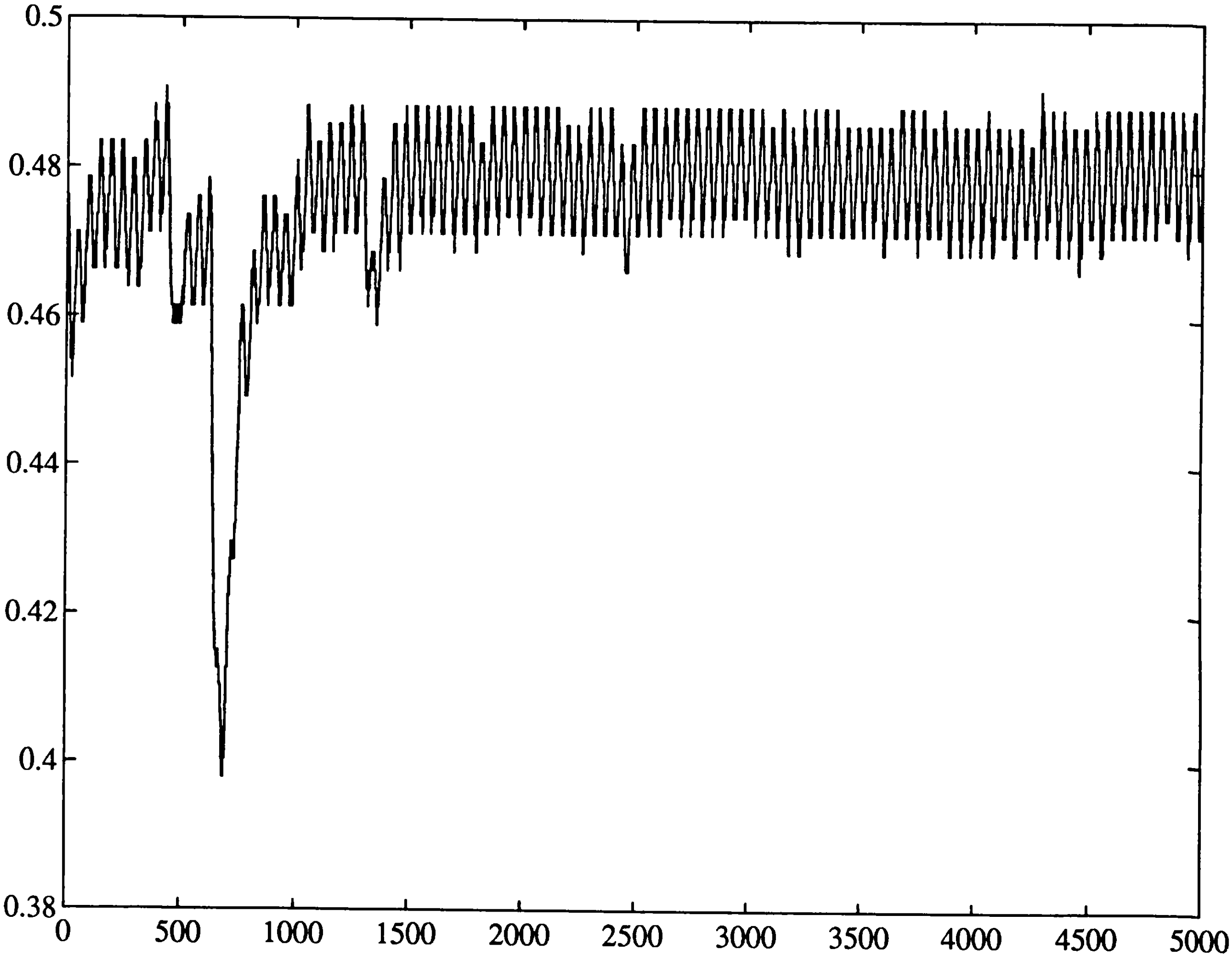

Figure 6-5.2: Irradiance - Time Strip Chart
(With the KBMS Adaptive Control System)

It can be seen from the above irradiance-time strip chart that the irradiance emitted from the cut front fluctuated in the beginning of the cut, when the cut quality is poor, and then became stable when the cut quality improved. The resulting kerf surface is shown in plate 6-5.2.

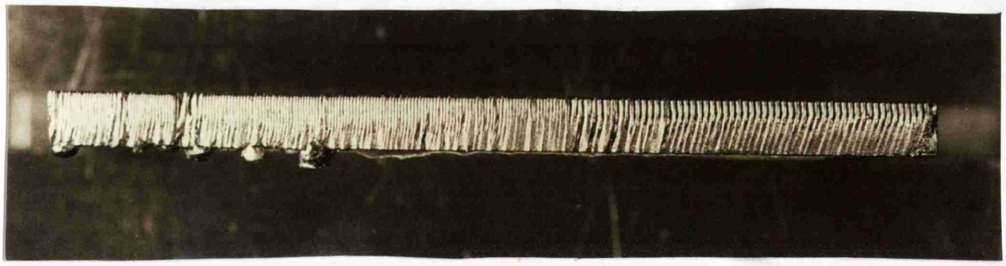

Plate 6-5.2: Kerf Surface of 4 mm Mild Steel
(With the KBMS Adaptive Control System)

From the above plate it can be seen that the quality of the kerf surface improved as the adaptive controller adjusted the laser beam feedrate according to the measurement of the cut front emitted irradiance.

Plate 6-5.3 shows the resulting kerf surface for different thicknesses of mild steel with the KBMS adaptive controller switched on, this should be compared with plate 6-5.1.

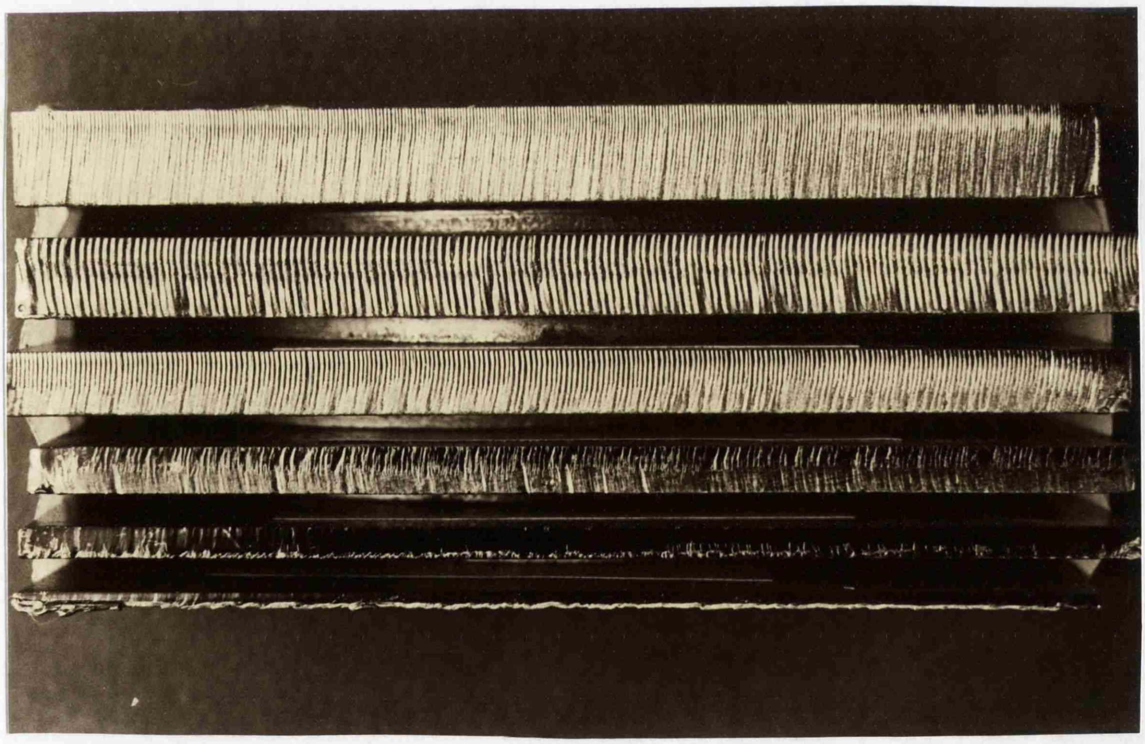

Plate 6-5.3: Kerf Surfaces of Different Thicknesses Mild Steel
(With Activation of KBMS Adaptive Controller)

Hence, the adaptive controller dramatically improved cut quality by optimising the feedrate.

6-6 References

[1] Reactive gas assisted laser cutting - physical mechanism and technical limitations, by Dieter Schuocker, Industrial Applications of Laser Technology, Apr. 1983

[2] Dynamic Phenomena in Laser Cutting and Cut Quality, by Dieter Schuocker, Appl. Phys. B 40, 1986

[3] Hydrodynamical instability of melt flow in laser cutting, by M.Vicanek, G. Simon, H. M. Urbassek, and I. Decker, J. Phys. D: appl. Phys. 20 1987

[4] Linear stability analysis of molten flow in laser cutting, by Ming-Jye Tsai and Cheng-I Weng, J. Phys. D: Appl. Phys. 26, 1993

[5] Toward a General Theory of Cutting: A Relationship Between the Incident Power Density and the Cut Speed, by K. A. Bunting and G. Cornfield, Transaction of the ASME, Feb. 1975

[6] Gas jet effect on laser cutting, by G. Chryssolouris and W. C. Choi, SPIE Vol. 1042 CO_2 Lasers and Applications, 1989

[7] Laser Material Processing, by W. M Steen, Springer - Verlag, 1991

[8] Conduction of Heat in Solids, by H. S. Carslaw and J. G. Jaeger, Oxford at the Clarendon Press, 1959

[9] Laser-Materials Interactions, by M. Bass, Encyclopaedia of Lasers and Optical Technology

[10] Industrial Applications of Lasers, by J. F. Ready, 1978

[11] Physical Processes in Laser-Materials Interactions, by M. Bertolotti, Plenum Press

[12]. Shortliffe, E. H., Dans, R., Axlin, S. G., Buchanan, B. G., Green, C. C. and Cohen, S. N. (1975). Computer-based consultations in clinical therapeutics: Explanation a rule acquisition capabilities of the MYCIN system. Comput. Biomed. Res., Vol.8, 303-320

[13]. Shortliffe, E. H., Buchanan, B. G. and Feigenbaum, E. A. (1979). Knowledge engineering for medical decision making: A review of computer-based clinical decision aids. Proceeding of the I.E.E.E., Vol. 23, p351-374

[14]. Buchanan, B. G. and Shortliffe, E. H. (1984). Rule-based expert systems: The MYCIN experiments of the Standard heuristic programming project. Reading, Mass. Addison Wesley Publishing Company.

[15]. Duda, R. O., Gaschning, J., Hart, A. E. Konolige, K., Barret, P. and Slocum, J. (1978). Development of the PROSPECTOR. Consultation system for mineral explorations. Final Report. S.R.I, 5821-6415. Projects. S.R.I. International Inc. Menlo Park. C.A.

[16]. Erman, L. D., Hayes, Roth, I., Lesser, V. R. and Reddy, D. R. (1980). The HEARSAY II speech understanding systems. Integration knowledge to resolve uncertainty. Computers Surveys, Vol. 12, 13-253.

[17]. Mac Dermott, J. R-1: A ruled-based configurer of computer systems. Carnegie Mellon University. Report CMU.CS, p80-119.

[18] M. Nelkon and P. Parker (1974). Advanced Level Physics, 3rd edition.

Chap 7

Spark Cone Image Evaluation Shell

PAGE

Nomenclature

α = absorption coefficient

f = focal length

$f(x,y)$ = image functionθ

$H(x,y)$= filter function

$I(x,y)$ = intensity distribution

λ = wavelength

$N(p,q)$= spectral density of the background noise

θ_R = incident angle of the read beam

θ_W = incident angle of write beam

$R(p,q)$= reference beam

$S^*(x,y)$= complex conjugate of the signal spectrum

$t_A(x,y)$= amplitude transmittance of the input plane

$U(x,y)$= field distribution

$w(x,y)$= Wiener filter function

z = distance between planes

7-1 Introduction

In gas assisted laser cutting, the workpiece is moved relative to the laser beam or vice versa. The material is made molten by the focused beam and then removed by a high pressure gas jet adjusted either coaxially or off-axially with the laser beam. Figure 7-1.1 illustrates the coaxial arrangement, which is normally adopted in industrial applications.

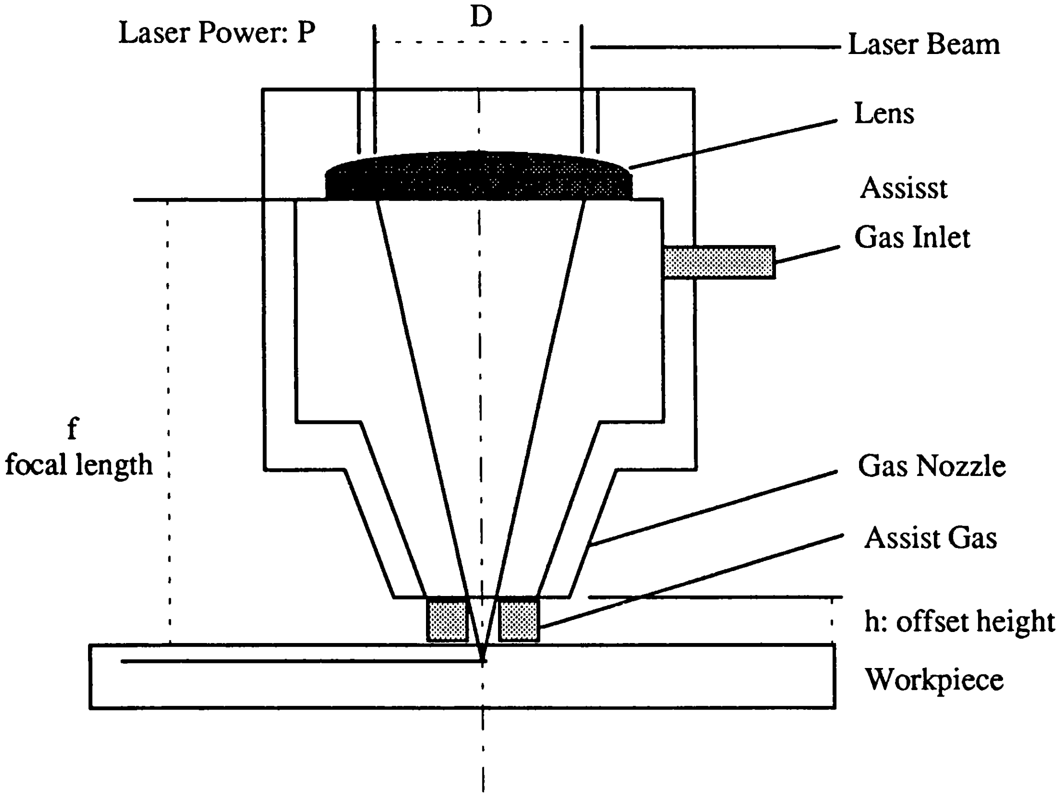

Figure 7-1.1: Coaxially Arranged Nozzle

A reactive gas is normally utilized for most ferrous-based metal targets to enhance the cutting effect. When the high speed reactive O_2 gas flows through the kerf and blows out from the nozzle-like lower surface, the high temperature liquid and partially vaporized metal burns in the O_2 gas. A characteristic spark cone is thus formed which is physically dependant upon the specific kerf geometry and gas dynamics. Process quality can be assessed through the analysis of this spark cone image.

Coherent optical information processing has developed since the availability of commercial lasers and the introduction of the first interferometrically generated complex filter by Vander Lugt [1] in the early 1960's. Coherent optical information processing may be exploited for pattern matching by image cross-correlation. Many different algorithms have been developed and optimised for particular problems, for example: classical matched filter (CMF), phase only filter (POF), synthetic discriminant function filter (SDF), minimum average correlation energy filter (MACE), and inverse filter, etc.

The availability of high purity photorefractive materials has now made it possible to perform updateable real-time cross correlation[2][3]. The frequency-plane correlation technique using Bismuth Silicon Oxide $Bi_{12}SiO_{20}$ (BSO) has been developed by several researchers[Herriau et al[4], Cooper et al[5], and Young et al[6].] Based on a non-degenerate four wave mixing interaction in the crystal, BSO, an updateable correlation may be realised. Figure 7-1.2 illustrates the necessary optical system. This particular pattern recognition technique is currently being constructed for the spark cone image evaluation, as it is capable of assessing the images in real-time.

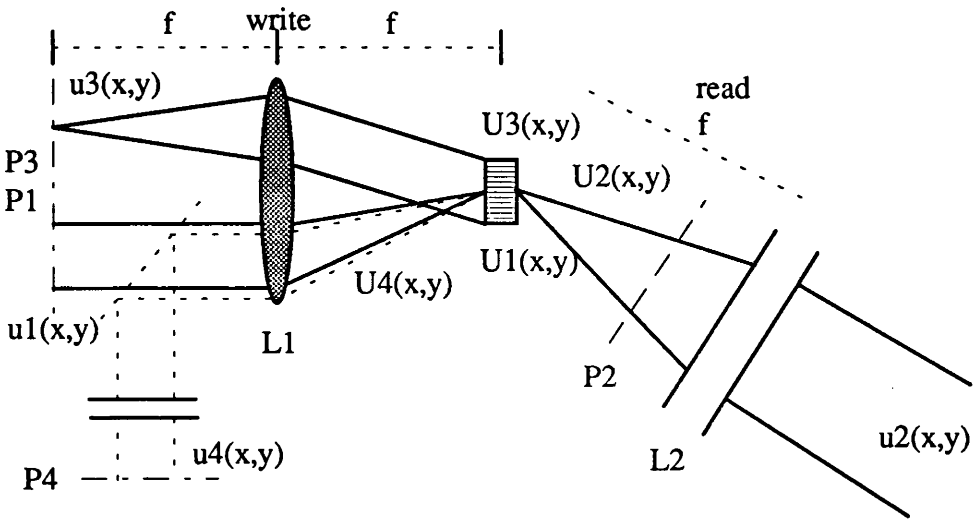

Figure 7-1.2: Non-Degenerate Four Wave Mixing Correlator

A refinement of the matched spatial filter multiplexing technique was suggested by Braunecker et al [7] and extended to the synthetic discriminant function filter by Casasent et al [8]. The advantage of this formulation is that it allows the on-axis correlation peak height to be controlled. Therefore, the in-class and out-of-class images can be distinguished through the measurement of the resulting cross-correlation peak height. A specific SDF filter can be encoded, by using the good cut spark cone images for different material thicknesses and different target materials. A high cross-correlation peak from the process spark cone image and the filter indicates a good cut quality. A low peak, on the other hand, indicates a poor cut quality. Digital simulations of the optical processor are implemented and the results are presented herein.

7-2 Theoretical Analysis

7-2.1 Basic Operation Performed by Coherent Optical Information Processing - the Fourier Transform

First, we refer to figure 7-2.1.

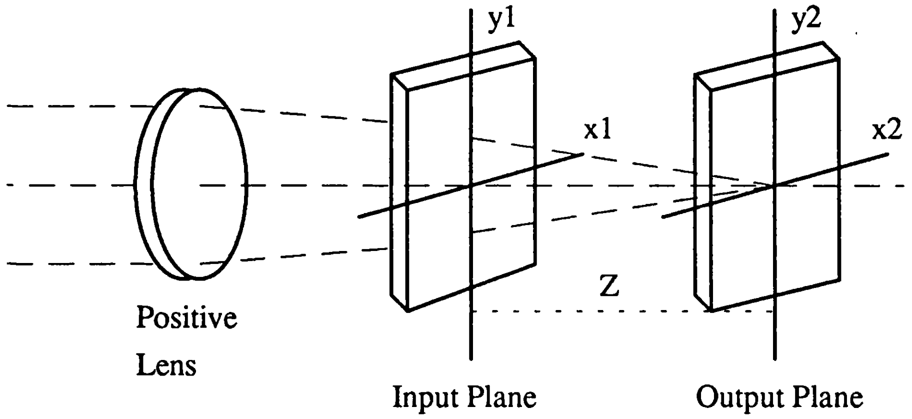

Figure 7-2.1: Optical Fourier Transform

An input transparency, (x_1, y_1) plane, is illuminated by a plane wave which is converging toward the focus at the origin of the output plane (x_2, y_2). Using a parabolic approximation to the spherical wavefront, we obtain a field distribution in the (x_1, y_1) plane given by

$$U_1(x_1, y_1) = U_0 \exp\left[-j\frac{\pi}{\lambda\ z}\left(x_1^2 + y_1^2\right)\right] t_A(x_1, y_1) \qquad (7\text{-}2.1)$$

where:

λ: is the wave length

$t_A(x_1, y_1)$: is the amplitude transmittance of the input plane

z: is the distance between the two planes

By using the Fresnel propagation law, the observed intensity in the output plane (x_2, y_2) becomes:

$$I_2(x_2, y_2) = \frac{I_0}{\lambda^2 z^2} \cdot \left| \int\int_{-\infty}^{\infty} t_A(x_1, y_1) \exp\left[-j \frac{2\pi}{\lambda z}(x_1 x_2 + y_1 y_2) \right] dx_1 dy_1 \right|^2 \quad (7\text{-}2.2)$$

Now, we consider the set-up in figure 7-2.2.

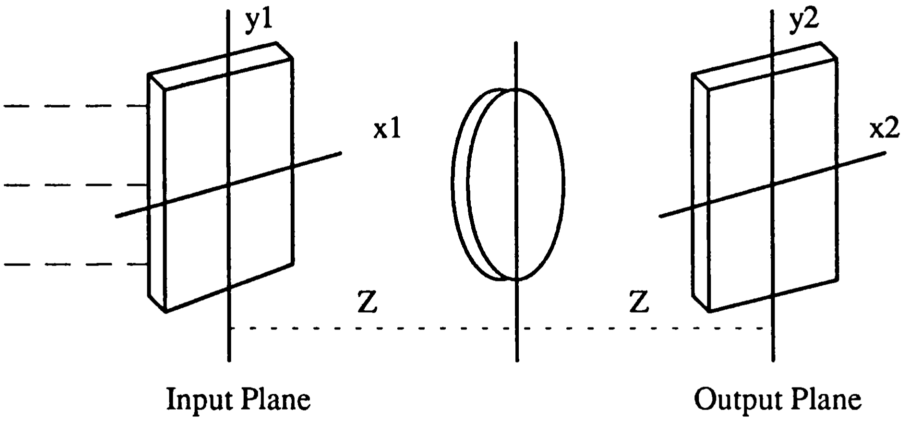

Figure 7-2.2: Focal Plane to Focal Plane Fourier Transform

The input transparency is placed in the front focal plane of a positive lens and the output intensity distribution is measured in the output plane which is placed in the rear focal plane of the positive lens. A plane wave is used instead of a spherical wave. This particular geometry also leads to the similar relationship, as that of the previous set-up, between these two planes, which is:

$$U_2(x_2,y_2)=\frac{U_0}{\lambda f}\int\int_{-\infty}^{\infty}U_1(x_1,y_1)\exp\left[-j\frac{2\pi}{\lambda f}(x_1x_2+y_1y_2)\right]dx_1dy_1 \quad (7\text{-}2.3)$$

where: f = is the focal length

That is, an exact Fourier Transform relation between the complex field in the input plane and the complex field in output plane. From the above analysis, it can be seen that a spherical lens can take the Fourier Transform of a complex distribution of light.

7-2.2 Image Matching Through Spatial Filtering

Convolution Integral:

The convolution of two functions is a significant physical concept in many diverse scientific fields. To be more specific, the convolution integral is given by:

$$y(t)=\int_{-\infty}^{\infty}x(\tau)h(t-\tau)d\tau=x(t)*h(t) \quad (7\text{-}2.4)$$

Function y(t) is said to be the convolution of the function x(t) and h(t).

The result of the convolution integral can be graphically explained as follow steps:

1.Folding: Take the mirror image of h(τ) about ordinate axis
2.Displacement: Shift h(-τ) by the amount t
3.Multiplication: Multiply the shifted function h(t-τ) by x(τ)
4.Integration: Area under the product of the h(t-τ) and x(τ) is the value of the convolution at time t

Therefore, from the above analysis, the convolution of two identical functions results in a triangle like shape, with a high peak, whose height depends on the particular shape of the function.

By taking the Fourier Transform of the both side of the convolution integral:

$$\int_{-\infty}^{\infty} y(t)e^{-j2\pi\, ft}dt = \int_{-\infty}^{\infty}\left[\int_{-\infty}^{\infty} x(\tau)h(t-\tau)d\tau\right]e^{-j2\pi\, ft}dt \qquad (7\text{-}2.5)$$

which is equivalent to:

$$Y(f) = \int_{-\infty}^{\infty} x(\tau)\left[\int_{-\infty}^{\infty} h(t-\tau)e^{-2\pi\, ft}dt\right]d\tau \qquad (7\text{-}2.6)$$

By substituting σ=t-τ, we conclude

$$Y(f) = \int_{-\infty}^{\infty} x(\tau)e^{-j2\pi\, f\tau}H(f)d\tau = H(f)X(f) \qquad (7\text{-}2.7)$$

The time domain convolution can therefore be calculated simply by: multiplication of the two functions in the frequency domain, then inverse Fourier Transform the result. This is also known as the convolution theorem.

Correlation Integral:

The correlation integral is given as:

$$z(t) = \int_{-\infty}^{\infty} x(\tau)h(t+\tau)d\tau \qquad (7\text{-}2.8)$$

Comparing the above expressions with that of the convolution integral, the two integrals are closely related; the only difference is there is no folding of one of the integrands in correlation. For the special case where either x(t) or h(t) is an even function, convolution and correlation are equivalent.

Again, by taking the Fourier Transform of both sides, a similar result to that of the convolution integral is obtained:

$$Z(f) = H(f)X^{*}(f) \qquad (7\text{-}2.9)$$

If x(t) and h(t) are the same function, the above equation is normally termed the autocorrelation function; if x(t) and h(t) differ, it is called the cross-correlation.

In the special case when x(t) is an even function then X(f) is purely real and $X(f)=X^{*}(f)$. The Fourier Transform of the correlation is identical to that of convolution integral. This is the case in most image processing problems, where only the real part of the Fourier Transform is taken into consideration.

7-2.3 Matched Filtering - With an Interferometrically Generated Filter:

When an incoming image f(x,y) is correlated with a reference image h(x,y), which has been encoded into a matched spatial filter; the result g(x,y) is related to the input through the simple convolution equation, where:

$$g(x,y) = \int\int_{-\infty}^{\infty} f(\xi,\eta)h(x-\xi,y-\eta)d\xi \ d\eta \qquad (7\text{-}2.10)$$

where h(x-ξ, y-η) is the response of the filter at coordinates (x, y) to a unit impulse (point source) at coordinates (ξ, η). Using the Convolution Theorem of Fourier analysis:

$$G(p,q) = F(p,q)H(p,q) \qquad (7\text{-}2.11)$$

where p and q represent the spatial frequency variables.

The output response of the filter will be the inverse Fourier Transform of G(p,q). This operation is performed by placing another spherical lens behind the filter at focal distance and measure the output from the rear focal plane. The coherent optical processing arrangement is shown in figure 7-2.3. A bright spot in the output plane indicates a high probability of similarity of the two images, and low-light levels indicate a low probability of similarity.

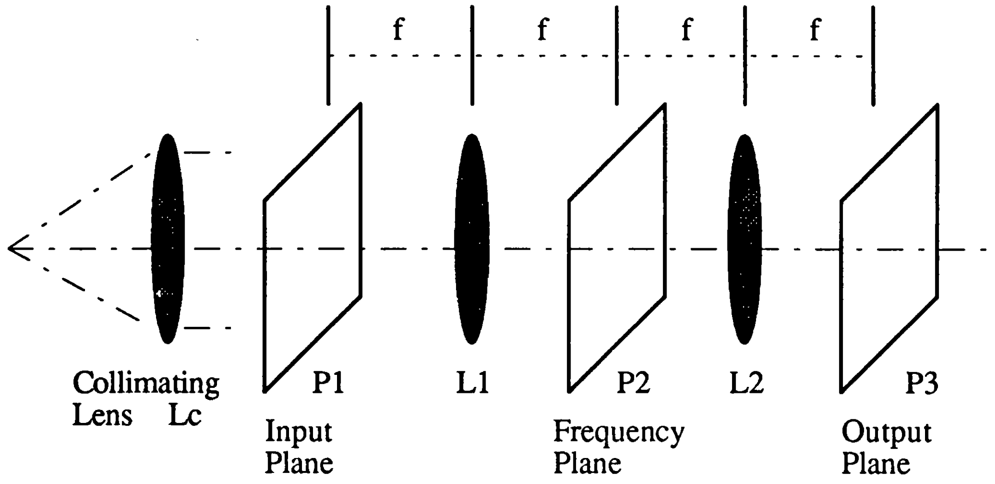

Figure 7-2.3: Coherent Optical Processing

The vital point of this matching technique is to establish an optimum filter which will be able to recognise the similar images and the distinguish them from dissimilar inputs. That is, to maximize the ratio of peak signal energy to mean square noise energy given by the filter function as follow:

$$H(p,q) = \frac{kS^{*}(p,q)}{N(p,q)} \qquad (7\text{-}2.12)$$

where:

k = is a constant chosen to make $|H(p,q)| < 1$ for a passive spatial filter

N(p,q) = is the spectral density of the background noise

$S^{*}(p,q)$ = is the complex conjugate of the signal spectrum

To realize this filter, we follow Vander Lugt's development. A Mach-Zehnder interferometer is modified to record the phase information in a light distribution by combining that distribution with a reference wave whose amplitude and phase distributions are known. The system arrangement is shown in figure 7-2.4.

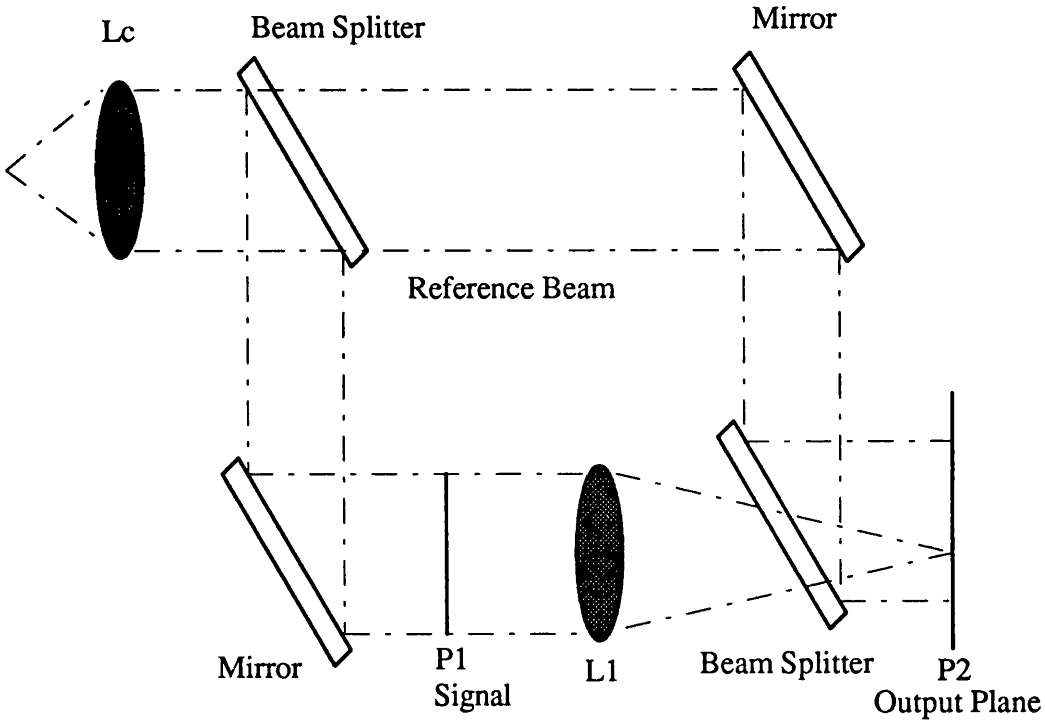

Figure 7-2.4: Modified Mach-Zehnder Interferometer

The Fourier Transform of the signal s(x, y) is to be found. As the system is constructed, the output in the rear focal plane of the lens L1 is:

$$\begin{aligned} G(p,q) &= |R(p,q) + S(p,q)|^2 \\ &= |R(p,q)|^2 + |S(p,q)|^2 + R^*(p,q)S(p,q) + R(p,q)S^*(p,q) \quad (7\text{-}2.13) \end{aligned}$$

Where:

R(p,q): represents the light coming from the reference beam

S(p,q): is the signal spectrum

By adjusting both the amplitude and phase of R(p,q), the phase information of $S^*(p,q)$ is contained in G(p,q) and can be recorded on film to realize the optimum filter. This filter can therefore be placed in the optical system at plane P_2 in figure 7-2.3. By taking the inverse transform of the light distribution in P_2 the output is given by:

$$\begin{aligned} \text{output} = \quad & \frac{1}{4\pi^2}\int\int_{-\infty}^{\infty} F(p,q)A(p,q)e^{j(px+qy)}dpdq \\ + \quad & \frac{1}{4\pi^2}\int\int_{-\infty}^{\infty} F(p,q)H^*(p,q)e^{j[(x-b)p+(y-c)q]}dpdq \\ + \quad & \frac{1}{4\pi^2}\int\int_{-\infty}^{\infty} F(p,q)H(p,q)e^{j[(x+b)p+(y+c)q]}dpdq \qquad (7\text{-}2.14) \end{aligned}$$

These three outputs are separated into three different locations. The third term appears off-centre from the optical axis by an amount x = -b, y = -c, this is the desired output from the filtering operation. By carefully selecting the b value (b greater than the length of signal in the x direction) and placing the output sensor properly, the result may be measured.

7-2.4 Spatial Filtering in BSO

The above algorithm relies on wet-processed holographic filters, and is therefore only capable of processing small numbers of reference image sets. It is therefore not suitable for the processing needs of iterative correlation, which is necessary for identification of large numbers of different reference images or for unconstrained recognition of three-dimensional objects. For such applications the filter function must be programmable in real-time.

By utilising the pattern analysis technique of image correlation, the height of the output peak is a measure of the degree of similarity of the two images. Recall the correlation theorem, the cross-correlation of two functions is equivalent to a multiplication of their complex field amplitudes in the Fourier plane, that is:

$$u_i(x,y) \text{ X } u_j(x,y) = U_i^*(x',y').U_j(x',y') \qquad (7\text{-}2.15)$$

where X denotes the cross-correlation operation, U_i and U_j denotes the Fourier Transforms. Through the use of the photorefractive material (BSO), a frequency-plane correlator capable of updating the filter function may be realised. Figure 7-1.2 illustrates the frequency-plane correlator design. The test input image $u_1(x,y)$ and the reference beam $u_3(x,y)$ both are placed in the front focal plane. The lens generates the Fourier Transform of both u_1 and u_3 at the photorefractive material (the BSO) which is placed in the back focal plane. These two input fields interfere and produce a phase grating in the photorefractive material. The complex modulation index of that grating, m_{13}, is given by:

$$m_{13} = \frac{2U_1(x',y')*U_3(x',y')}{\left(|U_1(x',y')|^2 + |U_3(x',y')|^2\right)} \qquad (7\text{-}2.16)$$

Since the distribution of $u_3(x,y)$ is uniform in the Fourier plane, the above equation can be rewritten as:

$$m_{13} = \frac{2U_1(x',y')*U_3}{(|U_1(x',y')|^2 + I_3)} \qquad (7\text{-}2.17)$$

Where U_3 is the constant field amplitude of the reference beam and I_3 is its intensity. The input distribution U1(x',y') is therefore encoded on a spatial carrier whose wavelength is determined by the angle between the reference beam and the zero spatial frequency component of the test input distribution. To perform the image correlation which is a multiplication in the Fourier plane, the photorefractive material is illuminated with the Fourier Transform of the second input distribution, $U_2(x',y')$. The zero spatial frequency component of this distribution has to be arranged to be Bragg matched to the grating carrier frequency which is given by:

$$\sin(\frac{\theta_R}{2}) = \frac{\lambda_R}{\lambda_w}\sin(\frac{\theta_w}{2}) \qquad (7\text{-}2.18)$$

where: λ_R = wavelength of the read beam

λ_W = wavelength of the write beam

θ_R = incident angle of the read beam

θ_W = interaction angle of the write beam

The reading field distribution $U_2(x',y')$ is then diffracted by the photo induced grating on the photorefractive material to produce the output field distribution, $U_4(x',y')$. Which is given by:

$$U_4(x',y') = Am'_{13}U_2(x',y') \qquad (7\text{-}2.19)$$

Where m'_{13} is the modified modulation index in the presence of the reading beam and A is a parameter which depends on the material and operation condition. The overall effect is to produce an output field of:

$$U_4(x',y') = U_1^*(x',y')U_2(x',y')W(x',y') \qquad (7\text{-}2.20)$$

Where W(x',y') is a spatial frequency weighting function given by:

$$W(x',y') = \frac{2A}{(|U_1(x',y')|^2 + I_3 + a|U_2(x',y')|^2)} \qquad (7\text{-}2.21)$$

The parameter 'a' reflects the degree of interaction of the reading beam with the grating. For a non-degenerate system, a << 1, the third term in the denominator may be neglected. Therefore equation 7-2.21 becomes:

$$W(x',y') = \frac{2A}{(|U_1(x',y')|^2 + I_3)} \qquad (7\text{-}2.22)$$

Therefore, from the analysis, it can be seen that the photorefractive response can produce the required field multiplication. That is the two-dimensional correlation of the two input functions. For true correlation, the weighting function is chosen to be spatially constant, i.e. $|U_1(x',y')|^2 << I_3$. And for edge-enhanced correlation, the weighting function is biased to high spatial frequencies, i.e. $|U_1(x',y')|^2 >> I_3$. Thus, by varying the intensity ratio of the writing beams, the correlation function discrimination can be altered in real time.

7-2.5 Rapid Pattern Recognition by Using SDF Filter

A SDF filter can be specified as the vector inner product between the space domain representation of the filter function, **H**, and the input training set image, $\mathbf{x_i}$, which satisfies the condition

$$\mathbf{x_i}(x,y) \bullet \mathbf{H}(x,y) = \mathbf{C_n} \qquad (7\text{-}2.23)$$

where $\mathbf{C_n}$ is the desired, user specified, on axis value. By solving the following equation:

$$\mathbf{a} = \mathbf{R}^{-1}\mathbf{C_n} \qquad (7\text{-}2.24)$$

The weighting coefficients, of **a**, for the SDF filter can be determined. And the SDF filter is thus formed as follows:

$$H(x,y) = \sum_{i=1}^{n} a_i x_i(x,y) \qquad (7\text{-}2.25)$$

This SDF filter can hereafter be used as the reference image in the above system. By constructing the SDF from spark cone images obtained with good cuts, the SDF filter can be used to assess the laser cut quality.

7-3 Digital Implementation and Simulation of Spark Cone Image Evaluation

7-3.1 Image Grabbing:

512 by 512 pixel images are grabbed through an ITEX 150 frame grabber and then passed to the host computer for further digital processing. The hardware connection is shown in figure 7-3.1.

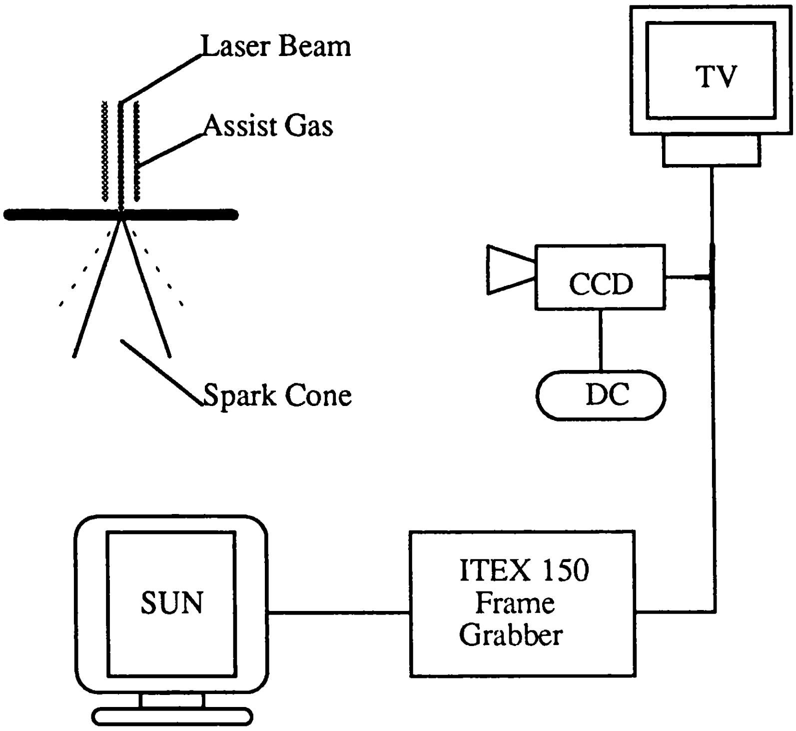

Figure 7-3.1: Spark Cone Evaluation System Diagram

The CCD camera is fixed on a framework attached to the nozzle head. The distance between the cutting point and CCD camera is set at 50 cm for every process. Zoom factor, f number and aperture of the camera are set to fix the conditions. The above arrangement will guarantee that the images formed on the CCD camera have the same geometrical relation. Images of the spark cone that form on the CCD camera are then transferred to the ITEX 150 frame grabber. Where, driven by commands from the host computer, they are grabbed and temporarily stored in one of the four buffers. The stored images are then transferred to the host computer for further analysis, they are also displayed on a side-connected TV for process monitoring.

Plate 7-3.1 is a spark cone image of a 3mm mild steel cutting process. From the analysis of its histogram, figure 7-3.2, it can be discovered that there are several layers of different intensity within the spark cone. For convenience, this spark cone is considered to consist of two separate sub-cones, an intense and more concentrated inner cone, and a lighter and sparse outer cone. Edge information of the inner cone is extracted to enhance the system discrimination ability. A program is implemented to digitally simulate the pre-processing.

7-3.2 Image Smoothing and Thresholding:

It can be seen from plate 7-3.1, that the outer cone consists of sparse spark particles and spark lines. These sparse points and lines do not preserve any consistent edge feature and present image processing difficulties and errors on later spark cone comparisons. Therefore, a spatial-domain image smoothing technique, neighbourhood averaging, followed by a thresholding procedure, is applied to the incoming image to eliminate these sparse particles and lines and explicitly present the inner cone.

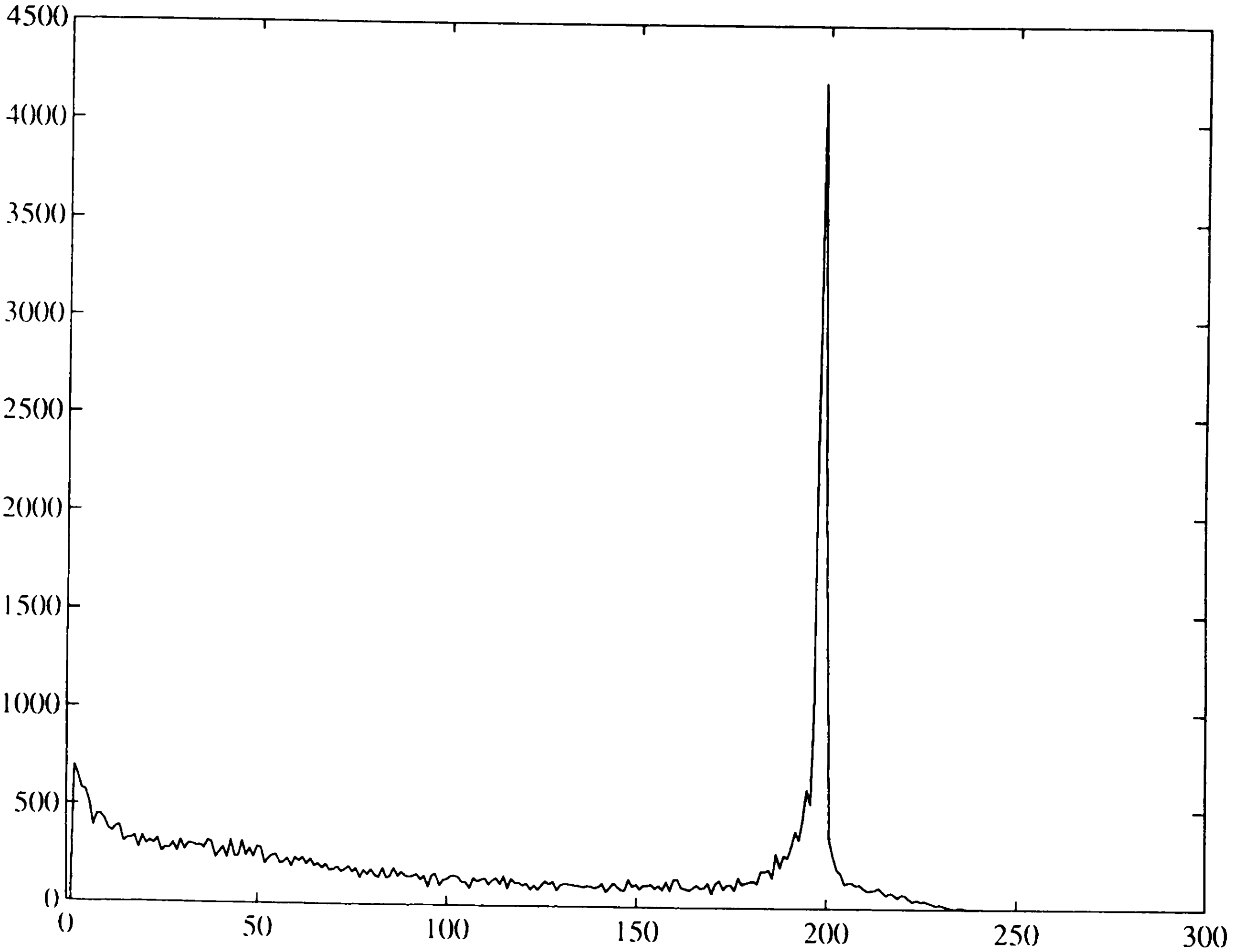

Figure 7-3.2: Histogram of The Original Spark Cone Image

A 5X5 neighbourhood is used to generate the smoothed image. The grey level at every point (x,y) on the smoothed image is obtained by averaging the grey-level values of the pixels of the original image contained in the 5X5 neighbourhood of (x,y). That is:

$$g(x,y)=\frac{1}{25}\sum_{(n,m)\in S} f(n,m) \qquad (7\text{-}3.1)$$

where f(x,y): the original image

g(x,y): the smoothed image

S: the set of co-ordinates of points in the neighbourhood of the point (x,y) including (x,y) itself

Plate 7-3.2 shows the smoothed image of plate 7-3.1.

Then the most populated intensity value (except value zero) is adopted as the threshold value for the thresholding procedure. Plate 7-3.3 is the result of the processing of plate 7-3.1. The inner cone is thus enhanced.

7-3.3 Edge Enhancement and Spark Cone Image Matched Filtering:

The abrupt change of grey-level value at the edges of an image are the high frequency data, in the frequency-domain, of a specific image. A low noise Difference of Gaussian (DOG) pass band algorithm was used to extract the edge information from the spark cone. As mentioned in the previous section, much work on the use of the photorefractive crystal Bismuth Silicon Oxide

(BSO) has been done by Huignard and co-workers[4] who demonstrated a Joint Transform correlator (JTC) configuration employing non-degenerate four wave mixing in BSO. And later by Cooper et al, and Nicholson et al when an alternative NDFWM was proposed. For this spark cone evaluation system, the principle adopted basically follows the structure of the system developed for industrial component inspection by Young et al [6]. A hologram is written to the BSO by the interference of U_1, the Fourier transform of u_1 the test image, and U_3, a plane wave reference beam of variable strength. U_2, the Fourier transform of u_2, is diffracted from the grating formed in the BSO to yield, after a further Fourier transform, the correlation between U_1 and U_2 at plane P4. For the steady state and ignoring any beam coupling, the grating is written as:

$$m(fx,fy)=\frac{2U_1^*(fx,fy)\exp(\frac{-\alpha_w z}{2})U_3\exp(\frac{-\alpha_w z}{2})}{|U_1(fx,fy)|^2\exp(-\alpha_w z)+|U_3|^2\exp(-\alpha_w z)+a|U_2(fx,fy)|^2\exp(-\alpha_r(d-z))} \tag{7-3.2}$$

where α_w, α_r is the absorption coefficient of the write and read beams in the BSO. A HeNe beam is used as the read beam and an Ar+ beam is used as the write beam.

Since 'a', the quantum efficiency of the interaction of the HeNe beam with the grating is only about 0.06 of that of the Ar+ beam, the above equation reduces to:

$$m(fx,fy,z)=\frac{2U_1{}^*(fx,fy)U_3}{|U_1(fx,fy)|^2+I_3} \qquad (7\text{-}3.3)$$

where U_3 is constant. (plane wave reference). Which is the same as equation 7-2.17. The beam ratio is defined as:

$$BR=\frac{Amplitude\_of\_U_1\_peak\_(at\_zero\_spatial\_frequency)}{Amplitude\_of\_plane\_wave\_reference\_beam\_U_3} \qquad (7\text{-}3.4)$$

When the beam ratio is set to a high value, for low frequency where $|U_1|^2 >> |U_3|^2$, equation (7-3.3) becomes:

$$m\approx\frac{2U_3}{U_1} \qquad (7\text{-}3.5)$$

Through the analysis on the frequency-domain, by Young [6], it was found that when a high ratio was chosen, the BSO filter is formed to exhibit a similar characteristic to that of a Difference of Gaussian (DOG) filter. Which preserves the high-pass characteristic and enhances the effect of the edges.

Plate 7-3.4 illustrates the result of the process on plate 7-3.1 with BR=20,

7-3.4 Cone Comparison-Matched Spatial Filtering

Following on from the discussion above. If the assumption of linearity is made between the grating modulation and the locally generated space charge field in the material, the amplitude of the diffracted field directly behind the grating, U_4 will be proportional to $m(f_x, f_y)$ and so can be written :

$$U_4(f_x,f_y)=mU_2(f_x,f_y) \tag{7-3.4}$$

The Fourier transform of U_4 gives the weighted correlation, u_4, between u_1 and u_2. When the beam ratio is set to a much higher value by attenuating the plane wave reference, where $|U_1|^2 >> |U_3|^2$, then

$$m \approx \frac{2U_3}{U_1} \tag{7-3.5}$$

Thus the low frequency components of U_2 are diffracted by the grating with very low efficiencies. At higher frequencies, where $|U_1| \approx |U_3|$, the modulation is nearer unity leading to the maximum diffraction efficiency. When the input image and reference image are matched the Fourier Transform of U_4, i.e. u_4, produces a high intensity peak in the Output plane. By measuring the height of this correlation output peak the similarity of the two images are assessed. Figure 7-3.3 shows a typical result when an in-class image is correlated with plate 7-3.4, it shows a very high peak at the centre point.

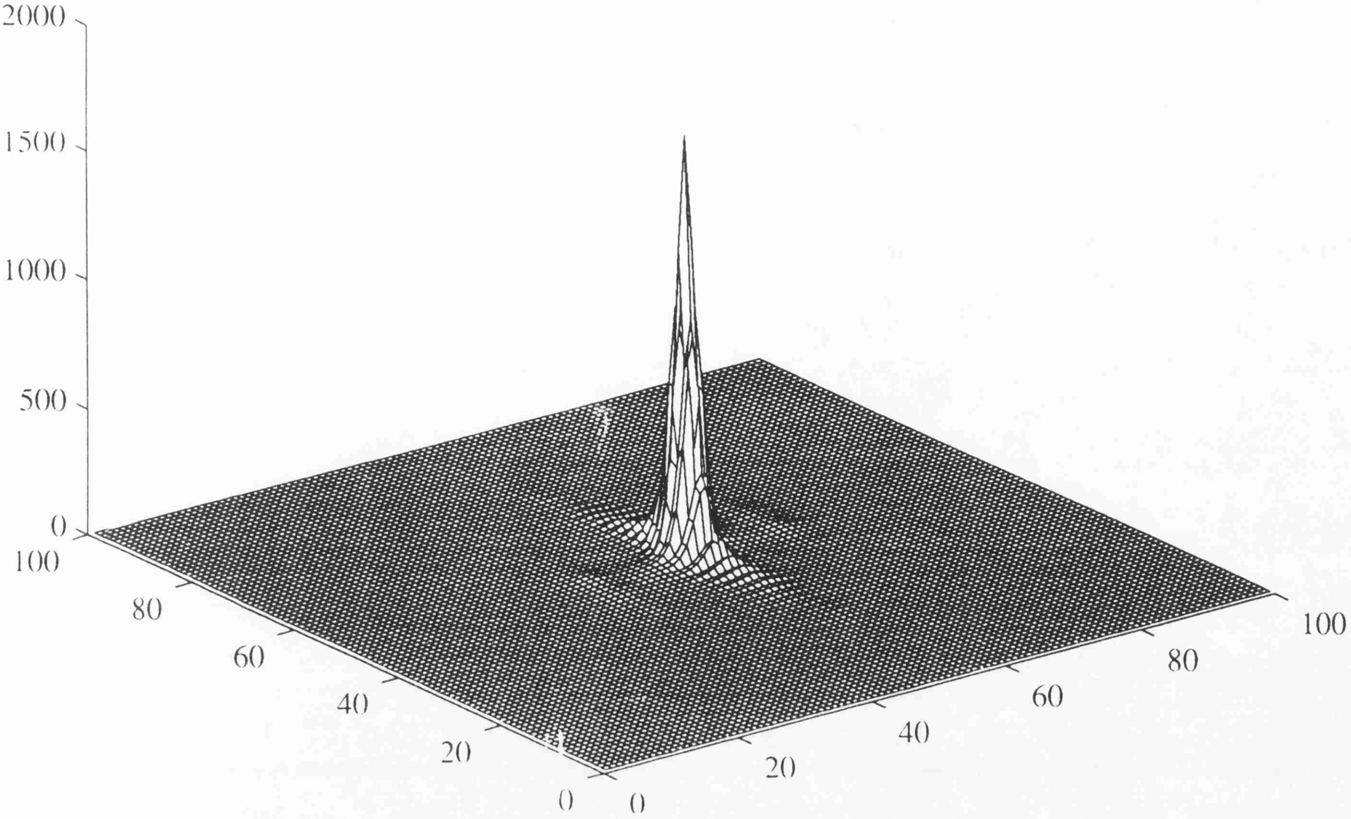

Figure 7-3.3: In-Class Image Correlation Result

7-3.5 Constructing the Synthetic Discriminant Function (SDF) Filter

The $\mathbf{x_i}(x,y)$ training set images for this SDF filter are chosen as the exit spark cone images for high quality cuts produced for different thicknesses of mild steel (in this case there are 6 images). The associated 6*6 correlation matrix, **R**, is tabulated in table 7-3.1.

	Image(1mm)	Image(2mm)	Image(3mm)	Image(4mm)	Image(5mm)	Image(6mm)
Image(1mm)	20.834723	0.31505	0.714349	0.64313	0.811684	1.023015
Image(2mm)	0.385307	7.344074	2.583085	2.043445	2.233399	0.199097
Image(3mm)	0.787047	2.650561	7.207281	2.329284	2.993124	0.252366
Image(4mm)	0.403891	2.157358	2.377481	7.466822	2.784486	0.418255
Image(5mm)	0.518961	2.361227	3.18524	2.811242	8.480209	0.918933
Image(6mm)	0.618913	0.240069	0.22605	0.543606	0.313862	17.085299

Table 7-3.1: Training Set Image Correlation Matrix

By solving equation (7-2.24):

$$\mathbf{a} = \mathbf{R}^{-1}\mathbf{C}_n \qquad (7\text{-}2.24)$$

The weighting coefficients, of **a**, for the SDF filter are obtained, see table 7-3.2:

	a1	a2	a3	a4	a5	a6
coefficient	0.382834	0.780977	0.643022	0.70765	0.405655	0.521982

Table 7-3.2: SDF Weighting Coefficient

The SDF filter is thus formed as equation (7-2.25):

$$H(x,y) = \sum_{i=1}^{N=6} a_i x_i(x,y) \qquad (7\text{-}2.25)$$

Plate 7-3.5 shows the resulting filter. Figure 7-3.4 illustrates the result when an in-class image (this means similar image) is cross-correlated with the filter. Figure 7-3.5 illustrates the result when an out-of-class image (a different image) is correlated with the SDF. The peak height is only 10% of that of the in-class image. The spark cones quality can be assessed by measuring the height of the cross-correlation function.

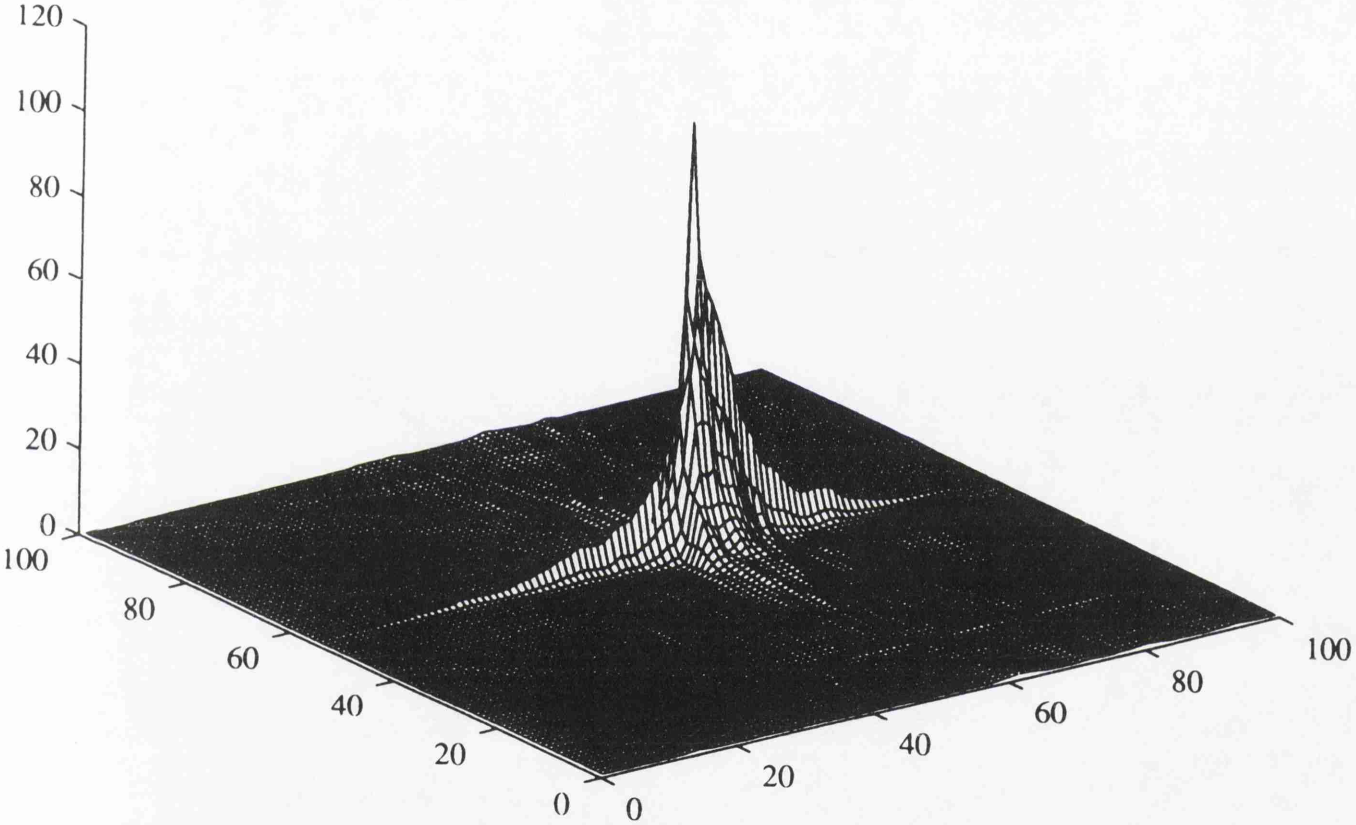

Figure 7-3.4: In-Class Image Correlation Result (Good Cut)

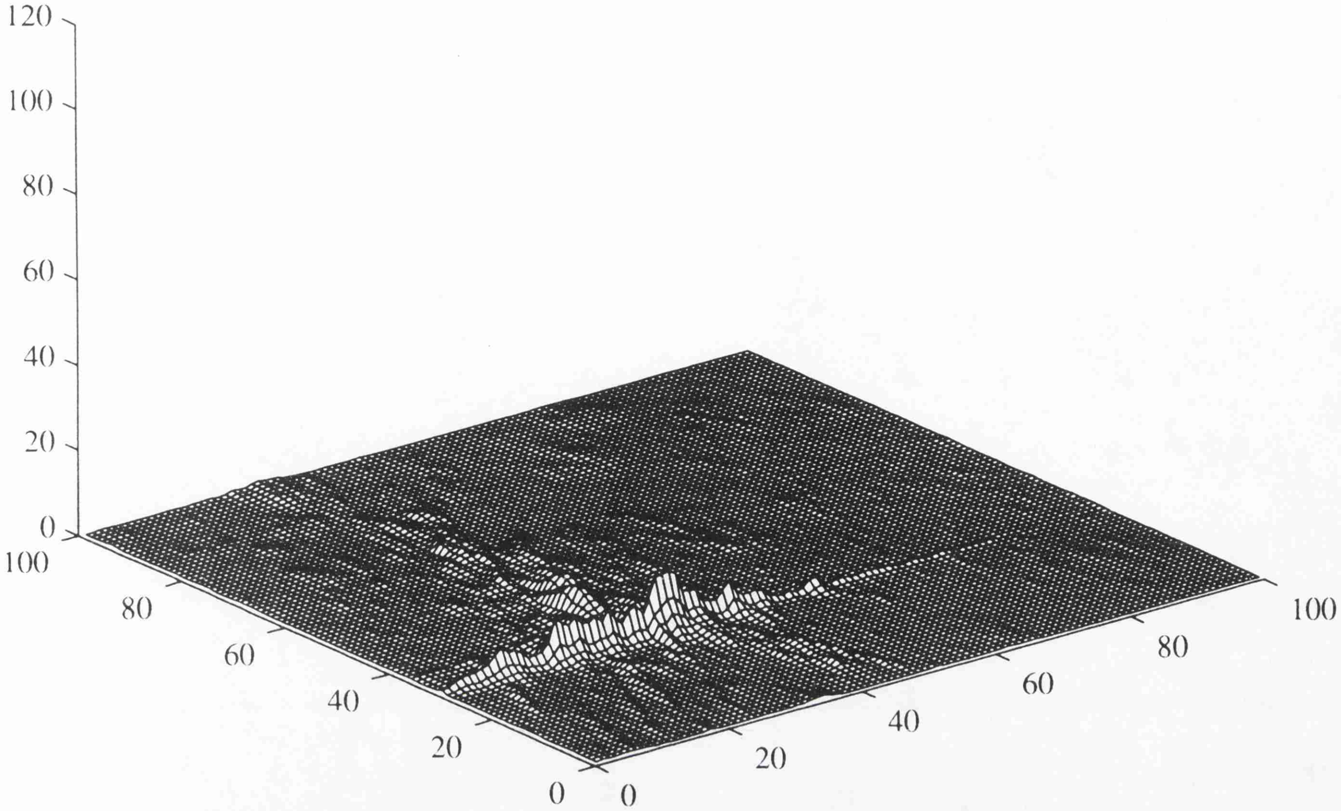

Figure 7-3.5: Out-Of-Class Image Correlation Result (Poor Cut)

7-4 Process Quality Analysis and Consultation Shell

The process quality analysis and consultation sub-system includes a cutting spark cone image grabbing unit, an image pre-processing unit, an image comparison unit, a results comparison analysis unit, an explanation unit to explain the analysis result, and an interface to communicate with the human operator.

Image Grabbing Unit:

The C programming language was used for the application program under the unix environment. Specific function calls from the ITEX image processing library were integrated into the application program to control the specialized digital image processing card. Commands were issued through this image grabbing unit from the operator or the central control unit to the ITEX 150 for grabbing, transferring and displaying the spark cone images.

Image Pre-processing Unit:

Digital image pre-processing techniques described in the theoretical analysis section were adopted to process the reference image from the data base and the image grabbed from the cutting process. First of all, images were smoothed by the averaging window to remove the high frequency noise; that is, the sparse lines and particles in the outer region. Then the smoothed images were thresholded to emphasize the inner intense spark cone. Finally, a digital technique which simulated the BSO method was used to extract the edge information of the thresholded image. The reason for using the edge information, is to generate a highly concentrated sharp peak for the two matched images. The digital simulation of the BSO correlator is described below:

(1) Normalize the energy of the image.
(2) Implement the Fast Fourier Transform on the image.
(3) Calculate the maximum Intensity and determine the Beam Ratio.

(4) Implement the BSO equation (7-3.2)(high pass filter) on the images (frequency domain). After this step, the images are ready for matched filtering.

(5) Inverse Fourier Transform of the above result to obtain the cross correlation.

Image Comparison Unit:

Cross-correlations of the pre-processed reference image and the pre-processed grabbed laser process spark cone images were used to determine the similarity between these two images. The correlation theorem described in sec 7-2.2 was used to implement the correlation. Frequency domain results obtained from the above pre-processing were multiplied and then inverse Fourier Transformed to get the correlation result. A digital implementation was used to simulate the optical cross-correlation operation.

Results Comparison Analysis Unit and Explanation Unit:

The matched filtering result for the two images presents a concentrated high peak in the image plane if the two images are very similar; otherwise, there will be no high peak value. By setting an appropriate threshold value to examine the resulting image plane, the similarity between the reference image and grabbed cutting spark cone images can be assessed. If the peak value is greater than the threshold value, the process is said to have a similar quality to a good cutting process. If not, then the quality of the process is assessed to be poor.

Interface Unit:

This is a graphical interface hosted by the SUN workstation for the system to communicate with the human operator. An X-window environment was used for the following advantages:

(1) mature and well developed package (built-in graphic interface library)
(2) hardware independent environment
(3) C language base environment for a uniform environment (i.e. UNIX)

The system diagram is illustrated as figure 7-4.1.

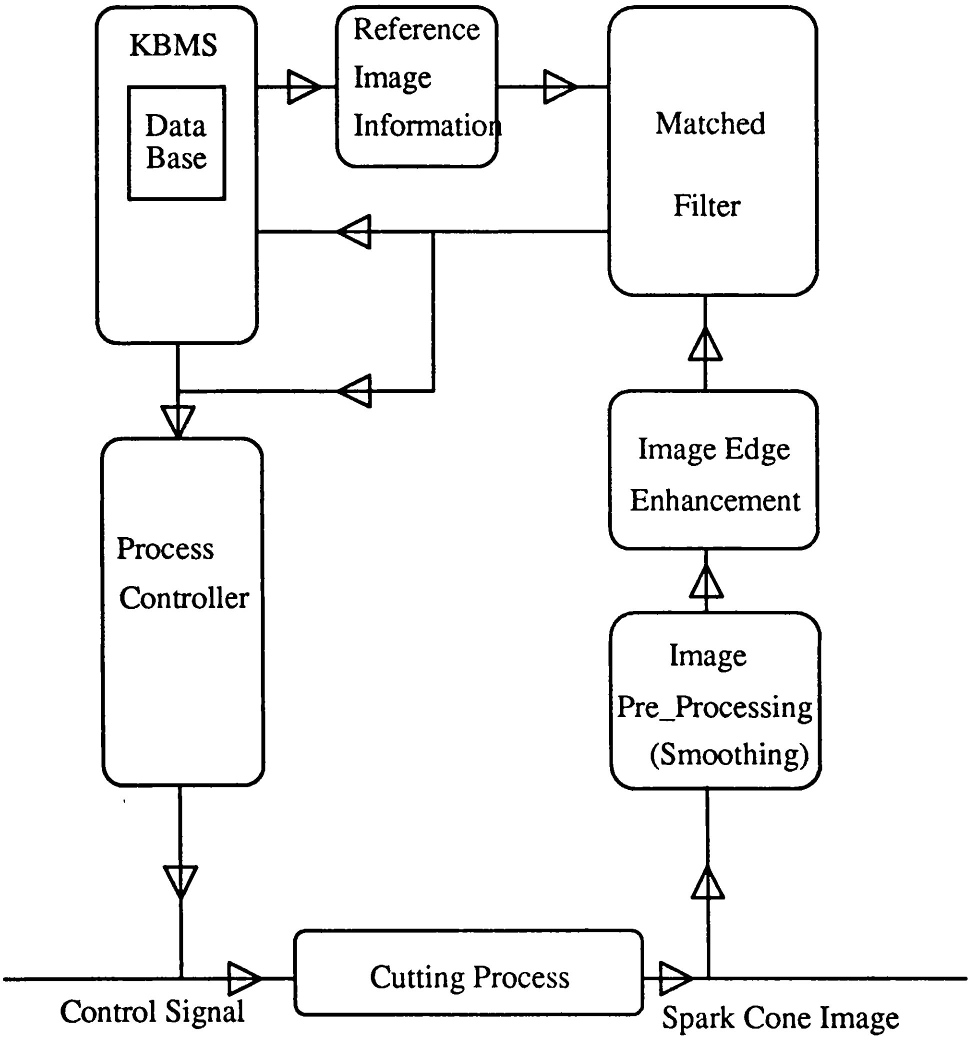

Figure 7-4.1: Digital Software System Diagram

7-5 Matched Spatial Filtering With Wiener Filter Based Synthetic Discriminant Functions (SDF)

The Wiener filter (WF) algorithm has been successfully exploited for image restoration and signal processing [9][10]. The algorithm has also been adopted for optical pattern recognition and evaluated to have better performance than that of CMF, POF, ACMF and conventional SDF. The WF is particularly useful when a high similarity exists between the in-class image, the image to be detected, and the out-of-class image which is to be rejected [11].

A specific SDF filter can be encoded, by using the WFs formed from the spark cone images recorded when cutting different thickness material. This algorithm incorporates the advantages of both the WF and SDF, giving good discriminatory capability between similar images, and a controllable correlation output, respectively. A high cross-correlation peak between the process spark cone image and the filter indicates a good cut quality. On the other hand, a low peak indicates a poor cut quality.

7-5.1 Wiener Filter

Assuming a linear and shift invariant optical system, the general model of a random point spread function image formation system can be written as:

$$g(x,y) = \int_{-\infty}^{\infty}\int_{-\infty}^{\infty} p(x - x_1, y - y_1) f(x,y) dx dy + n(x,y)$$

$$= p(x,y) * f(x,y) + n(x,y) \qquad (7\text{-}5.1)$$

where:
f(x,y) = object image function
g(x,y) = recorded image
n(x,y) = detection noise (out-of-class image)
p(x,y) = random spread point function
* = denotes the convolution operation

An estimate of f(x,y) is given by:

$$\hat{f}(x,y) = w(x,y) * g(x,y) \qquad (7\text{-}5.2)$$

where:
$\hat{f}(x,y)$ = an estimate for f(x,y)
w(x,y) = filter function

The error between the estimated object function and the real function is:

$$e = \left| f(x,y) - \hat{f}(x,y) \right|^2 \qquad (7\text{-}5.3)$$

The Wiener Filter is constructed by minimising the above equation with a least squares algorithm [12]. The Wiener filter is given by:

$$W(f_x,f_y)=\frac{P^*(f_x,f_y)|F(f_x,f_y)|^2+N^*(f_x,f_y)F(f_x,f_y)}{|P(f_x,f_y)|^2|F(f_x,f_y)|^2+|N(f_x,f_y)|^2+D(f_x,f_y)} \qquad (7\text{-}5.4)$$

where:

$$D(f_x,f_y)=P(f_x,f_y)F(f_x,f_y)N^*(f_x,f_y)+N(f_x,f_y)P^*(f_x,f_y)F^*(f_x,f_y) \quad (7\text{-}5.5)$$

F, N, P and W are the Fourier Transforms of f, n, p and w respectively

superscript * = complex conjugate

In pattern recognition applications, the noise is uncorrelated, i.e. independent noise, the correlation of the noise n(x,y) and the object function f(x,y) is zero. That is:

$$n^*(x,y)\otimes f(x,y)=0 \qquad (7\text{-}5.6)$$

$$f^*(x,y)\otimes n(x,y)=0 \qquad (7\text{-}5.7)$$

where: $\otimes$ = correlation operation

From the Correlation Theorem, equation (7-5.6), (7-5.7) may be expressed in the frequency domain as:

$$N^*(f_x,f_y)F(f_x,f_y)=0 \qquad (7\text{-}5.8)$$

$$F^*(f_x,f_y)N(f_x,f_y)=0 \qquad (7\text{-}5.9)$$

Hence, $D(f_x,f_y) = 0$ and the Wiener Filter transform function, $W(f_x,f_y)$, reduces to:

$$W(f_x,f_y) = \frac{P^*(f_x,f_y)}{|P(f_x,f_y)|^2 + |N(f_x,f_y)|^2 / |F(f_x,f_y)|^2} \qquad (7\text{-}5.10)$$

It has the following properties:

(i) As the noise tends to zero, i.e. $|N(f_x,f_y)| \to 0$, the Wiener Filter, $W(f_x,f_y)$, reduces to:

$$W(f_x,f_y) = \frac{P^*(f_x,f_y)}{|P(f_x,f_y)|^2} \qquad (7\text{-}5.11)$$

Which is the transform function of an Inverse Filter. Therefore, when the noise approaches zero, the Wiener Filter behaves like an Inverse Filter.

(ii) As the power of the object goes to zero (i.e. as $|F(f_x,f_y)| \to 0$) the Wiener Filter produces zero modulation. This alleviates problems associated with the zeros of $|F(f_x,f_y)|$ and results in the Wiener Filter being well conditioned.

In optical correlation, the point spread function is replaced by the object function, i.e. the in-class image function. The Wiener Filter transform function, thus, becomes:

$$W(f_x,f_y)=\frac{F^*(f_x,f_y)}{\left|F(f_x,f_y)\right|^2+\left|N(f_x,f_y)\right|^2/\left|F(f_x,f_y)\right|^2} \qquad (7\text{-}5.12)$$

where: $F(f_x,f_y)$ = in-class image function

$N(f_x,f_y)$ = out-of-class image function

Which encodes the in-class image and the out-of-class image into one filter. The filter so constructed has better performance than several traditional filters, as has been evaluated in [11], especially in distinguishing similar objects. This is particularly suitable for assessing the quality of the laser cutting process through the analysis of it's spark cone image. In the laser cutting process, spark cone images from a good quality cutting process and a poor quality cutting process are quite similar. They differ only in the scale of the sparser spark lines, a good cut has few sparse spark lines; whereas, a poor cut has an extensive sparse spark structure. Compare plate 5-3.8 with plate 5-3.11, in chapter 5, which depict the spark cone for a good cut and a poor cut, respectively.

7-5.2 Laser Cutting Spark Cone Characterisation

From Plate 5-3.8 to plate 5-3.11 in chapter 5, which are spark cone images for different dross attachment conditions for mild steel cutting processes. The plates run from plate 5-3.8, dross free, to plate 5-3.11, severe dross attachment. From these plates, it is found that the smaller the sparse spark region the cleaner the cut. There is a high degree of similarity between the images of plate 5-3.8 and plate 5-3.9; however, one is for a clean cut and the other has dross attached to the workpiece lower surface. It is for these circumstances that the wiener filter formulation is extremely useful.

7-5.3 Matched Spatial Filtering With WF Based SDF

Wiener Filter Based SDF

The Wiener Filter transform function is described by equation (7-5.12):

$$W(f_x,f_y)=\frac{F^{*}(f_x,f_y)}{|F(f_x,f_y)|^2+|N(f_x,f_y)|^2/|F(f_x,f_y|^2} \qquad (7\text{-}5.12)$$

By using the clean cut spark cone image as the in-class image and the low dross cut spark cone image as the out-of-class image, the WF for a specific thickness of mild steel cutting process was constructed. The quality of the laser cutting process can then be assessed by cross-correlating this filter with the process image. A high peak indicates a quality similar to the good cut. A lower peak indicates a poor cutting quality. Figure 7-5.1 is the result from a 4 mm mild steel good cutting process, and figure 7-5.2 results from a poor cutting process.

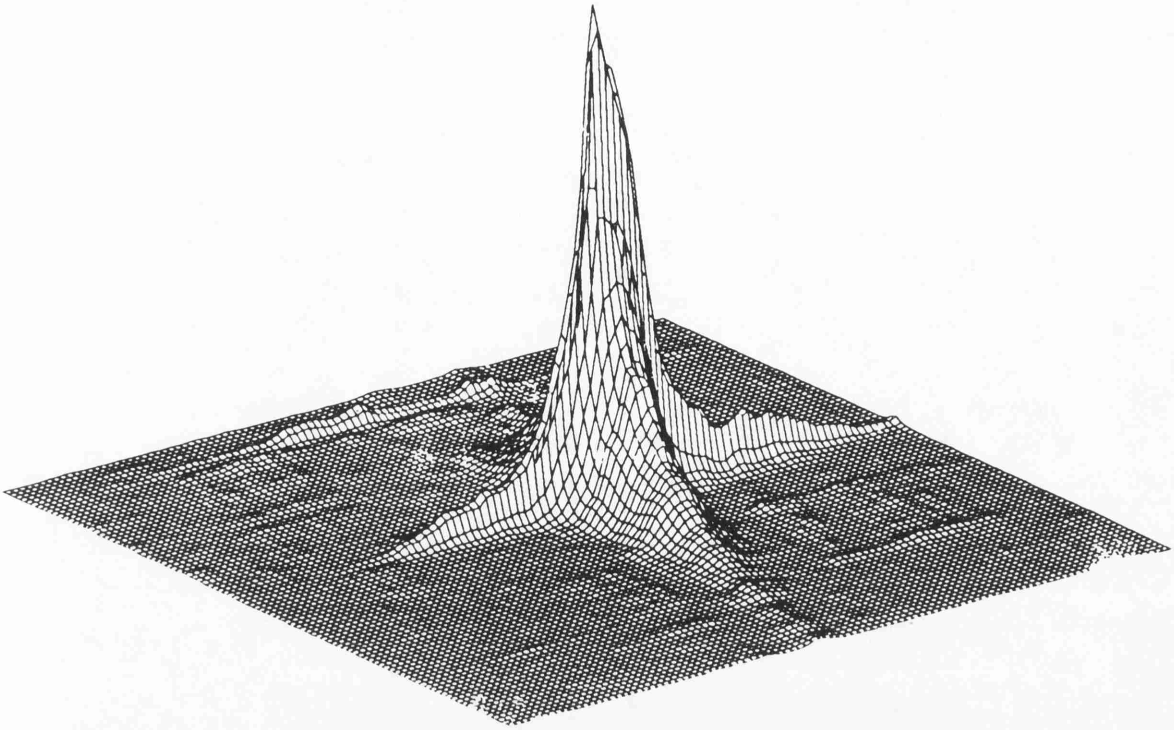

Figure 7-5.1: Cross-Correlation Result From Good Cutting Process Using a WF Filter - 4 mm Mild Steel

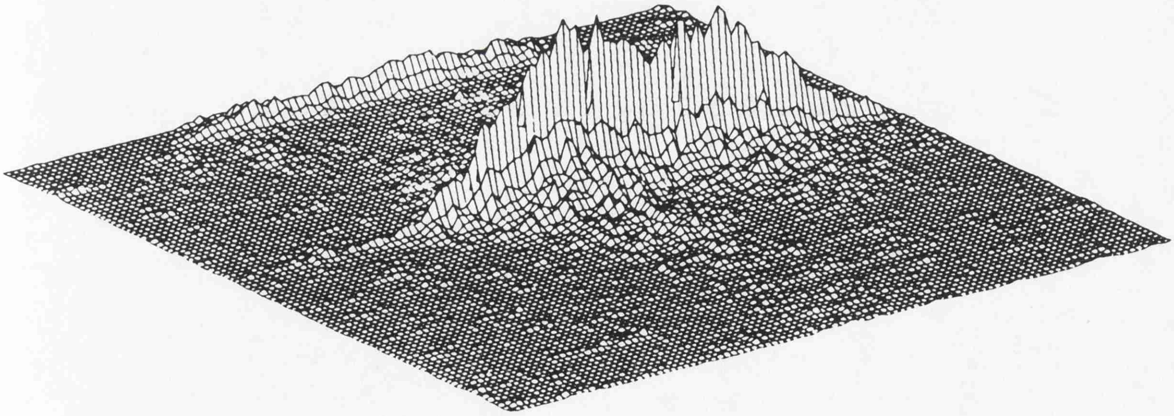

Figure 7-5.2: Cross-Correlation Result From Poor Cutting Process Using a WF Filter - 4 mm Mild Steel

The WF for different mild steel thicknesses was constructed by following the above procedure.

In constructing a synthetic discriminant function (SDF) filter, H(x,y), the following equation was solved to obtain the weighting coefficients.

$$\mathbf{a} = \mathbf{R}^{-1}\mathbf{C}_n \qquad (7\text{-}5.13)$$

where: **a** = the SDF weighting coefficients

C_n = the desired on axis output value

R = the correlation matrix $= \int\int f_i(x,y) f_j^*(x,y)\,dx\,dy$

where: $f_i(x,y)$, $f_j(x,y)$ are the i_{th}, j_{th} training set images

Hence, the SDF is formed from:

$$H(x,y) = \sum_{i=1}^{n} a_i f_i(x,y) \qquad (7\text{-}5.14)$$

A WF based SDF was therefore constructed by incorporating the WF transform function into equation (7-5.13) and solving for the required weighting coefficients, **a**. However, non-uniformly distributed correlation peak heights for in-class images may occur. As this significantly increases the ratio between the highest in-class correlation peak height and the lowest in-class correlation peak height, it degrades the overall discrimination capability of the filter. An iterative technique was used to adjust the relative peak heights so as to generate equal on-axis peak heights for all in-class correlations. The following equation was used to perform this iteration:

$$a_n^{i+1} = a_n^i + \alpha\left[C_n - C_1\left(\frac{|p_n^i|}{|p_1^i|}\right)\right] \qquad (7\text{-}5.15)$$

where: i = number of iteration steps

p = correlation peak height

α = damping coefficient

The threshold value was set to be one percent of the mean value of the correlation peak heights. Iteration stops when all the correlation peak heights fall within the threshold value. The resulting weighting coefficients were then used to construct the WF based SDF. The final weighting coefficients for the mild steel cutting process are tabulated in table 7-5.1.

a1	a2	a3	a4	a5	a6
0.382834	0.780977	0.643022	0.70765	0.405655	0.521982

Table 7-5.1: WF Based SDF Filter Weighting Coefficients

The resulting filter is shown in plate 7-5.1. This WF based SDF filter can thus be used in an optical correlator to assess the quality of a mild steel laser cutting process [13]. A high cross-correlation output peak, between the process image and the filter, indicates good cut quality; figure 7-5.3 illustrates the result. A low cross-correlation output peak indicates that the quality of the process is poor; figure 7-5.4 illustrates the result.

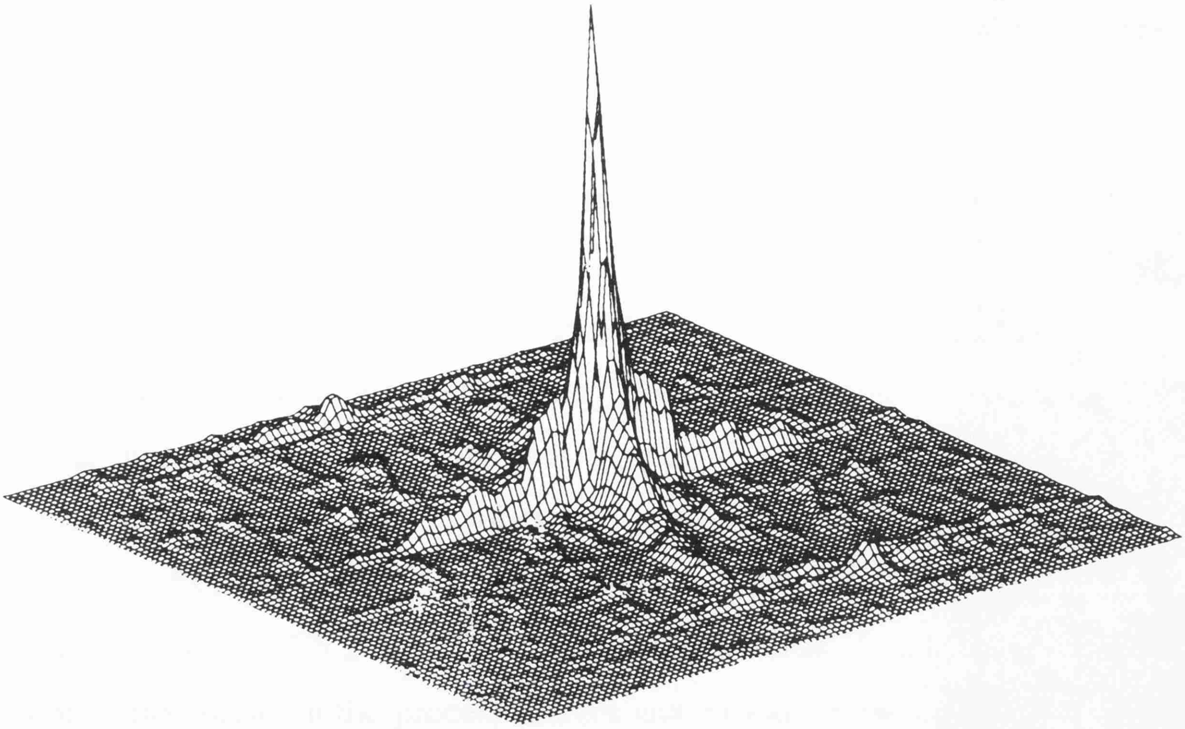

Figure 7-5.3: Cross-Correlation Result From In-Class Image
Using a WF Based SDF - 4 mm Mild Steel (Good Cut)

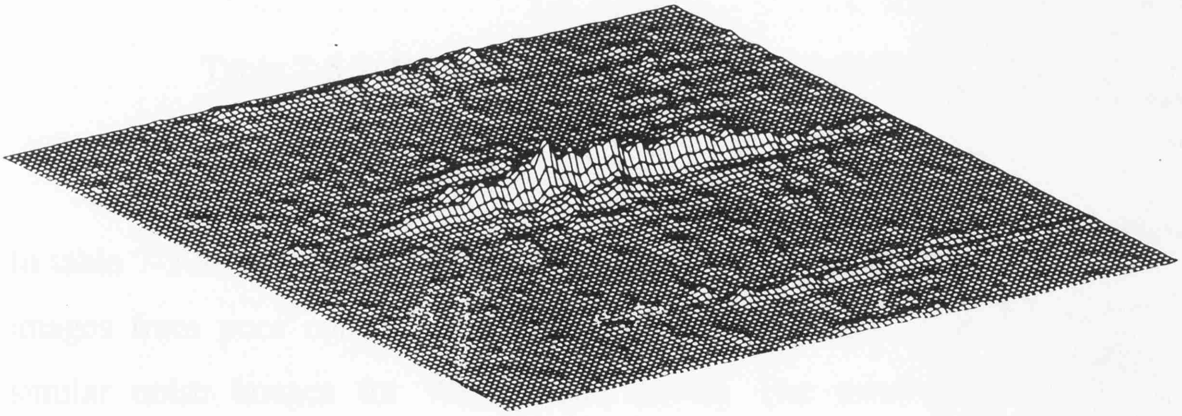

Figure 7-5.4: Cross-Correlation Result From Out-of-Class Image
Using a WF Based SDF - 4 mm Mild Steel (Poor Cut)

Constructing the WF With More Than One Out-of-Class Image

As mentioned previously, spark cone images generated during poor cutting processes may be similar to those for good cutting processes. Consequently, these images may make it difficult for the filter to distinguish a good cut process from a poor one. A solution to this problem is to combine a greater number of similar images from poor cutting processes into the construction of the WF. Table 7-5.2 lists the relative output peak heights of the cross-correlation between the process images and various Wiener Filters for 4 mm mild steel.

			Image from various quality laser cutting processes					
Filter		Good-Cut	Poor-Cut:1	Poor-Cut:2	Poor-Cut:3	Poor-Cut:4	Poor-Cut:5	Poor-Cut:6
WF-n2	Cross-	1	0.057624	0.160671	0.022425	0.175566	0.185687	0.321251
WF-n3	Correlation	1	0.095241	0.154374	0.118427	0.024655	0.147992	0.301716
WF-n4	Peak	1	0.096979	0.16576	0.170749	0.186851	0.021176	0.342648
WF-n5	Height	1	0.10092	0.166343	0.158215	0.170746	0.36685	0.017969

Table 7-5.2: Relative Cross-Correlation Peak Heights

In table 7-5.2, the various filters were constructed by combining two similar images from poor cutting processes as the noise image for WF-n2, three similar noise images for WF-n3, and so on. The results are presented graphically in figure 7-5.5.

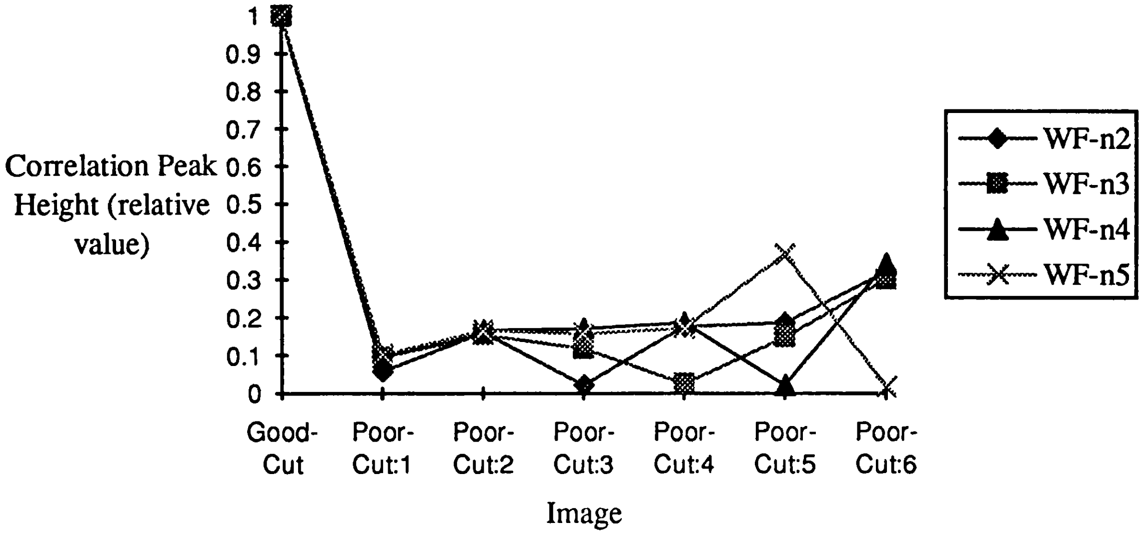

Figure 7-5.5: Relative Cross-Correlation Peak Heights

The maximum out-of-class image (poor cutting process) cross-correlation resulting from each filter is illustrated in figure 7-5.6.

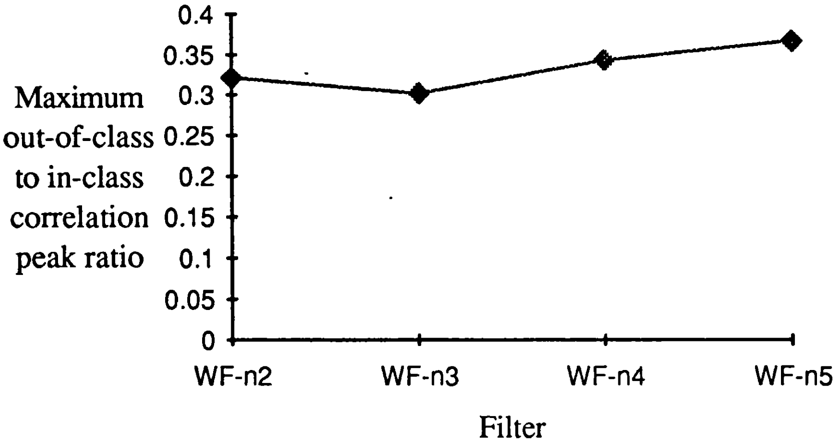

Figure 7-5.6: Maximum Out-Of-Class to In-Class Images Cross-Correlation Peak Ratio

By incorporating five similar spark cone images from poor cutting processes into the filter construction, the maximum cross-correlation output peak from the out-of-class image was 37% of that from the in-class image; hence, discrimination is excellent. It was found that the WF-n3 Wiener filter, constructed by incorporating three out-of-class images (poor cut images), gave the best discrimination performance. This indicates that if too many out-of-class images are incorporated into the filter, the information content saturates beyond the optimum discrimination level and performance deteriorates.

7-5.4 Conclusion

The Wiener Filter (WF) and Synthetic Discriminant Function (SDF) algorithms are combined to construct a matched filter which can be used in an optical correlator for assessing the quality of a laser cutting process. Images from good quality cutting processes and poor quality cutting processes are incorporated into the WF construction. This increases the filter's capability to differentiate between spark cone images that indicate a good quality, from very similar images that characterise a poor quality cutting process. With the SDF formulation, WFs for different material thicknesses were built into a single filter which is able to assess the quality of the cutting process for a specific material, i.e. mild steel, through the analysis of the height of the cross-correlation output peak. Furthermore, it was shown that the discrimination capability of the WF could be enhanced by including several out-of-class images. For these experiments three out-of-class images gave optimum performance.

7-6 Conclusion and Proposed Schematic for Optical Implementation

Characteristically intense spark cones were formed during dross free cutting processes. Sparse cones characterised processes where dross attached itself to the lower surface of the workpiece. The quality of the laser cutting processes can be evaluated by correlating the in-process grabbed spark cone images with reference images and measuring the height of the correlation peak. A high peak indicates a high similarity between images and a good cut quality. The Synthetic Discriminant Function (SDF) filter can be utilized to form an optimal filter for evaluating the quality of the cutting process. Spark cone images of cutting processes on different material thicknesses were used to construct an SDF filter, by calculating the SDF coefficients, an optimal filter was constructed and used to assess the cutting quality for mild steel. Figure 7-6.1 illustrates the design of an optical correlator with the SDF filter as the reference image. This device is currently under construction and will be capable of real-time control of the cutting process by monitoring the exit spark cone images.

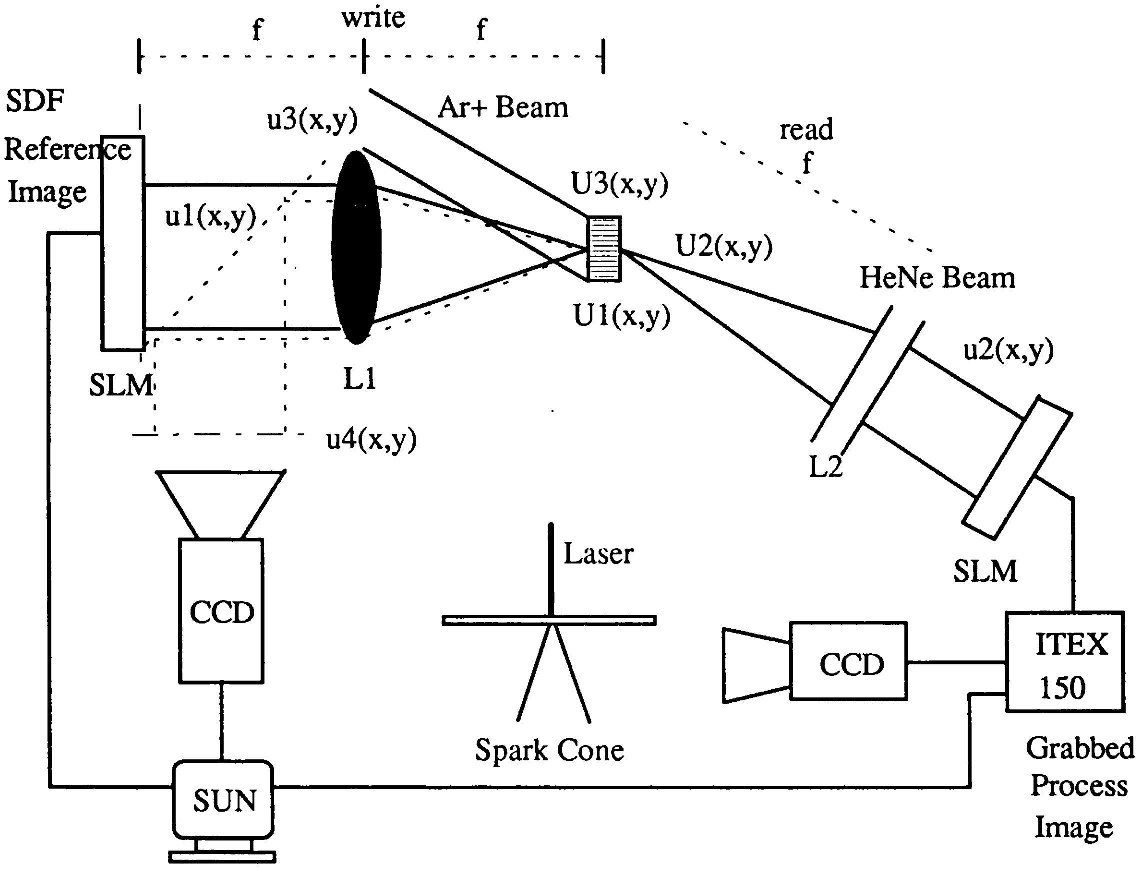

Figure 7-6.1: System Diagram of Updateable Correlator

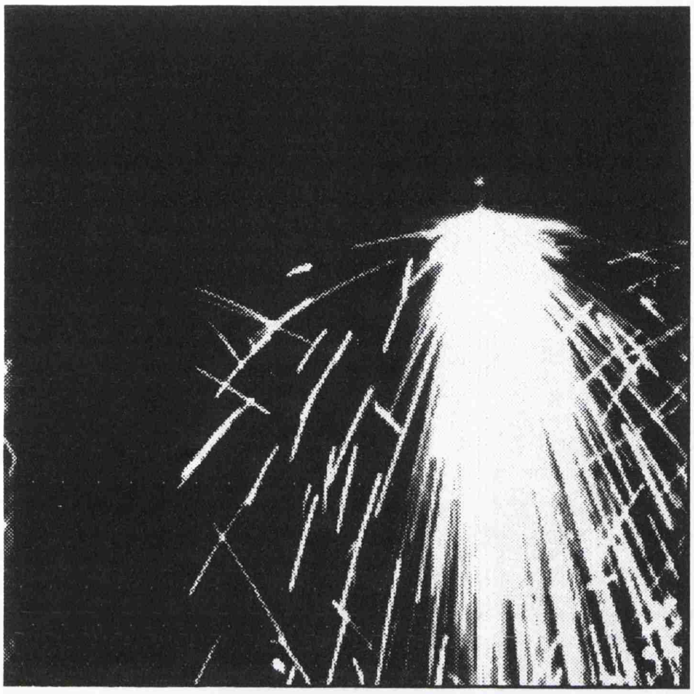

Plate 7-3.1: Original Spark Cone Image

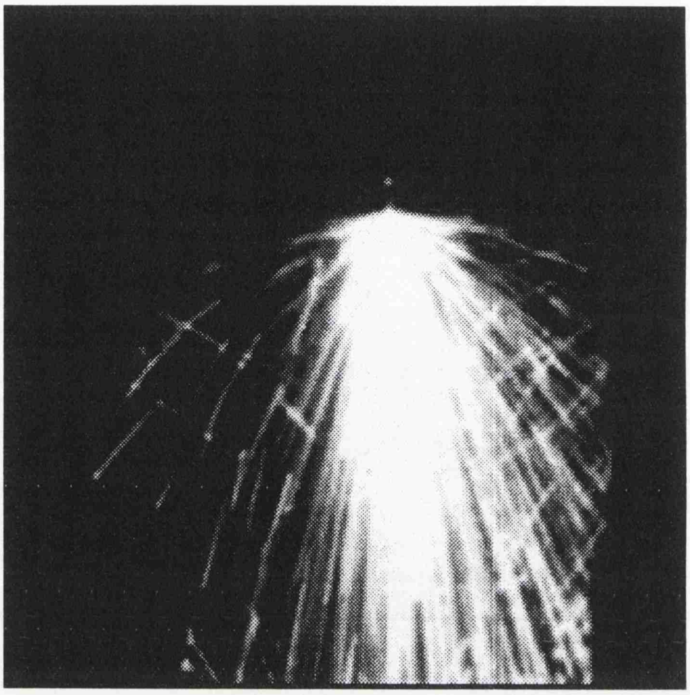

Plate 7-3.2: Spark Cone Image Smoothing

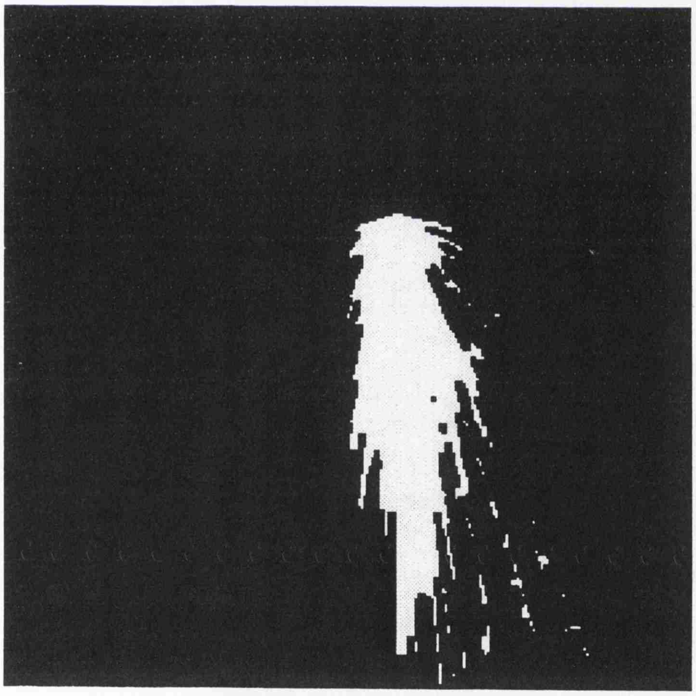

Plate 7-3.3: Spark Cone Image Thresholding

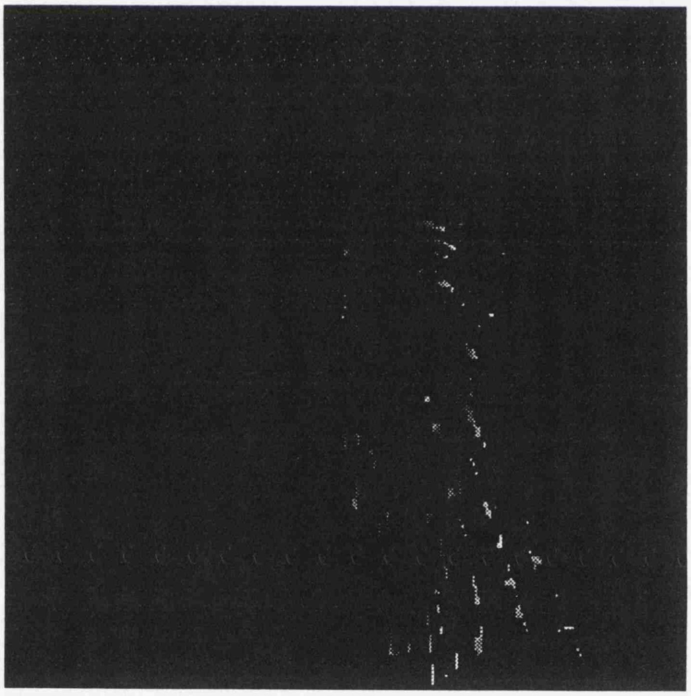

Plate 7-3.4: BSO Edge Enhancement

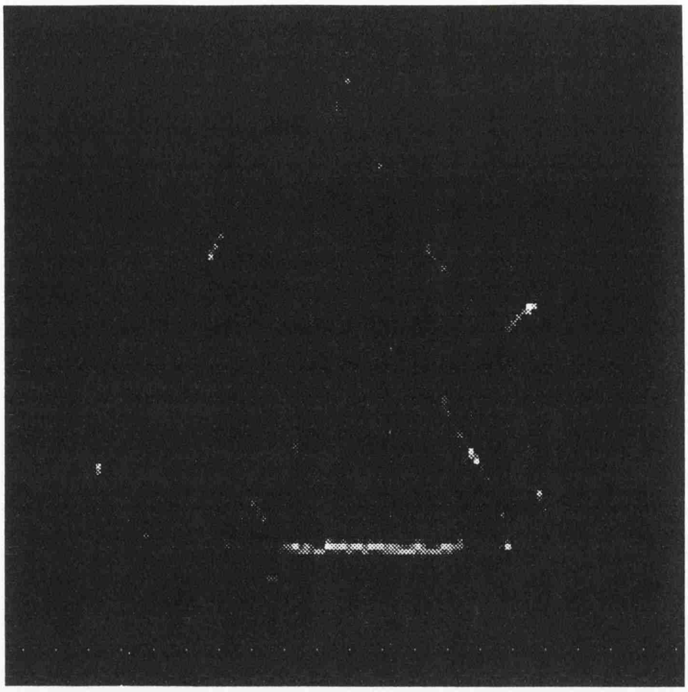

Plate 7-3.5: SDF Filter (Mild Steel Cutting)

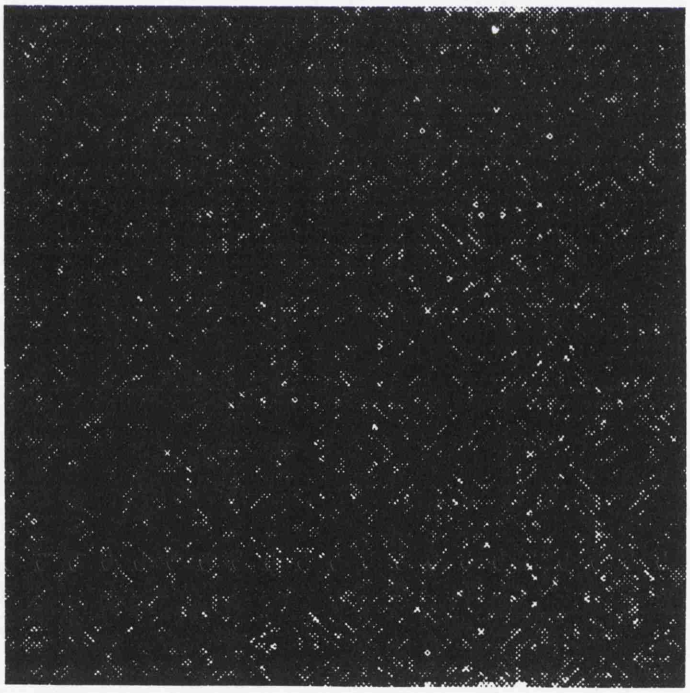

Plate 7-5.1: WF Based SDF Filter (Mild Steel)

7-7 References

[1] Signal Detection By Complex Spatial Filtering, by Vander Lugt, IEEE Transactions on Information Theory, 1964

[2] Photorefractive Materials And Their Applications To Optical Processing, by P. Foote, T. Hall, N. Aldridge, and A. Levenston, IEE Proc. Vol. 133, Pt. J., No. 1, 1986

[3] Efficiency And Polarisation Characteristics Of Photorefractive Diffraction In a $Bi_{12}SiO_{20}$ Crystal, by S. Mallick, D. Roude, and A. Apostolidis, JOSA, Vol. 4, No. 8, 1987

[4] Non Destructive Testing Using Real Time Holographic Interferometry In B.S.O. Crystals, by J. P. Herriau, A. Delboulbe, and J. P. Huignard, Proceedings of SPIE, Vol 398, April 1986

[5] Dynamic Frequency Plane Correlator, by I. R. Cooper, M. G. Nicholson, and C. R. Petts, IEE Proceedings, Vol 133, Pt. J, No. 1, Feb. 1986

[6] Design and Simulation of a Synthetic Discriminant Function Filter For Implementation in an Up-dateable Photorefractive Correlator, by R. C. D. Young and C. R. Chatwin, SPIE Vol. 1701 Optical Pattern Recognition III, 1992

[7] Optical Character Recognition Based On Non-redundant Correlation Measurements, by B. Braunecker, R. Hauk, and A. Lohmann, Appl. Opt. Vol. 18, 1979

[8] Unified Synthetic Discriminant Function Computational Formulation, by D. Casasent, Appl. Opt. Vol. 23, No. 10, 1984

[9] Digital Picture Processing: An Introduction, by L.P. Yaroslavsky, Springer-verlag, Berlin, 1985

[10] Digital Image Restoration, by H.C. Andrews and B.R. Hunt, Prentice-Hall Inc. Endlewood Cliffs, New Jersey, 1977

[11] Assessment of a Wiener Filter - Synthetic Discriminant Function For Optical Correlation, by R.K. Wang, C.R. Chatwin and R.C.D. Young, Optics and Lasers in Engineering, under review

[12] Quantitative Coherent Imaging, by J.M. Blackledge, Academic Press Limited, London, 1989

[13] Spark Cone Characterisation For Control of Laser Cutting, by M.Y. Huang and C.R. Chatwin, J. of Lasers in Engineering, 1994, in press

CHAPTER 8

Conclusions and Suggestions for Future Work

PAGE

8-1 Conclusion

The laser cutting process is influenced strongly by characteristics such as: power mode (i.e. CW or pulsed), power density, transverse mode, beam polarisation; set-up of operating system such as: beam delivery optics, nozzle type, assist gas type and gas pressure, beam focusing, laser beam operating position (offset), and feedrate; and characteristics of target material such as: conductivity, diffusivity, melting temperature, boiling temperature, latent heat of melting and vaporisation, plasma formation, exothermic chemical reaction with reactive gas O_2, and relevant viscosities. So many parameters are involved that inevitably laser cutting is a highly non-linear process.

Theoretical analysis, based on laser - material interaction, provided a basic model for the gas assisted laser cutting process. Empirical investigations of the relationship between the cut quality and the operational parameters (i.e. nozzle head offset distance which then determines the position of the focused beam spot, assist gas pressure, and laser beam feedrate) also established knowledge for laser cutting.

As long as the cut can be initiated, change of the focal height offset distance does not influence the size of the heat affected zone (HAZ). The kerf surface roughness is slightly increased when the offset distance is increased. The best position of the focused laser beam spot, for cutting mild steel up to 6 mm in thickness, is on the surface. Increasing the assist gas supply pressure reduces the size of the HAZ slightly; with little improvement on the kerf surface roughness. In the gas assisted laser cutting process, assist gas supply pressure is, therefore, normally set to an economic level. 2 bar is the optimum for this

CO_2 laser cutting system. The effects are more pronounced on the mild steel than stainless steel because of the higher viscosity of liquid phase stainless steel. For the same reason, dross attachment is normally found in stainless steel cutting; whereas, clean cuts are generally obtainable for mild steel. Slower feedrate increases both the size of the HAZ and the roughness of the kerf surface. That is, the cut quality is greatly affected by changing the laser beam feedrate. Therefore, feedrate was chosen as the major control parameter in the cutting system.

Spark cone images from the workpiece lower surface are analysed. An intense cone was observed when a clean cut was performed. Sparser spark cone images were characteristic of poorer quality cuts where dross attachment disturbs the gas-metal mixture flow.

A PC based, hierarchically structured environment that integrates a knowledge-based expert system, adaptive process control and pattern recognition techniques for controlling a laser cutting process was developed to assist the CO_2 laser cutting process. Knowledge of the laser cutting process for different materials, obtained from both theoretical analysis and empirical investigation, is organised and encoded into a rule-based system. An adaptive control algorithm based on on-line recursive parameter estimation and on-line control law synthesis was adopted for the highly non-linear cutting process control. Cutting speed was selected as the major control variable. Irradiance emitted from the cut front was used for the feedback signal to this adaptive controller. The irradiance signal feeds the recursive parameter estimator for system identification. Techniques of pattern recognition, which have been well developed in coherent optics, were applied to the cutting quality analysis by characterising the exit spark cone images of the gas assisted laser cutting process. A digital software program was developed, based on matched spatial filtering techniques using synthetic discriminant function (SDF) implemented in the photorefractive material (BSO), as the specific filter to assess the spark cone images generated during the laser cutting process. Images from the cutting processes were grabbed, edge enhanced and cross-correlated with a synthetic discriminant function filter which was synthesised from reference images known to give good cut quality. A high correlation peak, which indicates a good cut quality, is generated when an in-class spark cone image cross-correlates with the filter.

The SDF discrimination performance was enhanced by incorporating the Wiener filter into its construction, such that the in-class image, image from good cutting process, and out-of-class image, image from poor cutting process, were integrated into a single filter. It was found, through experimental investigation, that the incorporation of three out-of-class images gave optimum performance; if a greater number out-of-class images were incorporated into the filter its performance degraded.

8-2 Future Work

In laser cutting, the most difficult task is to determine the optimal operational parameters under different conditions for various materials. A precise, effective, and generalised cutting model will greatly reduce the cost for the complex control system and benefit academic researchers and industrial users. In studying the cutting phenomena, non-linear step-wise striation patterns were observed on the workpiece kerf surfaces. This particular phenomena provides another way of viewing the cutting process which will be enormously assisted by the newly developed science of chaos theory. Since, the non-linear, unpredictable nature of the laser cutting process lends itself to a chaotic description.

Models established from Chaos theory should be incorporated into the adaptive process controller to reduce the complexity of process models and hence improve the overall system response.

By tuning the filter response using input scene noise the system can be made to give a graded response rather than simply a binary accept/reject signal; this should be exploited to create an adaptive discriminant capability that allows the knowledge base to give a more measured assessment of quality.

Knowledge from laser cutting can be organised and built into a self-learning system. Which can then be incorporated into the adaptive process controller along with the spark cone image quality evaluation shell to provide a totally self-learning system which can learn and adjust itself during the cutting process and thus refine its knowledge base.

Appendix (A1): Polarization Control Unit

A1.1 Introduction

The efficiency and quality of laser processing is greatly affected by the direction of the polarization. Normally, the cutting process benefits from adjusting the laser polarization parallel to the processing trajectory. The laser beam polarization can be controlled by using a phase-shifting unit, integrated with a control circuit, in the beam delivery system.

A1.2 Unit Design

The Forth axis of the CNC controller was used as the rotating axis, this can be integrated into the control system by using another Heidenhain EXE602D. The unit system diagram is shown in figure A1.1. A circularly polarized laser beam enters the 4 mirror ECQ, which introduces a $1/4\ \pi$ phase shift to the beam, and converts the beam to a linear polarization state. The direction of the resulting polarization is decided by the direction of the 4 mirror ECQ. The desired processing direction of the polarization is controlled by rotating the 4 mirror ECQ with a rotation stage through the TNC controller. The integrated control circuit is shown in figure A1.2.

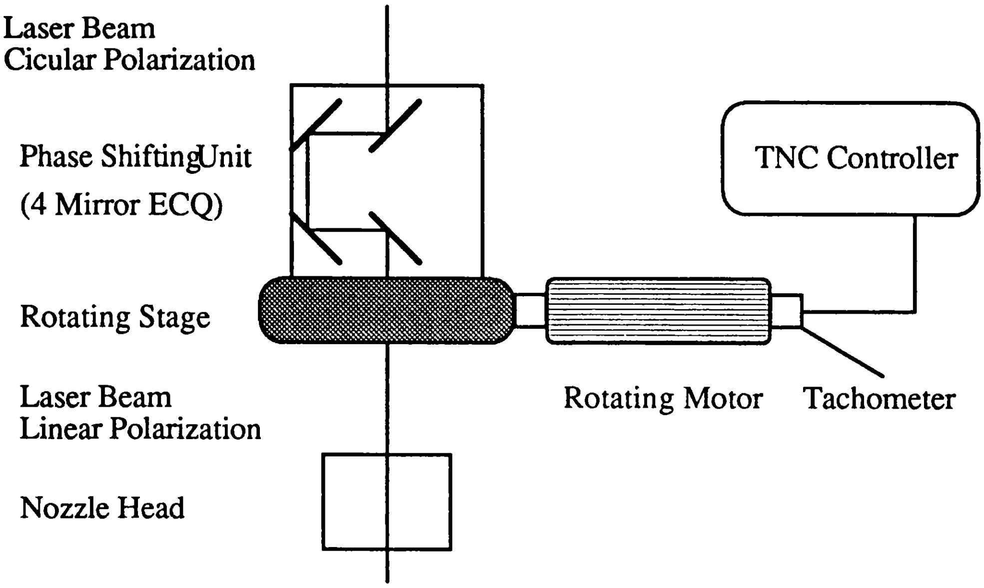

Figure A1.1: Polarization Control Unit Diagram

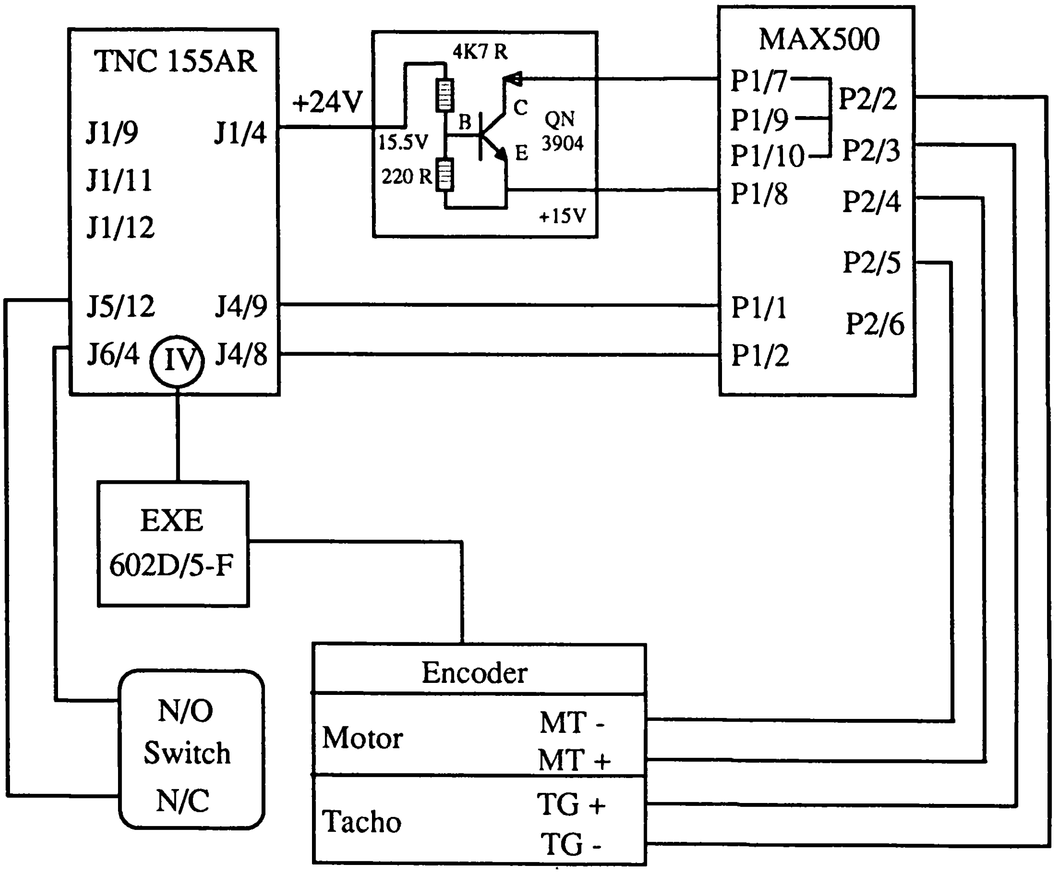

Figure A1.2: Control Circuit Diagram